

Gallium-based Ultraviolet Nanoplasmonics

by

Yang Yang

Department of Physics
Duke University

Date: _____

Approved:

Henry Everitt, Co-supervisor

April Brown, Co-supervisor

Gleb Finkelstein

Ying Wu

Ronen Plesser

Dissertation submitted in partial fulfillment of the requirements
for the degree of Doctor of Philosophy
in the Department of Physics in the Graduate School
of Duke University

2013

ABSTRACT

Gallium-based Ultraviolet Nanoplasmonics

by

Yang Yang

Department of Physics
Duke University

Date: _____

Approved:

Henry Everitt, Co-supervisor

April Brown, Co-supervisor

Gleb Finkelstein

Ying Wu

Ronen Plesser

An abstract of a dissertation submitted in partial fulfillment of the requirements
for the degree of Doctor of Philosophy
in the Department of Physics in the Graduate School
of Duke University

2013

Copyright by
Yang Yang
2013

Abstract

Nanometer-scale metallic structures have been widely and intensively studied over the last decade because of their remarkable plasmonic properties that can enhance local electromagnetic (EM) fields. However, most plasmonic applications are restricted to the visible and near infrared photon energies due to the limitations of the surface plasmon resonance energies of the most commonly used plasmonic metals: Au and Ag. Plasmonic applications in ultraviolet (UV) are of great interest because Raman scattering sections are larger and do not overlap fluorescence spectra. UV plasmonics also benefit from high spatial resolution and low penetration depth. However, an appropriate UV plasmonic material must be identified.

We proposed and demonstrated that gallium is a highly-promising and compelling material for UV nanoplasmonics through synthesis of size-controlled nanoparticle arrays, EM modeling of local field enhancement, ellipsometric and spatial characterization of the arrays, and analytical measurement of UV-enhanced Raman and fluorescence spectra. Self-assembled arrays of hemispherical gallium nanoparticles deposited by molecular beam epitaxy on a sapphire support are characterized with spatial and ellipsometric measurements.

Spin-casting a thin film of crystal violet upon these nanoparticles permitted the demonstration of surface-enhanced Raman spectra, fluorescence, and molecular photodegradation following excitation by a HeCd laser operating at 325 nm (UV). Measured local Raman enhancement factors exceeding 10^7 demonstrated the potential of gallium nanoparticle arrays for plasmonically-enhanced ultraviolet detection and remediation.

To the future.

Contents

Abstract.....	iv
List of Tables.....	xii
List of Figures.....	xiii
List of Abbreviations.....	xix
Acknowledgements.....	xx
1. Introduction.....	1
1.1 UV radiation and its applicaions.....	1
1.1.1 UV Raman spectroscopy and SERS.....	3
1.1.2 Fluorescence.....	8
1.2 Plasmonics and metallic nanoparticles.....	10
1.3 Motivations: UV SERS and gallium nanoparticles.....	12
1.4 Summary of work.....	16
2. Plasmonic Nanoparticles and their Optical Properties.....	18
2.1 Plasmonic nanoparticles.....	18
2.1.1 Nanoparticles.....	18
2.1.2 Plasmonics.....	20
2.2 Estimate of metallic NP's optical properties.....	28
2.2.1 A scattering setup.....	29
2.2.2 Rayleigh scattering.....	32
2.2.3 Mie scattering.....	39

2.2.4 Discrete dipole approximation.....	44
3. Polarization and Spectroscopic Ellipsometry	57
3.1 Polarization	57
3.1.1 Jones vector	58
3.1.2 Instantaneous optical field.....	58
3.1.3 State of polarizaiton (SoP).....	60
3.2 Reflection at surface.....	62
3.2.1 Fresnel equations.....	64
3.2.2 Reflection from dielectrics and metals.....	66
3.2.3 Jones matrix	71
3.3 Spectroscopic ellipsometry	72
3.3.1 Measured quantities	73
3.3.2 Measurement	75
3.3.3 Pseudodielectric function.....	78
4. Controlled Synthesis of Ga Nanoparticle Ensembles	81
4.1 Physical deposition process of metal NPs.....	81
4.1.1 Molecular beam epitaxy	81
4.1.2 Gallium nanoparticle ensemble growth mechanism	85
4.1.3 Deposition rate and Ga dose	90
4.2 Controlled synthesis	93
4.2.1 Controlled deposition parameters.....	93
4.2.2 In situ monitoring with spectroscopic ellipsometry	96

4.2.3 Samples.....	98
5. Spatial Characterization of Ga Nanoparticle Ensemble.....	100
5.1 Instrument.....	100
5.1.1 Atomic force microscopy	100
5.1.2 Scanning electron microscope	102
5.2 Spatial information of Ga NP ensembles.....	105
5.2.1 Ga NP ensembles overview	105
5.2.2 Statistics on NP morphology.....	106
5.2.3 Temperature impact on Ga NP ensemble morphology	112
6. Spectroscopic Ellipsometry Modeling	117
6.1 SE modeling principle	117
6.1.1 Effective medium approximation.....	117
6.1.2 SE model of Ga NP ensemble.....	118
6.1.3 Lorentz oscillator.....	120
6.1.4 Multilayer reflection	123
6.1.5 SE model fitting.....	126
6.2 SE modeling result.....	128
6.2.1 A typical sample.....	128
6.2.2 Modeling result for samples Y1 ~ Y7	133
6.2.3 Ga NP's LSPR mode	135
6.2.4 Size dependence of NP's LSPR mode	137
6.2.5 Single NP behavior of Ga NP ensemble's in-plane LSPR dipole mode	141

6.2.6 Comparison with theoretical modeling	144
7. Variable-angle SE and Mueller matrix.....	148
7.1 Variable-angle spectroscopic ellipsometry (VASE)	148
7.1.1 Principle and instrument	148
7.1.2 Variable-angle reflection	151
7.1.3 VASE measurement.....	156
7.2 Variable-angle Mueller matrix (VAMM).....	163
7.2.1 Stokes vector and Mueller matrix.....	163
7.2.2 Mueller matrix representation of reflection	167
7.2.3 Mueller matrix polarimetry	170
7.2.4 VAMM measurement.....	172
8. UV SERS and UV SEF: A Demonstration.....	180
8.1 Theory of Raman scattering	180
8.1.1 Molecular vibration	180
8.1.2 Raman scattering.....	183
8.1.3 Raman scattering intensity	185
8.2 Surface-enhanced Raman scattering	186
8.2.1 EM origin of SERS.....	186
8.2.2 Chemical origin of SERS	189
8.2.3 SERS active substrate.....	190
8.3 UV SERS: a demonstration	193
8.3.1 Instrument.....	193

8.3.2 Analyte.....	195
8.3.3 Sample preparation.....	196
8.3.4 Spectroscopy	197
8.3.5 Enhancement	199
9. UV SERS and UV SEPD: Hotspot Analysis.....	204
9.1 Temporal analysis	204
9.2 Spatial analysis	209
10. Conclusions and Perspectives	219
10.1 Conclusions.....	219
10.2 Perspectives	222
10.2.1 Improved structures and extended applications.....	222
10.2.2 Corrected modeling and spatially resolved characterization.....	223
10.2.3 UV plasmonic materials	225
References	227
Biography	249

List of Tables

Table 1.1: Bulk plasmon energy for common metals.....	13
Table 2.1: Local field enhancement $ g ^2$ profiles for Ga, Au, and Ag.....	35
Table 3.1: Jones vector representation of states of polarization	61
Table 4.1: Growth condistions for samples Y1 ~ Y7	99
Table 5.1: Statistics on NP morphology for sample Y1, Y3, and Y6	111
Table 6.1: Fitted SE model paramters for sample Y3	129
Table 6.2: Fitted SE model paramters for sample Y1 ~ Y 7	130
Table 7.1: Jones vector and Stokes vector representations of states of polarization	164
Table 7.2: Mueller matrix representation of basic optical elements	166
Table 9.1: Time constants for the fast and slow decays of the fluorescence and Raman signals under four different laser pump intensities	211
Table 9.2: Contribution of the various site enhancements to the overall SERS signal	217

List of Figures

Figure 1.1: Electromagnetic spectrum.....	2
Figure 1.2: Jablonski diagram of Raman scattering and fluorescence.....	9
Figure 1.3: Poynting vector plot of an Al sphere illuminated by light where resonance occurs (left) and where there is no resonance (right).....	11
Figure 1.4: LSPR energies of various nanostructures	14
Figure 2.1: Dispersion relation at the metal-dielectric interface	22
Figure 2.2: Schematic diagram of surface plasmon.....	22
Figure 2.3: Dielectric function of bulk gallium	24
Figure 2.4: Schematic diagram of localized surface plasmon	25
Figure 2.5: Time averaged charge density distributions for dipole and quadrupole LSPR modes	26
Figure 2.6: Schematic diagram of a scattering problem	29
Figure 2.7: Dielectric function of Ga by Drude model fitting.....	33
Figure 2.8: Local field enhancement $ g(\omega) ^2$ for a free standing spherical Ga NP in vacuum calculated by Rayleigh scattering	34
Figure 2.9: Contour plots of local EM field enhancement $ g_{EM} ^2$ surrounding a free standing spherical Ga NP in vacuum under Rayleigh approximation excited by external radiation at (a) 3.5 eV; (b) 5.0 eV; (c) 6.5 eV; and (d) 8.0 eV. (NP radius: 10 nm)	36
Figure 2.10: Energy dependence of maximum local EM field enhancement surrounding a free standing spherical Ga NP in vacuum under Rayleigh approximation	38
Figure 2.11: Extinction, scattering, and absorption efficiencies for free standing spherical Ga NP with different size parameters in vacuum.....	42

Figure 2.12: Extinction efficiencies for free standing spherical Ga NPs with different radii in vacuum	44
Figure 2.13: Scattering system of a hemispherical Ga NP on sapphire substrate for the modeling using DDA method	48
Figure 2.14: Absorption efficiencies for different NP/substrate setup (a) free standing spherical Ga NP; (b) spherical NP on square sapphire substrate; (c) free standing hemispherical Ga NP; and (d) hemispherical Ga NP on square sapphire substrate	50
Figure 2.15: Absorption efficiencies for hemispherical Ga NP in radius of (a) 20 nm and (b) 60 nm on sapphire substrate illuminating by light with different angle of incidence for s-polarized (solid line) and p-polarized (dashed line) wave	53
Figure 3.1: Instantaneous optical field ellipse.....	59
Figure 3.2: Schematic diagram of reflection and refraction at media interface	62
Figure 3.3: Amplitudes and phase shifts of reflectance and transmittance for s- and p- polarized wave at vacuum-sapphire interface.....	66
Figure 3.4: Amplitudes (a)(b) and phase shifts (c)(d) of reflectance for s- and p-polarization at vacuum-Ga interface (left) and vacuum-sapphire interface (right)	69
Figure 3.5: Basic configuration of spectroscopic ellipsometry	72
Figure 3.6: Conventions to calculate Δ in different quadrants of ρ	74
Figure 3.7: Schematic diagram of the in-house SE system.....	76
Figure 3.8: (a) measured SE parameters (Ψ, Δ) and (b) inferred pseudorefractive index $\langle \tilde{n} \rangle$ of a typical Ga NP sample	79
Figure 4.1: Schematic diagram of a typical molecular beam epitaxy system.....	83
Figure 4.2: Volmer-Weber growth mechanism.....	87
Figure 4.3: Refractive index of bulk sapphire	95

Figure 4.4: Evolution of pseudoextinction coefficient during Ga NP deposition	97
Figure 5.1: Schematic diagram of atomic force microscopy	100
Figure 5.2: AFM tip convolution effect	102
Figure 5.3: Schematic diagram of scanning electron microscope	103
Figure 5.4: 3D AFM image of a Ga NP ensemble	104
Figure 5.5: SEM image of a Ga NP ensemble measured at tilted (45°) position	106
Figure 5.6: SEM images of samples (a) Y1, (b) Y3, and (c) Y6 with NP identification	108
Figure 5.7: NP crosssectional radius distributions of samples (a) Y1, (b) Y3, and (c) Y6	108
Figure 5.8: NP coverage distributions of samples (a) Y1, (b) Y3, and (c) Y6	109
Figure 5.9: NP nearest neighbor edge-to-edge distance distributions of samples (a) Y1, (b) Y3, and (c) Y6	109
Figure 5.10: NP nearest neighbor edge-to-edge distance distributions for (a) small-small ($r < 40$ nm) NPs and (b) small-large ($r > 40$ nm) NP pairs on sample Y6	110
Figure 5.11: SEM images of Ga NP ensembles with the same LSPR energy deposited at (a) 25°C and (b) 700°C respectively	113
Figure 5.12: NP crosssectional radius distributions of Ga NP ensembles with the same LSPR energy deposited at 25°C and 700°C respectively	114
Figure 5.13: Scaled NP crosssectional radius distributions of Ga NP ensembles with the same LSPR energy deposited at 25°C and 700°C respectively	114
Figure 5.14: Pseudoextinction coefficient of Ga NP ensembles deposited at 25°C and 700°C respectively	115
Figure 6.1: SE EMA model for Ga NP ensembles on sapphire	120
Figure 6.2: Real and imaginary parts of the dielectric function of a Lorentz oscillator with $\omega_0 = 3, f = 1, \gamma = 0.5$	122

Figure 6.3: Multiple reflections from a two-layer structure.....	123
Figure 6.4: Measured and fitted SE parameters (Ψ, Δ) of sample Y3.	128
Figure 6.5: Pseudorefractive index (\tilde{n}) and SE model inferred refractive index \tilde{n} of sample Y3.	129
Figure 6.6: Measured and fitted SE parameters (Ψ, Δ) of samples Y1 ~ Y7.....	131
Figure 6.7: SE model inferred refractive index \tilde{n} of samples Y1 ~ Y7.	132
Figure 6.8: Reflection diagram of the SE probe light incident on a single hemispherical Ga NP on sapphire	134
Figure 6.9: EM field intensities surrounding a single hemispherical Ga NP on sapphire excited by (a) s-polarized light and (b) p-polarized light.....	134
Figure 6.10: Absorption efficiencies for (solid) in-plane and (dashed) out-of-plane LSPR modes of a single hemispherical Ga NP on sapphire	136
Figure 6.11: SE model inferred extinction coefficient κ of samples Y1 ~ Y7.....	138
Figure 6.12: SE model fitted Lorentz oscillator resonance energy ω_0 of samples Y1 ~ Y7.....	138
Figure 6.13: SE model fitted Lorentz oscillator damping constant γ of samples Y1 ~ Y7.....	139
Figure 6.14: SE model fitted Lorentz oscillator strength f of samples Y1 ~ Y7....	139
Figure 6.15: Measured dependence of SE model fitted Lorentz oscillator (a) resonance energy and (b) damping constant on the average cross-sectional diameter of samples Y1, Y3, and Y6.....	141
Figure 6.16: (solid) Mie scattering predicted extinction efficiency comparing with (dashed) SE model inferred extinction coefficient of NPs with the same radii ..	145
Figure 6.17: (solid) DDA method predicted absorption efficiency comparing with (dashed) SE model inferred extinction coefficient of NPs with the similar radii.	145
Figure 7.1: Structure of the in-house VASE system (top view)	149

Figure 7.2: Measured reflectance of p-polarized (pR) and s-polarized (sR) light from samples Y3, Y6, and Y7	152
Figure 7.3: Calculated reflectance of p-polarized (pR) and s-polarized (sR) light from vacuum-sapphire interface	153
Figure 7.4: Calculated (left) and measured (right) reflectance of p-polarized (pR) and s-polarized (sR) light of samples Y3 and Y6.....	155
Figure 7.5: Angle-resolved pseudoextinction coefficient of samples (a) Y3 and (b) Y6 measured by VASE	157
Figure 7.6: Energy-dependent scattering profile of sample Y6 at AOI = 40°.	160
Figure 7.7: Scattering spectra at 2.54 eV and 4.54 eV of sample Y6.	160
Figure 7.8: Schematic diagram of shadowing effect	161
Figure 7.9: Calculated Mueller matrix elements (a) m_{12} and (b) m_{33} of the reflection at vacuum-sapphire interface at different AOIs	168
Figure 7.10: Calculated Mueller matrix elements (a) m_{12} , (b) m_{33} , and (c) m_{34} of the reflection at vacuum-Gallium interface at different AOIs.....	169
Figure 7.11: Schematic diagram of the in-house Mueller matrix polarimeter	171
Figure 7.12: VAMM measured Mueller matrix elements $m_{11} \sim m_{34}$ of sample Y3	173
Figure 7.13: Predicted (dashed) and measured (solid) Mueller matrix elements m_{22} , m_{12} , m_{33} , and m_{34} of sample Y3.....	175
Figure 7.14: VAMM measured Mueller matrix elements $m_{11} \sim m_{34}$ of sample Y6	176
Figure 7.15: Predicted (dashed) and measured (solid) Mueller matrix elements m_{22} , m_{12} , m_{33} , and m_{34} of sample Y6.....	177
Figure 7.16: VAMM measured Mueller matrix elements m_{22} and m_{33} of samples Y5, Y6, and Y7.....	178
Figure 7.17: Peak energy in m_{22} at AOI = 20° of samples Y5, Y6, and Y7	178

Figure 8.1: Schematic diagram of the in-house Raman system.....	194
Figure 8.2: Molecular structure of crystal violet.....	195
Figure 8.3: Raman spectrum of 20 μM CV in ethanol solution (inset: Raman spectrum of 99.9% ethanol in solution).....	195
Figure 8.4: Measured CV SERS from Ga NPs in samples Y1, Y3, and Y6 compared to Raman signal from CV on bare sapphire by 325 nm UV laser excitation	198
Figure 9.1: Temporal evolution of Raman spectra from CV on (a) Ga NP side in sample Y6 and (b) bare sapphire	205
Figure 9.2: Temporal contour plot of Raman spectra from CV on Ga NP side in sample Y6 for the first 200 s.....	207
Figure 9.3: Raman intensities at 1617 cm^{-1} from CV on Ga NP and bare sapphire sides in sample Y6 for the first 1000 s	207
Figure 9.4: Direct Raman signal enhancement factor of sample Y6 for the first 1000 s.....	208
Figure 9.5: Time-dependent normalized (a) fluorescence and (b) Raman signals at 1617 cm^{-1} from CV on Ga NP side in sample Y6 excited by four different laser pump intensities	211
Figure 9.6: Dependence of relative Raman intensity at 1617 cm^{-1} from CV on Ga NP side in sample Y6 after 500 s on laser pump intensity normalized to the damage threshold of CV	214

List of Abbreviations

AFM	atomic force microscopy
AOI	angle of incidence
CV	crystal violet
DDA	discrete dipole approximation
EM	electromagnetic/electromagnetism
EMA	effective medium approximation
LSPR	localized surface plasmon resonance/resonant
MBE	molecular beam epitaxy
NIR	near infrared
NP	nanoparticle
(VA)MM	(variable-angle) Mueller matrix
(VA)SE	(variable-angle) spectroscopic ellipsometry
SEF	surface-enhanced fluorescence
SEM	scanning electron microscope
SEPD	surface-enhanced photodegradation
SERS	surface-enhanced Raman scattering/spectroscopy
SoP	state of polarization
UV	ultraviolet

Acknowledgements

Great wisdom is generous; petty wisdom is contentious.

Great speech is impassioned, small speech cantankerous.

– *Chuang-tzu (Zhuangzi)*

Scientific research is like “unweaving the rainbow”. Every time I think I meet the boundary of the subject, a “door” is opened and a completely unknown and more exciting world is waiting there. I am not alone while exploring the beautiful science world. People guide me when I get lost, push me when I feel tired, and encourage me when I doubt. This work cannot be completed without any of the advices, guidance and supports I received over the last 5 years or from my birth.

First, I would love to express my deepest appreciation to my co-advisors Dr. Henry Everitt in the Department of Physics and Dr. April Brown in the Department of Electrical and Computer Engineering at Duke, who brought me the best PhD experiences I can imagine. It’s really rewarding to have two co-advisors with similar but different backgrounds to share the insights and perspectives on both fundamental science and applied research, to guide me from different aspects and “interfere” constructively, and to support me in both detail and big frame. Their mentoring is immeasurable on my future.

The completeness of this thesis is not a merely personal effort. The experiments and theoretical explorations cannot be done without team work and collaborations. I am especially grateful for the help from Dr. Tong-Ho Kim, without whom no samples can be grown. The countless time when I was working with him in MBE lab is one of the most informative and enjoyable moments in my PhD studies. I would also love to thank the senior students Soojeong Choi and Pae Wu in the group, who helped me start the research when I joined the group in 2008, and Christopher Khoury and Kevin Lantz at Duke, who taught me experimental techniques keen to my research. Learning and working in a small but close research group extended far beyond the science and our colleague relationship has evolved into true friendship. Thanks all the former and current group members.

In addition to my labmates and collaborators at Duke, I am really grateful for the advices from Dr. Maria Losurdo in Italy on ellipsometry and Dr. Fernando Moreno and Dr. Francisco Gonzalez in Spain on computational modeling. Their enthusiasm towards science also spurs me on to continue advancing in the scientific research. I also thank John Callahan at Huntsville, AL who built advanced Raman system and made clear Raman measurement possible and Neset Akozbek for VASE and VAMM system.

Besides all the co-workers, I truly appreciate the generous supports from the Department of Physics and the Graduate School at Duke through the funding of Katherine Goodman Stern fellowship, Walter Gordy Fellowship, summer research fellowship, physics graduate teaching fellow, and graduate student conference travel fellowship. These fellowships help sharpen my abilities in teaching and research, provide me opportunities to travel and speak in conferences, and ensure the completeness of my thesis and defense in time without disturbance.

Last but not least, I want to thank my beloved families, my parents and my wife, who, without reservation, provide me with the best life. As always, wording becomes useless and is not enough to express all my deep gratefulness. The completeness of the thesis and my degree are all dedicated to them.

Thank you!

1. Introduction

1.1 UV radiation and its applications

When Sir Isaac Newton decomposed white sunlight into a spectrum of “rainbow” in his famous prism experiment in 1670s [1], people realized that light is more “colorful” than it was originally thought. In 1860s, James Maxwell developed the radiation theory of electromagnetic (EM) waves and generalized that all these colorful lights are indeed EM waves with different frequency [2]. Figure 1.1 shows an overview of EM spectrum [3]. In general, based on the differential properties of EM radiation, the spectrum is described in terms of spectral regions. Each associated with distinct applications. For example, radio waves, discovered in 1887 [4], are used to transfer information through space for their large diffraction limit. Gamma-rays, discovered in 1900 [5], are now widely used as a mean of killing cancer cells due to high photon energy.

Ultraviolet (UV) radiation was actually discovered before James C. Maxwell’s defining work on electromagnetic radiating. In 1801, J. Ritter found that the oxidation of silver chloride is faster when it was placed under the dark region of sunlight’s spectrum, next to the violet end, than under the visible region [6]. This radiation was referred to as “oxidizing rays” and “chemical rays” to emphasize

their impact on chemical reactivity. In the late part of the 19th century, the term “ultraviolet” was adopted by science community [7], where the prefix “ultra” means beyond in Latin. Currently, the term ultraviolet light usually denotes EM waves with wavelengths between visible light and x-rays, ranging from 400 nm to 10 nm (or approximately 3 eV to 124 eV in photon energy).

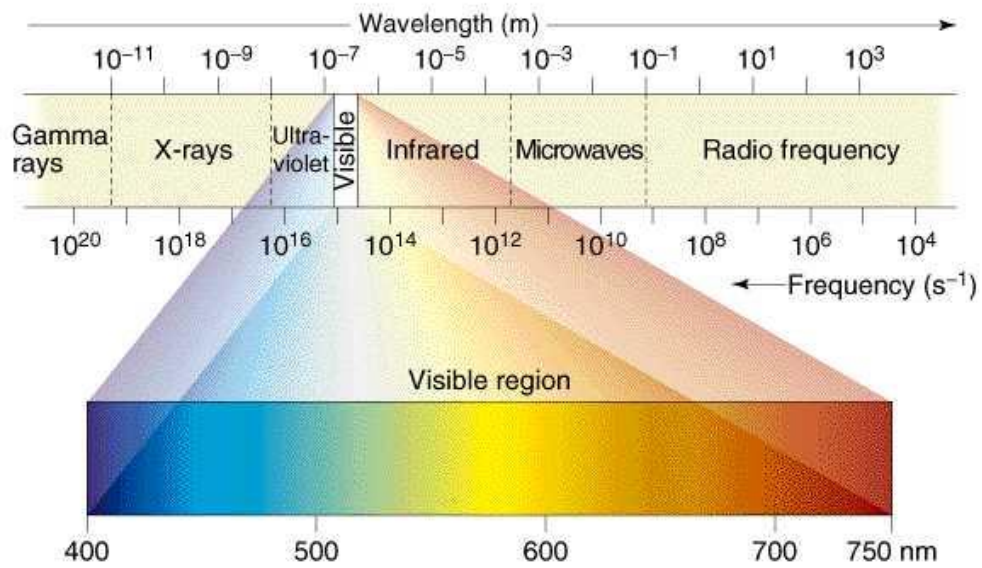


Figure 1.1: Electromagnetic spectrum [3].

As UV radiation is part of the spectrum of natural sunlight, it has been intensively exploited for many applications. The following list summarizes its applications:

- i. Spectroscopy: Fluorescence, UV Raman, UV-Vis

This work will use UV Raman scattering and fluorescence and will discuss their advantages in detail in the next Section.

ii. Chemical: Photodegradation, Disinfection, UV curing

UV radiation can break chemical bonds increasing the efficiency of oxidation. This process is referred to as photooxidation and photolysis [8].

For example, plastic products are protected from direct sunshine to reduce photodegradation to extend life while used plastics are exposed to UV radiation to increase degradation rate for environment protection [9]. This work will also involve potential applications in photodegradation.

iii. Engineering: UV Lithography [10], UV light-emitting diode [11]

Other applications of UV radiation include water purification, fire detection, bar code scanning, watermark authentication, etc., while this work will focus on UV Raman spectroscopy.

1.1.1 UV Raman spectroscopy and SERS

Raman spectroscopy, named after its discoverer Sir C. Raman, is an important spectroscopic technique widely used for molecule and bond identification in chemistry, biochemistry and biophysics [12-14]. Raman scattering probes vibrational, rotational, and other low-frequency excited modes in a system.

Molecular bonds possess different intrinsic vibrational or rotational frequencies. For example, N₂ has a strong Raman scattering at 2330 cm⁻¹ and O₂ at 1555 cm⁻¹ [15]. Stimulating and detecting these modes can provide a basis for molecular

detection. Since the discovery of Raman scattering in 1928, applications of the technique have been thwarted by the extremely low Raman scattering cross sections, which are in the range of 10^{-30} cm^{-2} [16]. Only a small fraction of incident phonons will undergo Raman scattering.

UV Raman scattering addresses the problem of low scattering cross section since the Raman intensity is proportional to ω^4 [15]. The number of research on Raman spectroscopy at shorter wavelengths has increased significantly during the past three decades due to the availability of UV lasers [17], including the 325 nm HeCd laser, the 244 nm Ar^+ laser, and frequency doubler and excimer lasers with excitations from 150 nm to 350 nm. Here we summarize the advantages of UV Raman spectroscopy:

i. Increased Raman scattering cross section

The Raman scattering cross section is proportional to ω^4 , where ω is the excitation frequency. For example, the Raman scattering cross section with 325 nm UV laser excitation is 14.4 times greater than that using 633 nm red laser excitation.

ii. Opportunity to use resonance Raman scattering

UV Raman scattering enables resonance Raman spectroscopy (RRS). When the excitation laser frequency coincides with a molecule absorption

peak, the Raman scattering cross section will increase dramatically by a factor of approximately 10^8 to 10^{12} due to increased light absorption [18]. The absorption bands for many organic and inorganic molecules are within the UV range. For example, diamond has a fundamental gap around 6 eV (206 nm) [19]; many semiconductors exhibit strong absorption above their band gap and many important semiconductors have band gap energies in the UV range [20]; and biological molecules such as nucleic and amino acids have strong absorption between approximately 220 nm and 280 nm [21-22]. Numerous studies demonstrated the efficiency of probing protein and DNA structures using UV resonance Raman spectroscopy (UVRRS) [23-25].

iii. Minimal fluorescence inference

Fluorescence is usually present under Raman scattering conditions using visible or infrared excitation. Fluorescence may be strong enough to completely mask the Raman scattering intensity due to the relatively high fluorescence cross section (10^{-13} cm²). No fluorescence has been reported for excitation below 280 nm. Therefore, Raman scattering under UV excitation minimizes interference from fluorescence. Clear UV Raman spectroscopy combined with normal fluorescence will provide better specifying information for analyte recognition [26-27].

iv. Small penetration depth

The optical penetration depth of UV light for high band gap semiconductors or alloys is much smaller than that of visible light, since UV light energy is above their band gaps. For example, the penetration depth of 633 nm visible light in Si is about 3000 nm while that for 244 nm UV light is about only 6 nm due to high optical absorption coefficient of UV light in Si. The relatively small penetration depth enables detailed near-surface analysis. UV Raman has been used to characterize surface stress in strained Si wafers [28] and to probe nanoscale ferroelectricity in BaTiO₃ thin films [29].

v. High Spatial Resolution

In 1873, E. Abbe generalized the diffraction limit for optical microscope as [30],

$$r = \frac{\lambda}{2n\sin\theta} \quad (1.1)$$

The formula indicates that light with wavelength λ traveling in a medium with refractive index n , and incident angle θ with respect to the optical plane of the microscope, will have minimum light spot radius r , where the term $n\sin\theta$ is called numerical aperture (N.A.). Therefore, the light spot size decreases with decreasing wavelength. The Raman system maker

HORIBA Jobin Yvon claims that the focused laser spot radius ranges from 0.7 μm to 0.45 μm with changing the laser line from 514 nm to 325 nm using a 100x objective with a N.A. of 0.9 [31]. This enables local detection and is named UV Raman microspectroscopy. The technique can be used to characterize the local properties of materials such as phase transition and grain size [32].

To summarize, Raman spectroscopy in the UV benefits from its high scattering cross section, potential resonance, and low fluorescence overlap. It also has potential applications in thin film and nanostructures characterizations with small penetration depth for surface analysis and high spatial resolution.

Another means of increasing the Raman scattering cross section is to directly increase the strength of excitation wave or local EM field surrounding the analyte. However, the effect was not observed until 35 years ago due to the lack of a known method for creating local EM field enhancement. In 1974, M. Fleischmann [33] qualitatively reported the first observation of enhanced Raman signal from adsorbed pyridine on an electrochemically roughened silver surface. R. Van Duyne [34] systematically verified the phenomenon later in 1977. Since then, significant amount of research has been focused on surface-enhanced Raman spectroscopy or surface-enhanced Raman scattering, known as SERS. Since 1977,

publications featuring SERS has grown dramatically to over 25000 annually. Enormous Raman enhancement factors have been reported in the literature ranging from several hundred to $10^{10} \sim 10^{11}$ and up to 10^{17} [35], which brings renewed interests in Raman spectroscopy. Such high enhancements improve the efficiency of Raman scattering for trace analysis, chemical analysis, and biomedical applications [36-39], such as single molecule detection [40-42] and single cell detection [43].

An enhanced signal could arise from enhancement of the local EM field and the polarizability of the target analyte. Therefore, several review papers [44-48] have generalized the potential mechanisms underlying SERS into two categories, EM origin and chemical origin respectively. For some special analytes, the chemical enhancement may be significant [49]. However, most reported papers stated the EM enhancement as the key factor for SERS. Theoretical estimations show that chemical enhancement may go up to 10^3 and EM enhancement may be as large as 10^{11} . The overall enhancement would be the product of the two above [50]. As a result, searching for ideal SERS substrate became a hot topic in scientific research.

1.1.2 Fluorescence

Fluorescence is the luminescence from substances resulting from UV excitation. Electrons will be excited to a higher singlet state and undergo both nonradiative

and radiative processes and return to ground state. The radiative process will emit light in a longer wavelength comparing to excitation light due to the existence of nonradiative processes. Figure 1.2 shows the Jablonski diagram, which shows general excitation processes among energy states, of both Raman scattering and fluorescence [51].

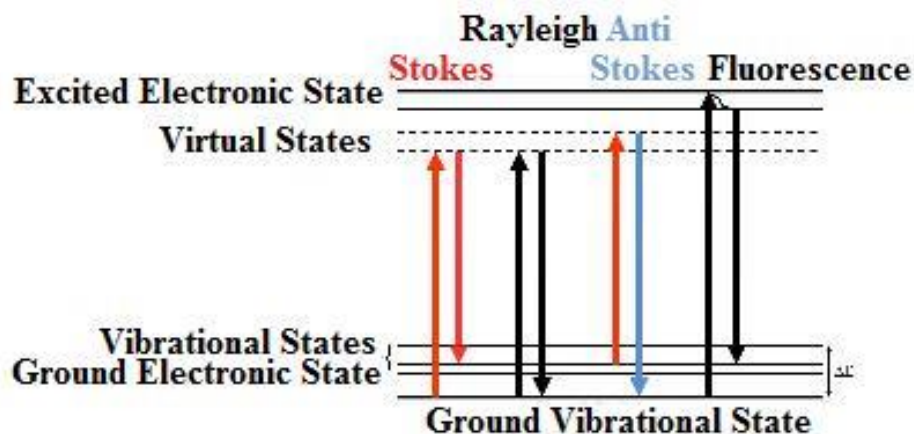


Figure 1.2: Jablonski diagram of Raman scattering and fluorescence [51].

Different electronic states in molecules will exhibit distinct fluorescence emission. For example, Rhodamine 6G has a peak emission at 550 nm and Acridine at 462 nm [52]. Therefore, fluorescence is widely used in bond detection, imaging, biology and medical research [53]. Fluorescence spectroscopy, which measures the spectrum of emitted light, is used to identify material composition [54]. Active fluorescent materials, or fluorophore, can be used to label and trace biomedical molecules and living cells [55-56].

Although the fluorescence cross section is about 10 times that of Raman scattering, when the analyte concentration is small, e.g. single molecule, the fluorescence signal is too weak to detect. Therefore, similar to SERS, the concept of surface-enhanced fluorescence (SEF) arises. The enhancement mechanism of SEF is much more complicated than SERS [57]. Charge transfer effects may dominate the process and sometimes reverse the enhancement. It has been reported that some SERS active substrates, e.g. Ag nanoparticles, actually quench fluorescence [58]. There are research efforts aimed at optimizing the surface condition enabling SERS and SEF simultaneously. A few experiments have reported concurrent SERS and SEF recently [59-60]. SEF still majorly relies on the enhancement of local EM field intensity and thus photon absorption.

In conclusion, both SERS and SEF require substrates designed to enhance local EM field intensity. In the next section I will introduce plasmonics which provides a basis for surface enhanced spectroscopy.

1.2 Plasmonics and metallic nanoparticles

The success of SERS and SEF is dependent on the development of metallic nanomaterial and nanostructures. The coupling of excitation light with surface plasmon resonances (SPR) or localized surface plasmon resonances (LSPR) in

nanostructures provides the origins of local EM field enhancement. Figure 1.3 clearly shows how a nanoparticle enhances the surrounding EM field [61]. The EM field will redistribute due to the coupling of the nanoparticle and external light to form field enhanced area on surface where the field intensity is much larger than the original incident field intensity. SERS and SEF effects will occur when analyte is placed in these areas.

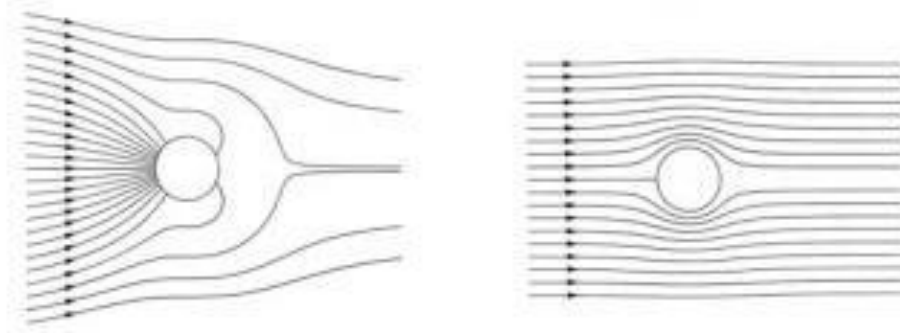


Figure 1.3: Poynting vector plot of an Al sphere illuminated by light where resonance occurs (left) and where there is no resonance (right) [61].

The SPR is the collective electron oscillation at the metal surface in response to external light [62]. For metallic nanoparticles (NPs), the charge density oscillation is confined to the NP, denoted by the term localized surface plasmon (LSP) with dipole LSPR energy limit at [62]

$$\omega_{\text{LSP}} = \frac{\omega_{\text{p}}}{\sqrt{3}} \quad (1.2)$$

where ω_{p} is the bulk plasmon energy of metals. The absorption of the LSP will reach its maximum at the localized surface plasmon resonance (LSPR) energy

where the LSP will undergo a critical damped oscillation and therefore transfer energy to enhance the local field surrounding the NP. When the resonance occurs, NPs will show a great enhancement of the local EM field as depicted in Figure 1.3. There are many factors which may alter LSPR energy such as NP's size, shape, composition as well as dielectric environment [62]. Chapter 2 will discuss their impacts in detail.

Researchers have demonstrated numerous SERS and SEF effects using metallic nanoparticles over the last decade. Enhancements have been reported on Ag, Au, alkali metals (Li, Na, K, Rb, and Cs), Al, Ga, In, Pt, Rh, and metal alloys among which Ag and Au nanoparticles shows largest enhancement due to their free electron features [63].

1.3 Motivation: UV SERS and gallium nanoparticles

To date, most SERS demonstrations exploit visible light excitation. We have discussed the advantages of UV Raman in Section 1.1. UV SERS will benefit from all of the advantages of UV Raman spectroscopy. Therefore, UV SERS is a promising tool for spectroscopy, detection and sensing.

However, as stated above, most SERS active substrates have been developed for applications using visible light excitation. This is mainly because that most of

currently available plasmonic nanostructures exploit metals with LSPR in the visible range. The enhancement efficiency will reduce significantly when excitation laser energy is far from NP's LSPR energy.

The upper limit of NP's LSPR energy can be simply estimated by Equation 1.2. Table 1.1 [64] summarized bulk plasmon energy ω_p for several commonly used metals. Figure 1.4 shows the limits of LSPR energies of some nanostructures. It is clearly that commonly used Ag and Au NPs cannot have LSPR within UV range due to their low bulk plasmon energy. Therefore, it is critical to search for new materials and nanostructures, whose LSPR can couple with UV excitation to enhance local EM field and thus exhibit strong UV SERS and SEF effects.

Table 1.1: Bulk plasmon energy for common metals [64].

metal	$\hbar\omega_p / \text{eV}$
Gold (Au)	8.89
Silver (Ag)	9.04
Aluminum (Al)	12.04
Indium (In)	12.8
Gallium (Ga)	14.05

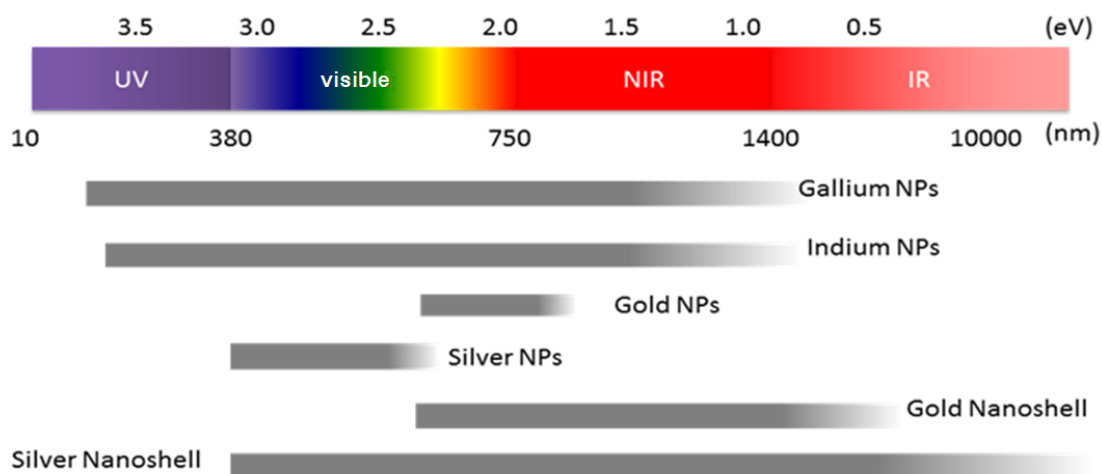


Figure 1.4: LSPR energies of various nanostructures.

Some efforts have been made in the past but very limited numbers of UV SERS active substrates have been reported. First UV SERS was not reported until 2003, almost 30 years after the first SERS observation. Ren et al. reported the first UV SERS on Ru and Rh [65], followed by other observations on transition metals Pd [66] and Co [67], Au electrodes [68-69], and Au@Pd and Au@Pt nanoshells [70]. However, SERS effects from these substrates are believed to rely on charge transfer mechanism [67][71], which limits the enhancement factor to the order of 100. Two other attempts have been made on Al, one at 244 nm [72] and the other at 257.2 nm [73]. The latter one reported an estimated enhancement factor of 50 while the former one did not quantify the enhancement. Van Duyne recently listed UV SERS as the future direction of SERS [45]. Therefore, searching for ideal UV SERS substrate remains as an open and challenging problem.

Due to the high bulk plasmon energy of Ga, the LSPR energy of Ga NPs is in the UV. The upper limit of the Ga NP LSPR energy is beyond 8 eV (155 nm). This fundamentally enables Ga NPs to couple with UV excitation and enhance local EM fields. Some other metals may also fit into this category like Al and In. However, in addition to its advantage on plasmonics, Ga possesses some advantages due to its material properties:

- i. Easy synthesis: Due to its low melting point and high surface energy, Ga can form well-shaped self-assembled hemispheroid NPs on solid supports at room temperature [74-75]. The synthesis of Ga NPs will be discussed in detail in Chapter 4.
- ii. LSPR stability [76]: Ga NPs form a very thin and stable oxidation layer (several nanometers). Even over months, the LSPR energy will only bare a small red shift of less than 0.3 eV. In contrast, Al NP exhibit LSPR energy shifts over 4 eV and LSPR of In NPs is almost completely dumped upon air oxidation.

In conclusion, it is very valuable to search for UV SERS substrate due to the lack of reported one in the literature and Gallium (Ga) is a promising candidate for this purpose due to its plasmonics and material features.

1.4 Summary of work

In this work, we proposed and demonstrated that gallium is a promising and compelling material for UV plasmonics through synthesis of size-controlled nanoparticle arrays, EM modeling of local field enhancement, ellipsometric and spatial characterization of the arrays, and analytical measurement of UV enhanced Raman and fluorescence spectra.

In Chapter 2, I will discuss firstly NP and its optical properties, and secondly, methods to estimate local field enhancement surrounding a NP. Preliminary calculations on Ga NPs will also be presented to demonstrate their advantageous plasmonic properties.

Chapter 3 will introduce spectroscopic ellipsometry (SE), which will be used to monitor Ga deposition and characterize Ga NP ensembles after growth.

Chapter 4 will explain controlled synthesis of Ga NPs with in situ SE monitoring in the ultrahigh vacuum growth chamber of molecular beam epitaxy (MBE).

Followed the synthesis, Chapter 5 will discuss the ex situ spatial characterization using atomic force microscopy (AFM) and scanning electron microscopy (SEM) to extract ensemble and local morphology information.

Chapter 6 and 7 will focus on optical characterization of Ga NPs including SE measurement, SE modeling, variable-angle SE, and Mueller matrix measurements to reveal the plasmon features of Ga NP samples and correlate with spatial information obtained in Chapter 5.

Chapter 8 and 9 will show the demonstration of UV SERS using Ga NPs and local enhancement factor analysis with concurrent observation of surface enhanced fluorescence and photodegradation.

Chapter 10 will conclude with perspectives on UV.

2. Plasmonic Nanoparticles and their Optical Properties

Plasmonic NPs can enhance surrounding EM field dramatically when excited by external radiations at their LSPR energies (Figure 1.3). This enhancement forms a basis for NPs' plasmonic applications like SERS. To perform these applications in the UV, NPs' LSPR energy shall also be in the UV. This chapter will discuss the dependence of NP's LSPR energy on their morphology and methods for estimating LSPR energies of various nanostructures. Preliminary calculations for Ga demonstrate that Ga is a promising candidate for UV plasmonics.

2.1 Plasmonic nanoparticles

2.1.1 Nanoparticles

The word nano is the prefix meaning billionth while NPs are small particles with typical length in at least one dimension sizing from several nanometers to several hundred nanometers. They are of great interest to researchers for their unique optical, thermal, mechanical, chemical and electronic properties due to their small dimension and high surface-volume ratio. For example, a spherical gold NP with diameter 3.2 nm contains only 1000 atoms while about 35% percent of them are at the surface [77]. The numbers of articles published in nano-title has grown exponentially since 1980s [78].

The famous example of using gold and silver “dust” in the Lycurgus cup is dated back to the 4th century in Late Roman. In ancient China, SnO NPs were coated on the surface of copper mirrors to resist oxidation as early as Zhou Dynasty (770 BC ~ 256 BC). However, systematic modern research did not begin until M. Faraday’s work in 1857 [79]. He prepared the first sample of pure “colloidal gold” and associated its distinctive color with particle size. Since then, controlled synthesis, characterization and application of NPs have been widely studied.

NPs can be categorized by their composition: metallic, semiconductor, oxides; by their shape: spherical, truncated, anisotropic, and by the number of constituents: homogenous and heterogeneous. One example of the heterogeneous NPs is nanoshell, such as a dielectric core covered by a thin metallic shell like Au-Au₂S [80], or two concentric metallic shells like Ga-Mg nanoshell [81]. The latter one also falls into the category of bimetallic NPs. In addition to core-shell structures, bimetallic NPs can also be in alloy structures like Ga-Mg alloy NPs [82]. Even though synthesized from one material, NPs may contain more than one phase. Coexistence of alpha and beta phases is discovered in Ga NPs [83]. The ex situ oxidation may also alter NPs’ composition to make them heterogeneous. For example, most silver and gold NPs in experiments actually bear a thin layer of native oxidation after synthesis.

Given these distinct structures, there are numerous applications of NPs in physics, material science, energy, chemistry, and biomedical field, such as high efficiency solar cell [84], high efficiency light-emitting diodes (LEDs) [85], nanogenerators [86], catalysis [87], enhanced optical coherence tomography imaging, and cancer therapy [88]. Most of these applications are based on their plasmonic properties which will be presented in the next section.

2.1.2. Plasmonics

Based on band theory, metal has Fermi level within conduction band. Valence electrons are no longer bound to individual atoms but can move freely within the metal. They are thus called conduction electrons. All the conduction electrons form a free electron gas in the metal and interact with immobile positive charged ion cores, nucleus and inner electrons, at lattice positions. This was first proposed by P. Drude in 1900 [89]. Based on this classical model, dielectric function of metals has the form,

$$\epsilon(\omega) = 1 - \frac{\omega_p^2}{\omega^2 - i\gamma\omega_p} \quad (2.1)$$

and

$$\omega_p = \sqrt{\frac{ne^2}{m\epsilon_0}} \quad (2.2)$$

where n is the free electron volume density, e is the unit electric charge, ϵ_0 is the permittivity of free space, and m is the effective electron mass. ω_p is called plasma frequency which is the intrinsic frequency of the free electron gas oscillation. This oscillation is also called plasma oscillation. γ is the damping constant coming from electrons scatterings due to interactions like electron-electron, electron-phonon and electron-defect collisions, and radiations [90].

The plasma oscillation is indeed a collective oscillation of free electron density. ω_p is the intrinsic properties of metals. To quantize plasma oscillation, the term plasmon was introduced. Plasmon is a quasi-particle associated with the plasma oscillation. Because it is a collective electron oscillation in three-dimensions (3D), it is also called bulk plasmon. Bulk plasmon energy is thus $\hbar\omega_p$ [90]. Table 1.1 listed bulk plasmon energies for some metals.

Now, let's explore how metal interacts with external EM wave. Many books work through the derivations, and here presented are the major results [91-92]. Consider an interface between a dielectric material and a metal. Figure 2.1 shows the dispersion relation at this interface. x represents the direction parallel to the interface while z is the direction perpendicular to the interface as shown in the inset of Figure 2.1. ϵ_d and ϵ_m are dielectric functions of the dielectric material and the metal respectively.

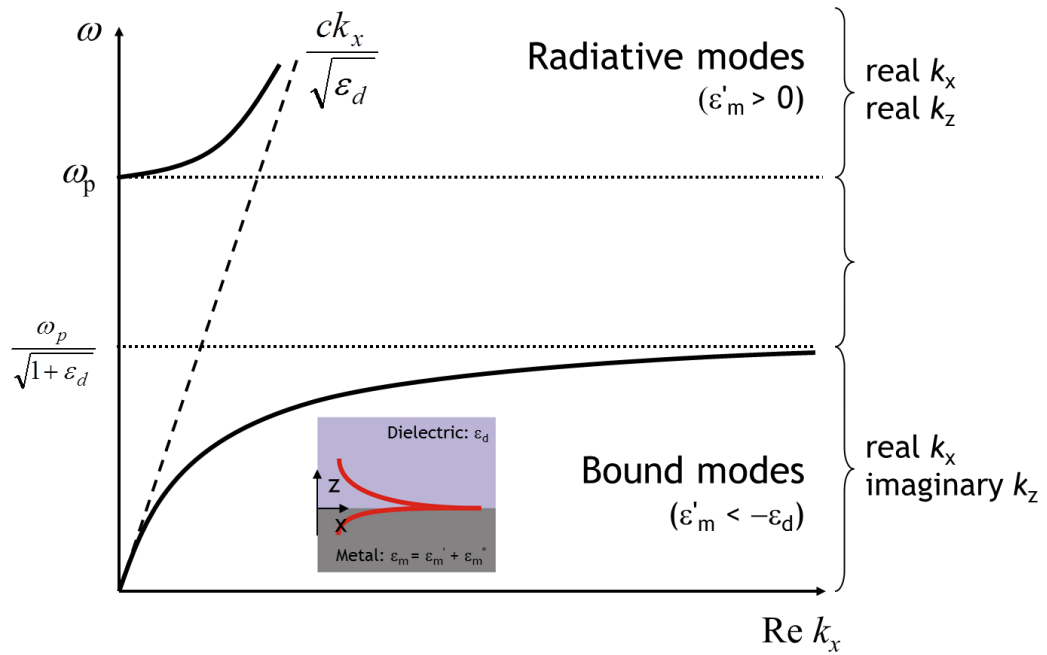


Figure 2.1: Dispersion relation at the metal-dielectric interface [93].

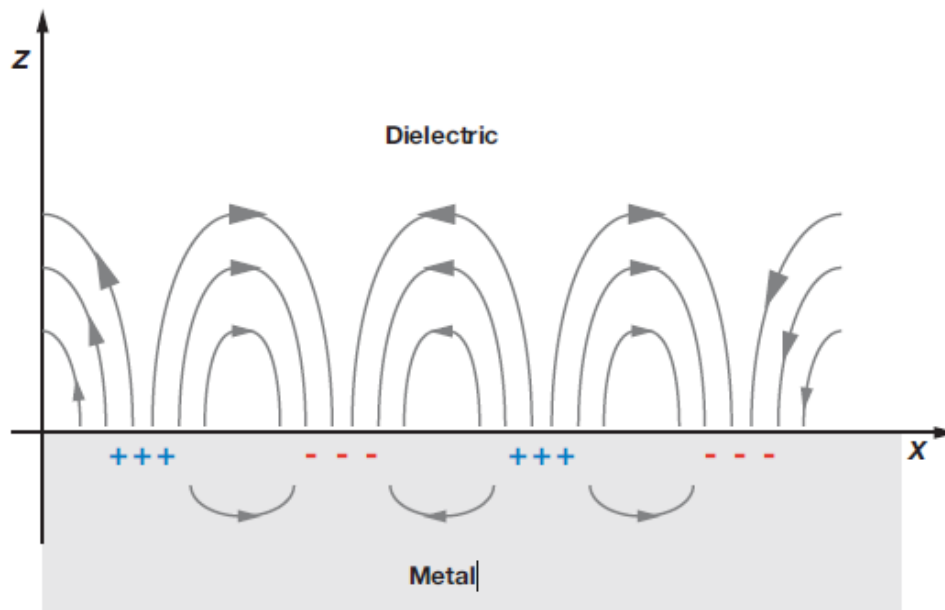


Figure 2.2: Schematic diagram of surface plasmon [93].

Consider an EM wave with frequency ω . For $\omega \geq \omega_p$, external wave can be transmitted in the metal. The dispersion relation is regulated by,

$$k = \frac{1}{c} \sqrt{\epsilon_d(\omega^2 - \omega_p^2)} \quad (2.3)$$

where c is the speed of light and k is the wave number of transmitted wave in the metal. For $\omega < \omega_p$, k becomes imaginary, which implies that the oscillation of electric field will decay exponentially as entering the metal to form evanescent wave. The possible wave propagation occurs if the wave is confined at surface. By matching the solution of Maxwell equation to the boundary conditions, the dispersion relation for the EM wave propagating along the surface is,

$$k_x = \frac{\omega}{c} \sqrt{\frac{\epsilon_m \epsilon_d}{\epsilon_m + \epsilon_d}} \quad (2.4)$$

This depicts the collective surface charge oscillation in response to external EM field as shown in Figure 2.2 [93]. Because it propagates within the surface, the quasi-particle associated with this motion is named surface plasmon to differ it from bulk plasmon. The lower curve in Figure 2.1 represents Equation 2.4, where the surface plasmon can be excited for $\omega < \omega_{SP}$. ω_{SP} is the asymptotical frequency when $k_x \rightarrow \infty$. Therefore,

$$\omega_{SP} = \frac{\omega_p}{\sqrt{1 + \epsilon_d}} \quad (2.5)$$

which is the upper limit of surface plasmon resonance. Recall that Ga has plasmon energy 14.05 eV. Given Equation 2.5, the upper limit of Ga SPR energy in vacuum ($\epsilon_d = 1$) is $\frac{\omega_p}{\sqrt{2}} = 9.93$ eV, which is in the UV.

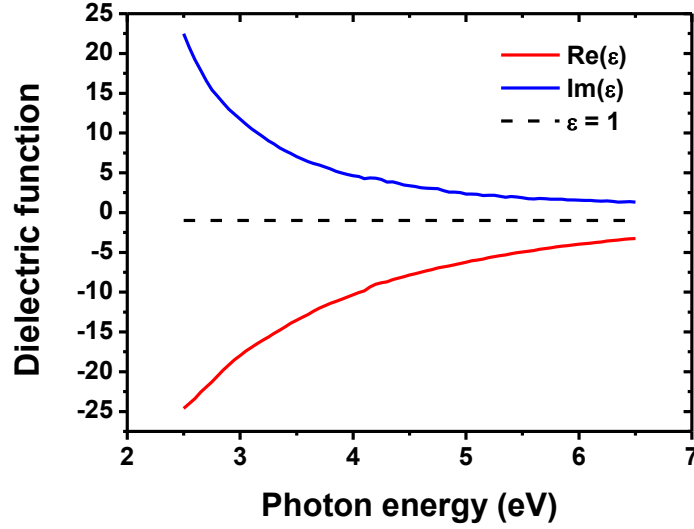


Figure 2.3: Dielectric function of bulk gallium.

Equation 2.4 suggests another criteria for surface plasmon excitation $\epsilon_d + \epsilon_m < 0$ as ϵ_m , the dielectric function of metal, is always negative when $\omega < \omega_p$. This requires $\epsilon_m < -\epsilon_d$. This is one of the major reason that gold and silver are currently widely used in surface plasmon applications in visible and near infrared range [94]. Figure 2.3 shows the dielectric function of Ga which is measured by our collaborator (Losurdo et al.) using spectroscopic ellipsometry from a 5 μm thick pure Ga thin film. Clearly, the real part of the dielectric function does not cross $\epsilon = -1$ (dash line) in the detection range (2.5 eV to 6.5 eV).

$\epsilon_m < -\epsilon_d$ is therefore always satisfied for Ga in vacuum ($\epsilon_d = 1$) in this range from visible to deep UV. This enables Ga to generate surface plasmon resonance under UV excitation. Therefore, Ga is a good UV plasmonic material in principle.

When metals are not in the form bulk or thin film but NP, similar charge oscillation can occur but is localized within NP given geometry restriction. Therefore, this type of charge oscillation is named localized surface plasmon (LSP). Figure 2.4 [93] shows the schematic diagram of LSP oscillation. Similar to bulk plasmon and surface plasmon, at resonance energy, LSP will undergo a critical damped oscillation and therefore transfer external EM field energy to enhance the local field surrounding the NP as shown in Figure 1.3. This resonance energy is called localized surface plasmon resonance (LSPR) energy.

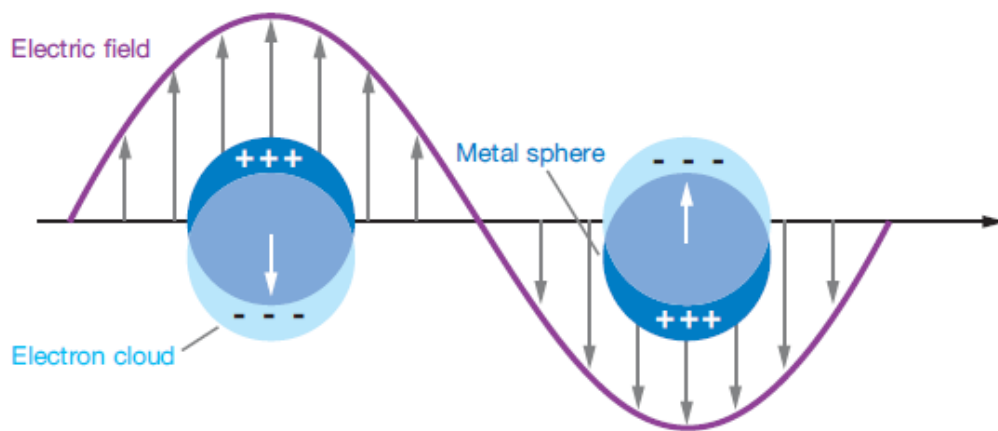


Figure 2.4: Schematic diagram of localized surface plasmon [93].

To determine LSPR energies and local field enhancement of NPs and other nanostructures, Maxwell equations for these nanogeometries must be solved. For spherical NPs, the well-known Mie calculation [95] provides exact solution. The LSPR energies are,

$$\omega = \omega_p \sqrt{\frac{1}{1 + \epsilon_d(l+1)}}, (l = 1, 2, 3 \dots) \quad (2.6)$$

where l is the angular momentum number originated from spherical harmonic expansion. It represents the dipole, quadrupole and higher order multipole oscillation modes of LSP. Therefore, the lower limit (red side) for LSPR energy is $\omega = \frac{\omega_p}{\sqrt{3}}$ when NPs are in vacuum. And the upper limit (blue side) approaches to surface plasmon resonance energy $\frac{\omega_p}{\sqrt{2}}$ when $l \rightarrow \infty$. Figure 2.5 shows the time averaged charge density distributions for these modes. Recall that the plasmon energy of Ga is 14.05 eV. The theoretical resonance energy of the dipole LSPR mode for small spherical Ga NP in vacuum is $\frac{\omega_p}{\sqrt{3}} = 8.11$ eV, which is in the UV. Therefore, this work will focus on exploiting gallium for UV plasmonics.



Figure 2.5: Time averaged charge density distributions for dipole and quadrupole LSPR modes.

Based on both theories and experiments, nanostructures' LSPR energies strongly depend on their composition, size, shape, dielectric environment [96], and interparticle coupling [97]. In general,

- i. Composition: Given equation 2.6, LSPR energy is directly related to metal's plasmon energy ω_p ($\hbar = 1$). Relatively large plasmon energy of Ga, comparing to Ag and Au, (Table 1.1) ensures that Ga NP can have LSPR energy in the UV.
- ii. Size: NP's LSPR will red shift when its radius increases. This can be demonstrated later by Mie calculation. Increase in NP radius will also split LSPR multipole modes further away [98]. This provides the potential to tune the LSPR energies of Ga NPs by controlling their size.
- iii. Dielectric environment: The dielectric function of surrounding medium directly effects LSPR energy given Equation 2.6. Even partially attached by some molecules, the LSPR energy of NPs may shift with significant amount. This constitutes the basis for LSPR molecule sensing [93]. Van Duyne reported 1.5 nm red shift in LSPR wavelength on Ag NPs for 1 pM streptavidin binding [99]. The presence of dielectric substrate will also red shift NP's LSPR energy due to image charge [100]. For our samples, Ga NPs are deposited on sapphire. The presence of substrate will shift Ga NPs' LSPR energies but will not alter NPs' function in the UV. Even

entirely surrounded by sapphire ($\epsilon_d = 1.8$), the dipole LSPR energy is

$$\frac{\omega_p}{\sqrt{1+2 \times 1.8}} = 6.55 \text{ eV, which is still in the UV.}$$

- iv. **Interparticle coupling:** When NP is surrounded by other NPs, strong interparticle coupling may occur. The strength of such coupling depends on interparticle distance [97], relative size [101], and incident light polarization relative to NP array's symmetry axis [102]. Strong coupling will blue shift NP's LSPR [97]. In our experiment, Ga NPs are randomly distributed on solid supports. Interparticle coupling plays an important role in their plasmonic features.

The parametric dependence of NP's LSPR energy above provides options to tune LSPR energy but make it difficult to estimate plasmonic properties for different nanogeometries. Next section will discuss how to estimate NP's LSPR energy.

2.2 Estimate of metallic NP's optical properties

In order to guide the synthesis of nanoparticles for plasmonic applications, like SERS, many analytical and numerical methods have been developed to study the local EM field surrounding nanostructures under external excitation. In this section, I will discuss these methods and show preliminary calculation results for Ga NPs to discuss the advantage of Ga in terms of its plasmonic features.

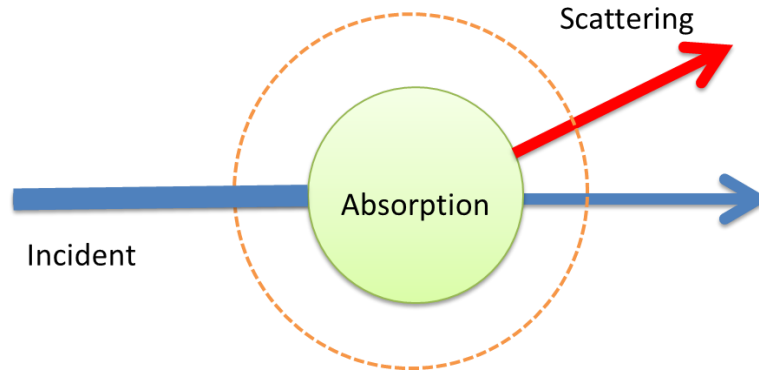


Figure 2.6: Schematic diagram of a scattering problem.

2.2.1 A scattering setup

In principle, the EM field surrounding a NP under excitation can be treated as a scattering problem and scattering profiles can be calculated from Maxwell equations in different ways. Figure 2.6 depicts the basic setup of a scattering problem. Two extra processes occur when incident EM radiation interacts with NP along with simple transmission: absorption and scattering. Now considering a closed surface S (dashed circle in Figure 2.6) surrounding the NP, there shall be no net energy flux on this surface due to the conservation of energy. Therefore,

$$E_{in} = E_{sca} + E_{abs} + E_{tra} \quad (2.7)$$

E represents the energy of each radiation. When there is no scattering medium, scattering and absorption do not occur and the transmitted radiation will be identical to the incident one. Given the definition of cross section, Equation 2.7 could be converted in terms of cross section and be rearranged as

$$E_{\text{in}} - E_{\text{tra}} = \sigma_{\text{sca}}E_{\text{in}} + \sigma_{\text{abs}}E_{\text{in}} \quad (2.8)$$

Equation 2.8 measures how much energy has lost while passing through a scattering medium. In experiments, it is easier to collect the intensity of incident and transmitted radiation, E_{in} and E_{tra} . Therefore, it is valuable to define a new process called extinction, which combines scattering and absorption and describes the total energy loss during the scattering. Given Equation 2.8, we have,

$$E_{\text{ext}} = \sigma_{\text{ext}}E_{\text{in}} = \sigma_{\text{sca}}E_{\text{in}} + \sigma_{\text{abs}}E_{\text{in}} \quad (2.9)$$

E_{ext} is the intensity of extinction radiation and σ_{ext} is called extinction cross section. Drop all the E_{in} in Equation 2.9, we have,

$$\sigma_{\text{ext}} = \sigma_{\text{sca}} + \sigma_{\text{abs}} \quad (2.10)$$

In order to compare scattering abilities among different geometries, a dimensionless quantity, efficiency Q , is more often used than cross section.

$$Q = \frac{\sigma}{S_g} \quad (2.11)$$

where S_g is the area of a geometrical cross section of the particle in a plane perpendicular to the direction of the incident radiation. Therefore, Equation 2.10 can be rewritten as,

$$Q_{\text{ext}} = Q_{\text{sca}} + Q_{\text{abs}} \quad (2.12)$$

Q_{ext} , Q_{sca} and Q_{abs} are extinction efficiency, scattering efficiency and absorption efficiency respectively. These are major quantities to characterize scattering.

NP will enhance local EM field as well as generating strong absorption and scattering when excited by external EM wave at NP's LSPR energy [103]. Q_{sca} and Q_{abs} curves can hence be used to predict NP's LSPR energy. Ideally, Q_{sca} and Q_{abs} may reach maximum concurrently. However, other effects, like edge scattering, entanglement of surface plasmon and bulk plasmon will result in different but close Q_{sca} and Q_{abs} peak energies. Complex models are needed to retrieve LSPR energy from either Q_{sca} or Q_{abs} curves. Practically, Q_{ext} , which combines both scattering and absorption, is much often used in the literature to estimate LSPR energy besides that extinction is easier to be measured.

In most cases, analytical results for these quantities are not possible or hard to obtain. Numerical calculations are widely used to predict optical properties of nanostructures [104]. In the next three subsections, I will discuss three calculation methods: Rayleigh scattering, Mie scattering and discrete dipole approximation (DDA) method. Rayleigh scattering provides analytical result under small NP limit; Mie scattering provides analytical solution for spherical particles but requires numerical calculations; and DDA is a numerical method based on dipole radiation and applicable for arbitrary nanostructures.

2.2.2 Rayleigh scattering

Let's first examine the simplest case. Consider a single, free standing, homogeneous and isotropic, spherical NP. When NP's length scale (diameter) is much smaller than the wavelength of the incident EM radiation, Rayleigh scattering occurs. It is an elastic scattering process named after Lord Rayleigh who discovered the phenomenon and used it to explain why the sky is blue [105]. The scattering efficiency of such NP is [36],

$$Q_{\text{sca}} = \frac{2^{13}\pi^3 a^6 \epsilon_d^2}{3\lambda^4} \left| \frac{\epsilon_m - \epsilon_d}{\epsilon_m + 2\epsilon_d} \right|^2 \quad (2.13)$$

where a is the radius of the sphere, λ is the wavelength of the incident EM wave. It indicates that scattering cross section is inversely proportional to the fourth power of the incidence EM wave wavelength or proportional to the fourth power of the incident wave frequency (energy). The enhancement comes from the term $\left| \frac{\epsilon_m - \epsilon_d}{\epsilon_m + 2\epsilon_d} \right|^2$ in Equation 2.14. Therefore, a local enhancement factor is defined as,

$$g(\omega) = \frac{\epsilon_m - \epsilon_d}{\epsilon_m + 2\epsilon_d} \quad (2.14)$$

Combing with Equation 2.13, $|g(\omega)|^2$, a frequency (energy)-dependent factor, depicts the degree of enhancement for a NP, which is a good estimation for NP's plasmonic properties. It is only valid when Rayleigh condition is met, which is the length scale of the sphere is much smaller than the incident wave length. Therefore, it is also called Rayleigh approximation.

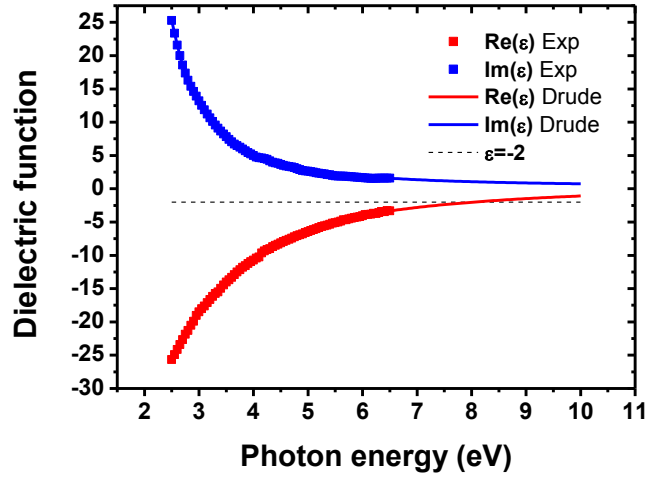


Figure 2.7: Dielectric function of Ga by Drude model fitting.

Equation 2.14 indicates that resonance occurs when $\epsilon_m + 2\epsilon_d = 0$. For a small spherical Ga NP in vacuum, the condition is $\epsilon_m = -2$. Figure 2.3 shows that the real part of ϵ_m does not cross -2 in the detection range. In order to obtain the full scattering profiles, we extended the dielectric function of Ga to deep UV range by fitting the experimental data with the Drude dielectric function (Equation 2.1). The extended dielectric function is plotted in Figure 2.7. Fitted $\omega_p = 13.6$ eV which is reasonable for Ga.

Figure 2.8 plots the $|g(\omega)|^2$ curve for Ga NP in vacuum under Rayleigh approximation using the dielectric function (DF) in Figure 2.7. The peak occurs at 8 eV as the real part of fitted Ga DF crosses -2 there. The peak value is about 9. Table 2.1 shows the similar calculation result for commonly used Au and Ag NPs

[106]. It is clear that only the resonance of Ga NP occurs within the UV range (8.0 eV). The resonance energies for Au and Ag are all in the visible range. This indicates again the fail of Au and Ag in UV plasmonics and the potential of Ga in UV plasmonics. Comparing the peak values among all three metals, the value of Ga is between those of Au and Ag, which indicates that Ga may exhibit similar enhancement in UV as good as gold in the visible range. The large value for Ag comes from its high electric conductivity and free electron density. Higher density electrons increase the ability to absorb and scatter incident radiation and thus increase the enhancement strength. The inter-band transitions for Au in the visible range lower its enhancement ability [106].

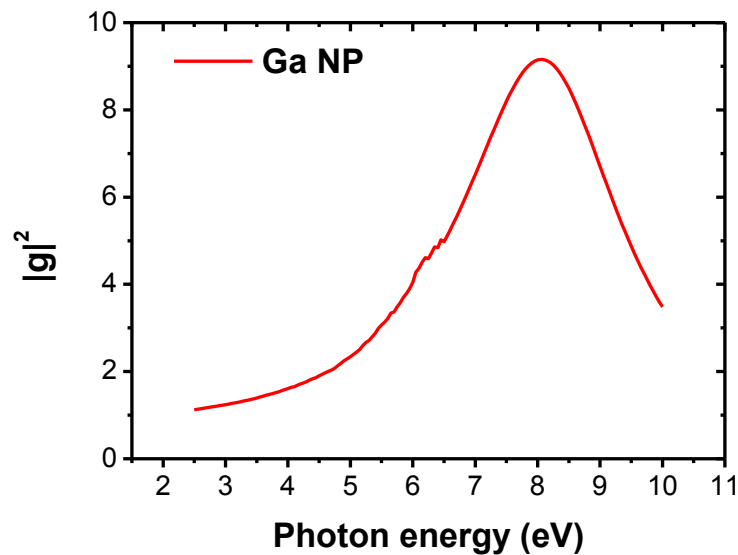


Figure 2.8: Local field enhancement $|g(\omega)|^2$ for a free standing spherical Ga NP in vacuum calculated by Rayleigh scattering.

Table 2.1: Local field enhancement $|g|^2$ profiles for Ga, Au and Ag.

	Ga	Au [106]	Ag [106]
Resonance energy (eV)	8.0	3.4	2.3
Max[$ g ^2$]	9	3	26
FWHM (cm^{-1})	20000	6100	2100

The third important quantity of $|g|^2$ is the full width at half maximum (FWHM) of the resonance peak. It indicates the function range, or bandwidth, of the enhancement. Although Ag bears high peak value at resonance, its bandwidth is about 2100 cm^{-1} . This sets the limit for the plasmonic application in continuous spectroscopy. For example, for a Raman mode at 2100 cm^{-1} , the enhancement of the scattering light will drop to one half from the excitation at resonance energy for Ag. This restricts its enhancement for Raman mode with large Raman shift. The enhancement bandwidth for Ga is very large comparing to Ag and Au due to its large damping constant, which lowers the resonance peak but increases the bandwidth. Plasmonic materials with large bandwidth have great potential in applications like optical communication and energy storage and transfer.

Under Rayleigh approximation, since NP size is much smaller than external EM field wavelength, the external field surrounding NP is uniform and quasistatic.

Local EM field outside of a free standing NP in a static EM field $E_0\hat{z}$ can thus be calculated from Laplace equation of electrostatic as [46],

$$\mathbf{E}_{\text{loc}} = E_0\hat{z} - ga^3E_0\left[\frac{\hat{z}}{r^3} - \frac{3z}{r^6}\hat{r}\right] \quad (2.15)$$

This depicts the EM field distribution surrounding a single spherical NP under Rayleigh approximation. The g factor is the same as in Equation 2.14.

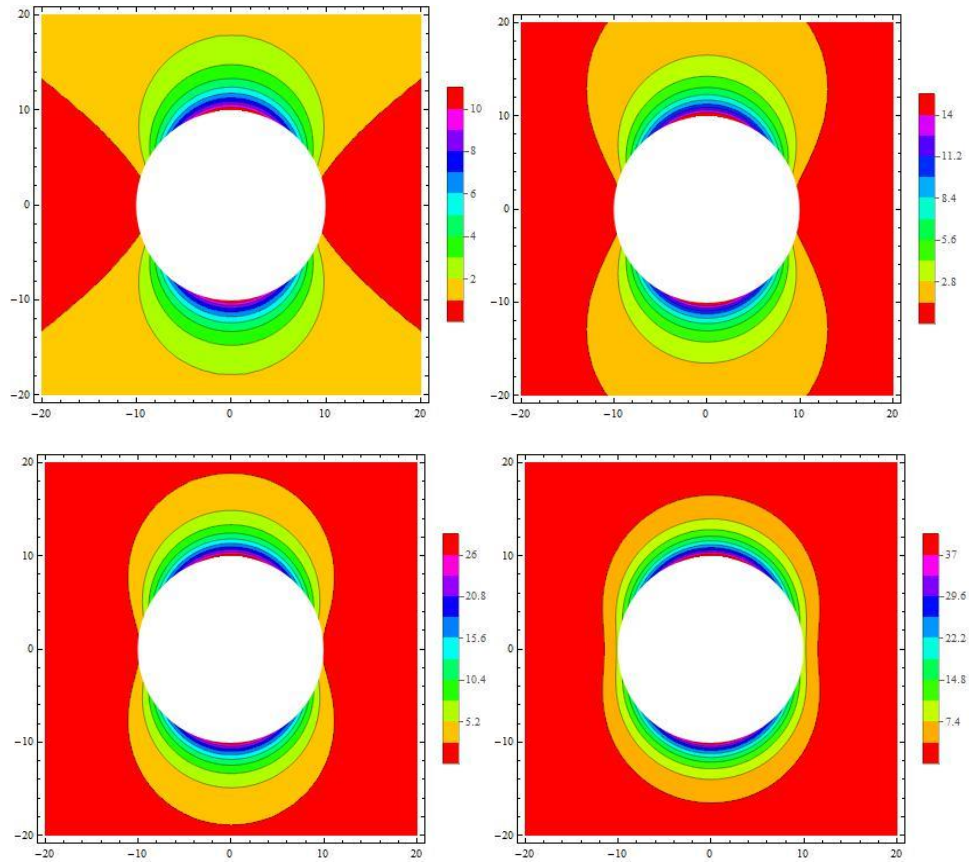


Figure 2.9: Contour plots of local field enhancement $|g_{\text{EM}}|^2$ surrounding a free standing spherical Ga NP in vacuum under Rayleigh approximation excited by external radiation at (a) 3.5 eV; (b) 5.0 eV; (c) 6.5 eV; and (d) 8.0 eV. (NP radius: 10 nm; horizontal and vertical axes represent x and z respectively).

Consider a Ga NP in the radius of 10 nm at the origin. In order to examine the enhancement ability of the NP, rewrite Equation 2.15 as,

$$\mathbf{g}_{\text{EM}} \equiv \frac{\mathbf{E}_{\text{loc}}}{E_0} = \hat{\mathbf{z}} - ga^3 \left[\frac{\hat{\mathbf{z}}}{r^3} - \frac{3z}{r^6} \hat{\mathbf{r}} \right] \quad (2.16)$$

$|\mathbf{g}_{\text{EM}}|^2$ directly measures the local EM field intensity enhancement at each site surrounding NPs. Figure 2.9a,b,c,d shows the contour plots of $|\mathbf{g}_{\text{EM}}|^2$ surrounding the Ga NP on the plane of $y = 0$ excited by external radiation at 3.5 eV, 5.0 eV, 6.5 eV, and 8.0 eV respectively calculated by Equation 2.16 and Equation 2.14 using Ga dielectric function from Figure 2.7.

The local field intensity enhancement depends on both the polar angle with respect to the external field and the distance to the NP. The static external field $E_0\hat{\mathbf{z}}$ is in $+\mathbf{z}$ direction. Maximum enhancement occurs along the \mathbf{z} direction (0° and 180°) near NP surface as plotted in Figure 2.9. External EM field induces dipole within the metallic NP. The dipole is along the external field direction (\mathbf{z} direction in this case). Charges will oscillate and stay longer near the two extrema of the oscillation. (Figure 2.5) The resulted field will be the composition of the original static field and the field from the induced dipole. An electric dipole will exhibit stronger field in the direction perpendicular to the dipole moment but less effect in the direction parallel to the dipole. The fields on both sides of the NP (90° and 270° to the original external field) will be cancelled out

by the induced dipole, while the field is enhanced due to the large time averaged charge density near the top and bottom of the NP. Recall that the resonance occurs at 8.0 eV. From Figure 2.9a to d, when photon energy is getting closer to resonance energy, the area with large enhancement is getting concentrated. The gradient of enhancement near the surface increases and so is the maximum enhancement value at the surface. In static external field, NP redistributes the surrounding field.

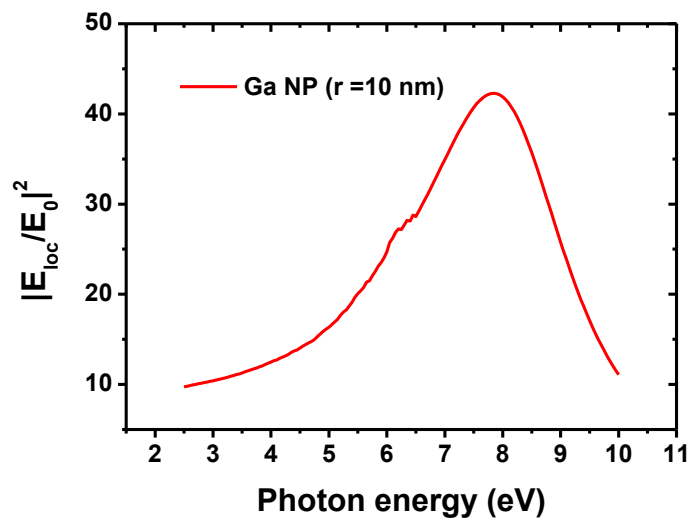


Figure 2.10: Energy dependence of maximum local EM field enhancement surrounding a free standing spherical Ga NP in vacuum under Rayleigh approximation.

Figure 2.10 plots the energy-dependent maximum enhancement value at the NP surface. Again, it reaches its maximum of approximately 42 at the resonance energy of approximately 8.0 eV. Similar calculation [46] shows that same

maximum enhancement value defined for Ag is about 85 at its resonance energy in the visible range. The enhancement for Ga in the UV is comparable with current plasmonic materials which demonstrated that Ga is a promising material for UV plasmonics. This approach can be used to qualitatively estimate the enhancement ability of NPs and compare with other metals.

Raleigh scattering works well for small particles but it is still an approximation to complete scattering solutions. In our experiments, NPs' radii are ranging from several nanometers to several hundred nanometers, which is close to the visible and UV photon wavelength (10 nm to 750 nm). Raleigh scattering may not be applicable for these NPs. Next section will discuss Mie scattering which is valid for spherical object in any size.

2.2.3 Mie scattering

Due to the symmetry of spherical geometry, spherical vector wave functions can be used to expand both incident and scattering fields and therefore the final solution takes the form of an analytical infinite series. This solution was first published by G. Mie in 1908 [95]. The scattering calculated by this method is thus called Mie scattering. It is valid for a single, free standing, homogenous sphere in any size.

Many books [107] along with the original paper of Mie [95] work through the derivation of the Mie solution. Here presented are general results. When a plane wave with wavenumber \mathbf{k} is incident on a spherical homogenous and isotropic object, the scattering efficiency and extinction efficiency are,

$$Q_{\text{sca}} = \frac{2}{(ka)^2} \sum_{l=1}^{\infty} (2l+1)(|a_l|^2 + |b_l|^2) \quad (2.17a)$$

$$Q_{\text{ext}} = \frac{2}{(ka)^2} \sum_{l=1}^{\infty} (2l+1)\text{Re}(a_l + b_l) \quad (2.17b)$$

where a is the radius of this object and a_l, b_l are referred to as Mie coefficients.

$$a_l = \frac{(nka)^2 j_l(nka)[kaj_l(ka)]' - (ka)^2 j_l(ka)[nkaj_l(nka)]'}{(nka)^2 j_l(nka)[kah_l(ka)]' - (ka)^2 h_l(ka)[nkaj_l(nka)]'} \quad (2.17c)$$

$$b_l = \frac{j_l(nka)[kaj_l(ka)]' - j_l(ka)[nkaj_l(nka)]'}{j_l(nka)[kah_l(ka)]' - h_l(ka)[nkaj_l(nka)]'} \quad (2.17d)$$

where j_l is the l^{th} order spherical Bessel function and h_l is the l^{th} order spherical Hankel function. n is the complex refractive index of the spherical object.

Equation 2.17 is valid for a homogenous spherical object standing in vacuum. It can be extended to similar systems with spherical symmetry. For example, if the object is standing in dielectric material with refractive index n_0 , relative refractive index n/n_0 should be used to calculate Mie coefficients. If the spherical object is not homogenous but has concentric layers, such as nanoshells, modified Mie coefficients are developed to solve the problem [108]. Mie calculation is also used to estimate the collective scattering profiles from a NP ensemble with

different radii [109]. Similar expansion idea is adopted by T-Matrix method to treat nonspherical objects [107].

Since Mie coefficients are expanded using infinite function series, convergence is the key issue for Mie calculation. Parameters for j_l and h_l are ka and nka . Firstly, notice that $ka = \frac{2\pi a}{\lambda}$, where λ is the incident EM field wavelength. Based on the properties of spherical Bessel functions, the cut off limit of the infinite summation series in Equation 2.17 are roughly equal to ka [110]. Therefore, when particle radius a is much larger than λ , more terms are needed in the summation. Inversely, when $a \ll \lambda$, i.e. $ka \rightarrow 0$, only the zeroth order functions are included. Equation 2.17 will actually reduce to 2.13, which is the Rayleigh approximation result. Secondly, nka is also one of the parameters for spherical functions. Given the discussion above, when a spherical object is made of high refractive index material, longer calculation is expected. Since ka is an important parameter in Mie calculation, it is often called size parameter and defined as,

$$x = \frac{2\pi a}{\lambda} \quad (2.18)$$

For NPs, convergence is indeed less problematic. Most NPs have radius from 10 nm to 200 nm in our experiments while the interested photon wavelengths are ranging from about 200 nm to 1000 nm (deep UV to near infrared). NP sizes are comparable but in most cases smaller than incident field wavelength. Only a few

terms are needed. Therefore, Mie calculation is the most common tool to estimate NP's LSPR [111-112].

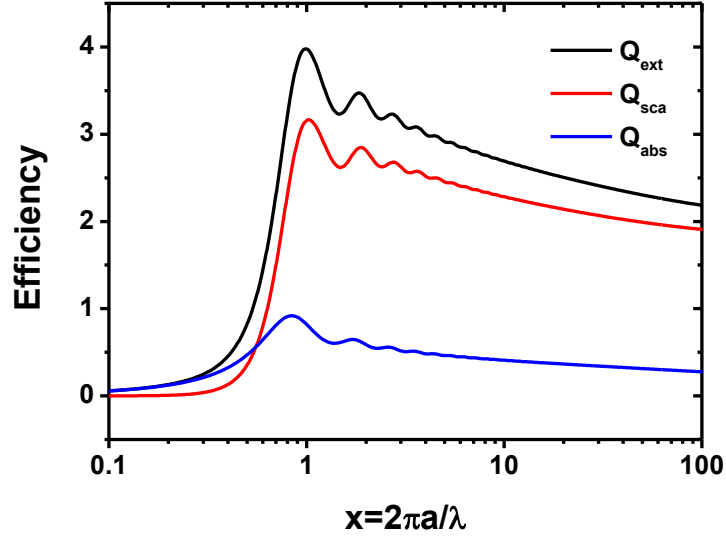


Figure 2.11: Extinction, scattering, and absorption efficiencies for free standing spherical Ga NP with different size parameters in vacuum.

Figure 2.11 plots Mie scattering profiles for free standing spherical Ga NP in vacuum with different size parameters x . Ga refractive index is converted from its dielectric function (Figure 2.3) using the basic relation,

$$n(\omega)^2 = \varepsilon(\omega) \quad (2.19)$$

The calculation used Mie calculation package, MiePlot 4.3 [113]. Extinction peaks around $x = 1$ indicating the proper NP size for field enhancement under different excitation wave. For example, if NP is excited by EM wave with 325 nm in wavelength, the NP with largest enhancement is about 50 nm in radius.

Below generalizes some important aspects of Figure 2.11:

- i. Absorption and scattering have slightly different peak positions with respect to size parameter x . This is due to the extra scattering at the edge. This peak difference may become much obvious for NP in large radius. Extinction efficiency curve is the convolution of absorption and scattering ones as shown in Equation 2.13.
- ii. Oscillation occurs due to the interference between transmitted and internal reflected light within NP. The period of the oscillation depends on the refractive index n of the NP.
- iii. Since Ga is conducting, its refractive index is a complex number with nonzero imaginary part which leads to absorption. Large absorption within the NP will reduce interference since internal reflected wave will not be able to travel long enough to interfere with transmitted wave. For large x , Q_{ext} decreases to 2 asymptotically.

Figure 2.12 shows extinction efficiencies for free standing spherical Ga NPs in vacuum with different radii ranging from 10 nm to 100 nm. The ripple curves are again due to the interferences. Each curve in Figure 2.12 is actually a special part of the curve in Figure 2.11 by fixing NP radius a while size parameter x is varying as photon wavelength or energy is changing. The peak at lowest photon

energy is the primary peak for extinction efficiency where largest local EM field enhancement is expected. When NP radius is increasing, this peak keeps redshifting which is consistent with experiments [75]. For NPs smaller than 60 nm in radius, their extinction peak is above 3.5 eV and in the UV range. It demonstrates again that Ga NP could have plasmon resonance in the UV and the resonance peak can be directly tuned by its size.

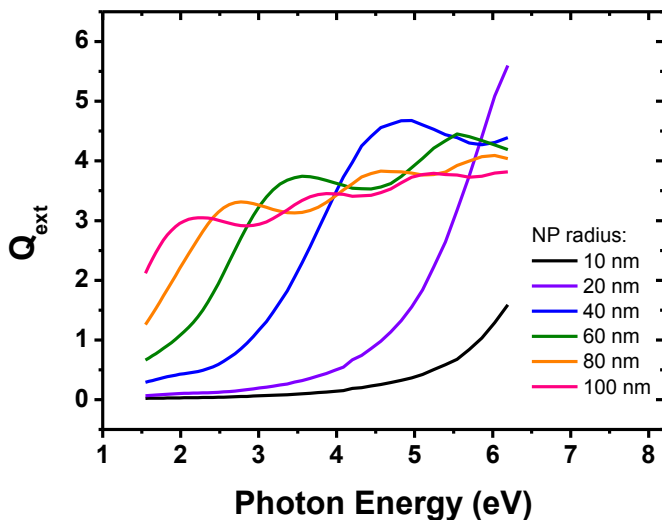


Figure 2.12: Extinction efficiencies for free standing spherical Ga NPs with different radii in vacuum.

2.2.4 Discrete dipole approximation

Mie scattering works well for free standing, homogenous, single spheres. However, in our experiments, NPs are deposited on solid supports and thus truncated. Randomly distributed NPs are close to each other and thus not free standing. Interparticle couplings play an important role in plasmon resonance.

Therefore, other methods are needed to calculate optical responses of arbitrary nanostructures. One of the numerical methods to solve for local EM field distribution for arbitrary structure is discrete dipole approximation (DDA).

DDA method was first introduced by H. DeVoe to investigate optical properties of molecular aggregates in 1964 [114]. E. Purcell and C. Pennypacker extended the original method to deal with retardation in EM radiation [115]. Principally, it is an approximation of the continuum media by a finite array of interactive polarizable dipoles. In theory, DDA method is applicable for arbitrary nanogeometries. It is widely used to examine plasmon properties of various nanostructures, including nanoparticles [96], nanodisks [116], nanorods [117], and other arbitrary-shaped nanostructures.

Consider a single dipole with polarizability α . The interaction between this dipole and local field \mathbf{E}_{loc} will induce a polarization known as,

$$\mathbf{P} = \alpha \cdot \mathbf{E}_{loc} \quad (2.20)$$

Notice that α is a 3×3 tensor and \mathbf{E}_{loc} is a 3×1 vector describing local field in all three orthogonal directions. DDA method discretizes the continuum media by dividing it into N unit cells. Each cell is represented by a dipole. The entire system is thus represented by N dipoles. For each dipole at position \mathbf{r}_i in the system, the local field around dipole i is the addition of the incident EM field

$\mathbf{E}_{\text{in}}(\mathbf{r}_i)$ and the induced radiation from all other N-1 dipoles in the structure at this position,

$$\mathbf{E}_{\text{loc}}(\mathbf{r}_i) = \mathbf{E}_{\text{in}}(\mathbf{r}_i) - \mathbf{E}_{\text{ind}}(\mathbf{r}_i) \quad (2.21)$$

Minus sign is for the sake of uniformity later in the derivation. Consider the incident field as a monochromatic plane wave with wavenumber k . Recall the radiation field at \mathbf{r}_i from a dipole \mathbf{P}_j at position \mathbf{r}_j is [118],

$$\mathbf{E}_{\text{dipole}}(\mathbf{r}_i, \mathbf{r}_j) = \frac{e^{ikr_{ij}}}{r_{ij}^3} \left[k^2 \mathbf{r}_{ij} \times (\mathbf{r}_{ij} \times \mathbf{P}_j) + \frac{(1-ikr_{ij})}{r_{ij}^2} (r_{ij}^2 \mathbf{P}_j - 3\mathbf{r}_{ij}(\mathbf{r}_{ij} \cdot \mathbf{P}_j)) \right] \quad (2.22)$$

where $\mathbf{r}_{ij} = \mathbf{r}_i - \mathbf{r}_j$ and $r_{ij} = |\mathbf{r}_{ij}|$. The i not in the subscript is the imaginary unit.

This equation includes the retardation effect of dipole radiation field. Therefore,

$\mathbf{E}_{\text{ind}}(\mathbf{r}_i)$ can be expressed as a sum of the entire radiation field in a matrix form,

$$\mathbf{E}_{\text{ind}}(\mathbf{r}_i) = \sum_{j \neq i}^N \mathbf{A}_{ij} \cdot \mathbf{P}_j \quad (2.23)$$

where \mathbf{A}_{ij} is a vector operator which can be derived from Equation 2.22 by dropping off \mathbf{P}_j . Insert Equations 2.21 and 2.23 in 2.20, we obtain that,

$$\mathbf{P}_i = \boldsymbol{\alpha}_i \cdot (\mathbf{E}_{\text{in},i} - \sum_{j \neq i}^N \mathbf{A}_{ij} \cdot \mathbf{P}_j) \quad (2.24)$$

For uniformity, let's define,

$$\mathbf{A}_{ii} = \boldsymbol{\alpha}_i^{-1} \quad (2.25)$$

Therefore, Equation 2.24 can be rewritten as,

$$\sum_{j=1}^N \mathbf{A}_{ij} \cdot \mathbf{P}_j = \mathbf{E}_{\text{in},i} \quad (2.26a)$$

or in a matrix form,

$$\mathbf{A} \cdot \mathbf{P} = \mathbf{E}_{\text{in}} \quad (2.26b)$$

where \mathbf{A} is a $N \times N$ tensor called interaction matrix, \mathbf{P} is a $N \times 1$ vector representing the polarization for each of the N dipoles in the system. \mathbf{E}_{in} is a $N \times 1$ vector describes the incident field at each dipole position. DDA method converts a differential equation question (Maxwell equations) to a linear algebra problem. The general complexity is $O(N^3)$ for the linear system. Homogeneous, isotropic and symmetric system may reduce the complexity to $O(N^2)$ [119].

Two types of input information are necessary for DDA calculation: geometry and refractive index. Equation 2.24 requires the position of each dipole \mathbf{r}_i . Equation 2.25 requires the dipole polarizability at each position. For an isotropic material, Clausius-Mossotti relation is applied. [119] Polarizability α is no longer a tensor but a constant which depends on the complex refractive index n of the material at position \mathbf{r}_i .

$$\alpha = \frac{3d^3}{4\pi} \frac{n^2 - 1}{n^2 + 2} \quad (2.27)$$

where d is the interdipole spacing.

The accuracy of DDA is dependent on the number of dipoles or the interdipole spacing [119]. The smaller the spacing is, the higher the accuracy will be. However, increase of dipole numbers will also increase both time and space complexity $O(N^3)$. Another factor impacting accuracy is the refractive index of

the target material. As shown in Equation 2.20, when n is very large, the ratio $\frac{n^2-1}{n^2+2}$ will be close to 1, which make the calculation difficult to differentiate α and insensitive to spatial changes. Research showed that DDA method performs best for materials with real part of refractive index around 1 ~ 2 [119].

Theoretically, DDA method can be applied to any geometry. The accuracy will be compromised in the area with large gradient, like sharp boundary, which is a common difficulty for most numerical methods. Several research have been done to compare DDA with other numerical methods [120-121]. DDA performs faster for simple geometries but fails when an array of NPs is present due to the rapid growth of storage space need.

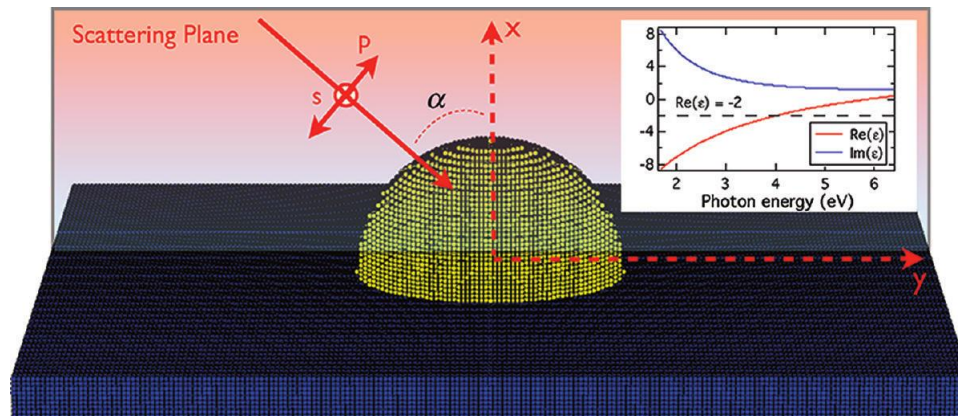


Figure 2.13: Scattering system of a hemispherical Ga NP on sapphire substrate for the modeling using DDA method (Inset: Ga dielectric function used in the calculation in Section 2.2.3 which is different from Figure 2.3).

Our collaborators (Moreno et al.) applied DDA method to calculate scattering profiles for hemispheroid Ga NP particles on pseudo semi-infinite cube-shaped sapphire substrate ($1000 \times 1000 \times 80$ nm) to compare and predict experiment results and guide synthesis [122]. Figure 2.13 depicts the lattice of composing dipoles mimicking the geometry. About 150,000 dipoles were used in the calculation to ensure accuracy (error level around 1%). Dielectric functions of Ga were presented in the inset of Figure 2.13. Scattering profiles were calculated for the photon energy ranging from 1.5 eV to 6 eV to cover visible to deep UV range. Systems with various NP radii ranging from 20 nm to 60 nm were calculated. Incident plane wave was also considered for various angles of incidence from 0° to 70° in order to compare with grazing angle incident SE measurements and predict normal incident Raman performance. The discussion below in this section will use α to represent angle of incidence as shown in Figure 2.13.

Absorption efficiency, Q_{abs} as defined in Equation 2.11, was considered for this calculation as for the range of NP radii of interest (20 ~ 60 nm), the extinction process is dominated by scattering and therefore $Q_{\text{abs}} = Q_{\text{ext}} - Q_{\text{sca}}$ more sensitively manifests multipolar effects. Also, since Q_{abs} is directly correlated with the imaginary part of refractive index which can be measured by SE, it is used to directly compare the SE measurement result later in this thesis.

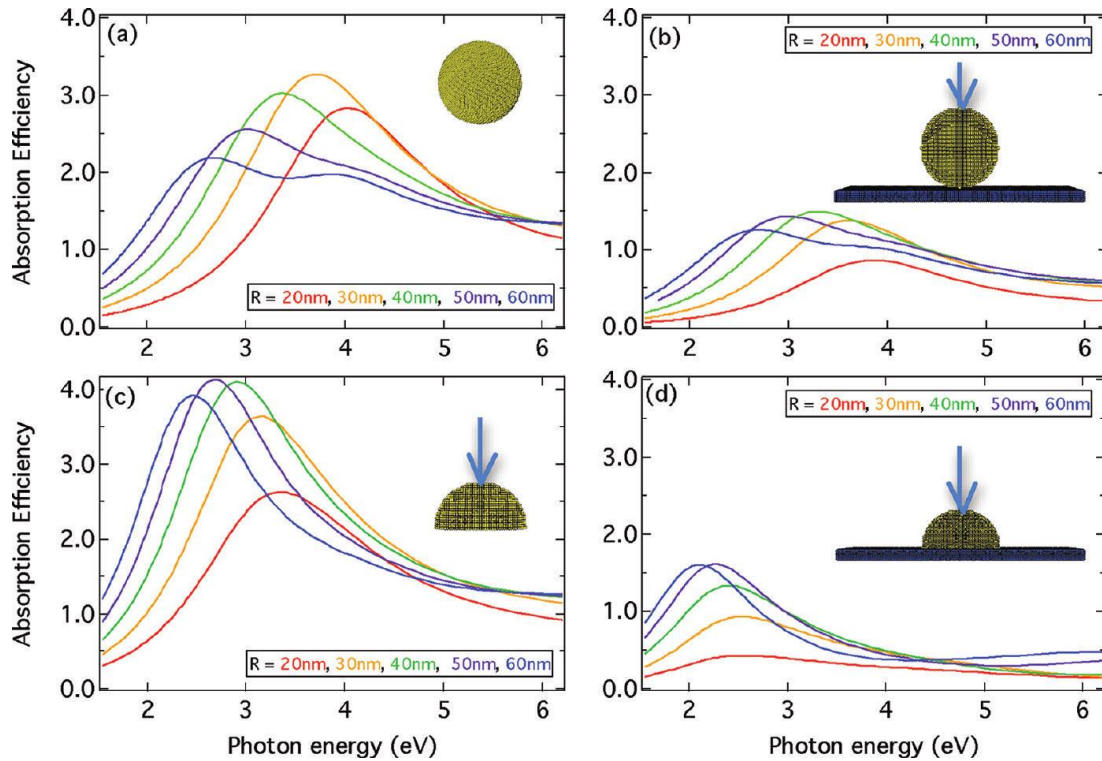


Figure 2.14: Absorption efficiencies for different NP/substrate setup (a) free standing spherical Ga NP; (b) spherical NP on square sapphire substrate; (c) free standing hemispherical Ga NP; and (d) hemispherical Ga NP on square sapphire substrate.

Figure 2.14 shows how size, shape and substrate alter the absorption efficiency of Ga NP. First, Figure 2.14a shows the calculated Q_{abs} as a function of photon energy for free standing spherical Ga NPs in vacuum of five different radii. The most obvious spectral feature of the isolated spherical NPs is the broad resonance that shifts and extends over the entire 1 ~ 6 eV range analyzed. As the radius of the Ga NP is increased, the maximum keeps shifting to the red (lower photon energy). When the particle radius increases to 60 nm, a second, quadrupolar resonance appears at approximately 4.0 eV. Due to the symmetry,

the spectra are invariant with respect to the incident angle and polarization of the incident field.

In theory, Figure 2.14a shall have the same result as Mie scattering (Figure 2.12). The differences come from a) minimal difference between absorption and extinction efficiency, and b) majorly, different Ga dielectric functions. The Ga DF used in DDA calculation as shown in Figure 2.13 inset is not as accurate as the one (Figure 2.3) used for Mie scattering calculation. The real part of the former DF crosses -1 line at approximately 5 eV while the latter DF at 8 eV, which would lead to smaller resonance energies in this DDA calculation. For the NP in the same radius, the peaks in Figure 2.14 are all on the red side of the peaks in Figure 2.12. However, DDA calculation here can still be used to examine the relative effect of size, substrate and shape, while for all other calculations, the most accurate DF (Figure 2.3) is used through this work.

The scattering behavior of an isolated NP changes when it rests on a dielectric surface. Incident EM field interacts with both the NP and the substrate, and interactions between them depend on the morphology (size and shape) and dielectric function of the NP and substrate. Figure 2.14b shows the calculated spectral response of spherical Ga NPs contacting a sapphire substrate at a single point. The region about the NP is illuminated with a linearly polarized Gaussian

beam at normal incidence, $\alpha = 0$ as in Figure 2.13. Due to the symmetry in horizontal plane, the polarization for normal incidence light does not alter the result. Small red shifts of maxima are detected, particularly in the smaller NPs, and the apparent decrease in absorption efficiency occurs because the geometrical normalization now includes the substrate (larger S_g in Equation 2.11). The primary reason that the shift is small is that the interaction between the nanoparticle and the substrate is weak. As discussed in Section 2.1, an image dipole of the NP is induced due to the presence of the substrate. The image dipole is on the other side of the original NP with respect to the substrate surface. As the NP size increases, the distance between the original NP effective and its substrate image dipole increases, thereby weakening the NP-substrate interaction. Therefore, only smaller NPs shows apparent peak energy shifts.

In our experiments, Ga NPs are truncated on solid supports, like sapphire, to form hemispherical shape. Therefore, it is critical to study the optical responses from hemispherical NPs. Being able to calculate nonspherical objects is also one of the advantages of DDA method. Figure 2.14c,d plots the hemispherical Ga NP without and with the presence of sapphire substrate. Both are again illuminated with a linearly polarized Gaussian beam at normal incidence. As compared to spherical NPs (Figure 2.14a), the resonance energy for the isolated hemisphere

(Figure 2.14c) of the same radius is clearly shifted to the red because of the increased and anisotropic confinement and reduced electronic restoring force. This red shift is further enhanced by the presence of the substrate (Figure 2.14d) because the image dipole is now closer to the surface, making the interaction significantly more intense than that corresponding to the spherical geometry.

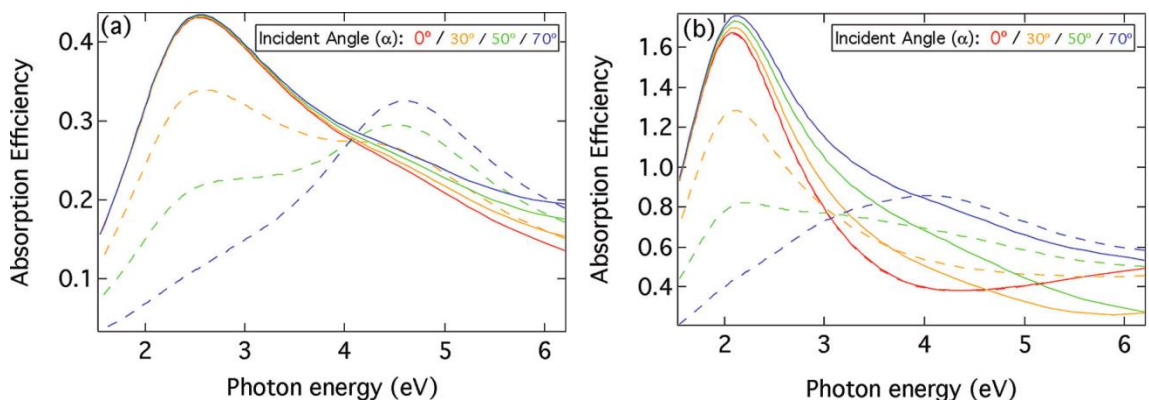


Figure 2.15: Absorption efficiencies for hemispherical Ga NP in radius of (a) 20 nm and (b) 60 nm on sapphire substrate illuminating by light with different angle of incidence for s-polarized (solid line) and p-polarized (dashed line) wave.

To this point, the analysis has only considered illumination at normal incidence $\alpha = 0$, so there have been no polarization-dependent effects. To illustrate the importance of shape, consider the effect of varying the angle of incidence, α , on the spectra from a hemispherical Ga NP on a sapphire substrate as shown in Figure 2.13. Figure 2.15 plots calculated Q_{abs} for Ga hemispheres with the cross-sectional radius of (a) 20 nm and (b) 60 nm, where the solid/dashed lines are for s- and p-polarized illumination respectively. S- and p-polarizations represent

the field components in EM wave whose electric field vector oscillates perpendicular and parallel to the plane of incidence respectively. (Detailed discussion about polarization will be presented in Chapter 3.) The spectra for normal incidence are identical for both polarizations as expected. The resonance energy red shifts from Figure 2.15a to b again due to the increase of NP size as shown in Figure 2.14d. The spectra for s-polarization remain relatively insensitive to incidence angle, while the spectra for p-polarization undergo a quenching of the lower energy peak and the emergence of a new high-energy peak with increasing angle of incidence.

To understand this shape-dependent behavior, recall that the induced dipolar response of the NP aligns with the polarization of the illumination. Thus, s-polarized illumination induces a dipolar response parallel to the substrate which is named in-plane mode. Here the “plane” is referred to the plane of surface. As the angle of incidence changes, the direction and amplitude of the total incident field vector on the NP vary only slightly due to the surface reflection from the substrate, which explains why the resonance is insensitive to incidence angle. By contrast, p-polarized incidence field induces a dipole moment that can be decomposed into two orthogonal components, one parallel to the substrate (in-plane mode) and one perpendicular to it, which is thus called out-of-plane mode.

Changing the incidence angle changes the relative amount of energy in each component: the perpendicular component grows and the parallel component shrinks as the incidence angle increases away from normal. Since the perpendicular component corresponds to an induced dipole along the smaller dimension of the nanoparticle, it is responsible for the higher energy resonance feature in Figure 2.15, while the parallel component corresponds to the lower energy feature. Therefore, as the incidence angle increases for p-polarized illumination, the high energy resonance increases in strength while the low-energy resonance decreases. The sum of the s- and p-polarized spectra approximates the scattering by circularly polarized illumination, and the two peaks separated by more than 2 eV.

In our experiments, optical responses of Ga NP/sapphire samples were monitored by in situ SE at 70° while Raman spectra were measured at normal incidence. Both in-plane and out-of-plane modes may occur in SE spectra while only in-plane mode contributes to normal-incidence Raman spectroscopy. Therefore, it is critical to control the in-plane mode, the lower energy resonance feature, during synthesis.

To summarize, the LSPR energy of Ga NP reaches the deep UV range and can be tuned by controlling NP size, shape and substrate. Ga NPs also possess larger

enhancement bandwidth and show comparable local field enhancement in UV comparing to Ag and Au in the visible range, which makes Ga a promising material for UV plasmonics.

Therefore, we will explore Ga NPs starting from their controlled synthesis (Chapter 4) to spatial (Chapter 5) and optical (Chapter 6 and 7) characterization and finally apply them for UV SESR and UV SEF (Chapter 8). Next chapter (Chapter 3) will first discuss the principle of spectroscopic ellipsometry which will be used to monitor and control the LSPR evolution during controlled synthesis of Ga NPs.

3. Polarization and Spectroscopy Ellipsometry

Chapter 2 shows that large local field enhancement will occur when NP's LSPR energy coincides with the external excitation. Therefore, in order to obtain large enhancement in the UV, NP samples shall possess LSPR energies in the UV. In order to guide synthesis, in situ spectroscopy ellipsometry (SE) is used to measure NP samples' LSPR energies. This chapter will present the principle of this measurement starting with a brief introduction to polarization.

3.1 Polarization

In 1669, Erasmus Bartholinus, a Danish scientist, observed two offset and orthogonal images when viewing through an Iceland spar, a macroscopic crystal of calcite [123]. This phenomenon is now the well-known double refraction and was attributed to the first discovery of polarization effect [124]. However, it was not well explained until the development of wave theory of light in 1800s.

Light polarization has been widely investigated by physicists. It is often used as a probe method in thin film science [125-127], granular material science [128], biology [129], chemistry [130], and geology [131], as well as applications in daily life, e.g. sunglasses, photography and 3D movie.

3.1.1 Jones vector

Based on Maxwell equations, a light ray is a transverse wave. In a right-hand coordinate system ($\hat{\mathbf{i}} \times \hat{\mathbf{j}} = \hat{\mathbf{k}}$), a plane wave propagating in the +z direction is,

$$\mathbf{E}(z, t) = \begin{pmatrix} E_x \\ E_y \end{pmatrix} = e^{i(\omega t - kz)} \begin{pmatrix} E_{0x} e^{i\delta_x} \\ E_{0x} e^{i\delta_y} \end{pmatrix} \quad (3.1)$$

The z component was omitted in Equation 3.1 as it is zero. This representation was first introduced by R. C. Jones in 1947 [132]. Although the original definition includes the $e^{i(\omega t - kz)}$ term, the time-independent vector is now usually called the Jones vector.

$$\mathbf{J} = \begin{pmatrix} \langle E_x \rangle \\ \langle E_y \rangle \end{pmatrix} = \begin{pmatrix} E_{0x} e^{i\delta_x} \\ E_{0x} e^{i\delta_y} \end{pmatrix} \quad (3.2)$$

It decomposes the vibrations of a plane wave into two orthogonal directions in the transverse plane and collects both amplitude and phase information. In practice, the Jones vector is normalized to the total intensity $I = \langle E_x E_x^* + E_y E_y^* \rangle$. Therefore, the amplitudes of the two components are between -1 and 1. In theory, any single plane wave can be well described by a Jones vector.

3.1.2 Instantaneous optical field

The two orthogonal oscillations represented by Jones vector in Equation 3.3 are called polarized components of the optical field, or polarizations. To examine different states of polarization (SoP), Equation 3.1 can be rewritten as,

$$\frac{E_x^2}{E_{0x}^2} + \frac{E_y^2}{E_{0y}^2} - 2 \frac{E_x}{E_{0x}} \frac{E_y}{E_{0y}} \cos\delta = \sin^2\delta \quad (3.3)$$

where $\delta \equiv \delta_y - \delta_x$, which is the phase difference between the two polarizations. Equation 3.3 is recognized as the equation of an ellipse showing that at any given time t and any position \mathbf{r} in the space, the instantaneous optical field forms an ellipse in the x - y plane which is perpendicular to the propagation direction ($+z$ in this case).

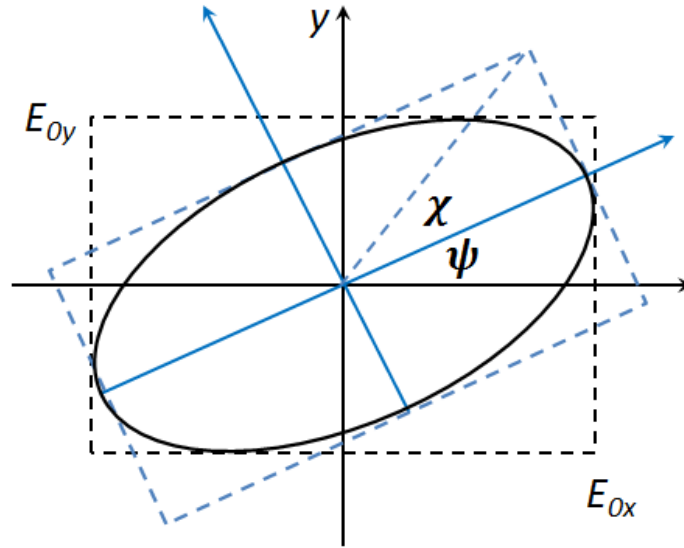


Figure 3.1: Instantaneous optical field ellipse.

As shown in Figure 3.1, given different values of E_{0x} , E_{0y} , and δ , the major and minor axes of the polarization ellipse do not necessarily overlap with x and y axes. ψ denotes the orientation angle (or angle of rotation) of the ellipse, which is the angle between the major axis and the x axis. And, χ is the ellipticity angle which is defined in the polarization ellipse.

3.1.3 State of polarization (SoP)

Equation 3.3 constructs different SoP given parameters E_{0x} , E_{0y} , and δ . In some special cases, it will collapse to simpler form to represent special SoP:

i. Linear polarization

$\delta = 0$ or π : Equation 3.3 becomes,

$$E_y = \pm \frac{E_{0y}}{E_{0x}} E_x$$

which is the equation of a straight line in the x-y plane with the angle of inclination $\theta = \text{Arctan}(\pm \frac{E_{0y}}{E_{0x}})$. The light is thus θ degree linearly polarized.

Specifically, when $E_{0y} = 0$ or $E_{0x} = 0$, the wave will oscillate along only x or y direction which is called x- or y- (linearly) polarized light respectively.

ii. Circular polarization

$E_{0x} = E_{0y} \equiv E_0$ and $\delta = \frac{\pi}{2}$ or $\frac{3\pi}{2}$: Equation 3.3 becomes

$$\frac{E_x^2}{E_0^2} + \frac{E_y^2}{E_0^2} = 1$$

which is the equation of a circle with radius E_0 . The light is thus circularly polarized. When $\delta = \frac{\pi}{2}$, the instantaneous optical field vector rotates clockwise from the point of view of the receiver, the light is right (hand) circularly polarized. Similarly, when $\delta = \frac{3\pi}{2}$, the light is left (hand) circularly polarized.

Table 3.1: Jones vector representation of states of polarization.

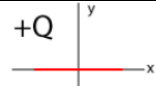
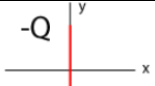
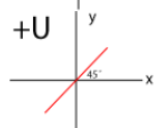
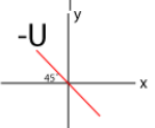
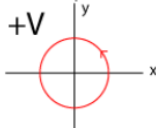
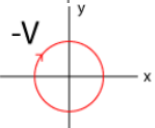
SoP	Jones vector	SoP	Jones vector
	$\begin{pmatrix} 1 \\ 0 \end{pmatrix}$		$\begin{pmatrix} 1 \\ 0 \end{pmatrix}$
	$\frac{1}{\sqrt{2}} \begin{pmatrix} 1 \\ 1 \end{pmatrix}$		$\frac{1}{\sqrt{2}} \begin{pmatrix} 1 \\ -1 \end{pmatrix}$
	$\frac{1}{\sqrt{2}} \begin{pmatrix} 1 \\ i \end{pmatrix}$		$\frac{1}{\sqrt{2}} \begin{pmatrix} 1 \\ -i \end{pmatrix}$

Table 3.1 summarizes six basic SoP and their Jones vector representations. When the light is in a specific SoP above, it is totally polarized. In the natural world, a beam of light (in +z direction) may consist of vibrations in all the directions in the x-y plane. The light is unpolarized when these vibrations all have the same intensity I_0 , i.e.,

$$I(\theta) = I_0, \forall \theta \in [0, 2\pi] \quad (3.4)$$

where θ is the azimuthal angle in the x-y plane. Sun light and most sources of EM radiations are considered to be unpolarized. When there is a preference for the direction in which it vibrates, $I(\theta)$ does vary for different θ and the light becomes partially polarized. A partially polarized light can be treated as a superposition of an unpolarized light and a totally polarized light. Degree of polarization (DoP) p is defined as [133],

$$p = \frac{I_p}{I_{\text{tot}}} \times 100\% \quad (3.5)$$

where I_p is the intensity of the polarized portion of the light and I_{tot} is the total light intensity. A totally polarized light has $p = 100\%$ and a unpolarized light has $p = 0\%$.

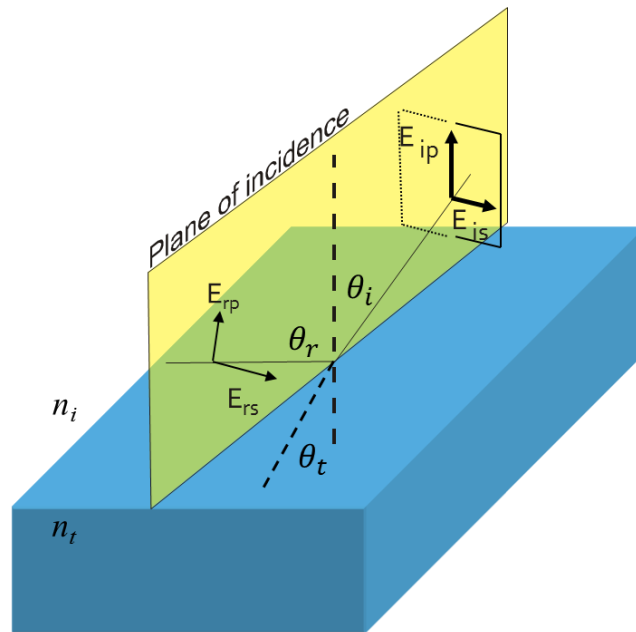


Figure 3.2: Schematic diagram of reflection and refraction at media interface.

3.2 Reflection at surface

Now, let's connect mathematical expressions to physical phenomena. Polarizations have been intensively studied at the interface of different media. Consider a simple plane wave propagating towards the interface of two semi-infinite media with refractive indices n_i and n_t respectively as illustrated in

Figure 3.2. The normal vector of the interface, and \mathbf{k} , the wave vector, form the plane of incidence. The vibrations of the light can be decomposed into two orthogonal directions with one lying in the plane of incidence and the other perpendicular to the plane of incidence. The in-plane (plane of incidence) component is named p-polarization or p-polarized light, while the out-of-plane component is called s-polarization or s-polarized light. The prefix s is from German word senkrecht for perpendicular, and p is from parallel.

At the interface, part of the incident light is reflected back to the same medium and part of it is refracted (transmitted) into the other medium. Snell's Law gives that [107],

$$\begin{cases} \theta_r = \theta_i \\ n_t \sin \theta_t = n_i \sin \theta_i \end{cases} \quad (3.6)$$

where, θ_i is the angle of incidence (AOI), θ_r is the angle of reflection, and θ_t is the angle of transmission. They are the angles between normal \mathbf{n} and incident, reflected and transmitted (refracted) light respectively. In the notations below, the subscripts i, r and t represent incident, reflected and transmitted light respectively.

3.2.1 Fresnel equations

Recall the boundary conditions of EM wave at free (no free charge and current) interface. They can be written using the s and p notation,

$$\begin{cases} n_t \sin \theta_t E_{t,p} - n_i \sin \theta_i (E_{i,p} + E_{r,p}) = 0 \\ n_t E_{t,s} - n_i (E_{i,s} + E_{r,s}) = 0 \end{cases} \quad (3.7)$$

Similarly, we can have two other equations from the continuities of \mathbf{H} and \mathbf{B} . The reflection and transmission ratios for s- and p- polarizations can thus be derived from these conditions. These ratios were first deduced by French scientist A. J. Fresnel [134]. These equations are thus called the Fresnel equations. The reflection ratios are,

$$\begin{cases} r_s = \frac{E_{r,s}}{E_{i,s}} = \frac{n_i \cos \theta_i - n_t \cos \theta_t}{n_i \cos \theta_i + n_t \cos \theta_t} = -\frac{\sin(\theta_i - \theta_t)}{\sin(\theta_i + \theta_t)} \\ r_p = \frac{E_{r,p}}{E_{i,p}} = \frac{n_t \cos \theta_i - n_i \cos \theta_t}{n_t \cos \theta_i + n_i \cos \theta_t} = \frac{\tan(\theta_i - \theta_t)}{\tan(\theta_i + \theta_t)} \end{cases} \quad (3.8a)$$

The transmission ratios are,

$$\begin{cases} t_s = \frac{E_{t,s}}{E_{i,s}} = \frac{2n_i \cos \theta_i}{n_i \cos \theta_i + n_t \cos \theta_t} = \frac{2 \sin \theta_t \cos \theta_i}{\sin(\theta_i + \theta_t)} \\ t_p = \frac{E_{t,p}}{E_{i,p}} = \frac{2n_i \cos \theta_i}{n_t \cos \theta_i + n_i \cos \theta_t} = \frac{2 \sin \theta_t \cos \theta_i}{\sin(\theta_i + \theta_t) \cos(\theta_i - \theta_t)} \end{cases} \quad (3.8b)$$

Equation 3.8 calculates complex ratios of reflection and transmission, giving both the amplitude and phase information for s- and p- polarizations among incident, reflected and transmitted light. The complete derivation of the Fresnel equations is available in most optics books [134], while the assumptions in the derivation are worthy of note:

- i. It assumes that both media at the interface are isotropic and uniform. For birefringence, dichromic or general anisotropic materials, the refractive index is no longer a complex number but a complex tensor. Similar but modified treatment must be processed. The reflection and transmission ratios cannot be simply expressed by Equation 3.8 [135].
- ii. It assumes $\mu_i = \mu_t$ for both media. Equation 3.8 simply expresses ratios in terms of n_i and n_t , which implies two media don't have distinct magnetic properties. This assumption is valid for major materials we used in our experiments: gallium and sapphire.
- iii. The derivation above deals with only one interface when two media are semi-infinite. In real cases, such as air-dielectric interface, the dielectric material might not be semi-infinite but rather being a film with finite thickness. Multiple reflections and transmissions shall occur at multiple interfaces while multiple reflections light beams will interfere with each other. The importance of this effect depends on the coherent time and the wavelength of the light source and the film thickness. This has been intensively explored in thin film science [136]. For our samples of Ga NPs on substrates, multilayer model is necessary. Chapter 6 will discuss reflections from multilayer systems.

3.2.2 Reflection from dielectrics and metals

Before further discussion, let's first explore reflections from the major materials used in our experiments: sapphire and gallium. Figure 3.3 shows the calculation of reflection and transmission ratios based on Equation 3.8 at the interface of vacuum ($n_i = 1$) and sapphire ($n_t = 1.8$). $|r|^2$ and $|t|^2$ are plotted instead of ratios themselves as the absolute square values are directly related to intensity (power). $R = |r|^2$ and $T = |t|^2$ are named reflection and transmission rate or reflectance and transmittance respectively. Phase changes of r_s and r_p are also plotted.

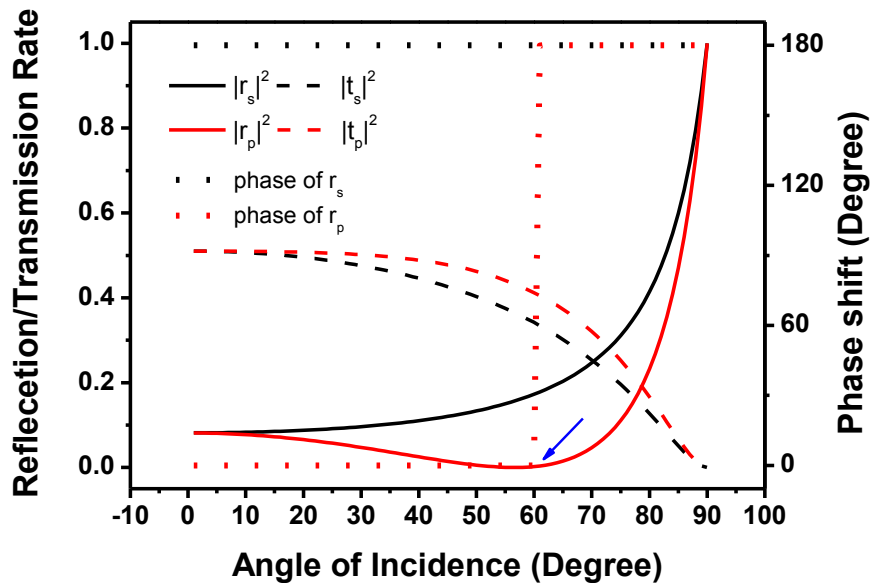


Figure 3.3: Amplitudes and phase shifts of reflectance and transmittance for s- and p- polarized wave at vacuum-sapphire interface.

Here, we summarize some important points,

- i. For $n_t > n_i$, all the ratios are real numbers. $R + T = 1$, given the conservation of energy. In Figure 3.3, T decreases and R increases with increasing angle of incidence.
- ii. There is a special angle of incidence, at which $|r_p|^2 = 0$ or $r_p = 0$. This can be predicted using Equation 3.8, let

$$r_p = \frac{\tan(\theta_i - \theta_t)}{\tan(\theta_i + \theta_t)} = 0$$

where $\tan(\theta_i - \theta_t)$ can't be zero, otherwise $\theta_i = \theta_t$ implying $n_i = n_t$, which indicates that it's not an interface of two different media. Therefore, we need $\tan(\theta_i + \theta_t) \rightarrow \infty$, that is

$$\theta_i + \theta_t = \frac{\pi}{2} \tag{3.9a}$$

Combing with Equation 3.6, we have,

$$\theta_t = \tan^{-1} \frac{n_t}{n_i} \equiv \theta_B \tag{3.9b}$$

θ_B is called Brewster's angle, named after the Scottish physicist Sir D. Brewster. For the reflection at the interface of vacuum and sapphire, $\theta_B = \tan^{-1} 1.8 = 60.9^\circ$. At this angle, all the p-polarized light will be transmitted but not reflected. The reflected light will only have s-polarization. It's a great source for linear polarizer.

- iii. The phase shift for s-polarized reflection light is always 180° regardless of the angle of incidence. For p-polarized reflection light, the phase shift flips from 0° to 180° at Brewster's angle. The 180° shift is called half wave loss. We can observe similar behavior for mechanic wave [137].

To explore another major material in our experiments, we calculated the reflection ratios at the ideal interface of vacuum and gallium ($n_t = \tilde{n}$). Different from dielectrics, metal has complex and energy-dependent refractive index as,

$$\tilde{n} = \tilde{n}(\omega) = n + i\kappa \quad (3.10)$$

Since the material is still optical isotropic and uniform, the Fresnel equations are still valid. Following discussions will focus on the properties of reflection since it is hard to measure transmission from metals as they are not transparent.

The refractive index of gallium was converted from the dielectric function shown in Figure 2.3 by Equation 2.19,

$$\tilde{n}(\omega)^2 = \varepsilon(\omega) \quad (2.19)$$

The values are then plugged in Equation 3.8. Figure 3.4 shows the reflectance and phase shifts for s- and p- polarized light as a function of both angle of incidence (vertical axes) and photon energy of incident light (horizontal axes). In order to directly compare with sapphire, similar plots were made for reflections at vacuum-sapphire interface and are placed side by side for direct comparison.

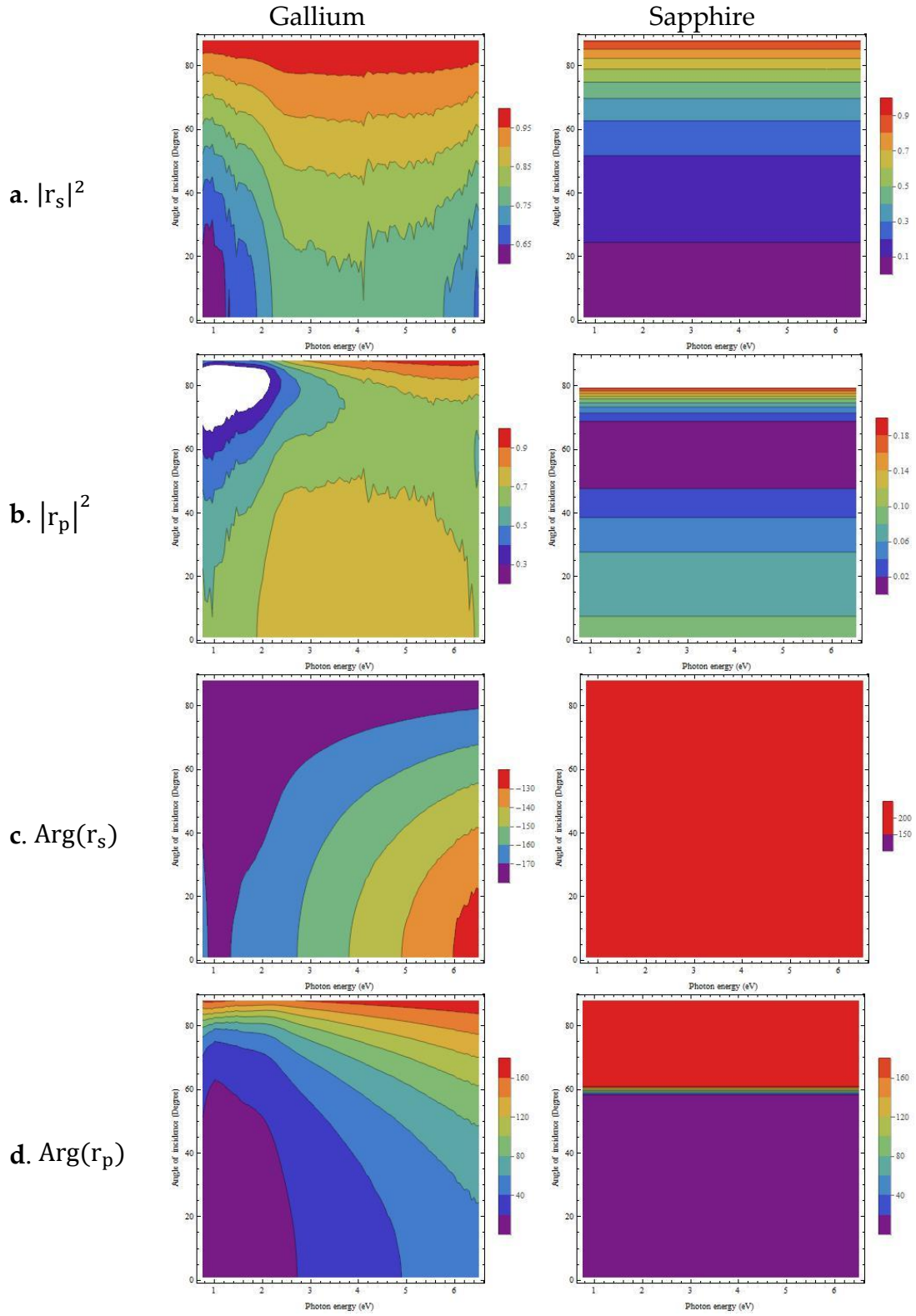


Figure 3.4: Amplitudes (a)(b) and phase shifts (c)(d) of reflectance for s- and p-polarization at vacuum-Ga interface (left) and vacuum-sapphire interface (right).

Comparing with dielectrics,

- i. Since the refractive index of sapphire is not energy dependent, all the two dimensional contour plots shows horizontal banded pattern. For vacuum-gallium interface, calculated quantities do vary with respect to energy. The noise in the plots is the entangled effect of the Fresnel equation and the complex energy-dependent refractive index of gallium.
- ii. In most of the photon energy range shown in Figure 3.4 (0.75eV to 6.5eV), reflectance for gallium is much higher (> 0.7) than that for sapphire at given AOI. It consists with the metal theory that when the incidence light frequency is smaller than the metal plasma frequency (14 eV for Ga), most light is reflected.
- iii. For AOI dependence, at given photon energy, $|r_s|^2$ of gallium increases when AOI increases, and $|r_p|^2$ decreases first and then increases. These trends are consistent with those for sapphire also shown in Figure 3.3. However, There does not exist an angle at which $|r_p|^2 = 0$. As shown in Figure 3.4c(left), but local minima for $|r_p|^2$ as a function of AOI for each photon energy. These minima are called pseudo Brewster's angle minima. Techniques are developed to use these minima to measure complex refractive index of metals.

- iv. The phase shifts are no longer binary values. The continuous phase shifts are highly related to metal absorption, or the imaginary part of the complex refractive index κ . Phase shift converges to $\pm 180^\circ$ when κ decreases to zero at higher photon energies.

3.2.3 Jones matrix

Fresnel equations (Equation 3.8) can also be expressed in a matrix form. Use s- and p- polarization directions instead of x and y axes, all the parameterization processes in Section 3.1 are still valid. The incident light is thus $(E_{i,s}, E_{i,p})^T$ and the reflected light is $(E_{r,s}, E_{r,p})^T$. Equation 3.8a can then be expressed in a matrix form,

$$\begin{pmatrix} E_{r,s} \\ E_{r,p} \end{pmatrix} = \begin{bmatrix} r_s & 0 \\ 0 & r_p \end{bmatrix} \begin{pmatrix} E_{i,s} \\ E_{i,p} \end{pmatrix} \quad (3.11a)$$

Or,

$$\mathbf{E}_r = \mathbf{J}\mathbf{E}_i \quad (3.11b)$$

This 2×2 matrix is called Jones matrix \mathbf{J} , which measures the transformation of SoP from incident light to outgoing light. The detailed discussions of Jones matrix will be presented in the next section.

3.3 Spectroscopic ellipsometry

Given Equation 3.11b, reflections at the interface of two media can be represented by a Jones matrix which can be calculated from refractive indices by the Fresnel equations. Or, if Jones matrix is measured, refractive indices of the two media can be retrieved from the measurement. This forms the principle of polarimetry. In this section, we will explore how to measure Jones matrix using SE and extract basic material optical properties from the measurement.

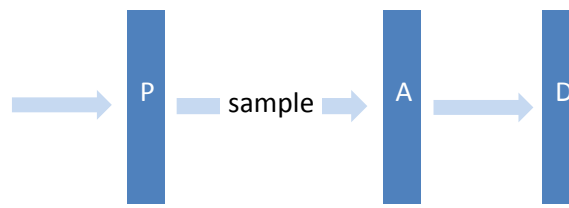


Figure 3.5: Basic configuration of spectroscopic ellipsometry.

Figure 3.5 depicts the basic configuration of spectroscopic ellipsometry in experiments. Polarizer (P) after light source generates initial SoP while the analyzer (A) analyzes the final SoP after the light interacting with samples. The final signals are received by detector (D). The SE system usually enables measurements in a wide range of photon energy from infrared (< 1.5 eV) to deep UV (> 5.5 eV) [138].

3.3.1 Measured quantities

Two orthogonal polarizations, p- and s-, regulated by the Fresnel equations (Equation 3.8) will behavior differently at the interface. SE measures the ratio of the reflection ratios of p- and s- polarizations which is defined as

$$\rho \equiv \frac{r_p}{r_s} = \frac{E_{r,p}/E_{i,p}}{E_{r,s}/E_{i,s}} \quad (3.12a)$$

ρ is often called complex reflectance ratio [138]. Instruments cannot directly measure a complex number. ρ can be decomposed into real and imaginary part.

$$\rho \equiv \frac{r_p}{r_s} \equiv \tan\Psi e^{i\Delta} \quad (3.12b)$$

where $\tan\Psi$ is the amplitude ratio upon reflection,

$$\tan\Psi = \frac{|r_p|}{|r_s|} = \text{Abs}(\rho) \quad (3.12c)$$

and Δ is the phase difference between the two reflection ratios,

$$\Delta = \text{Arg}(\rho) \quad (3.12d)$$

To define an angle associated with the amplitude ratio but not the ratio itself can limit the boundary of the observables. As $\frac{|r_p|}{|r_s|}$ is nonnegative, Ψ is defined in the first quadrant as

$$0^\circ \leq \Psi \leq 90^\circ \quad (3.13a)$$

In convention, the range of Δ is

$$0^\circ \leq \Delta \leq 360^\circ \quad (3.13b)$$

To express Δ using arctan function, we need to define Δ in different quadrants (Figure 3.6) to ensure the boundary in Equation 3.13b.

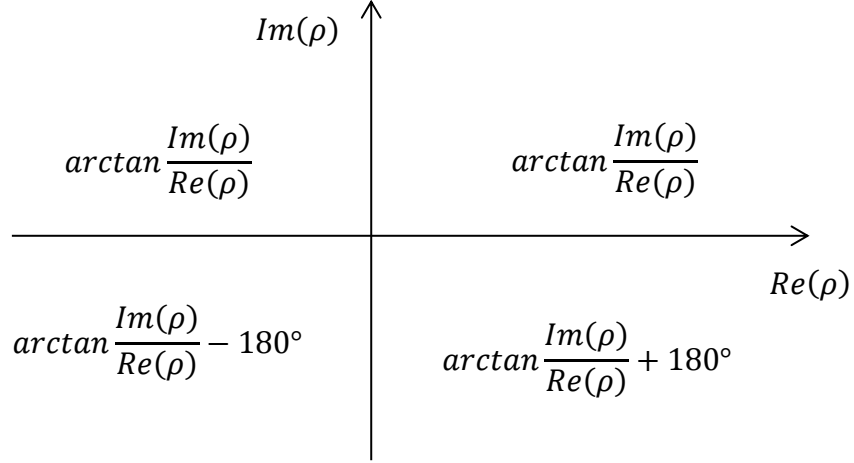


Figure 3.6: Convention to calculate Δ in different quadrants of ρ .

There shall be no difference if the measured quantity is $\frac{r_s}{r_p}$ instead of $\frac{r_p}{r_s}$. This article will follow the convention used by our SE instrument where $\rho \equiv \frac{r_p}{r_s}$ as defined in Equation 3.12. r_s and r_p regulated by the Fresnel equations can be plugged in Equation 3.12,

$$\tan\Psi e^{i\Delta} = \frac{r_p}{r_s} = \frac{n_i \cos\theta_i - n_t \cos\theta_t}{n_i \cos\theta_i + n_t \cos\theta_t} / \frac{n_t \cos\theta_i - n_i \cos\theta_t}{n_t \cos\theta_i + n_i \cos\theta_t} \quad (3.14)$$

The right side of the Equation 3.14 is expressed in terms of $(n_i, n_t, \theta_i, \theta_t)$. Given Snell's Law (Equation 3.3), only three of them are independent. In order to retrieve the refractive index n_t , Equation 3.14 can be rearranged as,

$$n_t = n_i \sin\theta_i \left[1 + \left(\frac{1-\rho}{1+\rho} \right)^2 \tan^2\theta_i \right]^{\frac{1}{2}} \quad (3.15a)$$

SE measurements are usually carried out when samples are placed in ambient air where $n_i = 1$. And the sample refractive index could be the complex index defined in Equation 3.10. Therefore, Equation 3.15 can be rewritten as,

$$\tilde{n} = n + i\kappa = \sin\theta_i \left[1 + \left(\frac{1-\rho}{1+\rho} \right)^2 \tan^2\theta_i \right]^{\frac{1}{2}} \quad (3.15b)$$

In the simplest case, Equation 3.15b can be directly used to calculate the sample complex refractive index when $\rho(\Psi, \Delta)$ is measured. In order to obtain valid results from Equation 3.15, samples shall satisfy the assumptions held by the Fresnel equations, e.g. isotropic, uniform and semi-infinite.

3.3.2 Measurement

A Horiba Jobin Yvon phase modulated SE was installed on the growth chamber in our experiments. It enables in situ (during deposition, kinetic) and ex situ (static) measurements at the angle of incidence fixed at approximately 70° . Data are collected with photon energy from 1.5 eV to 6.0 eV. The unpolarized light from a Xenon-lamp passes through a polarizer by an optical fiber. The light is then directed to the sample surface and reflected into the analyzer. The analyzer is composed of a retarder (phase modulator) and a polarizer. Parameters of the outgoing light is measured as a function of both time and photon energy. A schematic of our SE system is shown in Figure 3.7.

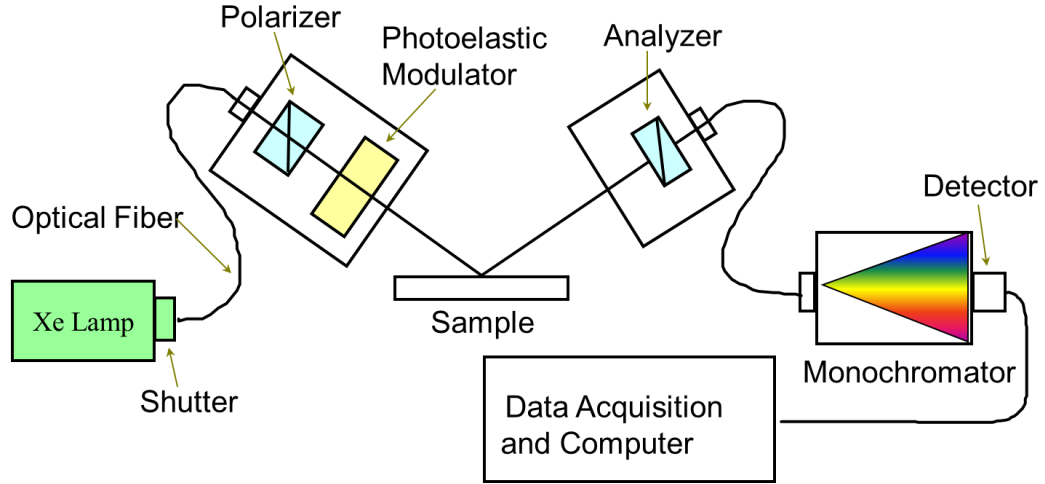


Figure 3.7: Schematic diagram of the in-house SE system.

In Jones calculus, we can represent the above process as,

$$\mathbf{E}_o = \begin{pmatrix} E_{o,s} \\ E_{o,p} \end{pmatrix} = \mathbf{J} \begin{pmatrix} E_{i,s} \\ E_{i,p} \end{pmatrix} \quad (3.16)$$

Here $\begin{pmatrix} E_{o,s} \\ E_{o,p} \end{pmatrix}$ is the outgoing light after passing the last polarizer in Figure 3.7.

Therefore \mathbf{J} represents the combined effect from optical elements and the sample.

Let's compose \mathbf{J} from each elements. In our experiment, both polarizers have transmission axes along 45° . A polarizer with transmission axes along 45° can be written in Jones matrix as,

$$\mathbf{J}_P = \begin{bmatrix} 1 & 1 \\ 1 & 1 \end{bmatrix} \quad (3.17)$$

A retarder is,

$$\mathbf{J}_R = \begin{bmatrix} e^{i\delta} & 0 \\ 0 & 0 \end{bmatrix} \quad (3.18)$$

And in SE measurement, sample's Jones matrix can be express by the measured parameters (Ψ, Δ) which is,

$$\mathbf{J}_S = \begin{bmatrix} 1 & 0 \\ 0 & \tan\Psi e^{i\Delta} \end{bmatrix} \quad (3.19)$$

Therefore, the overall Jones matrix for Figure 3.7 will be,

$$\mathbf{J} = \mathbf{J}_P \mathbf{J}_R \mathbf{J}_S \mathbf{J}_P \quad (3.20)$$

The measured quantity will be the intensity of the outgoing light. This intensity can be calculated from Equation 3.16 with Equation 3.17 through Equation 3.20.

$$I = |\mathbf{E}_o|^2 = [1 + (\sin 2\Psi \sin \Delta) \sin \delta + (\sin 2\Psi \cos \Delta) \cos \delta] I_0 \quad (3.21)$$

The phase modulator in the instrument is made of amorphous silica. It becomes birefringent when strained. A piezoelectric transducer is attached to it and produces a sinusoidal strain $\sin \omega t$ which regulates $\delta = F \cdot \sin \omega t$. Therefore, we can expand $\sin \delta$ and $\cos \delta$ terms in Equation 3.21 in series of $F \cdot \sin(m\omega t)$.

$$\begin{cases} \sin \delta = 2 \sum_{m=0}^{\infty} J_{2m+1}(F) \sin(2m+1)\omega t \\ \cos \delta = J_0(F) + 2 \sum_{m=1}^{\infty} J_{2m}(F) \sin(2m)\omega t \end{cases} \quad (3.22)$$

where J_m is the m^{th} order Bessel Function. F can be calibrated such that $J_0(F) = 0$.

Plug Equation 3.22 into 3.21, keep up to second order terms,

$$\frac{I}{I_0} = 1 + 2J_1(F)(\sin 2\Psi \sin \Delta) \sin \omega t + 2J_2(F)(\sin 2\Psi \cos \Delta) \sin 2\omega t \quad (3.23)$$

Therefore, measured $\frac{I}{I_0}$ is decomposed in $\sin(m\omega t)$ series and the coefficients of the first two Fourier components can be used to derive (Ψ, Δ) simultaneously.

3.3.3 Pseudodielectric function

Equation 3.15 can be used to directly calculate the complex refractive index of an isotropic, uniform and semi-infinite sample. Even though some samples might not strictly satisfy these conditions, Equation 3.15 can still be used to estimate the refractive index of a sample by measuring (Ψ, Δ) . To distinguish the calculated result from the real refractive index, it is named pseudorefractive index.

$$\langle \tilde{n} \rangle = \langle n \rangle + i\langle \kappa \rangle = \sin\theta_i \left[1 + \left(\frac{1-\rho}{1+\rho} \right)^2 \tan^2\theta_i \right]^{\frac{1}{2}} \quad (3.24)$$

For our Ga NP samples, this approach is used to estimate the LSPR energy of Ga NP ensemble [74-76]. The radius of the incident light beam spot is around 1 mm which is much larger than the typical length of NPs (10~100 nm). Collective optical response is measured from NP ensemble in the beam spot area. The calculated pseudorefractive index using Equation 3.24 characterizes the average optical response from the system of sapphire substrate and Ga NPs. Here, the effect of sapphire substrate on SE result is barely strong since sapphire is transparent in the measured photon energy region.

Figure 3.8 plots measured (Ψ, Δ) from a Ga NP ensemble on sapphire and its corresponding $\langle \tilde{n} \rangle$ calculated by Equation 3.24. The spectroscopy was measured at the resolution of 0.02 eV from 1.5 eV to 5.0 eV. The break around 4.2 eV and the noise above that photon energy in Ψ curve come from the change of the

grating in the SE instrument. A clear peak is presented in $\langle \kappa \rangle$ which measured the absorption of the sample. The peak around 3.8 eV indicates strong absorption occurs at this photon energy. While SE measured the collective optical response from the system of Ga NP ensemble and sapphire, this peak is primarily associated with the collective LSPR of the NP ensemble measured since sapphire is transparent in this photon range. Therefore, we have used this technique to estimate the LSPR of NPs during and after growth [74-76].

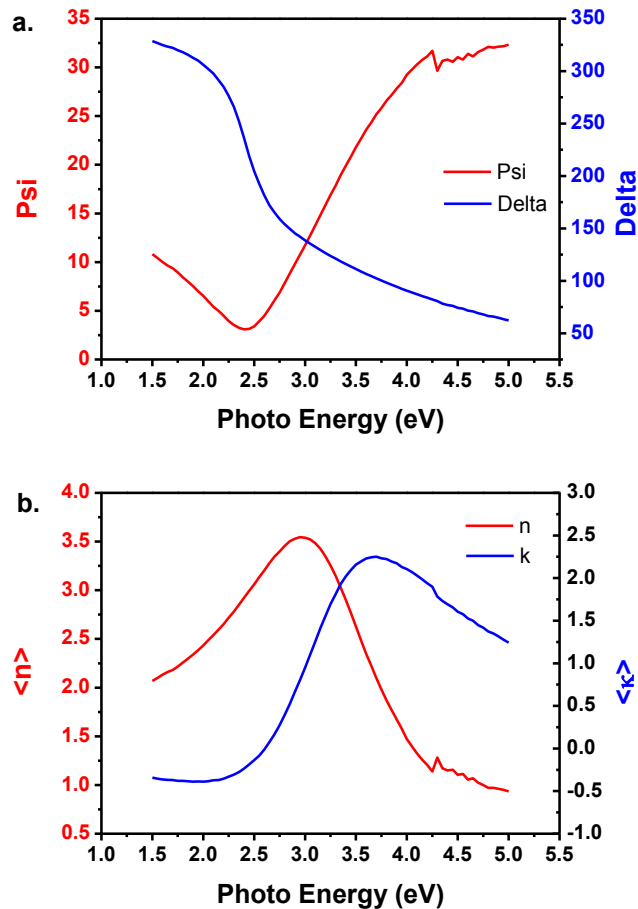


Figure 3.8: (a) measured SE parameters (Ψ , Δ) and (b) inferred pseudorefractive index $\langle \tilde{n} \rangle$ of a typical Ga NP sample.

Although Equation 3.24 gives good estimations of absorption profiles of Ga NP ensembles, $\langle \kappa \rangle$ actually drops below zero in some photon energy range (< 2.7 eV in Figure 3.8). It implies the failure of Equation 3.24, that is the sample does not well meet the assumptions held by the Fresnel equations. Previous research shows that negative $\langle \kappa \rangle$ is majorly due to multi-layer interference [139].

More complete model shall be implemented to interpret the measured SE data from Ga NP samples, which will be discussed in Chapter 6. However, since Equation 3.24 can well estimate the absorption peak, we will first use SE to monitor the growth process of Ga NPs. In the next chapter (Chapter 4), we will discuss MBE deposition of Ga NPs on solid supports with in situ SE monitoring to control the LSPR energy of grown sample.

4. Controlled Synthesis of Ga Nanoparticle Ensembles

Gallium nanoparticle ensembles were deposited on a variety of solid supports by physical vapor deposition. A molecular beam epitaxy system was used, which is equipped with in situ spectroscopic ellipsometry enabling real-time monitoring of the ensemble evolution and polarization-dependent far-field optical characteristics as discussed in the last chapter. The NP ensemble evolution follows the well-studied nucleation, surface diffusion, and coarsening growth of metals on non-reactive surfaces [140-141]. We find that the absorption peak of the NP ensemble keeps shifting to lower energy as deposition continues, which indicates a redshift of LSPR energies when NPs are growing in size.

4.1 Physical deposition process of metal NPs

4.1.1 Molecular beam epitaxy

Molecular beam epitaxy (MBE) is an ultra-high vacuum (UHV) crystalline growth technology developed at Bell Telephone Laboratories in 1960s [142]. Figure 4.1 shows a schematic diagram of a typical MBE system. The stainless-steel system is operated under UHV conditions (around 10^{-11} Torr idle and 10^{-7} Torr during deposition) ensuring the high purity of the resultant materials. The substrate on which deposition will occur is attached to a heated sample stage

near the center of the growth chamber and facing source ovens containing solid or liquid sources of the constituent materials. The sources are contained in effusion cells placed concentrically towards the substrate stage. A pneumatically-controlled shutter is placed between each source cell and the growth chamber to start and end the deposition. An ionization gauge is used to monitor the pressure in the growth chamber. Before deposition, the effusion cells are heated to the appropriate temperature for generating a specific flux. Under UHV condition, the mean free path of the beam constituents is larger than the cell-to-substrate separation, thus forming an atomic or molecular beam. As one example, the mean free path of N_2 is 10^8 cm at a chamber pressure of 10^{-10} Torr [143]. During deposition, the sample stage is maintained at the desired deposition temperature by the heating system.

MBE was developed as a tool for compound semiconductors synthesis [144] but is now widely used to grow a variety of materials ranging from oxides to metals. A key strength of the MBE process results from the combination of the UHV environment and the low growth rates exploited. Shuttering of the beam enables control of deposition to sub-monolayer (ML) thickness. Complex elemental material to multinary compounds can be synthesized with precise thickness and composition control. In addition to standard layered structures exploiting precise

two-dimensional control of thickness and composition, MBE is also used to synthesize nanostructures including nanowires [145], quantum dots [146], quantum rings [147], and topological insulator structures [148].

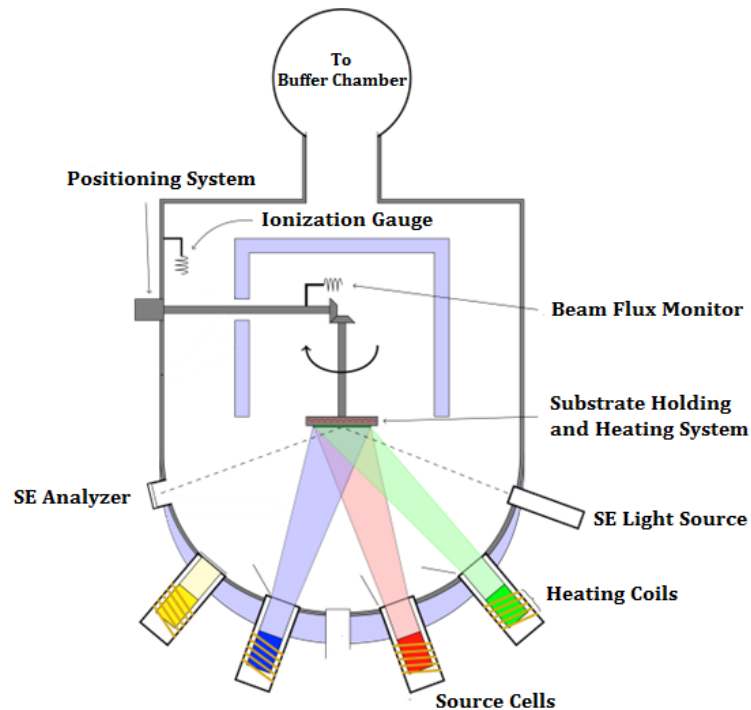


Figure 4.1: Schematic diagram of a typical molecular beam epitaxy system (adapted from Wikimedia Commons).

There are at least three significant advantages of using MBE to synthesize metallic nanoparticles:

- i. Precise control of deposited volume: The constituent metal beams can be impinge on the substrate at very low and controllable flux value ($\sim 10^{13}$ atom $\text{cm}^{-2}\text{s}^{-1}$) [149], and the deposition can be initiated and terminated instantaneously (with respect to the flux) through shutter control.

- ii. Integration with semiconductors and ultimately device structures: Nanoparticles can be deposited in the same system in which complex semiconductor structures are synthesized. This is important since utilizing two separate synthesis system typically requires exposing the surface to atmosphere thus creating an oxidized surface which may impact subsequent NP synthesis and/or device operation. Using an all-MBE process approach therefore enables the integration of NPs with semiconductor devices, such as plasmonically-enhanced light-emitters and detectors [150].
- iii. Reaction-free and agent-free synthesis: Comparing with chemical vapor deposition and solution-based synthesis, deposition in MBE requires no additional reactions and need not to introduce extra agents. This avoids unwanted reaction residues on NPs which may affect their optical properties.

The Ga NP ensembles for this work were synthesized using a Veeco GEN II plasma-assisted MBE system. 7N pure RASA MBE grade gallium purchased from United Mineral & Chemical Corp. with 99.99999% purity was evaporated from the same SUMO effusion cell. The SUMO cell is equipped with two heating coils (at the top and bottom of the effusion cell), heats the gallium source

material (bottom heater), and ensures a constant flux (top heater) by controlling the cell exit temperature. The cell was heated at approximately 900 °C (bottom) and 1000 °C (top). The growth mechanism will be discussed in the next section.

4.1.2 Gallium nanoparticle ensemble growth mechanism

The deposition of metals onto surfaces using physical vapor deposition has been studied for decades [151-152]. During deposition, atoms arriving from the gas phase are adsorbed on substrates. Adatoms will either adhere to substrate and become stable nuclei or diffuse on the surface and attach to another adatom to grow in cluster. The probabilities of these two competing processes depend primarily on the relative values of surface and interfacial energies of the substrate and metal overlayer,

$$\Delta\gamma = \gamma_a + \gamma_i - \gamma_s \quad (4.1)$$

where γ_a and γ_s are the surface free energy of adatom and substrate respectively. γ_i is the interfacial free energy between adatom and substrate. Depending on the value of $\Delta\gamma$, there are three major island growth mode [153-154]:

- i. $\Delta\gamma > 0$, Volmer-Weber (VW) growth: adatom-adatom interaction dominates and adatoms tend to form close packed three-dimensional islands like nanoparticles;

- ii. $\Delta\gamma < 0$, Frank-van der Merwe (FM) growth: substrate-adatom interaction dominates and adatoms tend to form thin films layer by layer;
- iii. $\Delta\gamma \sim 0$, Stranski-Krastanov (SK) growth: the intermediate condition between the above two and adatoms will form layers first and then islands or droplets.

γ_a and γ_s are both intrinsic properties of materials while γ_i depends on the strain and the strength of chemical interactions between them. γ_i will increase when the number of deposited layers grows as strain increases, which may turn $\Delta\gamma$ from negative value to positive resulting in a SK growth mode.

In this work, most Ga NP ensembles are deposited on sapphire. Due to the high surface energy of liquid gallium, sapphire acts as a hydrophobic surface. Ga atoms follow the VW growth mode and tend to form three-dimensional islands (i.e. NPs) with large contact angle [155-156]. Compared with gold and silver which have high melting temperature, it is difficult to maintain supersaturated adatom phase on substrate surface. Therefore, physical vapor deposition is not ideal to synthesize gold and silver nanoparticles unless at very high temperature (the melting temperature of gold is 1064 °C). Given the low melting temperature of Ga (29.7 °C), Ga can self-assemble to form regularly-shaped and isolated NPs on solid supports. This is one of the material benefits of Ga.

Many literatures reviewed the liquid phase metal nanoparticle formation in VW growth mode [157-159]. In general, Ga atoms will undergo a self-assemble growth process of a) adsorption, b) nucleation, c) diffusion, and d) coarsening as shown in Figure 4.2. After adsorbed by sapphire surface, Ga adatoms occupy selective sites first leading to nucleation, usually at surface inhomogeneity sites. A critical nucleation size is determined by Ga-Ga, Ga-sapphire surface tension. Those nuclei smaller than the critical size tend to shrink and disappear eventually while those larger than the critical size will absorb more diffusive Ga adatoms leading to a growth to minimize total surface energy. In the early stage of growth, nucleated clusters keep capturing atoms from supersaturated phase until reaching its equilibrium. After that, cluster distribution continues to evolve through cluster-cluster interactions such as ripening, sintering, and cluster migration (island diffusion). All the three processes tend to form larger clusters in favor of minimizing total surface energy.

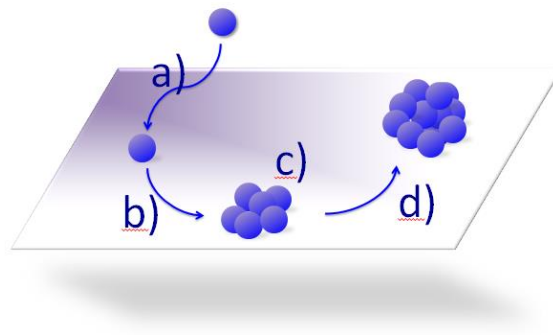


Figure 4.2: Volmer-Weber growth mechanism.

Ripening is a coarsening process when larger islands (NPs) tend to consume smaller NPs nearby because larger particles have smaller surface energy and therefore are energetically favored. However, complete dissolve of smaller NPs and coalescence with larger NPs require that adatoms can diffuse freely on the substrate surface. The ripening process is limited by the surface mobility of adatoms. Part of the smaller NPs may dissolve and coalesce with larger NPs, other smaller NPs may be left as residues. An alternative coarsening process is island diffusion. When substrate temperature increases, nucleated atoms can become active and migrate on substrate surface. The displacement of clusters' center of mass depends on the cluster size. In general, smaller clusters diffuse faster than larger clusters. When smaller cluster attaches to larger ones, they tend to form a single cluster to minimize total surface energy. Unlike ripening, two clusters will merge completely.

Both processes are dependent on surface mobility while ripening relies on single adatom diffusion and island diffusion is the aggregated diffusion of an entire cluster. Some literature also categorizes the two processes as adatom diffusion limited ripening and island diffusion limited ripening. The latter needs higher energy to be active. For our Ga NP ensemble growth at room temperature, adatom diffusion limited ripening plays the major role in the ensemble formation.

Therefore, as deposition continues on sapphire, an ensemble consisting of larger and smaller clusters is expected. A bimodal NP size distribution may be observed from samples. In the events of growth at elevated temperature, surface mobility of adatoms is increased. The mass transportation between smaller and larger NPs is more effective than that at room temperature. Adatoms tend to from larger cluster with less residues. With spatial characterization, we can measure resulted size distributions of NP ensembles which will be discussed in the next chapter.

Most of our Ga NP ensembles are deposited on sapphire at room temperature (300 K). At this temperature all of the imping Ga atoms that arrive at the substrate surface adsorb and contribute to the resulting ensemble. However, at higher temperatures, adatoms may also desorb from the surface before or after incorporation into nucleus or islands. Ga desorption rate is highly dependent on temperature. Previous experiments have shown that the desorption is not significant until the temperature is above 680 °C [160]. The relative incorporation and desorption rates of atoms into and out of islands determine the growth rate of islands and the resultant ensemble size distribution function. We will show in Section 5.3 that desorption can be used to modify the NP size distribution.

4.1.3 Deposition rate and Ga dose

As discussed above, Ga atomic beams incident on the substrate surface form nanoparticle ensembles as a result of a nucleation, diffusion, and coarsening process. The beam flux is dependent on source cell temperature. In order to quantify the beam flux, an ionization gauge is used to measure the beam equivalent pressure (BEP), which is related to the beam flux. The Clausius-Clapeyron relation gives the pressure as [161],

$$p = A \exp\left(-\frac{\Delta H}{k_B T}\right) \quad (4.2)$$

where ΔH is the evaporation enthalpy and k_B is the Boltzmann constant. Consider that a beam of atoms impinges onto sample surface with velocity v . The flux is thus,

$$J = nv \quad (4.3)$$

where n is the atom density. The units of J (in SI) are $m^{-2}s^{-1}$. The flux describes the number of atoms passing through a unit cross sectional area per unit time. However, based on a Maxwell-Boltzmann distribution, the atom velocities comprising the beam are not identical [162], but are given by,

$$f(v) = 4\pi v^2 \left(\frac{m}{2\pi k_B T}\right)^{3/2} \exp\left(-\frac{mv^2}{2k_B T}\right) \quad (4.4)$$

Therefore, the flux is determined using a weighted velocity as:

$$J_{avg} = \int nvf(v)dv \quad (4.5)$$

In order to relate the flux to the BEP using Equations 4.2 and 4.5, recall the ideal gas law:

$$p = nk_B T \quad (4.6)$$

Inserting Equation 4.6 into 4.2 and evaluating the integral, we obtain that:

$$J_{\text{avg}} = \frac{4p}{\sqrt{2\pi mk_B T}} \quad (4.7)$$

However, this is not the actual deposition rate as two additional factors must be considered.

- i. Incident angle: As shown in Figure 4.1, while the source effusion cells are placed towards the sample stage they are not aligned to the normal direction with respect to the substrate. Therefore, the arrival rate at the substrate is different from the cell flux by a factor of $\cos \theta$, where θ is the incident angle from the effusion cell to the substrate normal.
- ii. Sticking coefficient: The sticking coefficient is defined as the ratio of the concentration of atoms adsorbed on the surface to the total density of atoms that impinge on the substrate. It is highly dependent on temperature, beam coverage, constituent species, substrate type and morphology [143]. Our work uses 300K deposition of Ga on sapphire and the sticking coefficient is assumed to be constant in the experiments given identical growth conditions.

Therefore, the deposition rate of Ga is proportional to the BEP and given by,

$$r \propto \frac{\cos \theta}{\sqrt{2\pi mk_B T}} p \propto p \quad (4.8)$$

Our experiments were carried out using a fixed Ga BEP of $2.03 \sim 2.06 \times 10^{-7}$ Torr and ensembles were prepared with varying ensemble size distributions as a result of varying the deposition time. Therefore, we can label samples by deposition time. Dosage describes the total amount of material deposited on the substrate surface as a volume equivalent and is given by:

$$D = rt \quad (4.9)$$

where t is the total deposition time and r is the deposition rate.

We calibrated the deposition rate of Ga on sapphire at room temperature. $r = 0.314$ nm/s when BEP $p = 2.036 \times 10^{-7}$ Torr. Therefore, given the linearity of Equations 4.8 and 4.9 and our use of identical growth conditions with constant sticky coefficient, the dosage for the samples can be expressed in nm as,

$$D = \frac{\text{BEP}}{2.036} \times 0.314 t \quad (4.10)$$

where BEP is in 10^{-7} Torr and t is in seconds. Dosage is often expressed in atomic monolayer (ML) equivalent. For thin films, synthesis researchers are interested in how many layers have grown in a given amount of time. A similar definition can be used to describe our Ga samples synthesis. Using the lattice

constant for the α -phase fcc gallium crystal, $a = 0.451 \text{ nm} = 1 \text{ ML}$ [163], the total dosage can be expressed in ML as,

$$D = \frac{\text{BEP}}{2.036} \times \frac{0.314}{0.451} t = \frac{\text{BEP} \cdot t}{2.924} \text{ (ML)} \quad (4.11)$$

For example, one sample was deposited using a beam with a BEP of 2.046×10^{-7} Torr for 170 s. Therefore, the total dosage for this sample is 119 ML. The 119 ML equivalent describes the total amount of material adsorbed on the substrate despite the fact that the deposit results in three-dimensional islands. Dosage is used to characterize the synthesis of samples produced during these studies and is correlated with other physical quantities, like mean NP size in the ensemble.

4.2 Controlled synthesis

4.2.1 Controllable deposition parameters

As discussed above, there are at least three key parameters which can be adjusted that impact the characteristics of Ga nanoparticle ensembles:

- i. Dosage (BEP and time): In order to form well-distributed NP ensembles, we have optimized BEP at $2.03 \sim 2.06 \times 10^{-7}$ Torr. The fluctuation in BEP will effect dosage around 1% according to Equation 4.10. Therefore, deposition time is the major parameters we can adjust by controlling the open and close of Ga source effusion cell shutter.

ii. Substrate: As discussed in Section 4.1, the interfacial energy between the substrate and adsorbate determines the growth mechanism of nanoparticle ensembles. Fortunately, gallium possesses a relatively high surface energy at room temperature. Ga is hydrophobic with respect to most solid supports, like sapphire, which enables Ga to form truncated spherical clusters with large contact angle. Another factor in selecting the solid support is its optical properties. Given our optical application, we are concerned about the optical features in the visible and UV range for NPs and a solid support which is transparent within this range is preferable. Therefore, a dielectric substrate is preferred over a semiconductor or metallic substrate as the latter ones often have absorption in the visible and UV range. Figure 4.3 plots the complex refractive index of sapphire measured by spectroscopic ellipsometry. The imaginary part of the refractive index, or the extinction coefficient is around zero for the photon energy ranging from 1.5 eV to 5.5 eV. The real part of the refractive index is approximately 1.8 in the same photon energy range. In addition to its transparency, sapphire is also nonconductive. At room temperature, its resistivity is at approximately $10^{14} \Omega/\text{cm}$. As discussed in Chapter 2, a conducting substrate will alter the plasmonic properties of attached metallic NPs due to the image charge

effect. Therefore, a sapphire substrate will show minimum interference with respect to the optical properties of the Ga NP ensembles deposited on it. Most of samples in this work were deposited on 450 μ m thick sapphire (0001) substrates while GaN, GaAs, Si, SiC, and some other substrates were also used to explore the impact of substrate on NP growth.

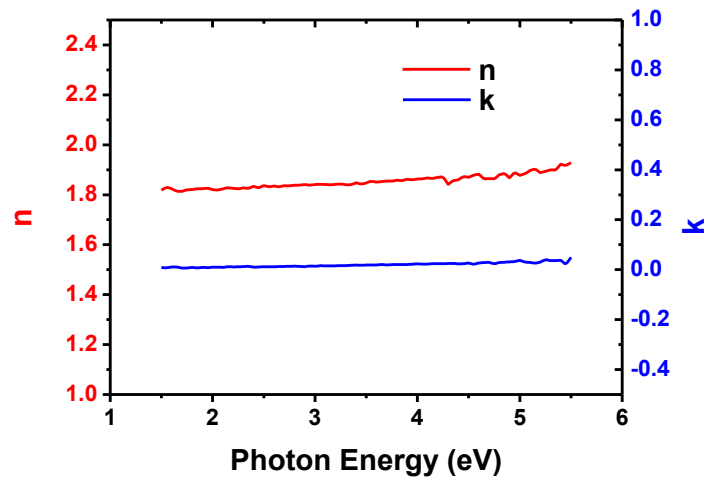


Figure 4.3: Refractive index of bulk sapphire measured by SE from a 440 μ m thick sapphire template.

- iii. Temperature: As discussed in Section 4.1, coarsening and desorption both depend on deposition temperature. For most of our samples, the synthesis was carried at room temperature (300K) for simplicity. Elevated deposition temperatures were also used to explore the impact of temperature on resulted NP ensemble size distribution.

Among all of the synthesis parameters, the deposition time is the one used most often to control the growth because deposition time is directly related to total Ga dosage and therefore is the controlling factor of NP sizes that directly affect NPs' plasmon resonance energies as discussed in Chapter 2. The deposition time is either pre-determined or dynamically decided with in situ monitoring. Spectroscopic ellipsometry, which was discussed in Chapter 3, was used to monitor the evolution of the optical properties during controlled synthesis.

4.2.2 In situ monitoring with spectroscopic ellipsometry

The MBE system used for these experiments is equipped with an in situ spectroscopic ellipsometry (SE). As shown in Figure 4.1, the SE source is emitted from one side of the MBE growth chamber and is incident on the sample surface with an angle of incidence at 70° . A grazing angle of incidence will maximize measurement accuracy. The light collector and analyzer are mounted on the other side of the growth chamber at the specular reflection angle. The HORIBA Jobin Yvon SE system (as discussed in Chapter 3) can simultaneously measure 32 points evenly spaced over the photon energy range of 1.38 eV to 6.5 eV. During in situ monitoring, the integral time is 0.2 s and the measurement interval is usually set at one second. (The rate can be as low as once per 0.2 s or can be set at a longer time to monitor a slower process.) At each second, SE will measure the

optical response from the sample and convert it to a pseudorefractive index as defined in Equation 3.24. We can thus estimate the plasmon resonance of grown sample from the imaginary part of the pseudorefractive index, pseudoextinction coefficient. Figure 4.4 shows the evolution of pseudoextinction coefficient during Ga NP ensemble deposition on sapphire.

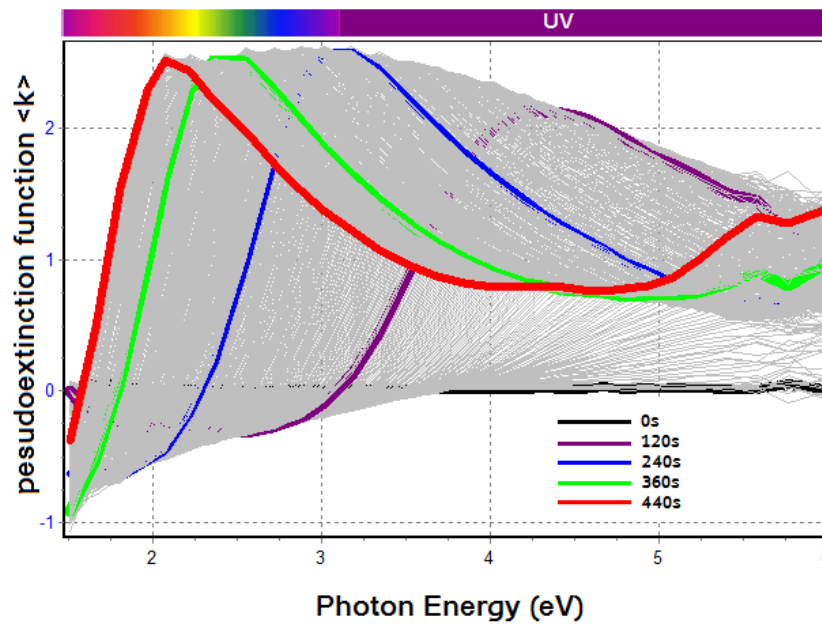


Figure 4.4: Evolution of pseudoextinction coefficient during Ga NP deposition.

At $t = 0$, the pseudoextinction coefficient curve represents that of the sapphire substrate. As deposition continues, a peak is formed, which redshifts with continued growth. The peak amplitude also increases as deposition time increases. Previous experiments [74-75] and modeling [122] (discussed in Section 2.2.4) in our group identified this peak as the in-plane LSPR mode associated

with the Ga NP ensembles. As deposition time keeps increasing, another peak enters the detectable range (green and blue curves in Figure 4.4). The high-energy peak is associated with the out-of-plane LSPR mode excited by the p-polarized component of the SE detection light [122]. For optical application like SERS, probe light excited from normal incidence can only excite in-plane LSPR mode. Therefore, in order to optimize samples for plasmonic applications, we shall tune the in-plane LSPR mode to a desired energy. We can watch the in situ evolution of the pseudoextinction coefficient from SE monitoring to halt the deposition when the low energy peak reaches the desired photon energy. This unique monitoring technology in our group enables us to implement controlled growth of a Ga NP ensemble in real time.

4.2.3 Samples

Ga NP samples on a variety of substrates were deposited during my research to study various effects on Ga NP spatial and optical properties. Some of them will be presented in the remaining part of the thesis to illustrate certain theories.

We will focus on the samples Y1 ~ Y7. They were used to carry out detailed analysis discussed in the remaining part of this thesis. They were grown on commercially-available bare c-plane sapphire (0001) substrates from Saint-Gobain at room temperature (300K). The sapphire substrate is 440 μm thick and

double-side polished. The substrate size is 11 cm × 11cm. Table 4.1 generalizes the deposition conditions for these 7 samples. The dosage is calculated using Equation 4.10. A detailed spatial and optical analysis of these samples will be presented in the next few chapters (Chapter 5 to Chapter 7).

Table 4.1:

Growth conditions for samples Y1 ~ Y7 (Deposition temperature: 300K).

Sample	BEP / 10^{-7} Torr	Deposition Time / s	Dosage / ML
Y1	2.0562	98	241
Y2	2.0562	122	300
Y3	2.0562	174	428
Y4	2.0453	280	684
Y5	2.0453	375	916
Y6	2.0562	487	1197
Y7	2.0451	732	1789

5. Spatial Characterization of Ga Nanoparticle Ensembles

As discussed in Chapter 2, the optical properties of NPs are highly dependent on their morphology. Therefore, it is critical to characterize synthesized Ga NP ensembles discussed in the last chapter with microscopic tools. Atomic force microscopy (AFM) and scanning electron microscope (SEM) are used for spatial characterization of Ga NP ensembles.

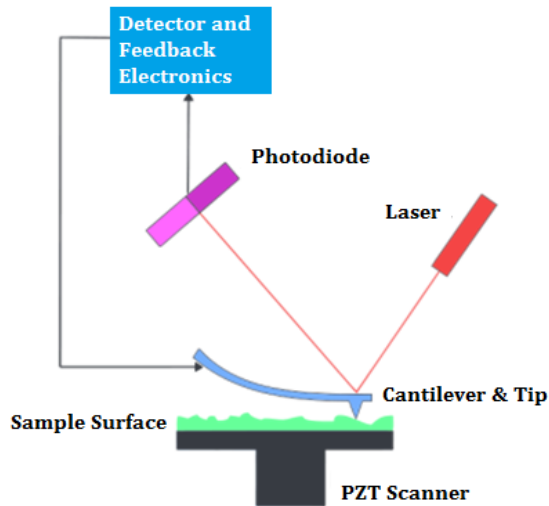


Figure 5.1: Schematic diagram of atomic force microscopy (adapted from Wikimedia Commons).

5.1 Instrument

5.1.1 Atomic force microscopy

AFM is a very high-resolution type of scanning probe microscopy, where a sharp tip scans the surface to measure surface topography. It was developed in 1986 at

IBM Research – Zurich [164]. Figure 5.1 shows the schematic diagram of AFM. A tip is mounted on a spring-like cantilever and will be deflected as the response of the force between the tip and the sample surface. The tip motion is detected by the reflected laser beam. There are several types of forces between tip and samples including mechanical contact force, van der Waals force, capillary force, chemical bonding, and electrostatic forces ranging from $10^{-11} \sim 10^{-6}$ N [164]. However, when the tip is very close to sample surface, the attractive force may be strong which will drag the tip and affect continuous measurement. Tapping mode is developed to bypass this problem. In this mode, a piezo stack oscillates the probe at or near the resonance frequency of the tip, and a piezo tube is slowly expanded until the amplitude is reduced to its pre-assigned value by approaching the sample surface. As the tip scans the surface, the feedback controller maintains the amplitude of the probe, and the calibrated applied voltage to the piezo tube is converted to the surface height. The height resolution of AFM can be smaller than 0.5 nm. It is often used to identify one monolayer difference for layered structures. Given the height information at each site, AFM images can be used to reconstruct 3D image of samples surface. A Digital Instrument Dimension 3100 AFM was used in our experiments.

Despite of the beautiful 3D reconstruction of AFM images, AFM has a well-known artifact of tip convolution. Figure 5.2 shows the cause of this artifact. Due to their finite size, AFM tips cannot reach the details of sample surface especially when the surface feature has length scale comparable to the tip. AFM tip will go along the red curves as shown in Figure 5.2 which does not reflect the real surface profile. In tapping mode, this effect is even magnified because the tip must maintain certain distance away from the sample surface. The typical radius of AFM tips used in our experiment is 10 nm. NPs with comparable radius may be measured at a larger cross sectional radius value. Although AFM is an ideal tool to measure height information of thin film surface, other microscopic measurements, like SEM, may be used to characterize nanostructures.

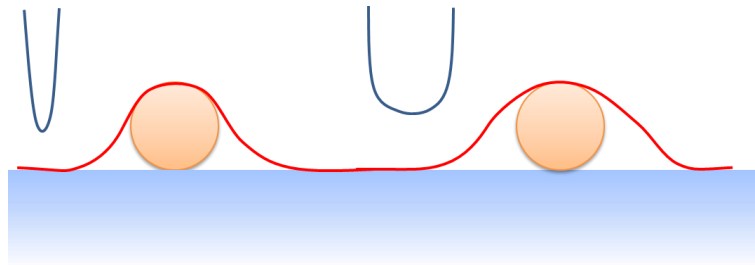


Figure 5.2: AFM tip convolution.

5.2.1 Scanning electron microscope

SEM is used to measure the local morphology of Ga NP ensembles, especially the dimensions of each NP. It captures two-dimensional images while electrons are

working as the probe beam. A FEI XL30 SEM was used in the experiments. It features secondary electrons detection, magnifications of over 300,000X, excellent depth of field and minimized sample charging. The highest resolution is smaller than 1 nm. Figure 5.3 shows the schematic diagram of SEM [165]. A beam of electrons, the primary electron beam, impinges onto the sample surface from the top. The energy of electron beam is selected at 5 keV given the tradeoff between resolution and conductivity of sapphire substrate. During measurement, a copper bonding may be used to wire connect sample surface and metallic sample holder to minimize electrons charging effect.

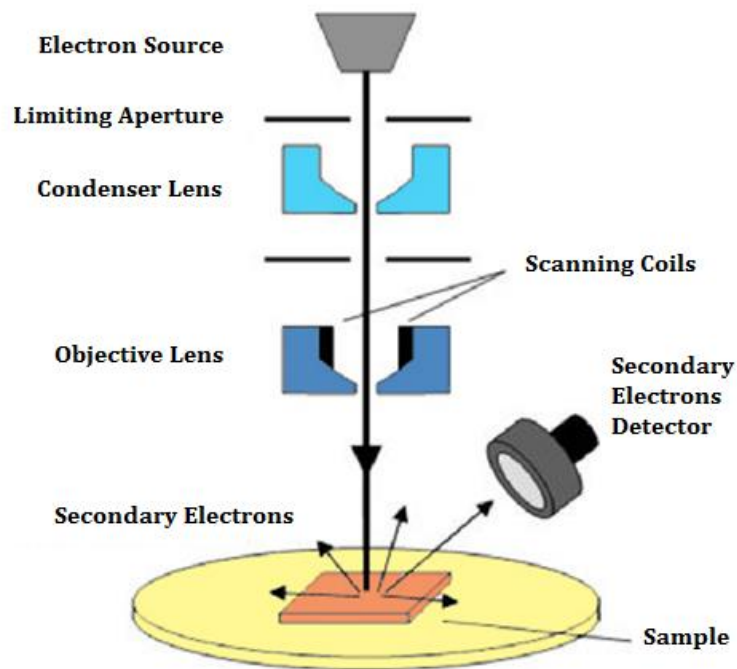


Figure 5.3: Schematic diagram of scanning electron microscope [165].

The primary electron beam interacts with the sample surface to generate secondary electrons due to the inelastic scatterings from the sample atoms. The scattering efficiency depends on the sample surface atom orbit structures, or simply the atomic number Z. Secondary electrons are then collected by special Everhart-Thomley detector, which can collect, accelerate electrons, and convert to photons eventually. The amount of photons emitted and detected is directly related to that of secondary electrons, which leads to different darkness on the user's screen. A gray-scale image is then recorded by the continuous scanning of the sample surface from point to point. An SEM image of tilted sample can also be captured as the sample stage can be tilted with respect to the vertically incident electron beam. Measurement results will be presented in the next section.

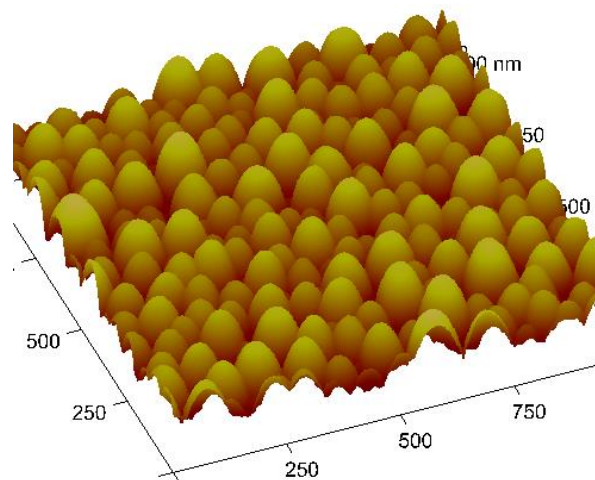


Figure 5.4: 3D AFM image of a Ga NP ensemble.

5.2. Spatial information of Ga NP ensembles

5.2.1 Ga NP ensembles overview

Figure 5.4 is an 3D AFM image of a Ga NP ensemble on sapphire in an area of $1\ \mu\text{m} \times 1\ \mu\text{m}$. As shown in the image shown, NPs with different sizes cover the entire surface to form Ga NP ensemble. NPs are truncated due to the sapphire substrate. Previous work in our group has been done to measure Ga NPs contact angles (based on height-radius ratio) where Ga were deposited on different semiconductor polar substrates to reveal the surface charge effect on NP formation [76].

However, due to the tip convolution effect, the cross sectional radius measured by AFM may not be precise. Previous research reported that height measurement on nanostructures using AFM in tapping mode can also be distorted [166]. Although AFM provides a vivid 3D view of NP ensembles, SEM is needed to quantify NP dimensions.

Figure 5.5 shows an SEM image of a Ga NP ensemble on sapphire at tilted (45°) position. It confirmed again the truncated hemispheroid shape of NPs. In this particular sample, there are plenty of smaller NPs surrounding large NPs, which is consistent with the coarsening process discussed in Section 4.1.2.

To summarize, Ga NPs on sapphire exhibit truncated hemispheroid shape. NPs are in different sizes to form a NP ensemble and randomly distributed on substrate. Therefore, optical properties of these Ga NP ensembles will be different from a perfect spherical NP discussed in Section 2.2.1. Numerical methods are necessary to model the plasmon resonance of these NPs as discussed in Section 2.2.4. Truncated shape and substrate must be included in the modeling.

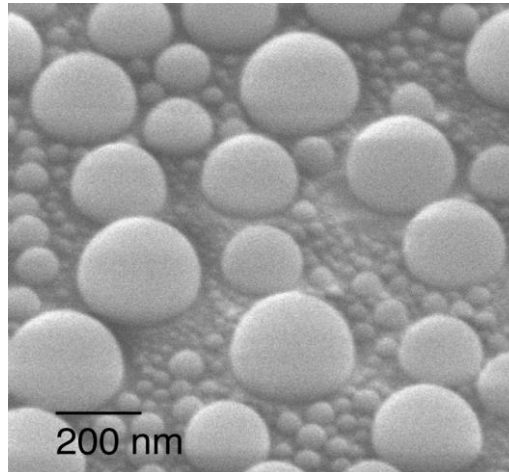


Figure 5.5: SEM images of a Ga NP ensemble at tilted (45°) position.

5.2.2 Statistics on NP morphology

Since SEM acquires more precise spatial information than AFM, SEM images are used to extract quantitative morphology information of Ga NPs, including total coverage, NP density, cross sectional radius, and nearest neighbor distance.

Figure 5.6 shows SEM images of 3 samples, Y1, Y3, and Y6 presented in Table 4.1. Since NPs are randomly distributed, a sub area on each sample defined by blue rectangle was randomly selected for simplicity. Each NP was identified by hand and masked with red color. Statistics are carried over these identified individual NPs on each sample.

Figure 5.7 plots the crosssectional radius distribution of each sample. From now on, we will simply use radius to refer to the crosssectional radius which can be measured from SEM images as SEM projects 3D profile to 2D. Y1 and Y3 bear unimodal radius distribution while Y6 possesses bimodal radius distribution. Recall that Y6 has longer deposition time, the existence of “leftover” smaller NPs is again consistent with the coarsening process discussed in Section 4.1.2. Although there are more smaller NPs (first modal) than larger NPs (second modal in the radius distribution) in Y6, the sample surface is still majorly covered by larger NPs as shown in Figure 5.8c, the coverage distribution of Y6. 75% of the sample surface was covered by NPs with radius larger than 40 nm. Figure 5.8a,b depict similar coverage distributions for the other two samples Y1 and Y3. As expected, compared to radius distribution, the peak shifts to larger values as NP with larger radius has larger coverage.

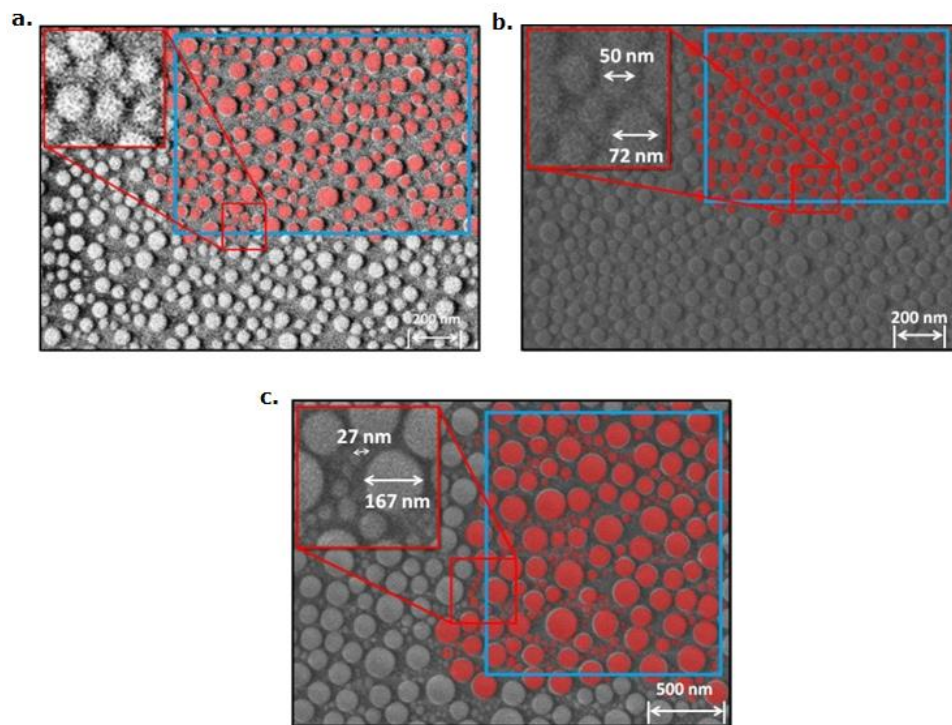


Figure 5.6: SEM images of samples (a) Y1, (b) Y3, and (c) Y6 with NP identification.

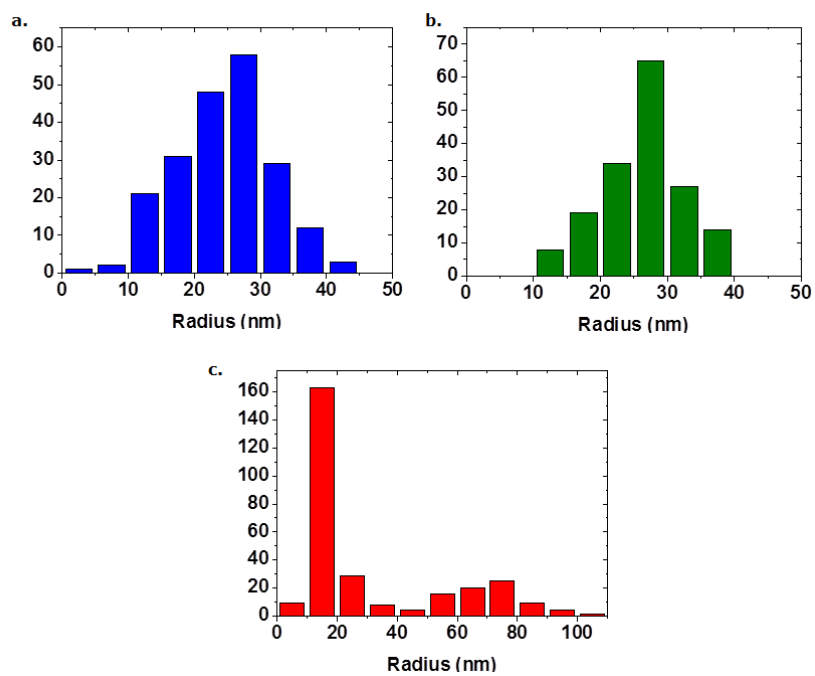


Figure 5.7: NP crosssectional radius distributions of samples (a) Y1, (b) Y3, and (c) Y6.

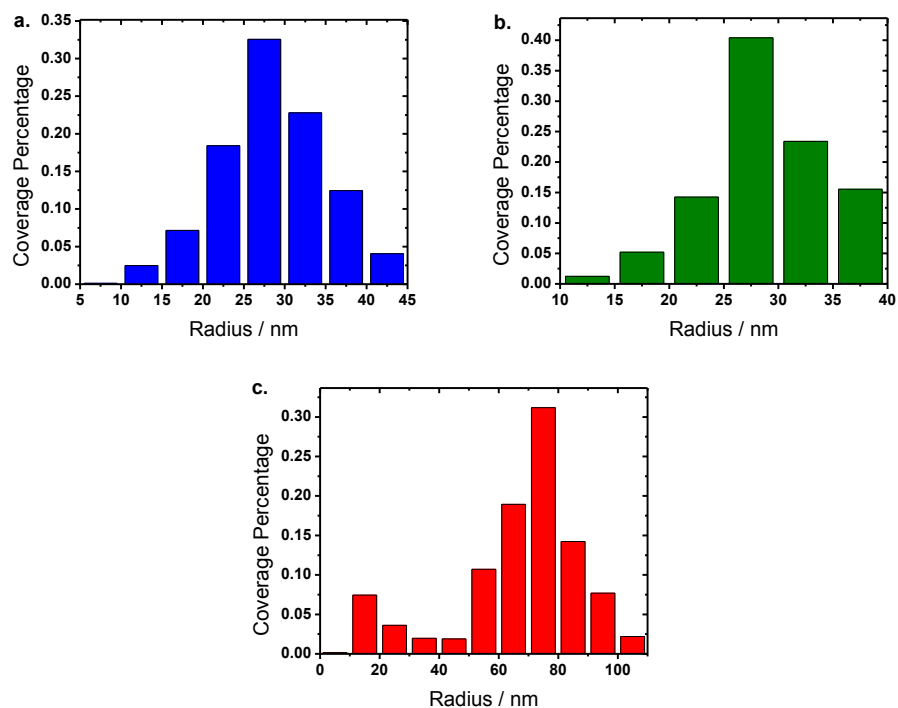


Figure 5.8: NP coverage distributions of samples (a) Y1, (b) Y3, and (c) Y6.

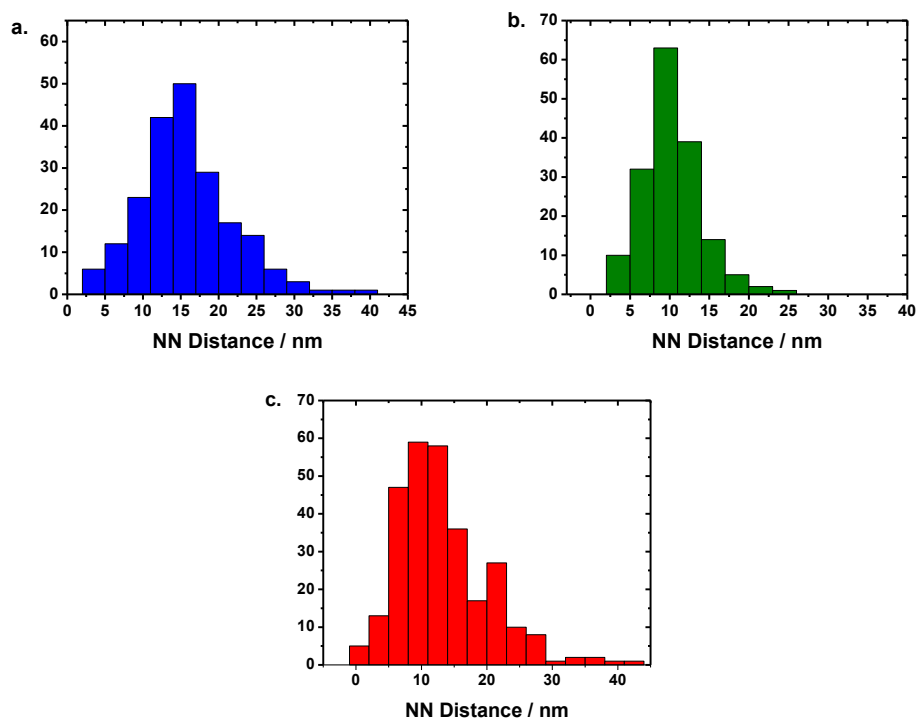


Figure 5.9: NP nearest neighbor edge-to-edge distance distributions of samples (a) Y1, (b) Y3, and (c) Y6.

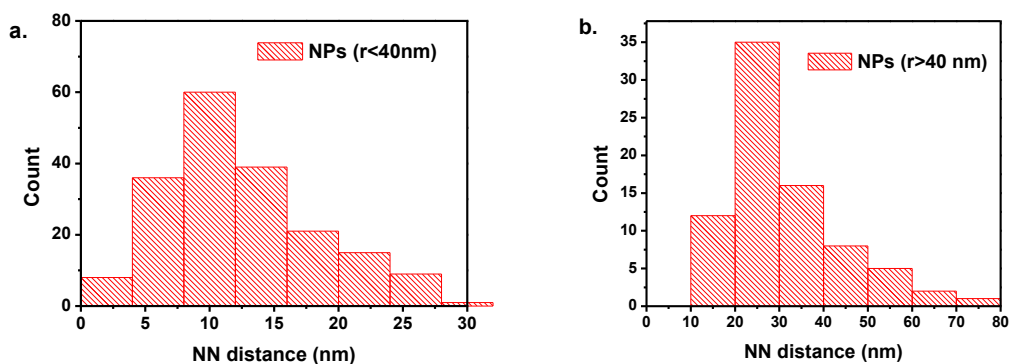


Figure 5.10: NP nearest neighbor edge-to-edge distance distributions for (a) small-small ($r < 40$ nm) and (b) small-large ($r > 40$ nm) NP pairs on sample Y6.

In addition to NP's size, it is also important to explore NP-NP gaps because NP-NP coupling is an important source of plasmon resonance which is affected by interparticle distance. (Section 2.1) Figure 5.9 shows NP nearest neighbor (NN) distance distribution for the 3 samples. Here NN distance is defined as the edge to edge distance.

The average NN distance for Y3 is smaller than Y1 as NPs in Y1 is more dilute (Figure 5.6). This is because Ga dosage for Y3 is larger than that of Y1 (Table 4.1). More Ga adatoms are available to form denser islands for Y3. Therefore, stronger NP-NP interaction is expected for Y3. For samples Y6, since it processes bimodal size distribution, Figure 5.10 examines NN distance distributions for the modes of smaller and larger NPs respectively. NN distance in Figure 5.10a shows the histogram of the distance between a small NP and the nearest small NP. "Small"

NP means its radius is less than 40 nm which is the segmentation boundary in Figure 5.7c. Figure 5.10b plots the histogram of the distance between a small NP and the nearest large NP.

Table 5.1: Statistics on NP morphology for samples Y1, Y3, and Y6.

	Y6	Y3	Y1
Dosage (ML)	1197	428	241
Density (μm^{-2})	104	131	173
Coverage	51.4%	43.7%	35.3%
Mean radius (nm)	16 / 70	26	24
FWHM of radius distribution (nm)	61	23	35
Mean NN distance (nm)	13	10	15

Table 5.1 generalizes major statistics on NP morphology of these 3 samples. When the NP dosage increases (longer deposition time), NP density decreases driven by coarsening and the overall coverage increases since more materials are deposited onto sample surface. Mean NP radius also increases as deposition continues. The radius distribution evolves from unimodal to bimodal. For Y6, FWHM value is calculated only for the radius distribution of larger NPs. To summarize, as deposition time extends, coarsening process forms larger NP and

leaves smaller NP residues. These statistics will be used to model NP plasmon properties and correlate with measured optical responses in Chapters 6 and 7.

5.2.3 Temperature impact on Ga NP ensemble morphology

Section 2.1 shows that NP's LSPR is highly dependent on NP's size. In our Ga NP ensembles, NPs are not monodispersed but possess a bell-shape distribution as shown in Figure 5.7. The overall LSPR energy measured will be the collective optical responses from each single NP. On one hand, it broadens the bandwidth of plasmonic enhancement; on the other hand, the entire surface is not efficiently excited under single wavelength excitation. NPs do not equally contribute to the overall enhancement as the excitation may not overlap with all of their LSPR energies. Therefore, in order to optimize the substrate to obtain larger overall plasmonic enhancement, it is valuable to narrow the size distribution of the NP ensembles.

Section 4.1.3 discussed several parameters which may impact the final formation of NP ensembles on solid surface including dosage, type of substrate, and temperature. Previous research showed that thermal deposition at higher temperature will effectively narrow resulted 3D island size distribution [167]. We attempted to deposit Ga on sapphire at elevated temperature, at which desorption process cannot be ignored.

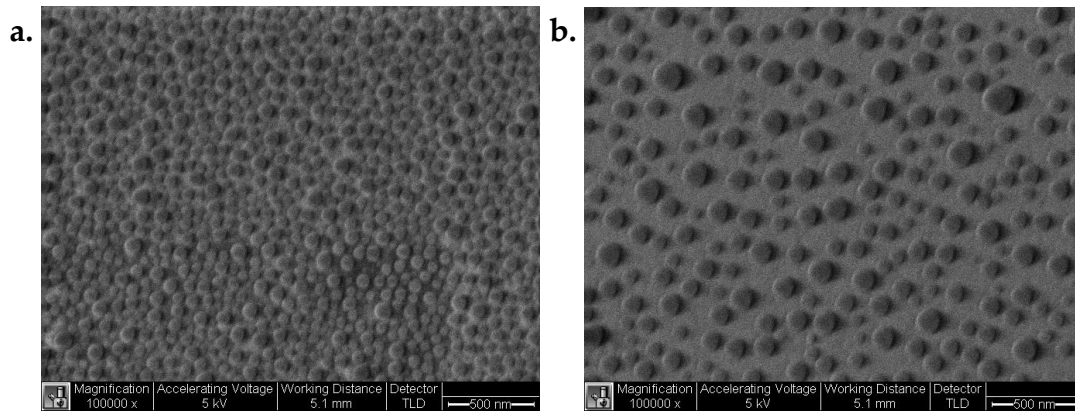


Figure 5.11: SEM images of Ga NP ensembles with the same LSPR energy deposited at (a) 25 °C and (b) 700 °C respectively.

Figure 5.11 shows SEM images of two Ga NP ensembles which were deposited at 25 °C and 700 °C respectively. They were tuned to the same pseudoextinction coefficient peak using the technique discussed in Section 4.2. From SEM images, resulted Ga NPs deposited at 700 °C are more dilute and there are much less smaller NPs than that grown at room temperature. As discussed in Section 4.1.2, there are two competing processes at higher temperature a) coarsening and b) desorption. Coarsening will merge small and large NPs to form single large NP while desorption will shrink NP size. Both processes will be enhanced as temperature increases. Smaller NPs will be eliminated by both processes. NPs become smaller while tiny NPs disappear when temperature increases.

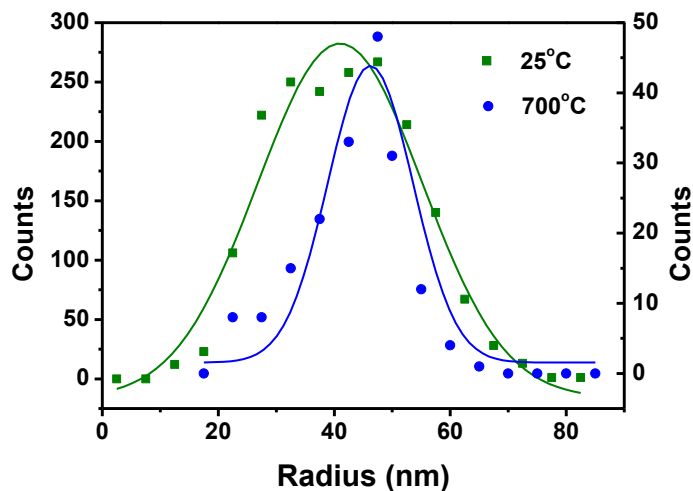


Figure 5.12: NP crosssectional radius distributions of Ga NP ensembles with the same LSPR energy deposited at (square) 25 °C and (circle) 700 °C respectively.

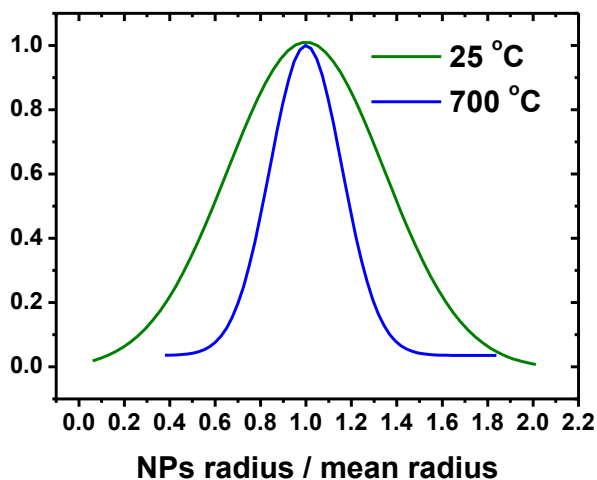


Figure 5.13: Scaled NP crosssectional radius distributions of Ga NP ensembles with the same LSPR energy deposited at 25 °C and 700 °C respectively.

Figure 5.12 plots the radius distributions for these two samples. In sake of clarity, points were plotted instead of histogram bars and normal distribution is used to fit the histograms as shown in solid lines. Radius distribution becomes narrower for the ensemble deposited at 700 °C compared to the one at 25 °C. In order to

make direct comparison, fitted normal distribution is scaled to standard form with respect to its mean value $F\left(\frac{r}{r_{\text{avg}}}\right)$. The FWHM of the scaled radius for 700 °C sample is approximately 40% of that for 25 °C sample as shown in Figure 5.13. Narrow in size distribution is also confirmed by NP's optical responses. Figure 5.14 plotted pseudoextinction coefficient $\langle\kappa\rangle$ for both samples. Although they have the same peak value, the width of the peak for the sample grown at 700 °C is narrower than that at 25 °C. The long tail in the high energy range of the $\langle\kappa\rangle$ curve for the 25 °C sample attributes to the optical responses from large amount of small NPs, which are eliminated in high temperature deposition. For the 700 °C sample, more NPs are in the size close to the mean radius. Therefore, $\langle\kappa\rangle$ is higher for the 700 °C sample. In general, elevating deposition temperature is an effective way to shrink NP size distribution.

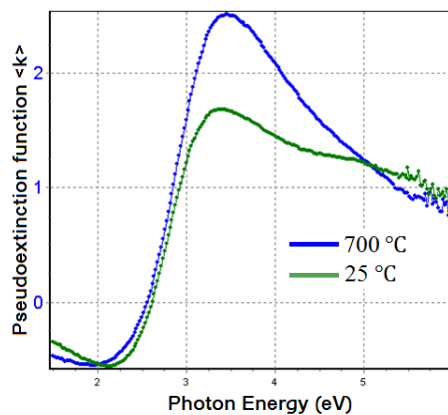


Figure 5.14: Pseudoextinction coefficients of Ga NP ensembles deposited at 25 °C and 700 °C respectively.

The discussion of the impact from the type of substrate on NP morphology is beyond the scope of this work. The research on Ga NP growth provides fruitful and systematic experimental data to understand fundamental thin film growth kinetics and mechanism. A variety of resulted NP ensemble morphology also provides extra dimensions to tune plasmon resonance for different plasmonic applications.

In conclusion, Ga forms truncated hemispheroid three-dimensional islands, nanoparticles, on sapphire. Ga NP ensembles deposited on sapphire possess a bell-shape size distribution. As deposition continues, the radius distribution migrates from unimodal to bimodal. Quantitative spatial statistics are extracted from SEM images. In the next chapter, I will discuss optical characterization of Ga NP ensembles using ellipsometric measurements and their correlation with these spatial statistics.

6. Spectroscopic Ellipsometry Modeling

The principle of spectroscopic ellipsometry (SE) was introduced in Chapter 3 and pseudorefractive index was used to estimate NP ensembles' LSPR energies during deposition as discussed in Chapter 4. However, the nonphysical value in pseudoextinction coefficient indicates the failure of Equation 3.24. In order to obtain meaningful plasmon resonance profiles and to correlate with spatial statistics acquired in Chapter 5, SE modeling is used to retrieve optical responses from measured SE data for Ga NP ensembles in this chapter.

6.1 SE modeling principle

6.1.1 Effective medium approximation

As discussed in Chapter 3, the refractive index of a uniform and isotropic semi-infinite layer can be directly calculated from measured SE parameters (Ψ, Δ) using Equation 3.15 which is derived from the Fresnel equations.

$$\tilde{n} = n + i\kappa = \sin\theta_i \left[1 + \left(\frac{1-\rho}{1+\rho} \right)^2 \tan^2\theta_i \right]^{\frac{1}{2}} \quad (3.15b)$$

When the layer is not perfect (e.g. surface roughness) or if the structure is not layered (e.g. spherical or elliptical), Equation 3.15 is no longer valid but can still be used to estimate a sample's pseudorefractive index using Equation 3.24.

$$\langle \tilde{n} \rangle = \langle n \rangle + i\langle \kappa \rangle = \sin\theta_i \left[1 + \left(\frac{1-\rho}{1+\rho} \right)^2 \tan^2\theta_i \right]^{\frac{1}{2}} \quad (3.24)$$

However, the calculated results showed nonphysical (negative) values in Figure 3.8 and Figure 4.4. In order to retrieve real optical properties, new models are needed to calculate \tilde{n} from (Ψ, Δ) . One of the commonly used models is effective medium approximation (EMA), which includes the structural variance from thin films but maintains the simplicity of using the Fresnel equations [168]. The principle of EMA is to treat a non-uniform structure as a uniform layer with an overall effective refractive index and still use the Fresnel equations to calculate optical responses from the layer. The effective refractive index is the volume-weighted addition of the refractive index of each component within the layer. For example, a rough Ga surface can be treated as a layer consisting of Ga and air. There are different versions of EMA [169-170], such as the Lorentz-Lorenz relation, the Maxwell Garnett Model, and the Bruggeman EMA. They are used to model a material's refractive index plus surface roughness and defects. The next section will discuss the application of EMA to our Ga NP ensembles on sapphire.

6.1.2 SE model of Ga NP ensemble

Different from a bottom-up calculation, which uses spatial information to determine volume weight and obtain effective refractive index from the bulk

values of each component, we use an effective refractive index to represent Ga NP ensembles because only the overall optical properties are of interest at the stage. For our samples, the model consists of two uniform and isotropic layers. As shown in Figure 6.1, the bottom semi-infinite layer accounts for the sapphire substrate and the top layer with finite thickness represents Ga NP ensembles deposited on sapphire. This model excludes the finite thickness effect of the substrate since we ignore the interface between the bottom of the substrate and the ambient air/vacuum. Given that the thickness of the sapphire substrate used in our experiments (440 μm) is much larger than the height of the NPs (up to 100 nm), the semi-infinite assumption for the substrate is indeed very precise for the modeling in this work. The same model was applied to explore similar silver nanoparticle ensembles on solid supports [171].

An effective refractive index is needed to model the overall optical properties of each layer. The choice of this function must reflect the physical process underlying each layer's optical responses. For example, dielectric plates are always modeled as $\tilde{n}(\omega) = n$; for noble metals, $\tilde{n}(\omega)$ can be expressed by the Drude model; for the asymmetry excitation in amorphous material, the Tauc-Lorentz model can be applied. In our model, the effective refractive index of the bottom layer is simply the refractive index of sapphire plotted in Figure 4.3, since

the single species layer is assumed to be uniform, isotropic and semi-infinite. For the top layer, Lorentz oscillators are introduced to represent Ga NP ensembles [171-172]. The next section will discuss Lorentz oscillators and their validity in modeling NP's plasmon resonance.

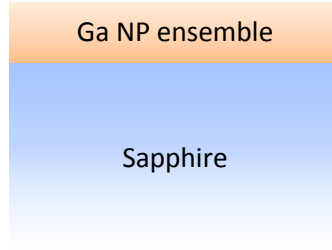


Figure 6.1: SE EMA model for Ga NP ensembles on sapphire.

6.1.3 Lorentz oscillator

Recall the dipole origins of plasmon resonance in Chapter 2. When the electric field interacts with a dipole, it will force the dipole to oscillate like a damped oscillator. The restoring force is from the interaction within the dipole between positive and negative charges with intrinsic resonant frequency ω_0 , the viscous (drag) force comes from the material composition and internal interactions (e.g. inelastic scatterings) and the driving force is the external electric field. This type oscillation is a Lorentz oscillator which follows the equation of motion:

$$m \frac{d^2x}{dt^2} + m\Gamma \frac{dx}{dt} + m\omega_0^2 x = -eE_0 e^{i\omega t} \quad (6.1)$$

where e is the absolute unit charge of an electron, m is the effective mass in the material, and Γ is the damping constant. The general solution to Equation 6.1 is

$$x(t) = -\frac{eE_0}{m} \frac{1}{\omega_0^2 - \omega^2 + i\Gamma\omega} e^{i\omega t} \quad (6.2)$$

where $x(t)$ represents the spatial deviation of electrons from positive charged centers at a time t . An electron and a corresponding positive charge with interparticle distance x constitutes an electric dipole. Therefore, the total dipole moment, or polarization is,

$$\mathbf{P} = -eN\mathbf{x} \quad (6.3)$$

where N is the electron volume density. Recall the definition of a dielectric function, which measures the polarization \mathbf{P} given an external field,

$$\mathbf{P} = (\varepsilon - 1)\mathbf{E} \quad (6.4)$$

Comparing Equation 6.3 and 6.4 and plugging in Equation 6.2, the dielectric function of this material is

$$\tilde{\varepsilon}(\omega) = 1 + \frac{e^2 N}{m} \frac{1}{\omega_0^2 - \omega^2 + i\Gamma\omega} \quad (6.5)$$

For localized surface plasmon resonance in NPs, each resonance can be described by one Lorentz oscillator. In general, multiple Lorentz oscillators are used which can be expressed as,

$$\tilde{\varepsilon}(\omega) = \varepsilon_1 + i\varepsilon_2 = \varepsilon_\infty + \sum_{j=1}^N \frac{f_j \omega_{0j}^2}{\omega_{0j}^2 - \omega^2 + i\gamma_j \omega} \quad (6.6)$$

where ω_{0j} , γ_j and f_j are the resonant energy, the damping constant and the amplitude for the j^{th} oscillator respectively. N indicates the number of oscillators included in the model.

Figure 6.2 plots the real and imaginary parts of a typical Lorentz oscillator. The imaginary part ϵ_2 reveals a clear peak at ω_0 and the width of the peak is proportional to γ . $\tilde{\epsilon}$ can be converted to a refractive index by the basic relation,

$$\tilde{n}^2 = \tilde{\epsilon} \quad (2.19)$$

To model Ga NP ensembles with Lorentz oscillators (Equation 6.6), N is the number of oscillators included in the model which depends on the number of LSPR modes observed in SE measurements. In most of our experiments, single or double oscillators were used. ω_0 correlates with the LSPR energy which is highly related to NP size. γ , the damping constant, is an intrinsic property of Ga and also related to NP size and size distribution.

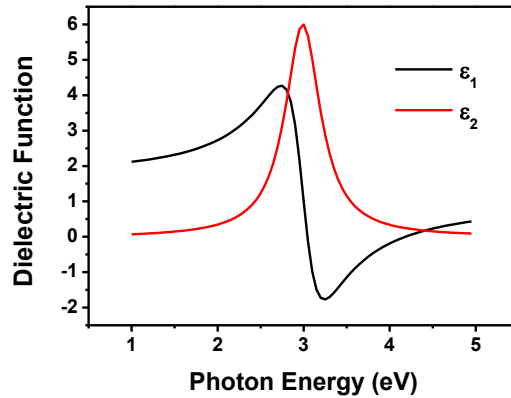


Figure 6.2: Real and imaginary parts of the dielectric function of a Lorentz oscillator with $\omega_0 = 3$, $f = 1$, $\gamma = 0.5$.

Now, Ga NP ensembles are modeled by a layer of Lorentz oscillators and a layer of sapphire. However, the Fresnel equations (Equation 3.8) only deal with reflection at one interface. In our model, there are two interfaces: a) vacuum – gallium and b) gallium – sapphire. The next section will discuss how to calculate reflection ratios from multilayers based on the Fresnel equations.

6.1.4 Multilayer reflection

To calculate reflection ratios from multilayers, reflections from all the interfaces must be included. Figure 6.3 illustrates reflections and transmissions occurring at each interface of adjacent layers. No reflection is considered from the bottom of the substrate, sapphire, as it is assumed to be semi-infinite in the model.

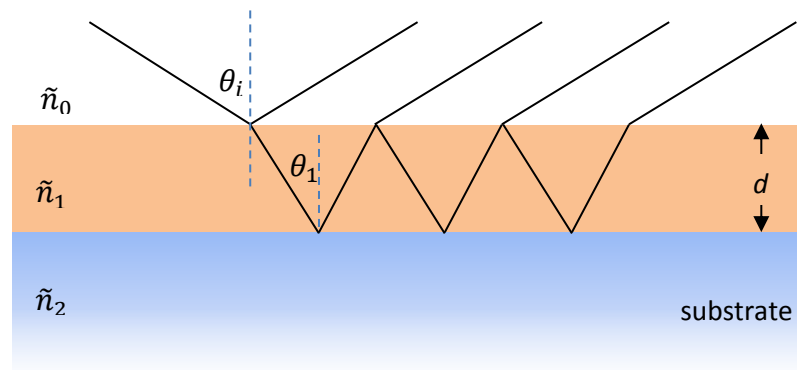


Figure 6.3: Multiple reflections from a two-layer structure.

Incident light radiates at the interface of the ambient air (\tilde{n}_0) and the top layer (\tilde{n}_1). Part of the light is reflected back to the air while the rest is transmitted into

the thin film and travels until it reaches the interface of the top layer (\tilde{n}_1) and the substrate (\tilde{n}_2). Reflection occurs at this interface and the light beam splits into reflected and transmitted components. The reflected light then travels towards the top interface and splits there again. Part of the light is transmitted into the air and the rest is reflected back to the top layer. After this, the reflected light will travel within the top layer and bounce between the two interfaces. For each “bounce”, part of the light will be transmitted into the substrate, which reduces the intensity of the reflected light each incidence with the interface. The total reflected light is thus the superposition of all the exiting light beams from the top layer into the ambient air. This infinite series of light beams are all from the incident light (thus coherent) and each beam differs by a fixed phase difference. Given the top layer thickness d , the phase difference between two adjacent exiting light beams is

$$\alpha = \frac{4\pi d n_1}{\lambda} \cos\theta_1 \quad (6.7)$$

where λ is the wavelength of the incidence light in vacuum and θ_1 can be calculated by Snell’s Law using the angle of incidence. To generalize the above process, the first exiting light beam is the one directly reflected and the electric field will be $r_{01}E_i$. r_{01} is the reflection ratio at the interface of \tilde{n}_0 and \tilde{n}_1 when light travels from \tilde{n}_0 to \tilde{n}_1 . In the discussion below, the subscripts of r and t will

have the same convention. The second exiting light beam undergoes one transmission from \tilde{n}_0 to \tilde{n}_1 , one reflection at \tilde{n}_1 and \tilde{n}_2 and one transmission from \tilde{n}_1 to \tilde{n}_0 . Combining with the phase difference, the electric field would be $t_{01}t_{10}r_{12}E_i e^{-i\alpha}$. Follow this analysis, all the exiting light beams from the top layer to the ambient air can be expressed as,

$$E_r = r_{01}E_i + t_{01}t_{10}r_{12}E_i e^{-i\alpha} + t_{01}t_{10}r_{12}(r_{10}r_{12})E_i e^{-i2\alpha} + \dots \quad (6.8)$$

The addition of this series of light beams is thus the total reflected light. Therefore, the total reflection ratio will be

$$r = \frac{E_r}{E_i} = r_{01} + \frac{t_{01}t_{10}r_{12}e^{-i\alpha}}{1-r_{10}r_{12}e^{-i\alpha}} \quad (6.9)$$

All the r and t with subscripts are the reflection and transmission ratios already given by the Fresnel equations (Equation 3.8) at the interface of two media. Two identities can be derived from Equation 3.8 [173]:

$$\begin{cases} r_{10} = -r_{01} \\ t_{01}t_{10} = 1 - r_{01}^2 \end{cases} \quad (6.10)$$

Therefore, Equation 6.9 can be rewritten as,

$$r = \frac{r_{01} + r_{12}e^{-i\alpha}}{1 + r_{01}r_{12}e^{-i\alpha}} \quad (6.11)$$

The derivation above does not specify the state of polarization. It is valid for both p - and s - polarized light. This does not mean $r_p = r_s$ since r_{01} and r_{12} have different values for p - and s - polarizations, but r_p and r_s have the same analytical form as in Equation 6.11. Recall Equation 3.12

$$\rho \equiv \frac{r_p}{r_s} \equiv \tan\Psi e^{i\Delta} \quad (3.12b)$$

SE measures the ratio of r_p and r_s . In Equation 6.11, r_p and r_s are a function of the top layer thickness d (Equation 6.7), the refractive indices of ambient air \tilde{n}_0 , top layer \tilde{n}_1 and substrate layer \tilde{n}_2 , the angle of incidence θ_i , and the incident light wavelength (or photon energy ω).

For SE measurements on Ga NP samples, all other parameters are known except for the top layer (Ga layer) refractive index \tilde{n}_1 and layer thickness d . Ideally, we can insert Equation 6.11 into Equation 3.12 and solve for the inverse function of \tilde{n}_1 in terms of (Ψ, Δ) , like what we obtained for a one-interface system. (Equation 3.15) However, there are three unknowns in Equation 6.11, the real and imaginary parts of the complex refractive index and the thickness of the top layer. It is generally not possible to solve for three unknowns given only two observables (Ψ, Δ) for each experiment setup (given θ_i and ω). Therefore, a fitting procedure is introduced, which will be discussed in the next section.

6.1.5 SE model fitting

Given equation 6.11 and 3.15, (Ψ, Δ) can be calculated from the thickness d , the refractive indices of the ambient air \tilde{n}_0 , the Ga NP layer \tilde{n}_1 , and the sapphire layer \tilde{n}_2 , and the AOI $\theta_i = 70^\circ$ at each photon energy ω for our two-layer model,

$$\rho = \tan\Psi e^{i\Delta} = \frac{r_{01,p} + r_{12,p} e^{-i\alpha}}{1 + r_{01,p} r_{12,p} e^{-i\alpha}} \bigg/ \frac{r_{01,s} + r_{12,s} e^{-i\alpha}}{1 + r_{01,s} r_{12,s} e^{-i\alpha}} \quad (6.12)$$

In order to obtain unknowns ($\tilde{n}_1(\omega)$, d), a nonlinear fitting procedure was carried out by HORIBA Jobin Yvon SE software DeltaPsi. The Levenberg – Marquardt algorithm is used to minimize the mean square error (MSE) χ^2 of the fitting [173-174],

$$\chi^2 = \frac{2}{M-m-1} \sum_{i=1}^M \frac{(\rho_{\text{exp}}(\omega_i) - \rho_{\text{cal}}(\omega_i))^2}{\sigma_i^2} \quad (6.13)$$

where M is the number of data points at different photon energies, m is the number of fitted parameters, ρ_{exp} is measured data, ρ_{cal} is calculated data by Equation 6.12, and σ_i^2 is the variation of the i^{th} data point. Since the refractive index of the Ga NP layer is represented by multiple Lorentz oscillators,

$$\tilde{\epsilon}(\omega) = \epsilon_1 + i\epsilon_2 = \epsilon_\infty + \sum_{j=1}^N \frac{f_j \omega_{0j}^2}{\omega_{0j}^2 - \omega^2 + i\gamma_j \omega} \quad (6.6)$$

the fitting parameters include Ga NP layer thickness d , ϵ_∞ , and ω_{0j} , γ_j , and f_j for each Lorentz oscillator. N is manually defined based on the number of resonance peaks in the pseudoextinction plot which is calculated by Equation 3.24.

Unlike some other optical measurements like X-ray and Raman, which show unique responses for different species, SE is majorly used to analyze sample details given the basic information of samples' structures and compositions. The fitting to these models might not be unique. Better results require well estimated

presets of fitting parameters. This information comes from sample growth and the deposition process before optical characterization. Therefore, fitting parameters d , ϵ_{∞} , ω_{0j} , γ_j and f_j are preset close to potential real values based on pseudorefractive index estimated from measured SE data.

6.2 SE modeling result

6.2.1 A typical sample

Figure 6.4 compares raw and fitted (Ψ, Δ) curves for sample Y3. All features are successfully fitted except for Δ over the energy range > 4.5 eV. The discontinuity and noise of Δ in this region again come from the change of SE spectrometer grating. Table 6.1 shows the fitted parameters for sample Y3. Only one Lorentz oscillator ($N = 1$) was included in the fitting since one absorption peak was observed from its pseudoextinction coefficient $\langle k \rangle$.

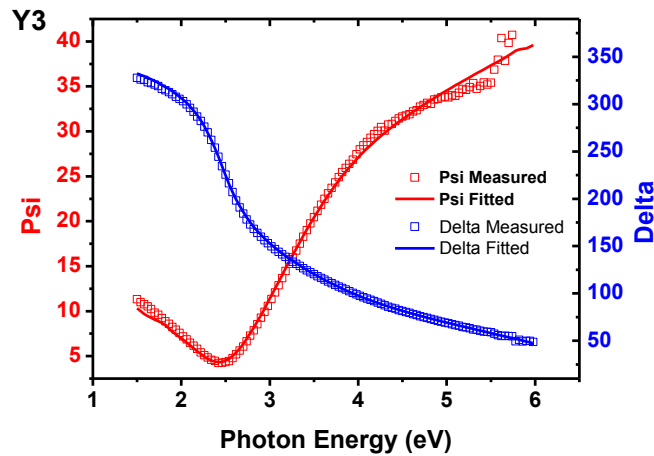


Figure 6.4: Measured and fitted SE parameter (Ψ, Δ) for sample Y3.

Table 6.1: Fitted SE model parameters for sample Y3.

Parameter	Fitted value
ϵ_{∞}	1.44 ± 0.02
f_1	3.95 ± 0.06
ω_{01} / eV	3.49 ± 0.02
γ_1 / eV	1.35 ± 0.02
d / nm	18.9 ± 0.5

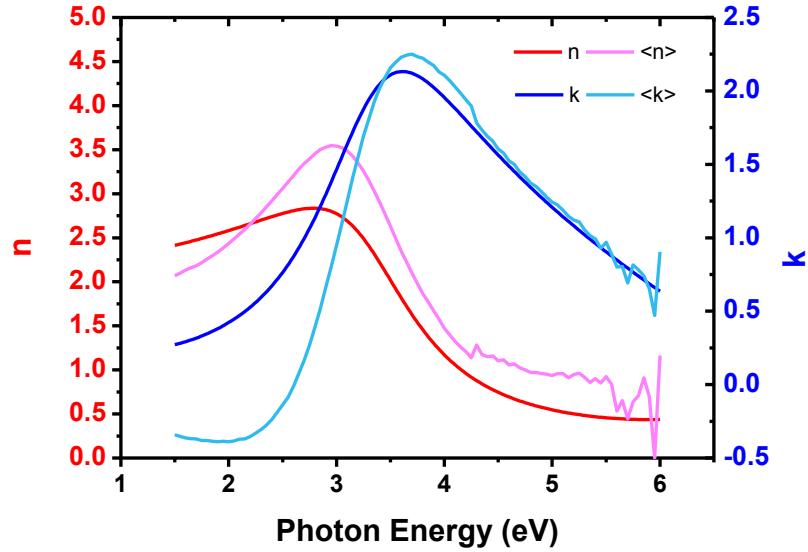


Figure 6.5: Pseudorefractive index $\langle \tilde{n} \rangle$ and SE model inferred refractive index \tilde{n} of sample Y3.

Figure 6.5 compares the pseudorefractive index calculated directly from Equation 3.24 and the refractive index generated by the fitted Lorentz parameters in Table 6.1 from Equation 6.6. Although the peaks in both curves are close, inferred k solves the problem of nonphysical negative values in $\langle k \rangle$ for the photon energy < 3 eV. Therefore, $\langle k \rangle$ can be used to roughly estimate the peak

position of absorption and the SE model inferred k shall be used to explore and determine the optical response of Ga NP ensembles. The discussion in Chapter 4 to use SE to monitor deposition is still valid as we were only concerned about the rough position of LSPR energy of Ga NP ensembles. However, for the following sections, fitted dielectric functions will be used as they reflect the physics origins.

Table 6.2: Fitted SE parameters for samples Y1 ~ Y7.

	ϵ_{∞}	f_j	ω_{0j} / eV	γ_j / eV	d / nm
Y1	0.95 ± 0.05	3.23 ± 0.04	4.16 ± 0.02	1.59 ± 0.02	11.6 ± 0.4
Y2	1.21 ± 0.02	4.01 ± 0.03	3.78 ± 0.01	1.44 ± 0.01	14.6 ± 0.2
Y3	1.44 ± 0.02	3.95 ± 0.06	3.49 ± 0.02	1.35 ± 0.02	18.9 ± 0.5
Y4	1.90 ± 0.06	5.28 ± 0.14	2.76 ± 0.01	0.92 ± 0.02	25.1 ± 0.8
Y5	0.86 ± 0.04	6.82 ± 0.18	2.16 ± 0.01	0.70 ± 0.02	21.9 ± 0.8
		1.19 ± 0.06	6.76 ± 0.08	2.20 ± 0.25	
Y6	0.95 ± 0.09	6.24 ± 0.24	1.77 ± 0.01	0.69 ± 0.02	24.7 ± 1.2
		2.25 ± 0.10	5.95 ± 0.10	3.27 ± 0.13	
		0.26 ± 0.08	4.75 ± 0.04	1.02 ± 0.18	
Y7	1.26 ± 0.05	17.5 ± 0.5	1.18 ± 0.01	0.28 ± 0.02	15.4 ± 0.4
		1.95 ± 0.03	4.81 ± 0.02	1.91 ± 0.03	
		0.71 ± 0.06	3.00 ± 0.01	1.33 ± 0.06	

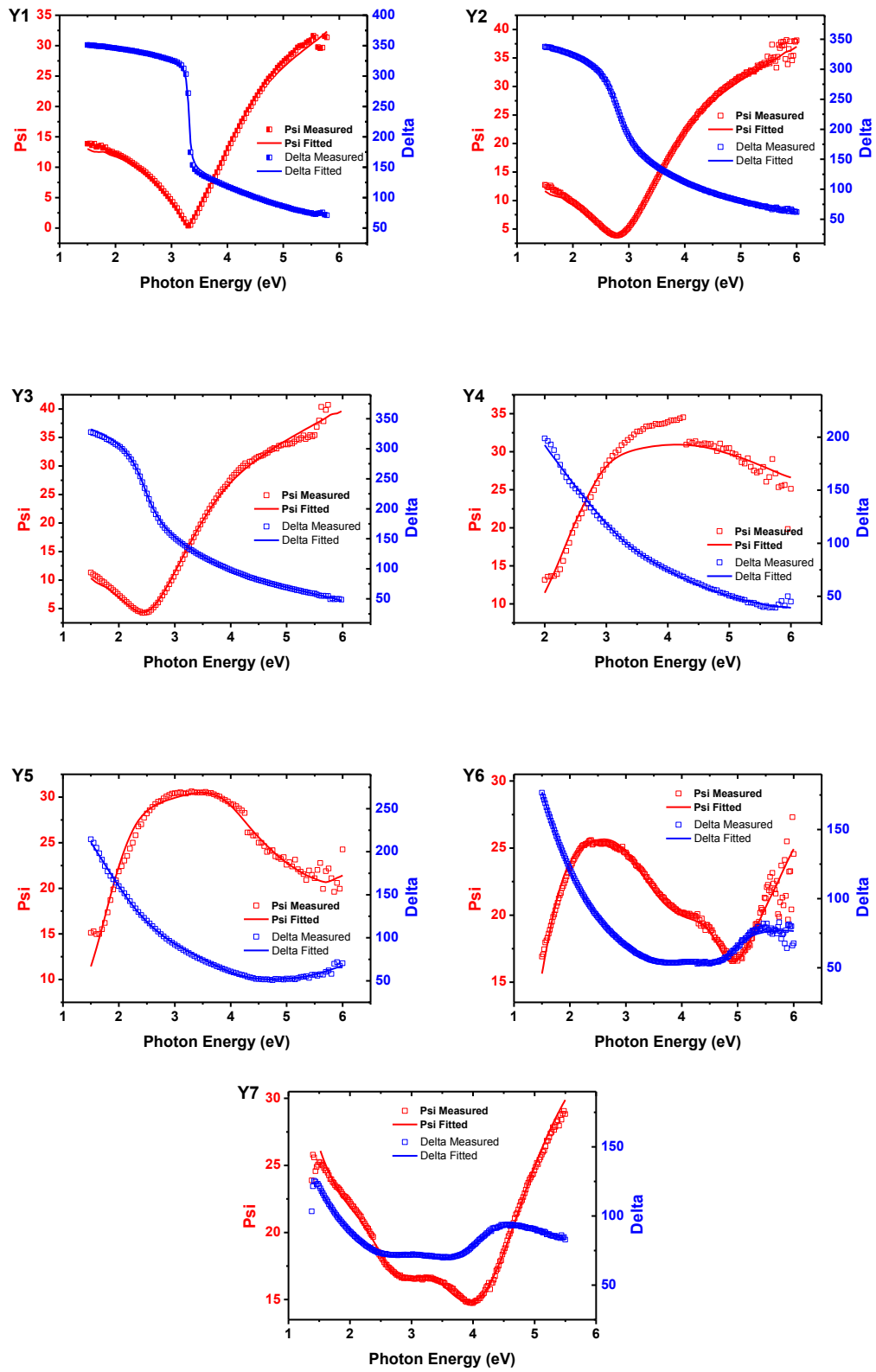


Figure 6.6: Measured and fitted (Ψ , Δ) of samples Y1 ~ Y7.

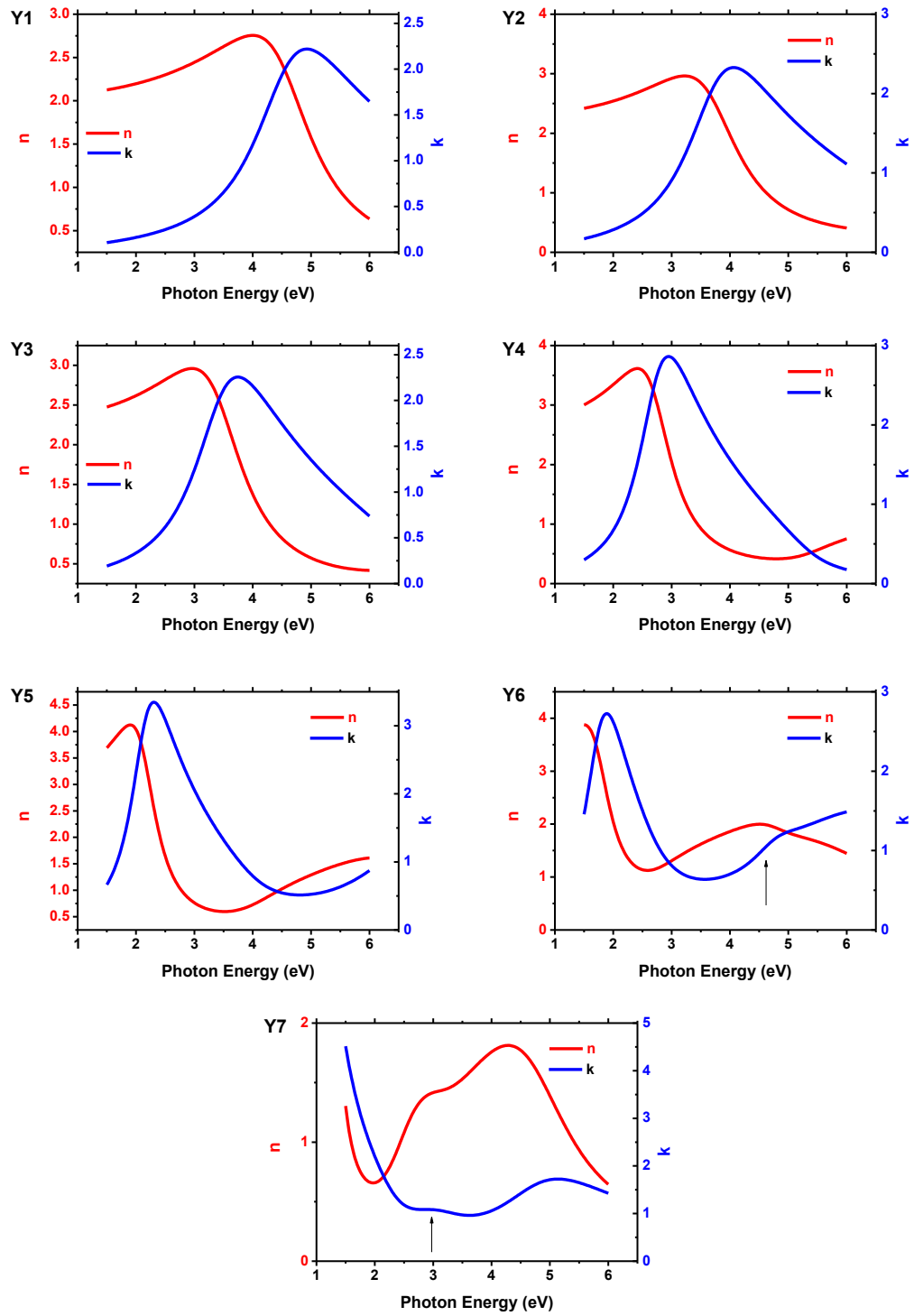


Figure 6.7: SE model inferred refractive index \tilde{n} of samples Y1 ~ Y7.

6.2.2 Modeling result for samples Y1 ~ Y7

The same fitting process was applied to a group of 7 (including sample Y3) samples with different deposition time, samples Y1 to Y7, whose dosages were presented in Table 4.1. Figure 6.6 compares measured and fitted (Ψ, Δ) for all 7 samples respectively. All the features are again well fitted except for the break at 4.2 eV and the noise above 5.0 eV due to the SE instrument limitations. A jump occurs at 4.2 eV in the Psi curve (red) for the sample Y4. This comes from the misalignment of the grating and the spectrometer after the change of the grating at 4.2 eV in the SE instrument. The following discussion will exclude this sample as the measurement was inaccurate.

Table 6.2 shows all the fitted parameters. ϵ_∞ is the asymptotic dielectric function when $\epsilon \rightarrow \infty$. In the original Drude free electron model, ϵ_∞ shall be 1. From the result, for most samples, ϵ_∞ is around 1. d is the equivalent thickness of the Ga NP layer in the model. It is not the physical heights of NPs. Compared with the physical dimensions acquired in Chapter 5 (presented in Table 5.1), d is smaller than the average NP height because the EMA model mixes the 3D hemispherical NPs and surrounding ambient air into a uniform thin layer. The equivalent thickness is a weighted result from both the volumes of Ga and vacuum. d increases from sample Y1 to Y4 as the volume of Ga also increases. The trend

stops from Y4 to Y5. Recall that Y5, Y6, and Y7 possess bimodal size distribution. The large amount of small NP residues will affect the weighted equivalent thickness. f_j represent the relative strength of absorption peaks. It increases with the increase of the NP size. The detailed discussion of ω_j and γ_j will be presented in the next few sections. For sample A7, half of the peak is out of the detection limit of our SE instrument. The peak was fitted by the measured portion of the peak within the SE detection range, which will jeopardize the accuracy.

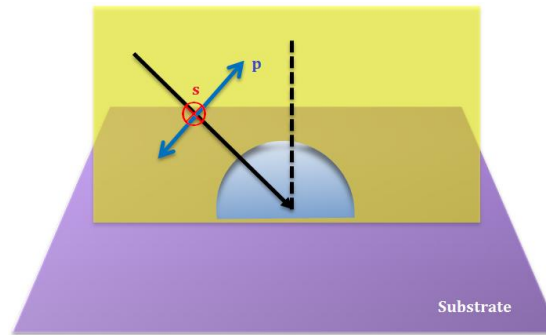


Figure 6.8: Reflection diagram of the SE probe light incident on a single hemispherical Ga NP on sapphire.

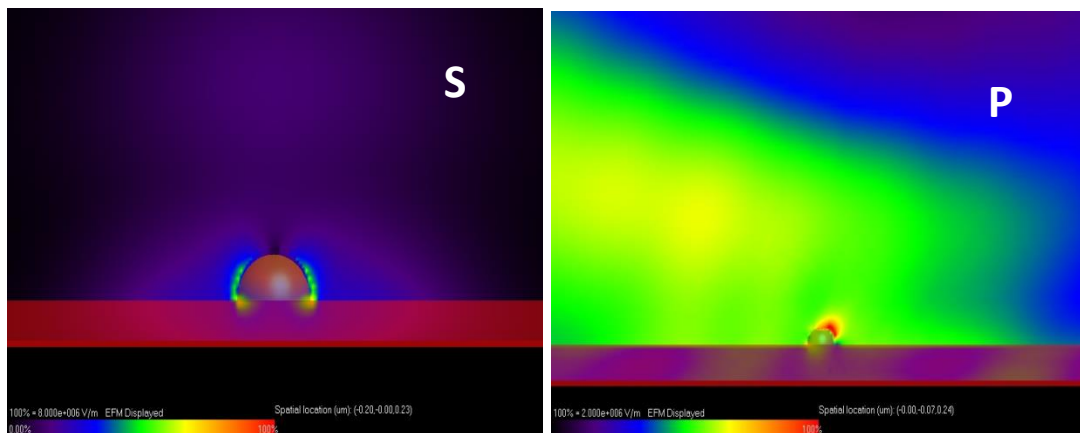


Figure 6.9: EM field intensities surrounding a single hemispherical Ga NP on sapphire excited by (a) s-polarized light and (b) p-polarized light.

6.2.3 Ga NP's LSPR mode

Different numbers of Lorentz oscillators are used for different samples. The number of Lorentz oscillators is equal to the number of absorption peaks. When a Ga NP ensemble is measured by SE, a probe light containing both s- and p-polarizations illuminates the sample surface with an angle of incidence of 70° as shown in Figure 6.8. Figure 6.9 depicts the electromagnetic field intensity surrounding one single truncated Ga NP on sapphire excited by each polarized light, calculated using the finite-difference time-domain (FDTD) method by our collaborator Moreno et al. in Spain. The s-polarized light will excite the LSP, creating oscillations parallel to the sample surface. Therefore, this collective electron oscillation is named the in-plane LSPR mode. Similarly, the p-polarized light will excite the LSP and create oscillations along the direction of p-polarization (the blue line in Figure 6.8). Unless the angle of incidence is zero, this oscillation will always have nonzero component perpendicular to the sample surface, which is called the out-of-plane LSPR mode.

Figure 6.10 plots the absorption efficiency of the in-plane and out-of-plane LSPR modes of a single Ga hemispherical NP on sapphire with radius 20 nm when the excitation is at an AOI of 70° calculated using the DDA method by our collaborator Moreno et al [122]. Since the in-plane mode reflects the dipole

moment along the crosssectional surface, it is associated with the length scale of the crosssectional diameter. For the out-of-plane mode, the dipole moment is along perpendicular direction which has a smaller dimension than that of the in-plane mode. Therefore, the LSPR energy, or the peak energy in the absorption efficiency curve, for the in-plane mode is smaller than that of the out-of-the plane mode. These two peaks are consistent in principle with the SE measurement and modeling result in Figure 6.7 and Table 6.2. For samples with short deposition time (Y1 ~ Y4), only one mode was shown which is the in-plane LSPR mode. When deposition continues, the in-plane mode peak keeps redshifting and the out-of-plane mode peak enters the measurable range (Y5 ~ Y7). For sample Y6 and Y7, the fitting was not optimized until a third Lorentz oscillator was introduced which was identified as the quadrupole in-plane mode [74-75].

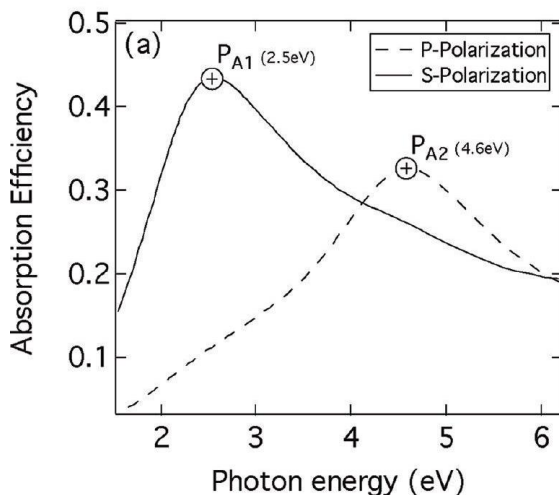


Figure 6.10: Absorption efficiencies for (solid) in-plane and (dashed) out-of-plane LSPR modes of a single hemispherical Ga NP on sapphire [122].

6.2.4 Size dependence of NP's LSPR mode

Deposition time increases from sample Y1 to Y7. The calculated extinction coefficients were plotted in Figure 6.11. As deposition continues, NP size increases and thus the peak in the extinction coefficient curve which represents the LSPR energy redshifts. The detailed morphology statistics were extracted from SEM images as discussed in Chapter 5 and we just calculated optical properties for each sample. The following discussion will correlate spatial and optical properties for our Ga NP ensembles in order to a) guide further synthesis and b) examine and improve estimation and modeling procedure.

To guide further synthesis, optical properties are examined with respect to Ga dosage as that is the parameter we used most to control Ga deposition. Figures 6.12 ~ 6.14 plots 3 fitted Lorentz oscillator parameters in terms of sample dosage D . Both the resonant energy ω_0 and the damping constant γ decrease when the dosage increases. Longer deposition times will result in larger NP dimensions. Therefore, associated LSPR modes will have lower resonant energies. Less confinement effect (surface scattering) leads to a smaller damping constant. Figure 6.16 shows that resonance amplitude (Lorentz oscillator strength) increases when dosage increases. As growth continues, more Ga is deposited on the substrate and therefore, more absorption will occur.

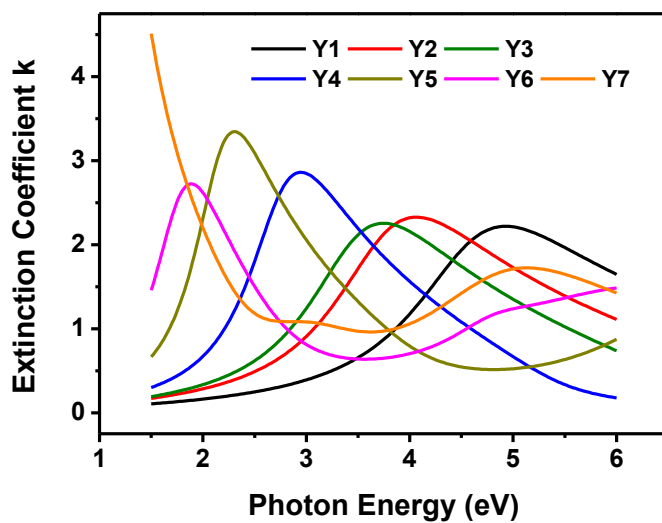


Figure 6.11: SE model inferred extinction coefficient κ of samples Y1 ~ Y7.

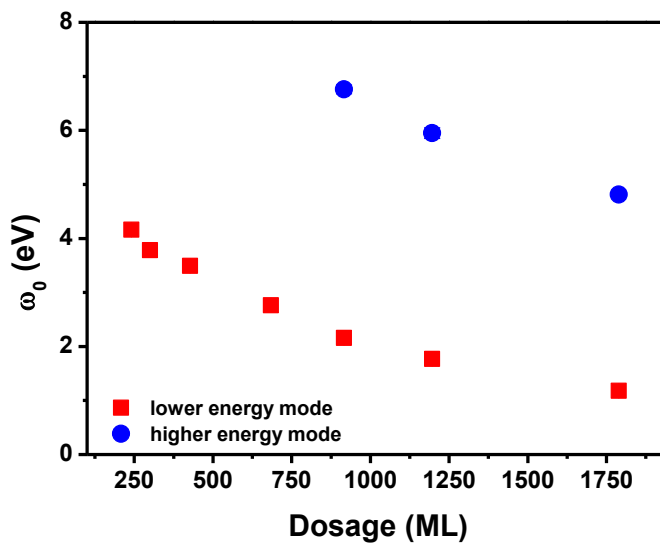


Figure 6.12: SE model fitted oscillator resonant energy ω_0 of samples Y1 ~ Y7.

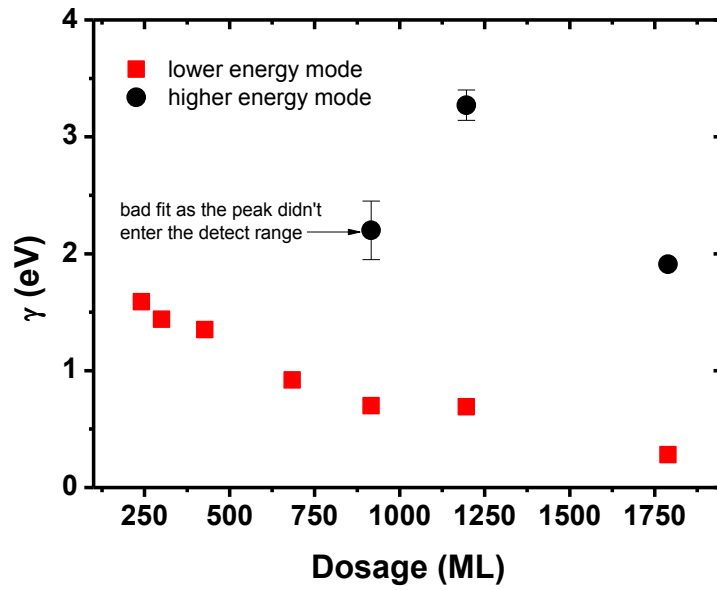


Fig 6.13: SE model fitted damping constant γ of samples Y1 ~ Y7.

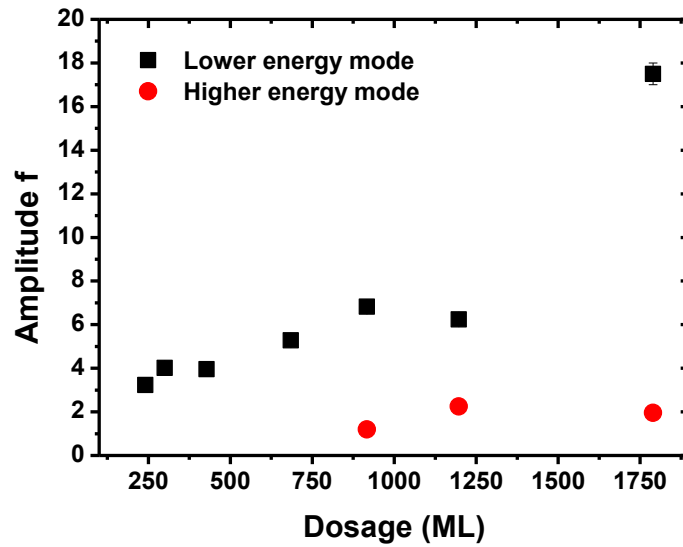


Figure 6.14: SE model fitted Lorentz oscillator strength f of samples Y1 ~ Y7.

These 3 plots include error bars (fitting errors) for each point. However, most error bars are too small to see from the plots. When the absorption peak is completely measured, the fitted parameters can be very accurate. Some points in these plots look off the trend. For example, the first black point in Figure 6.13, the damping constant for a higher energy mode. This is because the measured absorption peak is not completely within the detection region of our SE instrument (1.5 eV ~ 6 eV). For this data point, less than half of the peak was observed. The fitted peak is only an estimate of the real peak. The fitting error is thus significantly larger than other data points. Therefore, we choose three typical samples Y1, Y3, and Y6, which have completely observed absorption peaks and thus reliable fitted parameters, for further exploration on the correlation between fitted Lorentz oscillator parameters and local morphology of NP ensembles in a quantitative way. Detailed morphology statistics were reported in Table 5.1. And as discussed previously, for optical applications like Raman spectroscopy, probe light is incident from normal and therefore only the in-plane mode can be excited. The next section will focus on exploring size dependence of in-plane dipole mode parameters for Y1, Y3, and Y6.

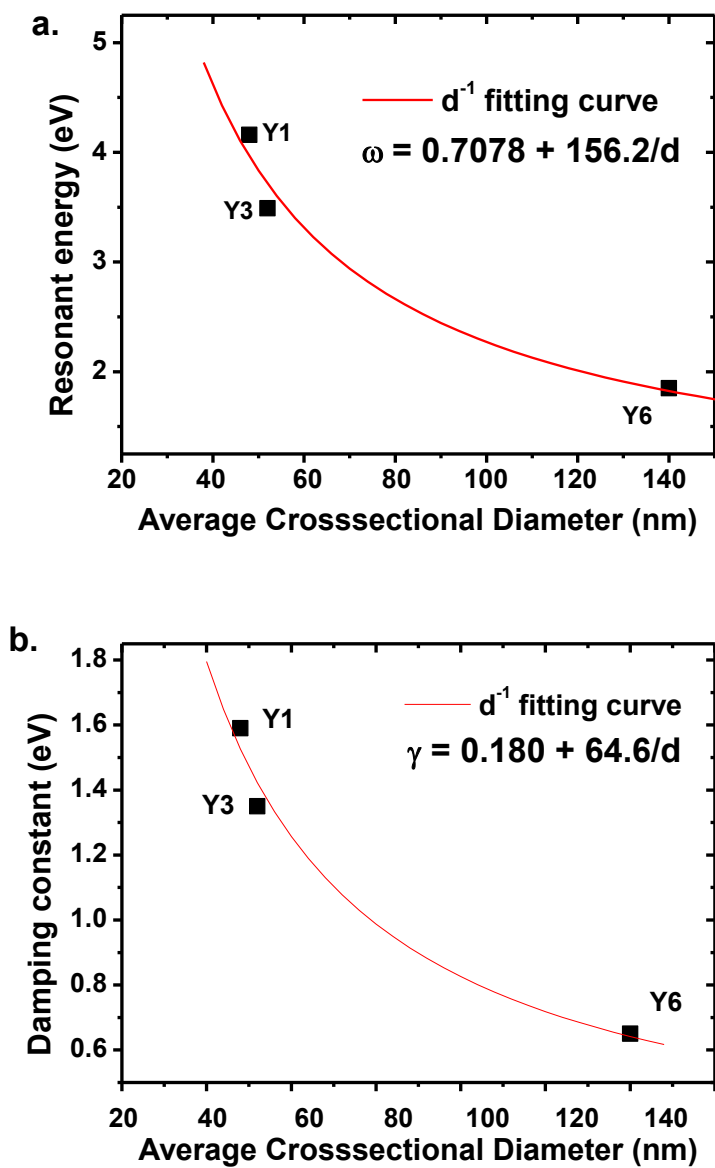


Figure 6.15: Measured dependence of SE model fitted Lorentz oscillator (a) resonance energy and (b) damping constant on the average crosssectional diameter d of samples Y1, Y3, and Y6.

6.2.5 Single NP behavior of Ga NP ensemble's in-plane LSPR dipole mode

Figures 6.15 plots the in-plane dipole mode Lorentz parameters, i.e. resonant energy and damping constant, in terms of average crosssectional diameter of

sample Y1, Y3, and Y6. Crosssectional diameter d , instead of radius r , is used because the diameter is the length scale directly associated with the in-plane LSPR mode. Both plots are well fitted by a $1/d$ curve. Although measured and fitted dielectric functions are a collective response from a randomly distributed truncated NP ensemble with bell-shape size distribution, the overall resonant energy and damping constant behavior like a single spherical NP in terms of the average crosssectional diameter of NP ensemble.

For the resonant energy, $\omega_0 = 0.708 + 156/d$ for ω_0 in eV and d in nm. Since the Lorentz model reflects the damped oscillatory motion of free electrons, the dependence of ω_0 on d does not arise from any model-dependent assumptions about confinement. Instead, this dependence is purely a consequence of the relationship between the size of the nanoparticle and the strength of the induced dipolar mode of the plasmon resonance due to retardation effects [122]. Since the ensemble represent a heterogeneous distribution of sizes, this observation indicates that the dominant plasmonic resonance is associated with single nanoparticle behavior; specifically, that of the dominant constituent nanoparticle in the ensemble. Since the diameter is linearly correlated with dosage, this relationship may be used to estimate the LSPR frequency for Ga NP ensemble in deposition chambers that do not have an ellipsometer.

For the damping constant, $\gamma = 0.18 + 65/d$ for γ in eV and d in nm. Similar behaviors were seen in small gold NPs [175], and Ga NPs [176]. Based on the Drude-Sommerfeld free electron model, the diameter dependent damping constant of a single NP is,

$$\gamma(d) = \gamma_0 + \frac{2Av_F}{d} \quad (6.14)$$

where γ_0 is the bulk damping constant and v_F is the Fermi velocity in the free electron model. When particle size decreases, the mean free path of the electrons is comparable with NP dimension, scattering at boundaries or the surface become significant. The $1/d$ represents the surface to volume ratio. In general, damping comes from a variety of scattering processes such as electron-electron scattering, electron-phonon scattering, and electron-defect scattering. Fitted $\gamma_0 = 0.18$ eV is much larger than the bulk damping constant of Ga which is 1.54 eV [64]. Again, the fitted γ is extracted from collective optical responses from the EMA layer which is a mix of Ga and vacuum. However, the $1/d$ dependence confirms the single-particle behavior of the in-plane LSPR dipole mode.

To summarize, the resonance energy and damping constant of the in-plane LSPR mode are inversely proportional to the average crosssectional diameter of Ga NP ensembles. This functional dependence can be used to estimate ensemble LSPR energy by measuring average size of NPs, or vice versa.

6.2.6 Comparison with theoretical modeling

Recall that we estimated Ga NP LSPR energy using analytical and numerical methods including Mie scattering and DDA in Chapter 2. This section will compare measured size dependence of LSPR profiles with predicted ones presented in Chapter 2. We have confirmed that measured extinction coefficient curves are consistent with DDA calculation in principle in Section 6.2.3, e.g. splitting of the in-plane and the out-of-plane modes.

Figure 6.16 compares the measured extinction coefficient and the ones calculated by Mie scattering. Dashed lines plot the fitted extinction coefficient for sample Y1, Y3, and Y6, while solid lines depict the extinction coefficient curves for spherical Ga NPs with the same corresponding average radius. The resonance peak obtained from the fitting is to the red side of the predicted one for the same radius, which is a combined effect of the substrate and the truncated NP shape. DDA calculations have already confirmed that both factors will redshift LSPR energy [122].

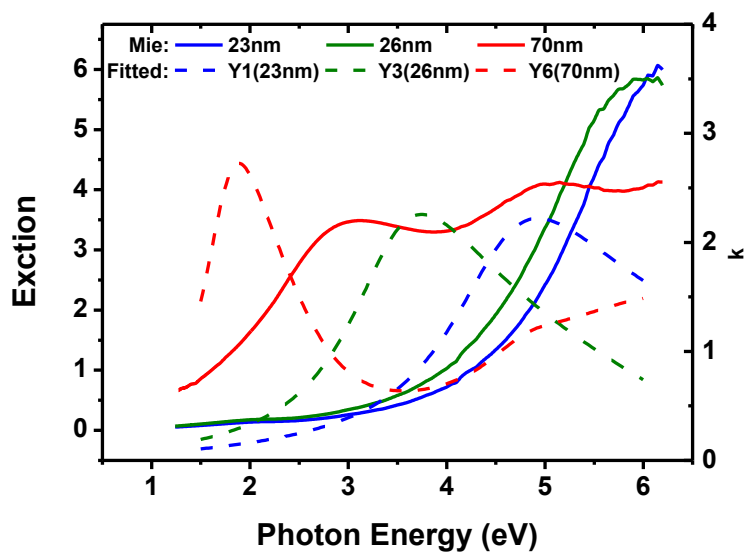


Fig 6.16: (solid) Mie scattering predicted extinction efficiency comparing with (dash) SE model inferred extinction coefficient of NPs with the same radii.

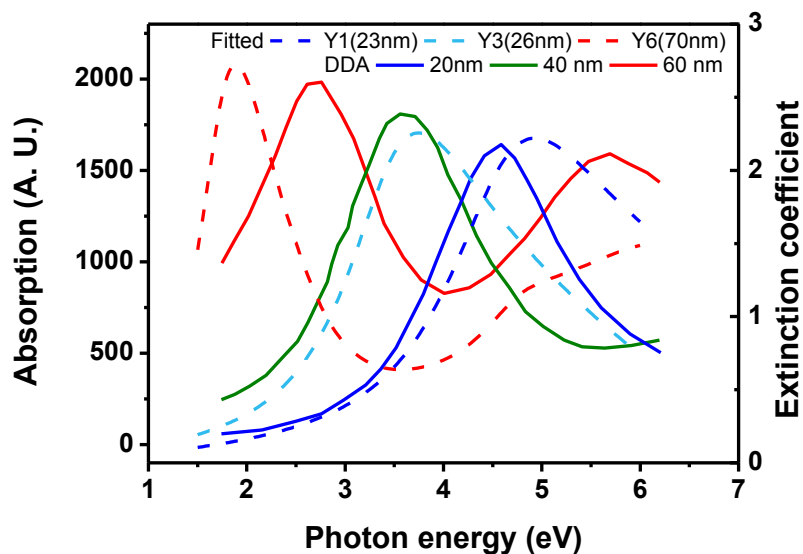


Fig 6.17: (solid) DDA method predicted absorption efficiency comparing with (dashed) SE model inferred extinction coefficient of NPs with the similar radii.

Figure 6.17 shows absorption curves of single hemispherical NP on sapphire with radius 20 nm, 40 nm, and 60nm respectively calculated with the DDA method by our collaborator Moreno et al. This calculation used the Ga refractive index converted from Figure 2.3, which is more precise than the one used in Section 2.2.4. DDA predicted absorption curves well reproduce measured features. The fitted peak of Y1 (23 nm) is at the blue side of the predicted peak (20 nm) due to the interparticle coupling effect which will blue shift NP's LSPR. However, the fitted peak of Y3 (26 nm) is at the red side of the predicted peak (20 nm) given that the average NP radius is increased and NPs with larger radii in the ensemble contribute more to the overall absorption. This is consistent with the longer tail to the right in the NP radius distribution of Y3 than that of Y1 shown in Figure 5.7. Interparticle interaction and ensemble distribution are two factors ignored by the DDA calculation above. Further calculations will include both factors which will be discussed in Chapter 10.

Although SE is a relatively mature technique to characterize bulk materials, layered materials, and thin films, its application in nanostructures still needs further exploration. Several SE models are developed specifically for nanostructures but most are based on EMA [172]. Thin island film (TIF) theory is recently introduced to explicitly include interparticle coupling within the NP

ensemble which obtained more precise fitting result than EMA based models [177]. Another major drawback of the SE measurements we discussed so far is that they are carried out at fixed angle of incidence, unlike flat thin films, shadowing effect from higher structures on surface may shield or interfere with incident light to lower structures. This effect was even observed on rough surface [178]. Grazing angle optical responses may be different when compared to normal incidence applications like Raman spectroscopy. Therefore, angle-scanning measurements are applied to these Ga NP ensembles including variable angle SE (VASE) and variable angle Mueller matrix (MM) measurements which will be discussed in the next chapter.

7. Variable-angle SE and Mueller Matrix

SE used in the previous chapters was operated at an AOI of 70° , while spectroscopies like Raman are usually measured at normal incidence. On one hand, under the thin film assumption, dielectric functions obtained in the last chapter can be used to predict the optical responses at other AOIs. On the other hand, optical responses vary with respect to AOI for certain structures due to multiscattering, multireflection, and shadowing effects. This chapter will present AOI-resolved optical properties of Ga NP ensembles measured by variable-angle spectroscopic ellipsometry (VASE) and variable-angle Mueller matrix (VAMM) measurements to a) examine the validity of the previous modeling and b) directly explore AOI-dependent NP ensembles' optical properties.

7.1 Variable-angle spectroscopic ellipsometry (VASE)

7.1.1 Principle and instrument

SE used to be performed at or near Brewster's angle (e.g. 70° in the last chapter) because the largest state of polarization change is expected [173]. This would allow us to maintain the highest precision. However, as compensators are introduced to the community, grazing angle incidence is no longer required and

SE can be performed at various angles of incidence. This measurement is referred to as variable-angle SE (VASE). VASE is highly recommended for thin films, index graded films, anisotropic materials and nanostructures like our Ga NP ensembles [179-180]. VASE measurements enable us to understand NP's optical responses which cannot be revealed at oblique angles. VASE has been used to characterize thin films [181] and nanoparticles to study growth processes [182] and anisotropic effects [183]. The data acquisition and analysis process for VASE is the same as those for fixed angle SE. The angle of incidence is now another input of the Fresnel equations or Equation 6.11.

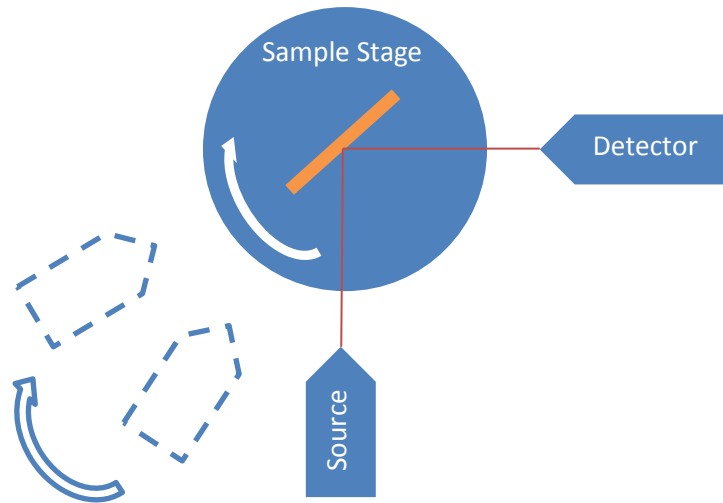


Figure 7.1: Structure of the in-house VASE system (top view).

In our experiments, energy- and AOI- resolved SE is measured by a J. A. Woollam Co., Inc. VASE system in reflection mode. Figure 7.1 depicts the top

view of the system. Samples are placed vertically on the sample stage which can rotate around its center normal axis. The source arm of the system consists of a polarizer (FP, fixed polarizer) and a rotating compensator/retarder (RC) and the detector arm includes a rotating analyzer (RA). The spectra of each energy-dependent elements are measured ranging from 1.24 eV to 4.94 eV with the revolution at 0.1 eV. The detector arm is fixed while the source arm can rotate concentrically but independently of the sample stage, which enables the detector to collect light signals at variable angles of incidence (AOI) and variable angles of scattering (AOS). Therefore, this instrument is able to carry out various types of energy-dependent measurements:

- i. VASE: $AOS = AOI$, AOI varies, reflection mode;
- ii. Variable-angle Reflectance: $AOS = AOI$, AOI varies, reflection mode;
- iii. Scattering: for each AOI, AOS can change independently to detect scattering signals at each AOS, reflection mode.

In our experiments, variable-angle data was collected at the AOI of every 10° from 20° to 80° from normal. Scattering data was collected at a 1° interval. The incident beam spot size is 1 mm in radius which is much larger than the typical dimension of Ga NPs (~ 100 nm). Collective optical responses are measured from Ga NP ensembles to eliminate the effect of randomness.

7.1.2 Variable-angle reflection

VASE can also measure variable-angle reflectance. While the detector arm is fixed, the source arm can rotate concentrically and concurrently with the sample stage to ensure that the detector is collecting reflection light at specular reflection angle. With the polarizer in the source arm, the instrument can measure reflectance of p-polarized light (pR) and s-polarized light (sR) separately.

Figure 7.2 plots measured reflectance (pR and sR) for 3 samples (Y3, Y6, and Y7) at different AOIs. In general, one major reflectance peak is observed for both polarizations at most AOIs except for pR at large AOIs (70° and 80°). Also, except for pR at 70° and 80°, the absolute value of pR decreases and sR increases when AOI increases. The first trend is energy dependent while the second one is AOI dependent. We will discuss both in further detail below.

As discussed before, there are two types of Ga NP samples, one with unimodal size distribution (like Y3) and the other with bi-modal size distribution (like Y6 and Y7). The following discussion will explore the different optical responses from both types of samples. Let's first look at the simpler case Y3, which only shows the in-plane LSPR mode in the detectable photon range.

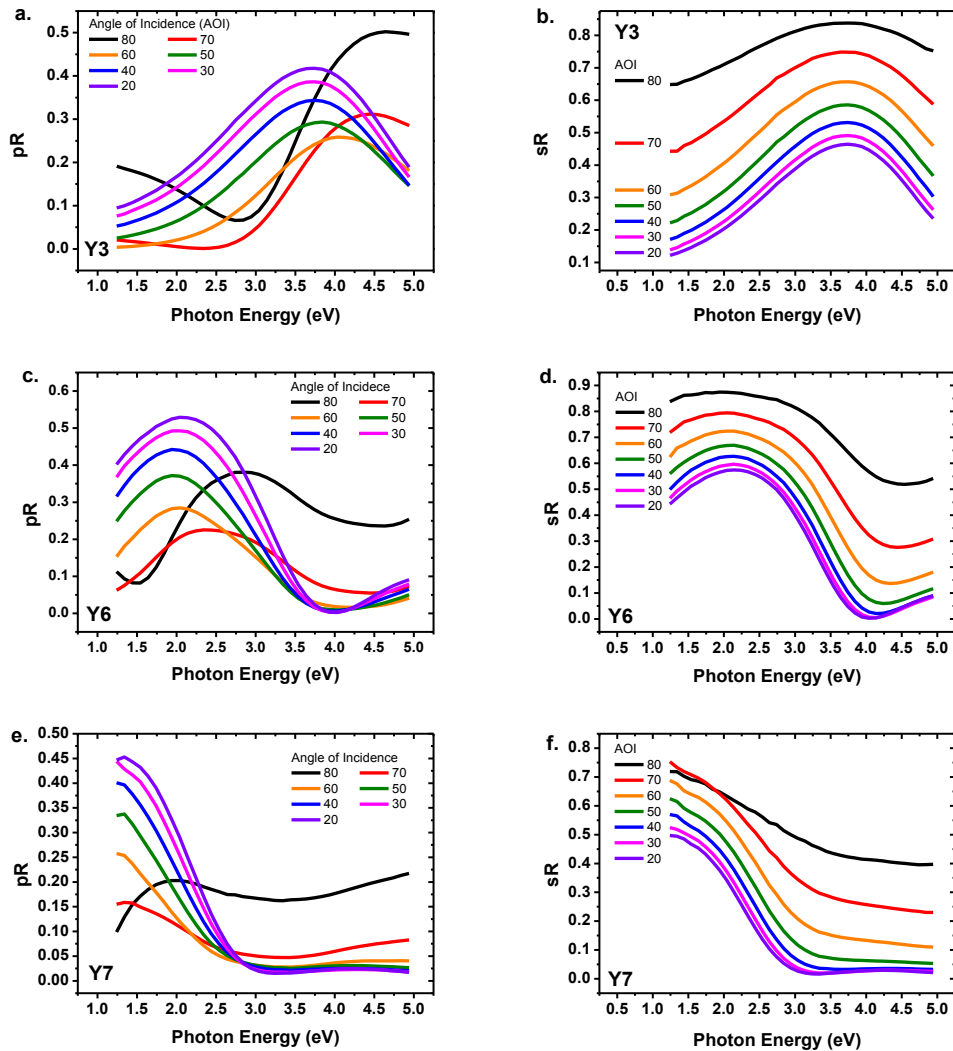


Figure 7.2: Measured reflectance of p-polarized (pR) and s-polarized (sR) light from samples Y3, Y6, and Y7.

First, let's explore the reflectance dependence on AOI. It is valuable to compare it with reflectance from a semi-infinite sapphire layer as its refractive index is not energy-dependent but a constant 1.8. Figure 7.3 plots pR and sR at the vacuum-sapphire interface calculated by the Fresnel equations. Clearly, sR increases monotonically with the increase in AOI; pR first decreases to zero when AOI

increases from 20° to 60° which is Brewster's angle at a vacuum-sapphire interface and then increases with the increase in AOI.

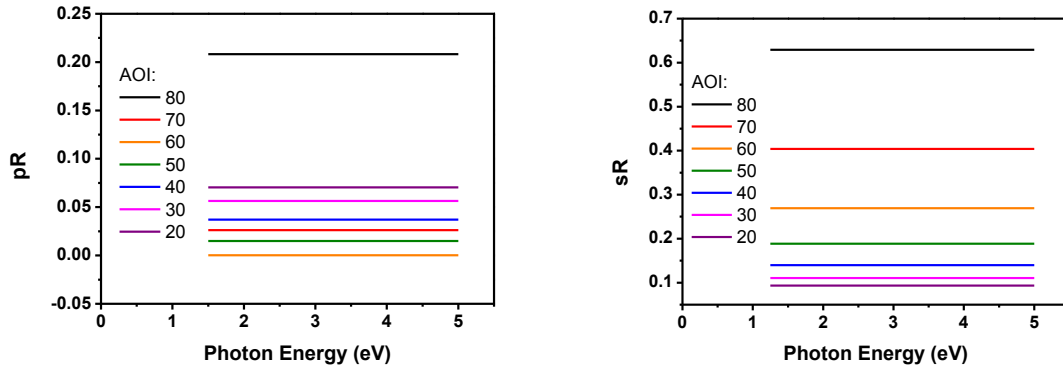


Figure 7.3: Calculated reflectance of p-polarized (pR) and s-polarized (sR) light from vacuum-sapphire interface.

Similar angle-dependent trends are observed from Ga NP ensembles (Figure 7.2), especially at lower photon energies where pR approaches zero at AOI of 70° . This is due to the low absorption (small extinction coefficient κ value) and high n value of the refractive index of the sample in this energy range. In Figure 7.2a, in the higher energy range, although pR is not close to zero, there exists a minimum at each photon energy. For example, the minimum of reflectance is between 70° and 80° for 3.5 eV, between 60° and 70° for 4.0 eV, and between 50° and 60° for 4.5 eV. These are pseudo Brewster's angles discussed in Section 3.2.2 which is similar to Brewster's angle. The reflectance reaches a minimum but not zero at pseudo Brewster's angle due to a nonzero extinction coefficient κ . In the photon

energy range above 3 eV, the pseudo Brewster's angle decreases with the increase in photon energy as the pR curves at lower AOIs keep crossing the curves at higher AOIs from left to right. This follows the monotonically decrease in n to the blue side of 3 eV as shown in the refractive index plot in Figure 6.7-Y3.

Second, let's examine the energy-dependent behaviors. The peaks in both reflectance curves are again associated with the peak in the refractive index n . At AOI of 70° and 80° , pR seems to behave off the trend, which is the entangled effect of reflection at pseudo Brewster's angle and peaks in refractive index. Similarly, the decrease in the relative peak heights in Figure 7.2b with the increase in AOI is also an overall effect of the absorption peaks in n and the simple reflectance dependence on AOI shown in Figure 7.3. Comparing reflectance curves among Y3, Y6, and Y7, the peaks redshift from Y3 to Y7 as their in-plane LSPR energies also redshift. (Chapter 6) This confirms again that the reflectance peaks are associated with the in-plane LSPR mode.

Since Ga NP samples were modeled by a two-layer structure, pR and sR can be directly calculated using multilayer reflection Equation 6.11. Figure 7.4 shows calculated and measured pR and sR for samples Y3 and Y6 side by side.

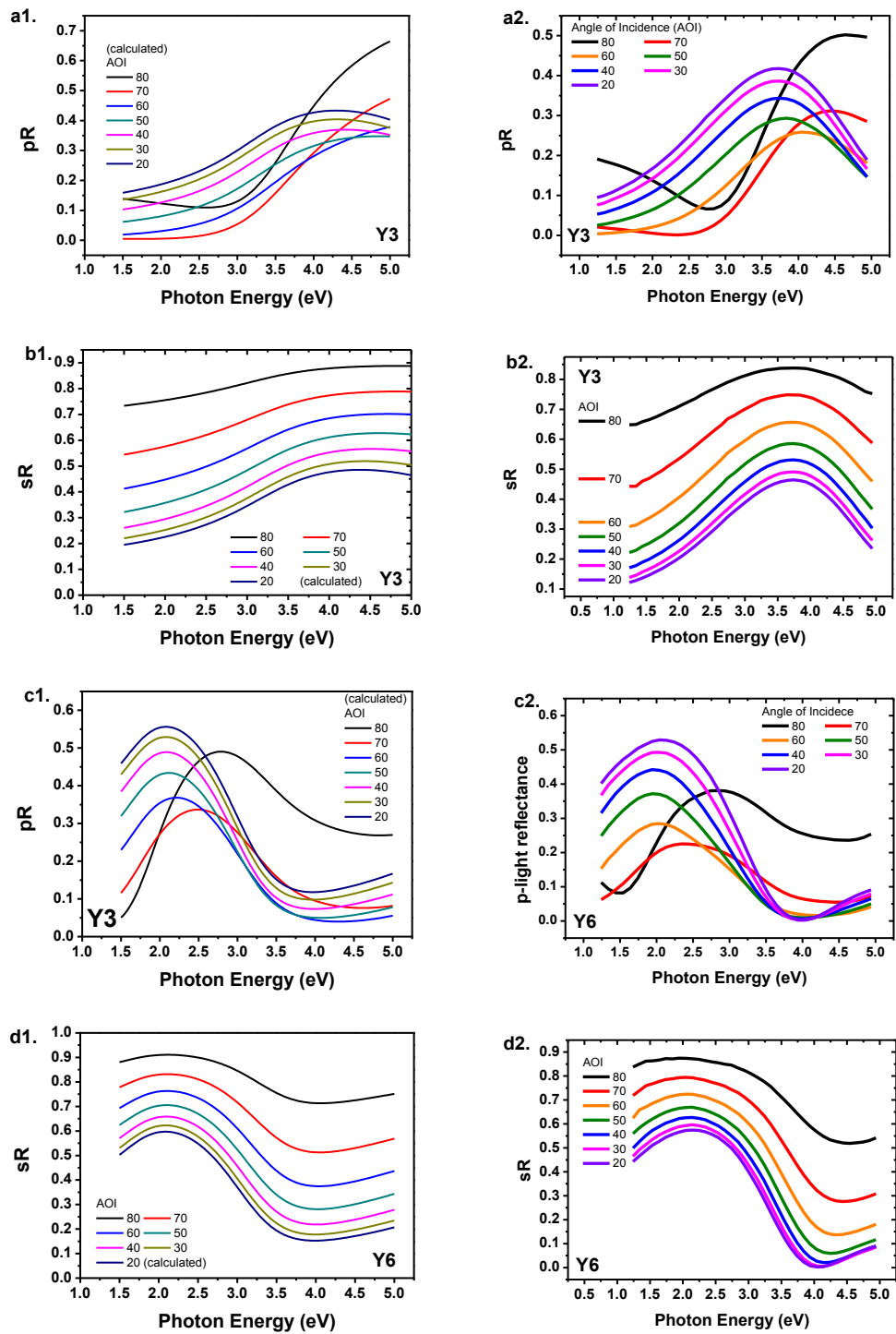


Figure 7.4: calculated (left) and measured (right) reflectance of p-polarized (pR) and s-polarized light (sR) for samples Y3 and Y6.

For Y3, the calculated curves agree with the measured ones very well. They reproduced all the features and trends as discussed above. This demonstrates that the two-layer mode we used to model NP dielectric function is accurate enough for the in-plane mode. The collective behavior of in-plane modes can be well described by their corresponding Lorentz oscillators. For Y6, the peaks around 2 eV in pR and all features in sR are reproduced as these peaks are again associated with the lower energy in-plane mode of Y6. The only feature that is not well demonstrated is in pR curve around 4 eV. In Figure 7.3c1, pR decreases while AOI decreases from 60° to 20°. However, the measured data shows that the absolute values of reflectance are all close to zero in this AOI range (Figure 7.3c2). There is a significant amount of decrease in reflection for p-polarized light at 4 eV. Most of the incident light is either absorbed or scattered away from the specular direction. A strong dispersion effect is expected at approximately 4.0 eV for sample Y6 with small AOI, which needs further exploration.

7.1.3 VASE measurement

VASE measurements were carried out for Y3 and Y6, which represent samples with unimodal and bimodal size distributions respectively. Figure 7.5a plots the pseudoextinction coefficient $\langle k \rangle$ curves calculated from VASE data for sample Y3. The red solid curve was measured at 70° using fixed angle SE in the MBE growth

chamber right after deposition while all the other curves were measured 1 year after deposition and the sample was stored in open air. The $\langle k \rangle$ peak redshifts from 3.58 eV to 3.50 eV. This shift is accounted by the oxidation at the Ga surface [76]. Compared to other metals, especially Au and Ag, this shift amount is nominal and the bell shape of the absorption peak is well maintained even after 1 year open-air storage. This confirms again Ga's good oxidation-resistance feature. The $\langle k \rangle$ curves from 20° to 70° almost overlaps with each other. This implies that the in-plane LSPR mode associated with this absorption peak is independent of AOI since the s-polarized light remains unchanged. The decrease in amplitude for the $\langle k \rangle$ curve at 80° is due to the grazing angle scattering which reduces the detectable strength of the reflected light.

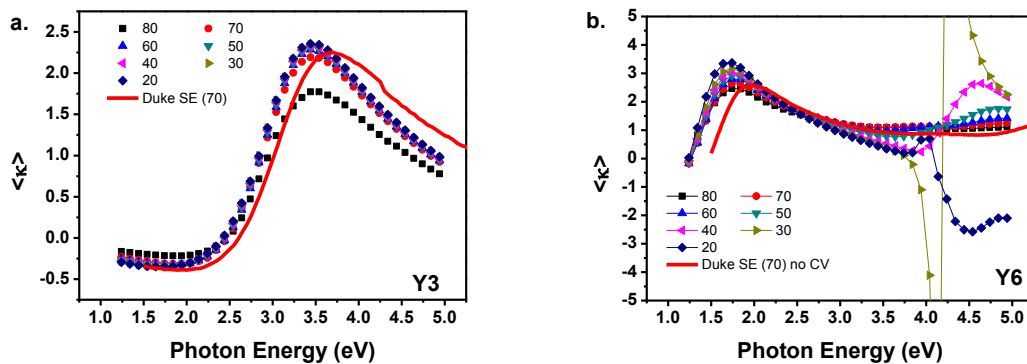


Figure 7.5: Angle-resolved pseudoextinction coefficient of samples (a) Y3 and (b) Y6 measured by VASE.

For sample Y6, which has a bimodal size distribution, Figure 7.5b plots its AOI resolved $\langle \kappa \rangle$. Note two observed features

- i. Peaks at 1.8 eV: The peaks are associated with the lower energy in-plane LSPR mode of Y6, which are similar to the peaks at 3.5 eV of Y3 in Figure 7.5a. As expected, the in-plane LSPR mode does not change with respect to AOI since s-polarized light remains invariant.
- ii. Features around 4.0 eV: The features are AOI-dependent. For larger AOIs the peak does not exist or is beyond the detection range. When AOI decreases, a peak appears and redshifts. Its intensity is enhanced initially and decreases when AOI decreases from 30° to 20° . We previously identified the high energy peak in $\langle \kappa \rangle$ curve as the out-of-plane LSPR mode which is excited by the p-component in the incident light. (Sections 2.2.4 and 6.2.3) The p-polarization can be decomposed into two orthogonal directions, the one parallel to the sample surface and the other one perpendicular to the surface. The first component will oscillate the same way as the in-plane mode and thus has the same LSPR energy (1.8 eV in this case). The second component will oscillate along the vertical dimension of the Ga NP and have a higher LSPR energy due to the hemispherical shape of our Ga NPs. As AOI keeps decreasing, the vertical

component shall be reduced and therefore the high-energy peak in $\langle\kappa\rangle$ curve will decrease but remain at the same photon energy. However, this is not observed in Figure 7.5b. The single particle behavior discussed in Section 6.2 is no longer precise enough to explain this feature. This anomalous feature comes from the collective behavior of the Ga NP ensembles which might include the integrated interaction between large NPs and the surrounding small NPs. A strong dispersion effect occurs around 4 eV which is consistent with the measured pR curve (Figure 7.2c).

In order to examine this dispersion effect, a scattering profile was measured for Y6 at AOI = 40°. While the source arm and the sample stage are fixed, the detect arm can rotate around the sample stage collecting scattered light from the sample at variable angles. Figure 7.6 plots scattered light from -40° to 60° with respect to the specular reflection angle. The z axis measures the relative scattered light intensity in terms of the incident light which is p-polarized. Strong off-specular scattering occurs at 4.5 eV, which is consistent with the peak position of the $\langle\kappa\rangle$ curve at AOI = 40° (pink curve) shown in Figure 7.5b. Figure 7.7 compares the scattering spectra at two photon energies 2.54 eV and 4.54 eV. The scattered light intensity around 30° at 4.54 eV is about one third of that at the specular angle, which is significant.

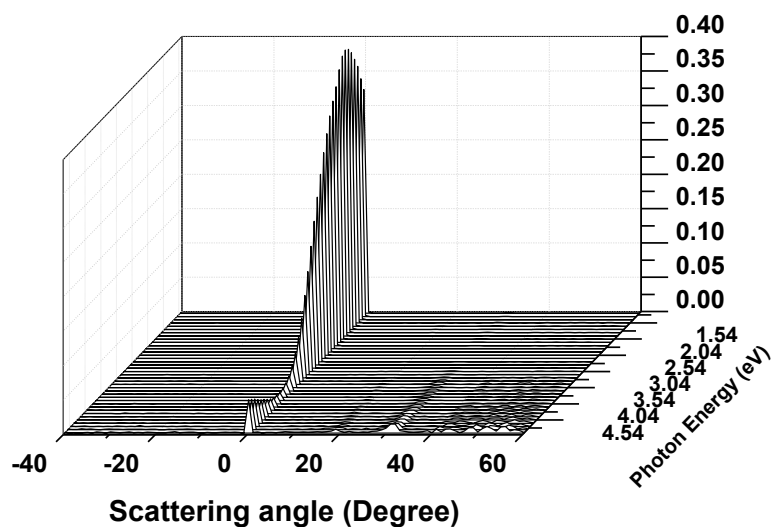


Figure 7.6: Energy-dependent scattering profile of sample Y6 at AOI = 40°.

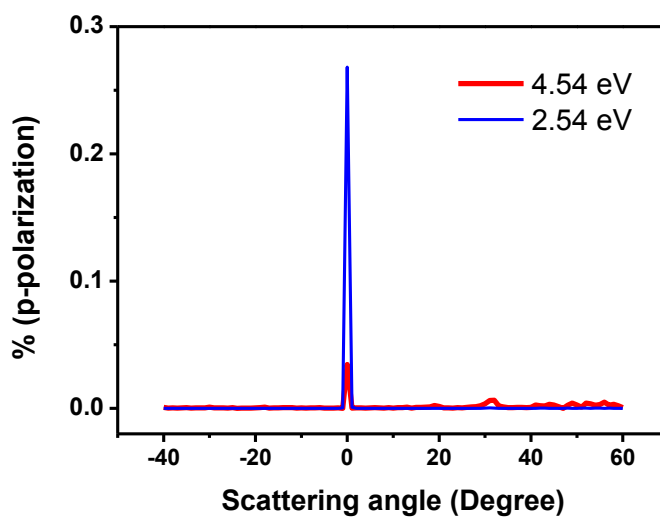


Figure 7.7: Scattering spectra at 2.54 eV and 4.54 eV of sample Y6.

Figure 7.5 plots pseudoextinction coefficient $\langle k \rangle$ curves but not fitted ones as discussed in Chapter 6 because the dispersion around 4 eV can no longer be fitted with a simple Lorentz model. Recall that Y6 possess a bimodal size

distribution. Large NPs are surrounded by small NPs very closely packed. Figure 7.8 depicts a unit cell of this configuration: a pair of asymmetrical NPs. Assuming light is incident from the left, there exists a critical incident angle θ_c above which large NPs will prevent surrounding small NPs from directly interacting with the incident light.

$$\cos\theta_c = \frac{R-r}{R+r+d} \quad (7.1)$$

where R and r are the radii of the large and small NPs respectively, and d is the edge-to-edge interparticle distance.

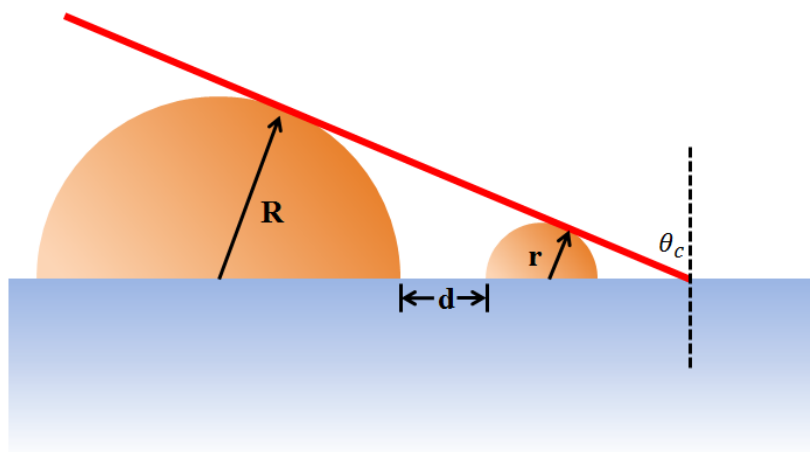


Figure 7.8: Schematic diagram of shadowing effect.

The spatial information of Y6 (Table 5.1) is used to estimate θ_c for Y6: $R = 70$ nm, $r = 15$, and $d = 13$. Given Equation 7.1, $\theta_c = 56^\circ$. When AOI is larger than 56° , excitation light cannot be directly incident on the smaller NP due to the shadowing effect of the larger NP as gallium is certainly not transparent in this

photon range (1.5 eV to 6 eV). Especially at LSPR energy, light will be mostly absorbed by the larger NP and the smaller NP cannot be excited. Recall that the single-particle behavior of LSPR mode discussed in Chapter 6 was measured at grazing angle, e.g. 70° , which is larger than $\theta_c = 56^\circ$. Therefore, single-particle model was valid there but failed when it was used to predict variable-angle behaviors as discussed above. Strong interparticle coupling and collective optical effects cannot be revealed by 70° fixed angle SE. This is one of the key reasons that variable-angle measurement is necessary.

While shadowing effect may explain the difference between optical responses measured by grazing angle and near normal incident light, the origin of the strong dispersion and off-specular scattering at near normal incidence, which are from collective responses of Ga NP ensembles, still needs further exploration (Chapter 10). Both SE and VASE measure only two variables (Ψ, Δ) from samples. In order to obtain more optical information, more independent variables are needed. The next section will introduce Mueller matrix polarimetry.

7.2 Variable-angle Mueller matrix (VAMM)

7.2.1 Stokes vector and Mueller matrix

Let's start with a brief introduction to the basic concepts used in Mueller matrix polarimetry. In Section 3.1.2, the Jones vector was introduced to represent light. However, it cannot completely describe all the states of polarization (SoP) (total, partial and un-polarized light). In 1952, G. G. Stokes suggested the use of a set of 4 quantities to describe all the SoP, which later became Stokes vector [184]:

$$\mathbf{s} = \begin{pmatrix} S_0 \\ S_1 \\ S_2 \\ S_3 \end{pmatrix} = \begin{pmatrix} I \\ pI \cos 2\psi \cos 2\chi \\ pI \sin 2\psi \cos 2\chi \\ pI \sin 2\chi \end{pmatrix} \quad (7.2)$$

where I is the total intensity, p is the degree of polarization defined in Equation 3.5, ψ is the orientation angle, and χ is the ellipticity angle of the polarization ellipse shown in Figure 3.1. The four Stokes parameters satisfy,

$$(pS_0)^2 = S_1^2 + S_2^2 + S_3^2 \quad (7.3)$$

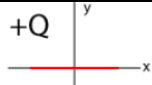
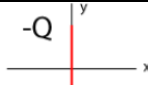

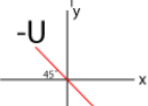
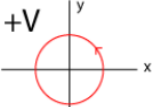
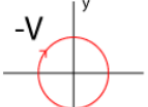
In the simplest case, a plane wave that propagates in $+z$ can be expressed as,

$$\mathbf{s} = \begin{pmatrix} S_0 \\ S_1 \\ S_2 \\ S_3 \end{pmatrix} \equiv \begin{pmatrix} I \\ Q \\ U \\ V \end{pmatrix} = \begin{pmatrix} \langle E_x E_x^* + E_y E_y^* \rangle \\ \langle E_x E_x^* - E_y E_y^* \rangle \\ \langle E_x E_y^* + E_y E_x^* \rangle \\ \langle i(E_x E_y^* - E_y E_x^*) \rangle \end{pmatrix} = \begin{pmatrix} I \\ I_x - I_y \\ I_{45} - I_{-45} \\ I_{\text{right}} - I_{\text{left}} \end{pmatrix} \quad (7.4)$$

The operator $\langle \dots \rangle$ denotes a time average. Each Stokes parameter corresponds to an intensity difference between a pair of states of polarization. S_0 is the total

intensity. S_1 is the intensity difference between the horizontal (x-) and vertical (y-) linear polarized components. S_2 represents the intensity difference between 45° and -45° (or 135°) degree linear components. And, S_3 is the intensity difference between right and left circularly polarized components. For the sake of comparability, Stokes vector are usually normalized with the total intensity I . Therefore, $S_0 = 1$ and S_1, S_2, S_3 are all real numbers and valued between -1 and 1.

Table 7.1: Jones vector and Stokes vector representations of states of polarization.

SoP	Jones vector	Stokes vector	SoP	Jones vector	Stokes vector
+Q 	$\begin{pmatrix} 1 \\ 0 \end{pmatrix}$	$\begin{pmatrix} 1 \\ 1 \\ 0 \\ 0 \end{pmatrix}$	-Q 	$\begin{pmatrix} 0 \\ 1 \end{pmatrix}$	$\begin{pmatrix} 1 \\ -1 \\ 0 \\ 0 \end{pmatrix}$
+U 	$\frac{1}{\sqrt{2}} \begin{pmatrix} 1 \\ 1 \end{pmatrix}$	$\begin{pmatrix} 1 \\ 0 \\ 1 \\ 0 \end{pmatrix}$	-U 	$\frac{1}{\sqrt{2}} \begin{pmatrix} 1 \\ -1 \end{pmatrix}$	$\begin{pmatrix} 1 \\ 0 \\ 0 \\ -1 \end{pmatrix}$
+V 	$\frac{1}{\sqrt{2}} \begin{pmatrix} 1 \\ i \end{pmatrix}$	$\begin{pmatrix} 1 \\ 0 \\ 0 \\ 1 \end{pmatrix}$	-V 	$\frac{1}{\sqrt{2}} \begin{pmatrix} 1 \\ -i \end{pmatrix}$	$\begin{pmatrix} 1 \\ 0 \\ 0 \\ -1 \end{pmatrix}$

Jones vectors and Stokes vectors can both be used to represent SoP. However, they are different in the following ways:

- i. The elements of the Jones vectors are complex numbers while those of Stokes vectors are all real. Jones vectors explicitly include both amplitude and phase information while Stokes vectors measures relative intensities.

- ii. Each Jones vector can be converted into a unique corresponding Stokes vector, (Table 7.1) but not vice versa. Jones vector and Stokes vector function the same for totally polarized light while Stokes vector can also be used to describe partially polarized and unpolarized light. For unpolarized light, $\mathbf{S} = (1,0,0,0)^T$.

Similarly to the Jones matrix, when incident and outgoing light are represented by their Stokes vectors \mathbf{S}_i and \mathbf{S}_o respectively, the manipulation between them is a 4×4 matrix:

$$\mathbf{S}_o = \mathbf{M}\mathbf{S}_i \quad (7.5)$$

where \mathbf{M} is called Mueller matrix (MM). It was first introduced by H. Mueller in 1943 [61]. It contains the complete light-matter interaction information of an object. A MM measurement has been widely used to study various types of optical media, such as layered thin films, inorganic, organic and bio- molecules, radiation systems, and metamaterials [185-189]. A MM has the form

$$\mathbf{M} = \begin{bmatrix} m_{11} & m_{12} & m_{13} & m_{14} \\ m_{21} & m_{22} & m_{23} & m_{24} \\ m_{31} & m_{32} & m_{33} & m_{34} \\ m_{41} & m_{42} & m_{43} & m_{44} \end{bmatrix} \quad (7.6)$$

Unlike the Jones matrix, all the elements in a MM are real numbers. In practice, MM is often normalized with m_{11} so that $m_{11} = 1$ and all other 15 elements are valued between -1 and 1.

Table 7.2: Mueller matrix representation of basic optical elements.

name	Mueller Matrix	Effect
horizontal linear polarizer	$\begin{bmatrix} 1 & 1 & 0 & 0 \\ 1 & 1 & 0 & 0 \\ 0 & 0 & 0 & 0 \\ 0 & 0 & 0 & 0 \end{bmatrix}$	Convert to horizontal linearly polarized light
vertical linear polarizer	$\begin{bmatrix} 1 & -1 & 0 & 0 \\ -1 & 1 & 0 & 0 \\ 0 & 0 & 0 & 0 \\ 0 & 0 & 0 & 0 \end{bmatrix}$	Convert to vertical linearly polarized light
ϕ degree retarder	$\begin{bmatrix} 1 & 0 & 0 & 0 \\ 0 & 1 & 0 & 0 \\ 0 & 0 & \cos\phi & \sin\phi \\ 0 & 0 & -\sin\phi & \cos\phi \end{bmatrix}$	$\begin{cases} E'_x = E_x e^{i\phi/2} \\ E'_y = E_y e^{-i\phi/2} \end{cases}$
quarter-wave retarder $\phi = 90^\circ$	$\begin{bmatrix} 1 & 0 & 0 & 0 \\ 0 & 1 & 0 & 0 \\ 0 & 0 & 0 & 1 \\ 0 & 0 & -1 & 0 \end{bmatrix}$	Convert between $\pm 45^\circ$ linearly polarized light to right/left circularly polarized light
half-wave retarder $\phi = 180^\circ$	$\begin{bmatrix} 1 & 0 & 0 & 0 \\ 0 & 1 & 0 & 0 \\ 0 & 0 & -1 & 0 \\ 0 & 0 & 0 & -1 \end{bmatrix}$	reverse ellipticity and orientation of the polarization ellipse
α degree Rotator	$\begin{bmatrix} 1 & 0 & 0 & 0 \\ 0 & \cos 2\alpha & \sin 2\alpha & 0 \\ 0 & -\sin 2\alpha & \cos 2\alpha & 0 \\ 0 & 0 & 0 & 1 \end{bmatrix}$	Rotate the major and minor axes simultaneously
perfect depolarizer	$\begin{bmatrix} 1 & 0 & 0 & 0 \\ 0 & 0 & 0 & 0 \\ 0 & 0 & 0 & 0 \\ 0 & 0 & 0 & 0 \end{bmatrix}$	Transform to unpolarized light
partial depolarizer	$\begin{bmatrix} 1 & 0 & 0 & 0 \\ 0 & a & 0 & 0 \\ 0 & 0 & b & 0 \\ 0 & 0 & 0 & c \end{bmatrix}$	$a, b, c < 1$; Transform to partial polarized light

Mueller matrix \mathbf{M} can be used to characterize the overall effect of an optical element as simple as a linear polarizer or as complex as the NP ensemble we are exploring. Table 7.2 generalizes Mueller matrices for some basic optical elements which can manipulate the SoP of light with two orthogonal polarizations:

- i. Diattenuator (polarizer): changes the amplitudes of both components
- ii. Retarder (Compensator): introduces phase shift between components
- iii. Rotator: rotates both orthogonal components
- iv. Depolarizer: reduces the degree of polarization

7.2.2 Mueller matrix representation of reflection

Similar to Equation 3.11 where the Fresnel equations are expressed in terms of the Jones vector and matrix, the analytical form of \mathbf{M} can also be derived to represent the Fresnel equations using the definition of the Stokes vector and the Mueller matrix. Many textbooks give the complete derivation [134]. At the interface of vacuum ($n_i = 1$) and a semi-infinite dielectric plate (refractive index \tilde{n}), the Mueller matrix representing the reflection is,

$$\mathbf{M} = \begin{bmatrix} 1 & \frac{\cos^2\theta_- - \cos^2\theta_+}{\cos^2\theta_- + \cos^2\theta_+} & 0 & 0 \\ \frac{\cos^2\theta_- - \cos^2\theta_+}{\cos^2\theta_- + \cos^2\theta_+} & 1 & 0 & 0 \\ 0 & 0 & -\frac{2\cos\theta_+\cos\theta_-}{\cos^2\theta_- + \cos^2\theta_+} & 0 \\ 0 & 0 & 0 & -\frac{2\cos\theta_+\cos\theta_-}{\cos^2\theta_- + \cos^2\theta_+} \end{bmatrix} \quad (7.7a)$$

where,

$$\theta_{\pm} = \theta_i \pm \theta_r \quad (7.7b)$$

θ_i and θ_r are angle of incidence and refraction respectively. In this case, there are only 2 pairs of nontrivial elements. Figure 7.9 plots m_{12} and m_{33} for the reflection

at vacuum-sapphire interface with different angles of incidence. The refractive index of bulk sapphire (Figure 4.3) was used to calculate θ_r in Equation 7.7 by Snell's Law. Two observations are worthy of note:

- i. $m_{12} = 1$ when $\theta_i = 60^\circ$. $m_{12} = 1$ indicates that the sample is acting as a linear polarizer. Recall that Brewster's angle $\theta_B \sim 60^\circ$ for sapphire. When incident light is reflected at Brewster's angle, outgoing light only has s-polarization.
- ii. For normal incidence, $\theta_i = 0^\circ$, $m_{33} = -1$. Based on Table 8.2, a phase difference of 180° will be generated between two polarizations when $m_{33} = -1$. While for normal incidence, it means s-polarized light will possess a 180° phase shift. This is the expected half wave loss for reflection.

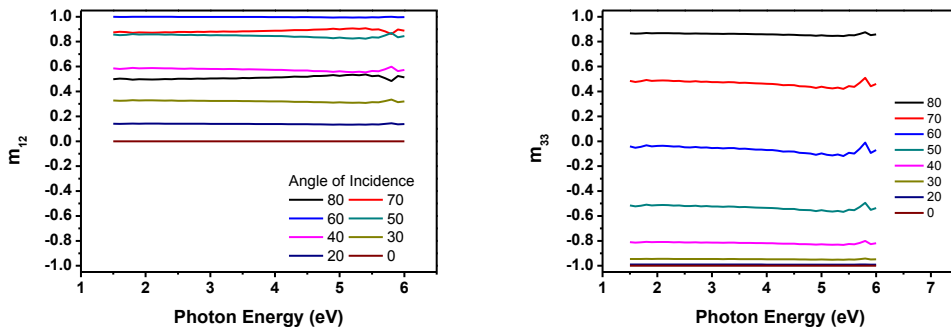


Figure 7.9: Calculated Mueller matrix elements (a) m_{12} and (b) m_{33} of the reflection at vacuum-sapphire interface at different AOIs.

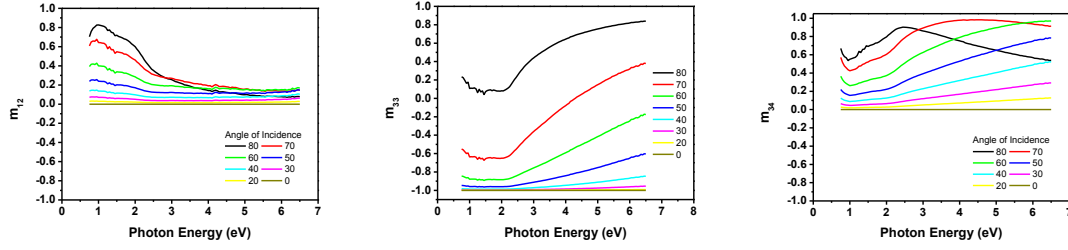


Figure 7.10: Calculated Mueller matrix elements (a) m_{12} , (b) m_{33} , and (c) m_{34} of the reflection at vacuum-Gallium interface at different AOIs.

For a semi-infinite metallic plate, the Mueller matrix is different from Equation 7.7. At the vacuum-metal interface, the Mueller matrix for reflection is,

$$\mathbf{M} = \begin{bmatrix} 1 & \frac{\rho_s^2 - \rho_p^2}{\rho_s^2 + \rho_p^2} & 0 & 0 \\ \frac{\rho_s^2 - \rho_p^2}{\rho_s^2 + \rho_p^2} & 1 & 0 & 0 \\ 0 & 0 & \frac{2\rho_s\rho_p\cos\Delta}{\rho_s^2 + \rho_p^2} & \frac{2\rho_s\rho_p\sin\Delta}{\rho_s^2 + \rho_p^2} \\ 0 & 0 & -\frac{2\rho_s\rho_p\sin\Delta}{\rho_s^2 + \rho_p^2} & \frac{2\rho_s\rho_p\cos\Delta}{\rho_s^2 + \rho_p^2} \end{bmatrix} \quad (7.8a)$$

where ρ_s and ρ_p are the amplitudes of the reflection ratios for s- and p- polarized light. And $\Delta = \varphi_s - \varphi_p$.

$$\begin{cases} r_s = -\frac{\sin(\theta_i - \theta_r)}{\sin(\theta_i + \theta_r)} \equiv \rho_s \tan\varphi_s \\ r_p = \frac{\tan(\theta_i - \theta_r)}{\tan(\theta_i + \theta_r)} \equiv \rho_p \tan\varphi_p \end{cases} \quad (7.8b)$$

r_s and r_p can be calculated from the Fresnel equations. There are three pairs of nontrivial MM elements. Figure 7.10 plots m_{12} , m_{33} , and m_{34} for the reflection at the interface of vacuum and semi-infinite Ga film which satisfies the assumptions of the Fresnel equations. Let's summarize some observations:

- i. There does not exist an AOI at which $m_{12} = 1$. This is consistent with the previous discussion about pseudo Brewster's angle minima.
- ii. m_{34} becomes non zero due to the imaginary part in the complex refractive index of metal. The large value of m_{34} implies a significant retardance effect [190-191].

The differences between MM for isotropic and semi-infinite dielectric and metallic plates are from the imaginary part of the refractive index. Since material absorption majorly impacts in-plane vibrations (s-polarization), larger phase shifts are induced between s- and p- polarized light, especially at large AOIs where the difference between s- and p- components is significant.

7.2.3 Mueller matrix polarimetry

Mueller matrix polarimeter is used to measure part of or the entire 16 MM elements. Figure 7.11 shows the schematic diagram of a MM polarimeter consisting of a polarization state generator (PSG) on the source/input side and a polarization state analyzer (PSA) on the detect/output side.

In our experiments, energy- and incidence angle- dependent MM are measured by a J. A. Woollam Co., Inc. VASE system in reflection mode, the same as for the VASE measurement in Section 7.1. The PSG of the system consists of a polarizer

(FP, fixed polarizer) and a rotating compensator/retarder (RC) on the source arm and its PSA includes a rotating analyzer (RA) on the detector arm. Given the configuration (FPRC/RA) of this particular polarimeter, the first 3 rows of the MM can be measured [134], which are determined by the Fourier coefficients of the total intensity detected in terms of azimuth angle of the rotating analyzer. All measured elements are normalized to m_{11} . The spectra of each energy-dependent elements are measured ranging from 1.24 eV to 4.94 eV with the revolution at 0.1 eV. The detector arm is fixed while the source arm can rotate concentrically with the sample stage.

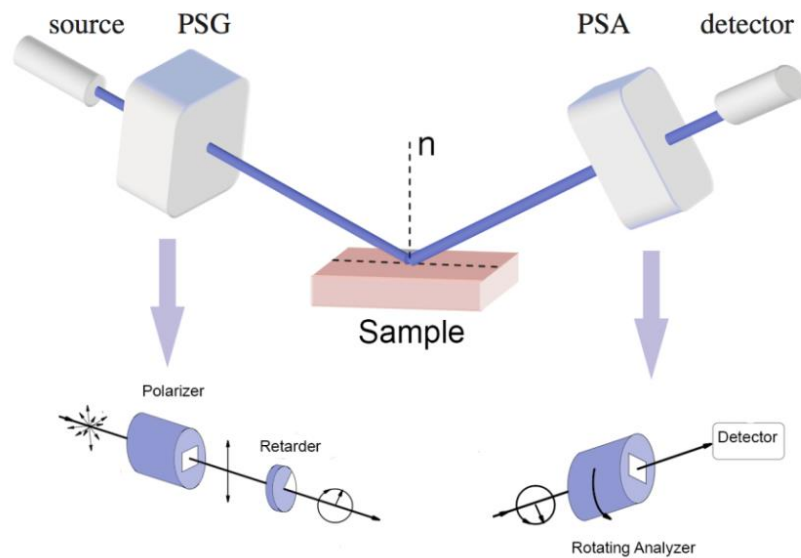


Figure 7.11: Schematic diagram of the in-house Mueller matrix polarimeter.

7.2.4 VAMM measurement

Again, two typical samples are examined by VAMM, Y3 and Y6 which have unimodal and bimodal size distributions respectively. Figure 7.12 plots measured first three rows of the Mueller matrix for sample Y3. Some general behaviors include:

- i. The off-diagonal elements, $m_{13}, m_{14}, m_{23}, m_{24}, m_{31}, m_{32}$, for Y3 are almost zero (within 1% error, insets in Figure 7.12) throughout the entire photon energy region. This is an indication of almost none depolarization effect which can also be justified from the fact that $m_{22} = 1$.
- ii. $m_{12} = m_{21}$ due to the in-plane symmetry, which again confirms the in-plane randomness of the Ga NP ensembles.

Now, let's explore the nontrivial elements m_{12} , m_{33} and m_{34} . As discussed previously, m_{12} represents the linear polarization effect of the sample. The degree of polarization of the outgoing light will increase if m_{12} moves away from zero. m_{12} is related to the reflectance ratio of p- and s- polarized light. Especially at Brewster's angle, the reflected light will only have s-polarization and $m_{12} = 1$. In Figure 7.12, m_{12} approaches 1 at lower energy at approximately 70° . This is consistent with the observation in the reflectance curves in Figure 7.2. While at a higher energy range, m_{12} is no longer zero due to the nonzero value of κ in the

refractive index since the outgoing light can no longer be totally linearly s-polarized. As discussed above, reflectance for both p- and s-polarization light (pR and sR) will form a peak around the same photon energy as the peak in sample's refractive index. However, due to the initial large value in sR, the increase in pR is larger than that in sR. This will increase the relative ratio of the p-component over the s-component in reflected light and thus m_{12} will move away from 1. Therefore, a concave dip is observed around the absorption peak energy (3.5 eV ~ 4.0 eV) in m_{12} for each AOI. The off-trend behavior at 70° and 80° are from the overall effect of the sample's absorption peak and pseudo Brewster's angle minima, which is consistent with the pR plots in Figure 7.2c.

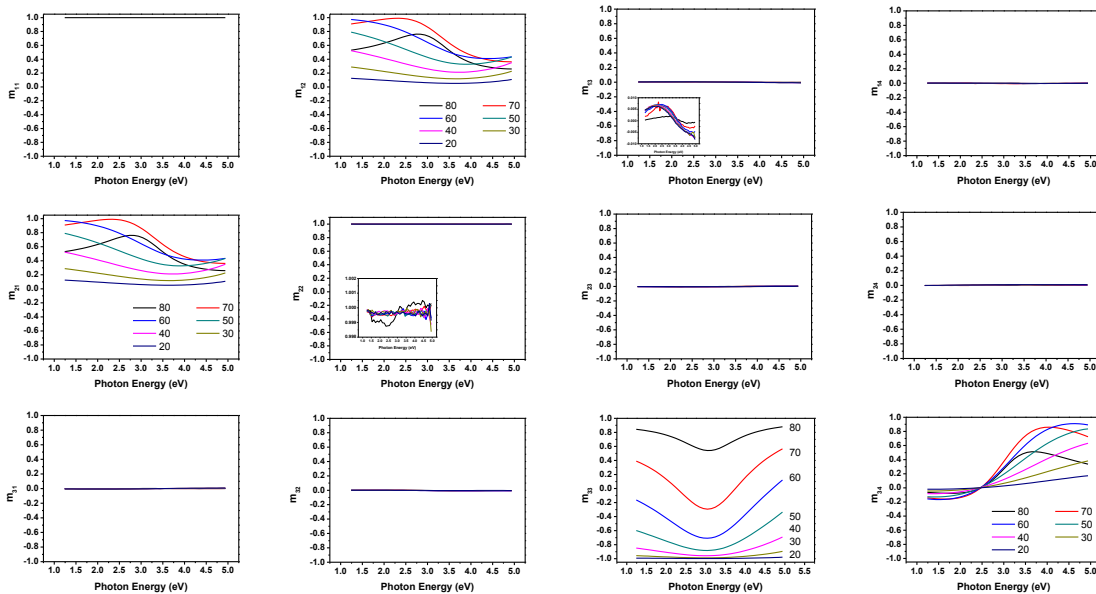


Figure 7.12: VAMM measured Mueller matrix elements $m_{11} \sim m_{34}$ of sample Y3.

m_{33} describes the phase difference between p- and s- polarizations in terms of 180° . For a constant refractive index, m_{33} will be a flat horizontal line and approach -1 as AOI decrease. At normal incidence, $m_{33} = -1$, which accounts for the half wave loss. In Figure 7.12, m_{33} follows the above trends in principle while it is altered by a dip around 3.0 eV to 3.5 eV. This dip is formed because of the sample absorption peak in the refractive index. m_{34} represents a similar phase difference but in terms of 90° .

Although the fourth row of the MM is not measured due to the instrument restriction, it can be inferred from the first three rows. Comparing Figure 7.12 with Equation 7.8a, zero values in off-diagonal elements indicate that Equation 7.8a is good enough to characterize the optical properties of Y3 where only 3 MM elements are nontrivial. Therefore, $m_{41} = m_{42} = 0$, $m_{43} = -m_{34}$, and $m_{44} = m_{33}$.

With fitted refractive index as obtained in Section 6.2, Mueller matrix elements can be calculated using Equation 7.8. Figure 7.13 compares calculated nontrivial MM elements and measured ones for Y3. Major features are well reproduced. This agreement suggests that scattering profiles measured from Ga NP ensembles with unimodal size distribution may be understood as a response of free electrons within non-interacting nanoparticles responding to the incident

EM field and scattering at the surface in a manner affected by nanoparticle geometry, the substrate, and surface adsorbates and oxides. It again confirms the validity of the effective medium model and single-particle behaviors for samples like Y3 as discussed in Chapter 6.

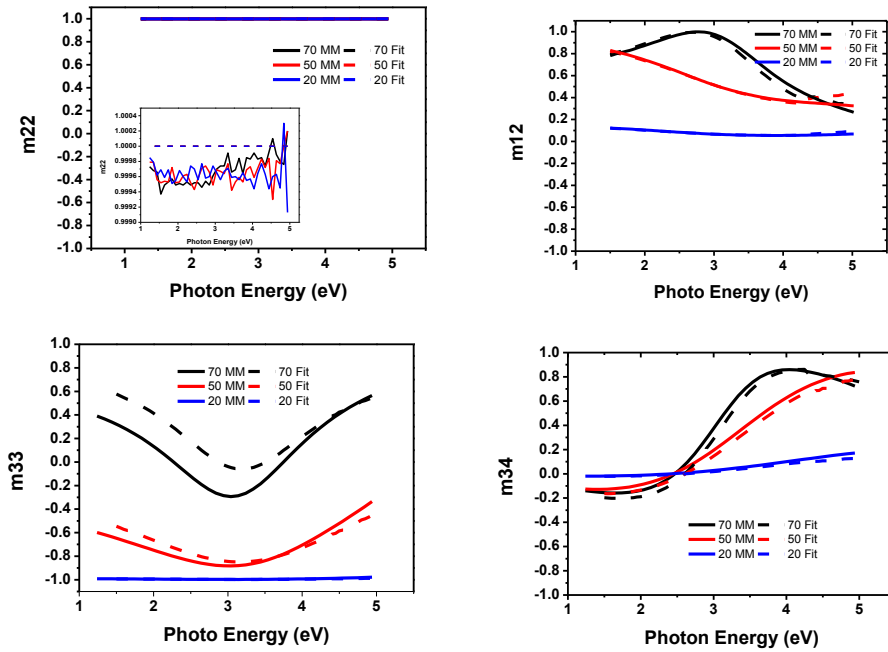


Figure 7.13: Predicted (dashed) and measured (solid) Mueller matrix elements m_{22} , m_{12} , m_{33} , and m_{34} of sample Y3.

Sample Y6, which has bimodal size distribution, is examined in the same way. VASE suggests that strong dispersion effects are expected at approximately 4.0 eV for this sample at small AOIs. This is confirmed by the Mueller matrix data shown in Figure 7.14. The off-diagonal elements, m_{13} , m_{14} , m_{23} , m_{24} , m_{31} , m_{32} , for Y6 are no longer zero at approximately 4.0 eV for small AOIs. The amplitudes of

these elements are great than 5% of 1, which is of great significance. Also, $m_{22} \neq 1$. Both suggest a depolarization effect from the sample.

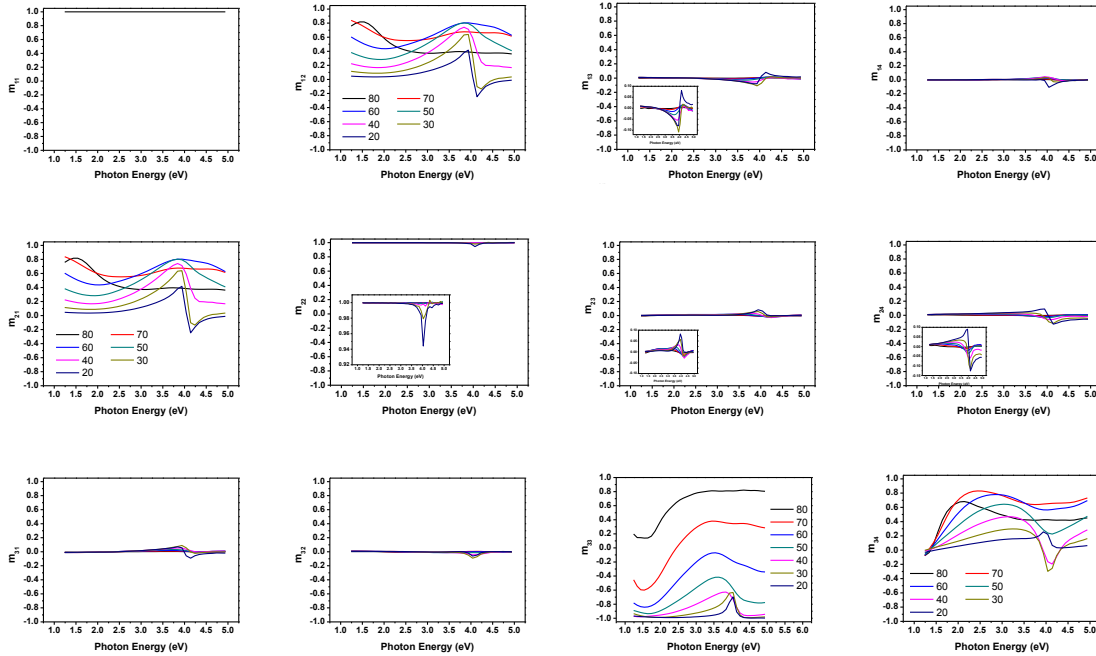


Figure 7.14: VAMM measured Mueller matrix elements $m_{11} \sim m_{34}$ of sample Y6.

Most features of m_{12} , m_{33} , m_{34} are expected following the discussion for sample Y3 above. The convex peaks in m_{12} and m_{34} and the concave dips in m_{33} are associated with the lower energy absorption peak in Y6's refractive index around 1.5 eV ~ 2.5 eV which accounts for the in-plane LSPR mode. Unexpected features are observed at 4.0 eV for small AOIs including the dips in m_{22} , nonzero values in off-diagonal elements, dispersive peaks in m_{12} and m_{21} , and peaks in m_{33} . They occur at the photon energy where strong dispersion effect and off-specular

scattering was observed in variable-angle reflectance and VASE measurements. The observed anomalous features are consistent among all variable-angle measurements.

Figure 7.15 compares calculated (dashed) and measured (solid) nontrivial MM elements for Y6. Similar to Y3, dashed lines are calculated by Equation 7.8 using the fitted refractive index plotted in Figure 6.7-Y6. Features are well reproduced at large AOIs for all three elements. But for AOI = 20° curves, the calculated MM elements cannot reproduce the measured features around 4.0 eV.

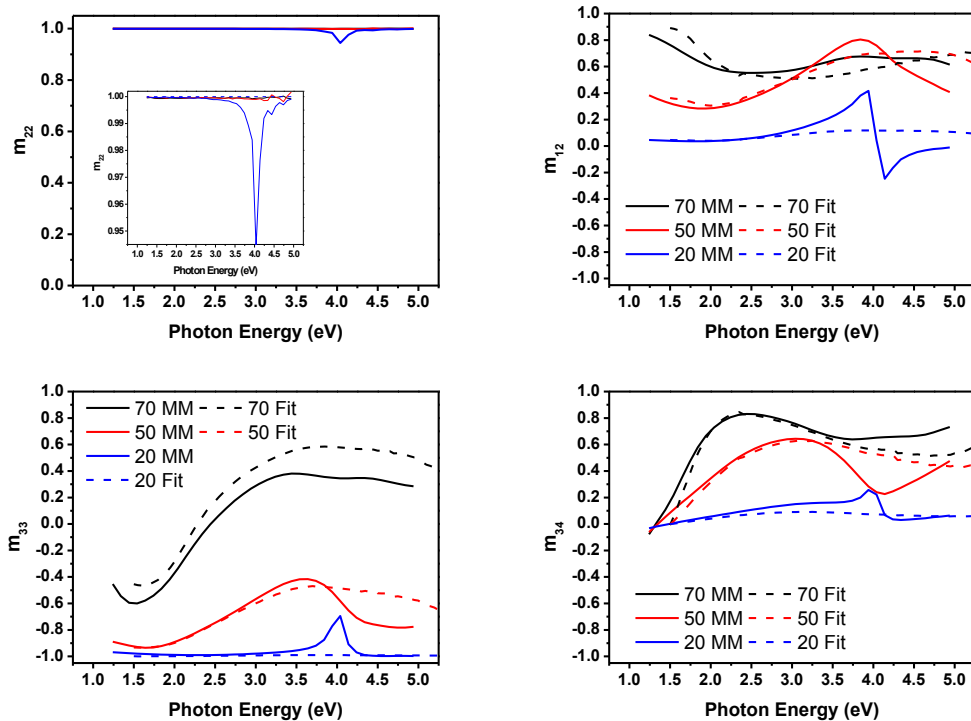


Figure 7.15: Predicted (dashed) and measured (solid) Mueller matrix elements m_{22} , m_{12} , m_{33} , and m_{34} of sample Y6.

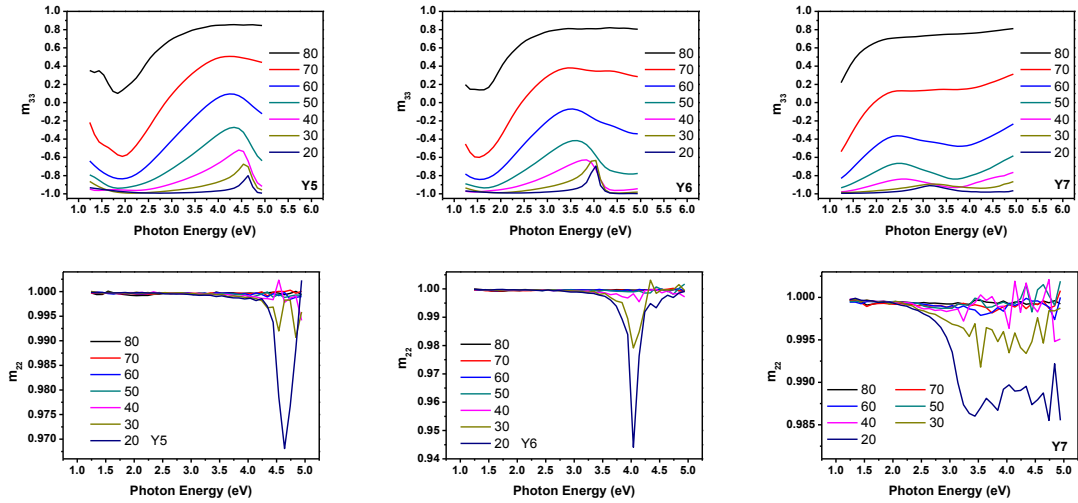


Figure 7.16: VAMM measured Mueller matrix elements m_{22} and m_{33} of samples Y5, Y6, and Y7.

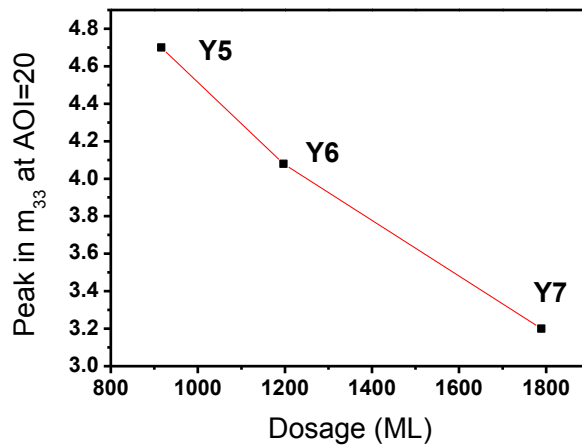


Figure 7.17: Peak energy in m_{33} at $\text{AOI} = 20^\circ$ for samples Y5, Y6, and Y7.

In order to further explore this unpredicted feature, samples Y5 and Y7 are measured by VAMM as well. Similar features are observed from both samples.

Figure 7.16 plots their m_{22} and m_{33} elements along with Y6. Figure 7.17 plots the

peak energy position of this feature (extracted from the peaks in m_{33} at AOI = 20°) versus dosage for the three samples. The peak energy of this feature is inversely related to dosage, which implies that this is a NP size related feature. Figure 7.16 compares peaks in m_{33} and m_{22} . m_{22} has a non-unit value ($m_{22} \neq 1$) at the same photon energy where these unpredicted features appear. Recall Table 7.2. $m_{22} < 1$ indicates a strong depolarization effect.

The origins of the depolarization effect are various. Common causes include large surface roughness, film thickness inhomogeneity, backside reflection from a weakly absorbing substrate [172], and plasmon resonance of nanostructures [183]. Preliminary modeling and experiments attempt to reveal the origin of this depolarization for our samples will be discussed in Chapter 10 as our future work. At this stage, we conclude that it is a collective effect from NP ensembles with asymmetrical size distributions.

In the last three chapters, we characterized both spatial and optical properties of our Ga NP samples. In the next Chapter, SERS measurements are performed on these samples to demonstrate that Ga nanostructures are great candidate for UV plasmonic applications and also to correlate SERS performance with samples' spatial and optical properties.

8. UV SERS and UV SEF: A Demonstration

Surface-enhanced Raman spectroscopy (SERS) uses the surface-enhanced Raman scattering (SERS) effect to obtain enhanced Raman scattering signals for molecule detection and material analysis. This chapter will firstly review the principle of Raman scattering and mechanism of SERS and secondly show a demonstration of UV SERS on Ga NP ensembles combined with UV surface-enhanced fluorescence (SEF).

8.1 Theory of Raman scattering

Raman scattering is an inelastic scattering of EM waves by a scattering medium, analyte, and usually involves the excitation of analyte's vibrational states.

8.1.1 Molecular vibration

For molecules consisting of N atoms, the total number of degrees of freedom (DoF) is $3N$. Three of these DoF are used to describe molecule translations and three of them are for rotations except for linear molecules where only two types of rotations exist. Therefore, $3N - 6$ DoF are left to describe inter-atom movements, i.e. vibrations. For general molecules, there are $3N - 6$ possible modes of vibrations while there are $3N - 5$ possibilities for linear molecules [192].

For example, for a diatomic molecule like H₂, the only possible vibration is the stretching of the H-H bond. When two bonds are close to each other, they can interact and form group vibrations. Group vibration is the most common characteristic vibrations in organic molecules, e.g., the characteristic symmetric breathing mode from the group vibration of the benzene ring.

Consider the simplest case, bond stretching in a diatomic molecule, to study vibration states. Many books [192-194] treat this stretching as a simple harmonic oscillation (SHO) regulated by the potential,

$$V(q) = \frac{1}{2}Kq^2 \quad (8.1)$$

Where K is the force constant and q is the normal coordinate for stretching, which is the displacement with respect to the equilibrium position between two atoms. The energy states for SHO are constantly separated,

$$E_v = \hbar\omega_0 \left(v + \frac{1}{2} \right) \quad (8.2)$$

where ω_0 is the intrinsic vibration frequency determined by atom effective mass m and force constant K,

$$\omega_0 = \sqrt{\frac{K}{m}} \quad (8.3)$$

In reality, the potential between the two atoms is not simple harmonic but can be approximated by a Morse potential [195],

$$V(q) = D_e(1 - e^{-aq})^2 \quad (8.4)$$

where D_e is the dissociation energy and a controls the “width” of the potential curve. The eigenvalues of the energy states can be obtained by solving the Schrodinger equation [195].

$$E_v = \hbar\omega_0 \left(v + \frac{1}{2} \right) - \frac{(\hbar\omega_0)^2}{4D_e} \left(v + \frac{1}{2} \right)^2 \quad (8.5)$$

where

$$\omega_0 = a\sqrt{2D_e/m} \quad (8.6)$$

The second term in Equation 8.5 indicates the anharmonicity of the vibrational states regulated by the Morse potential in Equation 8.4.

Equation 8.2 is actually a linear approximation of Equation 8.5. Usually, the excitation energy to the first vibrational states is about several hundred to several thousand cm^{-1} ($10000 \text{ cm}^{-1} = 1.24 \text{ eV}$), which is usually less than the excitation energy to the first electronic state (several eV). And the displacement is usually small [195]. The following derivation will still use the SHO solution (Equation 8.1 to 8.3) as a good approximation for small displacement. $\{q_i\}$ and $\{\omega_i\}$ measures the normal coordinates and frequencies of all the vibrational modes. For different molecules, their vibrational frequencies are unique. This forms the basis for molecule detection and analysis.

8.1.2 Raman scattering

In classic theory, external radiation will induce an electric dipole when interacting with matter,

$$\mathbf{p} = \boldsymbol{\alpha} \cdot \mathbf{E} \quad (8.7)$$

where \mathbf{E} is the electric field vector of the incident wave with frequency ω_i ,

$$\mathbf{E} = \mathbf{E}_0 \cos(\omega_i t) \quad (8.8)$$

and $\boldsymbol{\alpha}$ is the polarizability tensor of the molecule. Each component in the tensor can be expanded by normal coordinates $\{q_i\}$,

$$\alpha_{\rho\sigma} = (\alpha_{\rho\sigma})_0 + \sum_k \left(\frac{\partial \alpha_{\rho\sigma}}{\partial q_k} \right)_0 q_k + \dots \quad (8.9)$$

For a specific vibrational mode q_k , tensor $\boldsymbol{\alpha}$ will have the form,

$$\boldsymbol{\alpha}_k = \boldsymbol{\alpha}_0 + \boldsymbol{\alpha}'_k q_k \quad (8.10)$$

where $(\boldsymbol{\alpha}'_k)_{\rho\sigma} = \left(\frac{\partial \alpha_{\rho\sigma}}{\partial q_k} \right)_0$ and the displacement is,

$$q_k = q_{k0} \cos(\omega_k t) \quad (8.11)$$

Insert Equations 8.8, 8.9 and 8.11 into Equation 8.7, we obtain,

$$\mathbf{p} = \boldsymbol{\alpha}_0 \mathbf{E}_0 \cos(\omega_i t) + \boldsymbol{\alpha}'_k \mathbf{E}_0 q_{k0} \cos(\omega_i t) \cos(\omega_k t) \quad (8.12a)$$

Using a trigonometric identity, it can be rewritten as,

$$\mathbf{p} = \boldsymbol{\alpha}_0 \mathbf{E}_0 \cos(\omega_i t) + \frac{\boldsymbol{\alpha}'_k \mathbf{E}_0 q_{k0}}{2} \{ \cos[(\omega_i - \omega_k)t] + \cos[(\omega_i + \omega_k)t] \} \quad (8.12b)$$

Or,

$$\mathbf{p} = \mathbf{p}(\omega_i) + \mathbf{p}(\omega_i - \omega_k) + \mathbf{p}(\omega_i + \omega_k) \quad (8.12c)$$

The first dipole has the same radiation frequency as the incidence wave, which is the well-known elastic Rayleigh or Mie scattering. The second and the third terms contribute to the inelastic Raman scattering. The scattered EM wave will possess an energy shift (wavenumber shift) from the incident field, known as Stokes shift ($\omega_i - \omega_k$) and anti-Stokes shift ($\omega_i + \omega_k$).

Figure 1.2 shows the transition diagram for these three processes. Analyte absorbs photons from the incident EM wave and is excited from the ground state to higher virtual energy states. If the analyte relaxes back to the original ground state, it will reemit photons at the same energy (frequency) as the incident wave, which is the Mie scattering or Rayleigh scattering (under the small particle approximation). There are chances that the analyte will relax back to the higher vibrational state and reemit photons with lower energy comparing to the incident photons. This inelastic scattering process is thus called Stokes Raman scattering. Another possibility is that the analyte is originally at some higher vibrational state and excited to higher virtual energy states. When the analyte relaxes back to the ground state, it emits photons with higher energy. This process is called anti-Stokes Raman scattering. The energy difference between absorbed and reemitted photons is called a Raman shift, which is equal to the excited vibrational states energy with respect to the ground state.

Equation 8.12c describes how light interacts with one of the vibrations. Similar expression can be obtained for other vibrational modes. As each vibration has different intrinsic vibrational frequencies, a different Raman shift is assigned to each vibration, known as a Raman mode. The presence of a vibrational mode in Raman spectroscopy is regulated by selection rules [192]. Therefore, Raman spectroscopy is usually plotted as scattering intensity vs. Raman shift and each intensity peak is identified as one Raman mode. The (relative) intensities, widths, and peak positions of Raman modes indicate the composition, structure and other properties of the analyte.

8.1.3 Raman scattering intensity

The detected Raman scattering is from the radiations of induced polarizations in Equation 8.12c. With incident EM wave field vector E_0 at frequency ω_i surrounding the analyte, the Raman scattering intensity I will be [193],

$$I_R = \frac{\omega_s^4 \langle |\mathbf{p}|^2 \rangle}{32\pi^2 \epsilon_0 c^3} \equiv \sigma |E_0^2| \quad (8.13)$$

where σ is the Raman scattering cross section, $\langle \dots \rangle$ denotes a time average, and ω_s is the frequency of the scattering EM wave including Raman shifts.

$$\omega_s = \omega_i \pm \omega_k \quad (8.14)$$

Notice that Raman scattering intensity is proportional to the fourth power of Raman scattering frequency and the square of the change of polarizability given Equations 8.12 and 8.13,

$$I_R \propto \omega_s^4 |\alpha'_k|^2 |E_0^2| \quad (8.15)$$

8.2 Surface-enhanced Raman scattering

Based on Equation 8.15, there are at least three ways to enhance Raman scattering, increasing the frequency of incident field ω , increasing incident field intensity $|E_0^2|$, and altering molecule states to change its polarizability.

For ω , it indicates that UV excitation can enhance Raman signals. It is one of the benefits of performing Raman spectroscopy in the UV as discussed in Chapter 1. However, this enhancement is restricted by the availability of lasers and detectors. Therefore, researchers have focused on altering the latter two terms to enhance Raman signals. These two factors thus contribute to the two basic mechanisms of SERS effect, the EM origin and the chemical origin [44-48].

8.2.1 EM origin of SERS

As discussed in Chapter 2, NPs can enhance surrounding EM field intensity E_{loc} with respect to the incident field E_0 at frequency ω_i as,

$$E_{loc} = g(\omega_i)E_0 \quad (8.16)$$

where g is called the local field enhancement factor and can be calculated using many methods (Section 2.2). According to Equation 8.7, the induced dipole moment of the analyte will be enhanced by $g(\omega_i)$. Unlike the radiation from an isolated dipole, the total Raman field has two components [196],

$$E_R = E_{DIP} + E_{SC} \quad (8.17a)$$

The first term E_{DIP} is the direct dipole radiation field from the analyte, i.e., the second or the third term in Equation 8.12c, whose strength is proportional to the dipole moment of the analyte. Therefore,

$$E_{DIP} \sim g(\omega_i)E_0 \quad (8.17b)$$

The second term E_{SC} is the secondary induced scattered field due to the presence of the NP. The interaction between the dipole of the analyte and the metallic NP results in an equivalent dipole at the center of the NP. Kerker et al. showed that the strength of this dipole field E_{SC} from this “new” dipole is also enhanced by a factor of g but at the Raman scattering frequency ω_s with respect to the original dipole field E_{DIP} of the analyte by matching the boundary conditions at the NP surface [196-197]. Therefore,

$$E_{SC} \sim g(\omega_s)E_{DIP} \sim g(\omega_s)g(\omega_i)E_0 \quad (8.17c)$$

To the first order approximation [198], the leading term of the intensity enhancement is thus,

$$I_{SERS} \sim |g(\omega_i)|^2 |g(\omega_s)|^2 |E_0^2(\omega_i)| \quad (8.18)$$

Comparing Equation 8.13 and 8.18, the total enhancement of SERS will be,

$$\frac{I_{\text{SERS}}}{I_{\text{R}}} = |g(\omega_i)|^2 |g(\omega_s)|^2 \quad (8.19)$$

This defines the theoretical SERS EM enhancement factor (EF). When Raman shift is small, $g(\omega_i) \approx g(\omega_s)$. Equation 8.19 is approximately,

$$\text{EF}_{\text{EM}} = |g|^4 \quad (8.20)$$

If a local field enhancement factor is calculated for certain geometry, this forth power dependence relation is generally used to estimate the expected overall enhancement factor in theory for this nanostructure [198]. Figure 2.9 plotted local EM field intensity enhancement $|g|^2$ surrounding a spherical Ga NP which can be converted to SERS EF using Equation 8.20.

As shown in Figure 2.9, SERS EF is both angular- and distance- dependent due to the nature of dipole radiation. Recall Equation 2.16, which describes the EM field outside of a free standing NP in a static external EM field $E_0 \hat{\mathbf{z}}$,

$$\mathbf{E}_{\text{loc}} = E_0 \hat{\mathbf{z}} - \frac{\epsilon-1}{\epsilon+2} a^3 E_0 \left[\frac{\hat{\mathbf{z}}}{r^3} - \frac{3z}{r^6} \hat{\mathbf{r}} \right] \quad (2.16)$$

Maximum \mathbf{E}_{loc} occurs along the incident EM field direction. The leading enhanced field term decays as r^{-3} . According to Equation 8.20, local EF will decay as r^{-12} [199]. Combing with the increase of total surface area as r^2 , overall SERS signal shall decay as r^{-10} [200],

$$I_{\text{SERS}} \propto \left(\frac{a+r}{a} \right)^{-10} \quad (8.21)$$

where a is the NP radius and r is the distance from NP surface. This effect will be magnified when NPs are small.

In conclusion, the SERS effect is highly localized. Only specific areas near a NP surface have potential large EF. These areas are known as hotspots. Most reported huge SERS EFs ($10^{12} \sim 10^{15}$) are claimed to be originated from hotspots [201]. Theoretical estimations and experiments showed that hotspots occur for nanostructures with large curvature and fractal shape [50]. They become the most important source for SERS enhancement. Single molecular detection can be achieved when the analyte is placed in a certain hotspot [42]. It is critical to study both overall enhancement and local EM field enhancement in hotspots.

Despite the general success of EM theory for SERS, several criticisms have been reported regarding retardation effect and nonlocal effect [44]. Both questioned the fourth power dependence of the local field enhancement (Equations 8.19 and 8.20). However, EM theory is still a good assessment, if not exact, to compare similar nanogeometries and to estimate potential enhancement factors.

8.2.2 Chemical origin of SERS

Up-to-now, the EM origin of SERS does not involve a specific type of analyte or specific Raman mode. It predicts a uniform enhancement. However, this is not

observed in experiments. On the same silver surface, CO produces 50 times higher SERS intensity than N₂ [202]. Raman modes were not enhanced by the same ratio in most SERS experiments [44].

During SERS experiments, analytes are placed on metal surfaces or close to metallic nanostructures. Charge transfer may occur between metal and molecules [44]. This effect may alter the Raman polarizability of the metal-molecules system from isolated molecules to create additional electronic states and cause a resonance. Such a resonance will contribute to the overall SERS enhancement, known as a chemical enhancement. The order of chemical EF is usually less than 10² [46]. The detailed discussion of chemical origin of SERS is beyond the scope of this thesis. However, two major properties of chemical mechanism are worthy to note due to the essence of charge transfer effect. First, chemical originated SERS effect only occurs for the first monolayer of molecules at the metallic surface. Second, the effect is molecule-selective and cannot be generalized to other analytes.

8.2.3 SERS active substrate

Since the observation of the first SERS effect on solid metal surface, searching for SERS active substrate providing higher enhancement is key to SERS applications in addition to the research on SERS mechanisms. There are currently two major

types of SERS active substrates: solid-based and solution-based [203]. The development of a solution-based SERS active media is majorly due to the involvement of wet-chemical synthesis methods of metallic nanoparticles. Perfect spherical and mono-dispersed Au and Ag colloids are easier to be synthesized in solution than by traditional thermal processes. Solution-based SERS enables the direct use of synthesized NPs in solution without being transported to other solid supports. Analytes are directly mixed with NPs in solution. The major challenges for solution-based SERS include dissolubility of analytes, disturbance from solvent, spatial uniformity within the solution, etc.

Solid-based SERS substrates are more popular in research and applications due to stability and reproducibility while the major drawback for solid-based substrates including the difficulty of obtaining reference data to calculate the enhancement factor and the permanent damages of the analytes on the substrate surface.

Here presented are some generalized criteria for an ideal SERS active substrate. The first criterion is the substrate's local and overall enhancement. The enhancement factor can be estimated using analytical or numerical calculations or measured in SERS experiments. In addition, there are other concerns to assess the performance of a SERS substrate in experiments [204]:

- i. Sensibility: threshold of the minimum amount of analyte to generate a detectable signal. Single molecule SERS has been explored and reported [16][40].
- ii. Selectivity: same or similar enhancement for a variety of analytes. SERS enhancement primarily from the EM origin will be similar for different analytes while chemical originated SERS enhancement is highly analyte-selective.
- iii. Stability and reproducibly: repeatable enhancement. This is one of the advantages of a solid-based substrate. In addition to maintaining its geometry, substrates also need to conserve its plasmon features under thermal fluctuation and oxidation over time.
- iv. Optical clarity: no or little interference with the analytes' Raman modes. Some substrates, especially solvents, may exhibit their own Raman modes which can overlap with the analytes'.

For our SERS substrate, Ga NP ensemble on sapphire, we have discussed its stability in Chapter 2. Preliminary calculation also shows its enhancement in the UV based on the EM origin and therefore, it shall not be significantly analyte-selective. The only concern is the Raman scattering from the sapphire substrate [205]. However, all the sapphire Raman modes are below 800 cm^{-1} while most

Raman modes of common analytes are above 1000 cm^{-1} , since vibrations in crystals are from phonons while those in molecules are from bonds between atoms. All the above factors make a Ga NP ensemble on sapphire an ideal substrate for UV SERS.

8.3 UV SERS: a demonstration

Chapter 1 presented the advantages and current status of UV SERS. A very limited number of UV SERS experiments are reported. Furthermore, majority of them is based on chemical effects. This opens up great opportunities in this field. This section will show the first demonstration of UV SERS using crystal violet with Ga NP ensembles on sapphire in the literature.

8.3.1 Instrument

An in-house Raman system was built and used in our experiment. Figure 8.1 depicts the structure of the system (courtesy of J. Callahan). A HeCd laser operating at 325 nm with maximum output power of 13 mW acts as the source. To reduce any spectral noise a notch filter is placed after the laser source. The first set of off-axis-parabolic-mirrors (OAPM) (1 and 2 in Figure 8.1) acts as a 6x beam expander, and collimates the source into a 50/50 beam splitter. Reflected photons from the beam splitter pass to the third OAPM and are focused onto the

sample. The well-focused beam spot area is approximately $50 \mu\text{m}^2$. Specular and diffuse reflection from the sample is collected and collimated by the third OAPM and passed back to the beam splitter. The beam is sent through a 325 nm RazorEdge ultrastep long-pass edge filter to reject the laser source, but not the spectra, and a 532 nm RazorEdge ultrastep short-pass edge filter blocks possible low frequency fluorescence from the samples. Collected photons are then focused into an all silica fiber by the fourth OAPM. The system has $\text{N.A.} = 0.45$. The fiber is directly coupled to a 30 cm spectrometer with a holographic 1200 grove/mm grating blazed at 300 nm, and a liquid nitrogen cooled Princeton Instruments, UV-coated charge-coupled device (CCD). Detector dark counts and cosmic ray spikes were subtracted for all spectra presented.

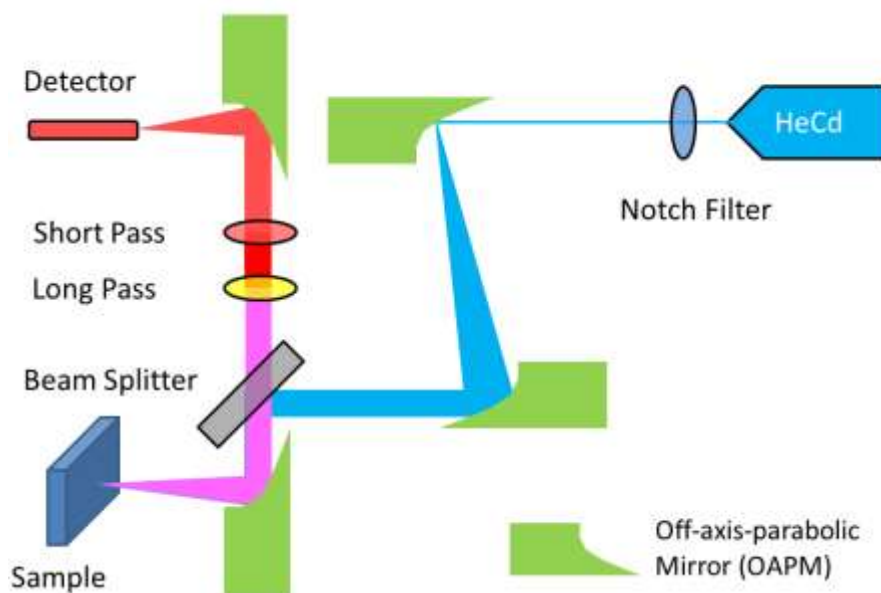


Figure 8.1: Schematic diagram of the in-house Raman system.

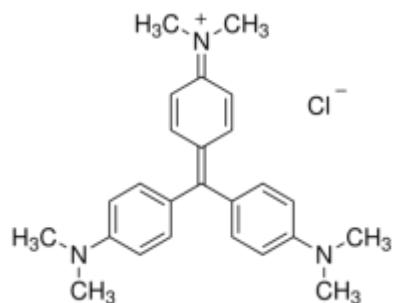


Figure 8.2: Molecular structure of crystal violet.

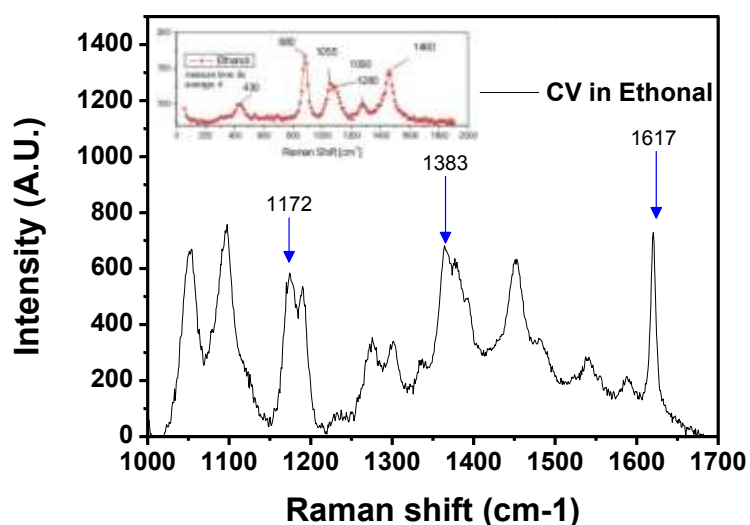


Figure 8.3: Raman spectrum of 20 μM CV in ethanol solution (inset: Raman spectrum of ethanol by Sacher Lasertechnik Group).

8.3.2 Analyte

Crystal violet (CV), $\text{CH}(\text{C}_6\text{H}_4\text{N}(\text{CH}_3)_2)_3$, was chosen as the analyte. It is a common dye used in Raman analysis for its stability and strong Raman scattering. Previous reports on UV SERS also used CV as the analyte [72]. It is a tri-*p*-dimethylaminophenyl carbonium ion, in which the three benzene rings are

symmetrically arrayed around a central carbonium atom. Commercially available CV is usually in the form of $\text{CH}(\text{C}_6\text{H}_4\text{N}(\text{CH}_3)_2)_3\text{Cl}$ with molecular weight 407.98. Figure 8.2 shows its molecular structure.

High grade CV was dissolved in 99.9% ethanol. Both were purchased from Sigma-Aldrich. The solubility of CV in ethanol is 13.87 g for 100 ml [206]. 40.80 mg CV was dissolved in ethanol at room temperature to make 50 ml solution which is below the saturation limit. The solution was diluted 100 times before characterization. The concentration of the final solution is 20 μM . Figure 8.3 shows the normal Raman spectroscopy of this solution excited by 325 nm laser compared to the Raman spectroscopy of ethanol only in the inset to reveal the Raman modes from CV. It shows three characteristic CV Raman modes. The peaks at 1172 cm^{-1} , 1383 cm^{-1} , and 1617 cm^{-1} are from C-H in-plane bending and two C-C stretching vibrational modes of the aromatic ring, respectively [207-208]. Again, they do not interfere with the Raman modes from the sapphire impurities.

8.3.3 Sample preparation

Sample Y1, Y3, and Y6 were used in this demonstration. They were synthesized as discussed in Chapter 4. Detailed local morphology information was presented in Chapter 5. Their optical properties were discussed in Chapters 6 and 7. Y3 has the in-plane LSPR mode energy at 3.8 eV (about 325 nm), while the in-plane

LSPR energies for Y1 and Y6 are on each side of 325 nm respectively, which makes three samples at “blue”, “resonance” and “red” to the laser excitation wavelength for representation.

With our collaborator K. Lantz [209], 20 μ M CV solution was spin casted onto a substrate at 1500 rpm at room temperature for 3 min to produce a 5 nm thick uniform coating. The substrates were dried for 15 min to ensure ethanol evaporation and minimize the distance between CV molecules and substrate surface. Atomic force microscopy (AFM) confirmed the uniformity of the conformal molecular layer that thinly coats the surface of the NPs, which ensures the same amount of CV was attached to the surface of sapphire and Ga NP at the same time for direct comparison [209].

8.3.4 Spectroscopy

Raman spectroscopy was measured on sapphire and Ga NP sides respectively by the same confocal microscope with a 0.45 numerical aperture shown in Figure 8.1. Laser was operated at 5 mW. Signals were integrated for 180 s. Figure 8.4 plots Raman intensities measured for the three samples Y1, Y3, and Y6. Raman spectra measured on sapphire side of the three samples were identical. Therefore, only one spectrum was shown as the reference which is measured on sample Y6. This also confirms that a direct comparison among samples is valid.

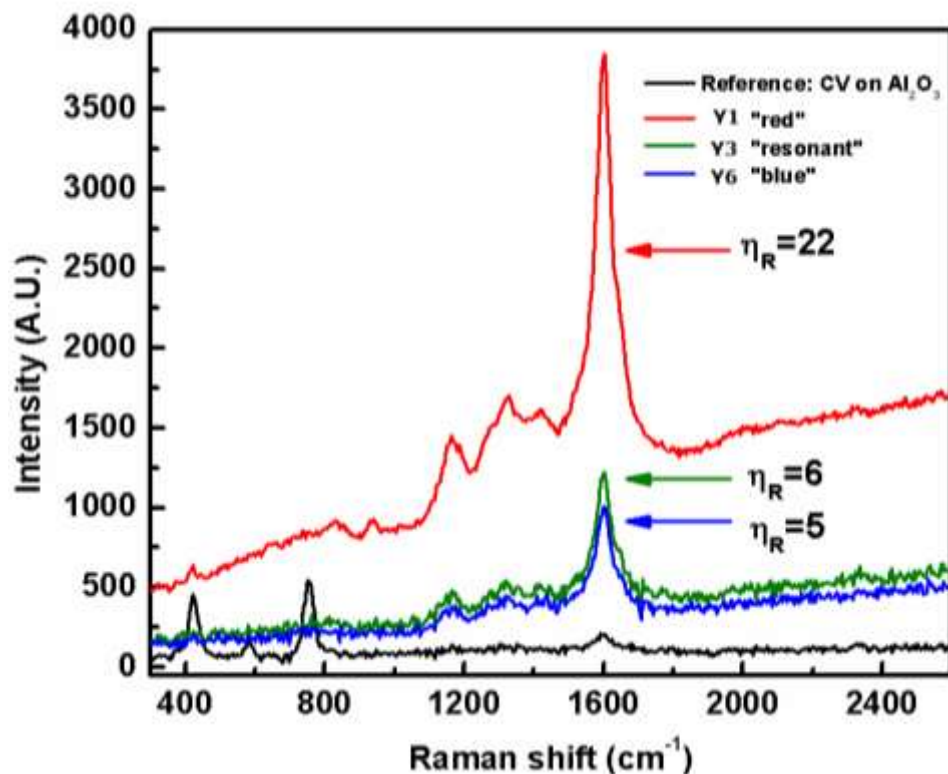


Figure 8.4: Measured CV SERS from Ga NPs in samples Y1, Y3, and Y6 compared to Raman signal from CV on bare sapphire by 325 nm UV laser excitation.

A clear Raman signal enhancement is observed from the three samples compared to bare sapphire. Three CV Raman modes at 1172 cm^{-1} , 1383 cm^{-1} , and 1617 cm^{-1} mentioned above are clearly observed above a broad fluorescence band that increases with increasing wavelength (Raman shift). A comparison of the spectra taken from substrate regions without and with the Ga NPs graphically indicates that each substrate produces enhanced CV Raman signals and fluorescence for all three features. Note that any resonant Raman enhancement affects both regions equally, and nonresonant Raman signals may exhibit an even stronger

enhancement. Because the reference and enhanced spectra are similar in form, the enhancement observed is purely caused by the local plasmonic (and perhaps, though less likely, a charge transfer) effect. We observed, by the first time, UV SERS on Ga NPs combined with UV SEF.

8.3.5 Enhancement

Figure 8.4 shows clearly an enhancement in overall Raman signals on SERS-active samples Y1, Y3, and Y6 compared to bare sapphire. The overall intensity contains both Raman scattering and fluorescence. Fluorescence baseline was subtracted from each spectrum to obtain Raman and fluorescence intensity separately. This section will quantify the enhancement based on this method.

It is easier to define enhancement factor during theoretical calculations like Equations 8.6, 8.19 and 8.20. In experiments, normal Raman spectroscopy and SERS are usually measured separately. Besides that, even for solid-based SERS substrate, most normal Raman spectroscopy was taken from analytes in solution for simplicity. This brings difficulties to obtain real enhancement. The estimated enhancement factor for entertain Raman mode is usually defined as,

$$EF_{\text{SERS}} = \frac{I_{\text{SERS}}/N_{\text{SERS}}}{I_{\text{Raman}}/N_{\text{Raman}}} \quad (8.22)$$

where I_{SERS} is the signal intensity for this Raman mode in SRES and I_{Raman} is the corresponding signal intensity in normal Raman spectroscopy. Both intensities are normalized by the number of molecules present or contribute to each spectroscopy. While the Raman intensities are measured quantities in the experiments, estimation of number of molecules brings large difficulty and uncertainty.

In our experiments, we casted same conformal thin film of analytes on Ga NP side and bare sapphire side. Molecule surface densities are assumed to be identical on both sides. SERS spectra were measured from analytes on Ga NP substrates and normal Raman spectra were measured from analytes on bare sapphire side. Accounting for the fact that Ga NP ensembles have more surface area than bare sapphire, the enhancement factor in our experiments is,

$$\eta = \frac{I_{\text{Ga}}}{I_{\text{sapphire}}} / \frac{A_{\text{Ga}}}{A_{\text{sapphire}}} \quad (8.23)$$

where $\frac{A_{\text{Ga}}}{A_{\text{sapphire}}}$ is the surface area ratio of Ga NP ensemble and bare sapphire which can be calculated from NP radius distribution shown in Chapter 5 given the hemispherical shape of Ga NPs. The ratio is 1.353, 1.437, and 1.525 for Y1, Y3, and Y6 respectively. Equation 8.23 directly assesses the enhancement for the presence of Ga NPs. It is valid for both Raman enhancement η_{R} and fluorescence enhancement η_{F} .

As the Raman mode at 1617 cm^{-1} is most clear to identify, separated Raman and fluorescence intensities at this Raman shift from each spectrum were used to calculate enhancement. A quantitative comparison of the strength estimates the Raman enhancement factor η_R to be 5, 6, and 22 for the “blue” Y6, “resonant” Y3, and “red” Y1 substrates, respectively. The weak fluorescence between 329 nm and 355 nm ($400 \sim 2600\text{ cm}^{-1}$ in Figure 8.4) is similarly enhanced, with net fluorescence enhancement factors η_F of 2, 3, and 9, respectively.

Note that the enhancements are not strongest when the aggregate LSPR energy coincides with the laser (“resonant” sample Y3), suggesting a more complex process must be responsible for the enhancements observed. The fluorescence is enhanced by the increased absorption of the pump field near the NPs but is strongly suppressed at wavelengths where the fluorescence overlaps the LSPR. [210-213] This explains why the largest η_F occurs for the substrate with the largest NPs whose LSPR is not resonant with the fluorescence near 325 nm. It is interesting that this “red” substrate Y6, with its bimodal size distribution, also produced the largest η_R . Similar visible wavelength SERS measurements of the analyte cresyl fast violet deposited on similar Ga NP substrates revealed that the “blue” substrate with the smallest, most tightly packed NPs (45 nm mean radius, 16 nm mean spacing) produced the largest η_R , followed by the “red” substrate

with a bimodal size distribution [214]. Together, these observations suggest that enhancement occurs between NPs that are in close proximity in a manner that depends on excitation wavelength.

It has long been recognized that strong SERS and SEF signals may be measured from analyte in the small gap, hotspot, between two NPs whose coupling depends exponentially on their spatial separation. This effect is responsible for the behavior seen in previous visible wavelength SERS measurements in which the coupled Ga NPs are of roughly equal size [214]. However, it was recently argued that a tightly coupled large and small metallic NP dimer constitutes a superior combination for enhanced optical scattering [101][215]. In this configuration, the larger NP acts as an enhanced absorbing “antenna”, while the smaller NP acts as a “resonator” enhancing the field strength, thereby providing a larger Raman enhancement than either NP can alone. This occurs most effectively in the “red” substrate, because of the bimodal distribution of small halo NPs surrounding and coupled to large NPs, and it is that substrate which exhibits the greatest η_F and η_R for UV SEF and SERS, respectively. Together, these observations suggest that under long wavelength (i.e., visible) illumination the small NPs with a unimodal size distribution are simultaneously large enough to be good absorbers but small enough to produce strong enhancements;

however, as the illumination wavelength approaches the size of the NPs (i.e., UV), the asymmetric NP dimers accomplish both absorption and enhancement more effectively.

The leading in-plane LSPR peaks of these 3 samples were measured by SE at 70° degree. For Y6 which has a bimodal size distribution, the smaller NPs do not contribute significantly to the LSPR measured by grazing incidence SE because of their inefficient absorption and shadowing by the larger NPs. This was discussed in Chapter 7 where another feature around 4.0 eV shows up for Y6 at near normal incidence, which coincides with excitation laser at 3.81 eV.

In conclusion, we observed, by the first time, UV SERS on Ga NPs combined with UV SEF. Strongest enhancement is not related to SE measured LSPR peak but possible hotspots within asymmetric NP pairs from the sample with bimodal size distribution, which is consistent with VASE and VAMM observations. Further modeling and spatially resolved characterization is needed to confirm strong local enhancement at these interparticle gaps, or hotspots, which will be discussed in Chapter 10. Nevertheless, we will exploit an alternative experimental approach to estimate local enhancement and signal contribution distributions by analyzing time- and laser intensity- dependent Raman spectra in the next Chapter.

9. UV SERS and UV SEPD: Hotspot Analysis

In the previous chapter, we showed the first observation of UV SERS and UV SEF on Ga NPs using crystal violet (CV). The observed enhancement appears modest because the reported values represent an aggregate enhancement over the entire CV-coated Ga NP ensemble surface. As stated in Chapter 8, strong SERS and SEF signals may come from analytes in the small gaps between NPs, known as hotspots. This chapter will present the spatial distribution of the local enhancement and their contribution to the overall signal by analyzing the spectra temporally and spatially. Since sample Y6 possess highest direct enhancement factor, the analysis in this chapter will focus on sample Y6.

9.1 Temporal analysis

Raman spectra using the same setup measured from another site on the sample surface were integrated for 1 s at each second from the start of illumination for the total of 3000 s. 3000 Raman spectra were captured from Ga NP side and sapphire side respectively. Figure 9.1 shows some representative Raman spectra at different time from each side. The intensities are much lower than Figure 8.5 due to the short integration time. Raman modes at 1172 cm^{-1} and 1383 cm^{-1} become hard to identify in the noisy background while the Raman mode at 1617

cm^{-1} remains clear. The following analysis will focus on this Raman mode. Two Raman modes below 800 cm^{-1} are again from the sapphire substrate.

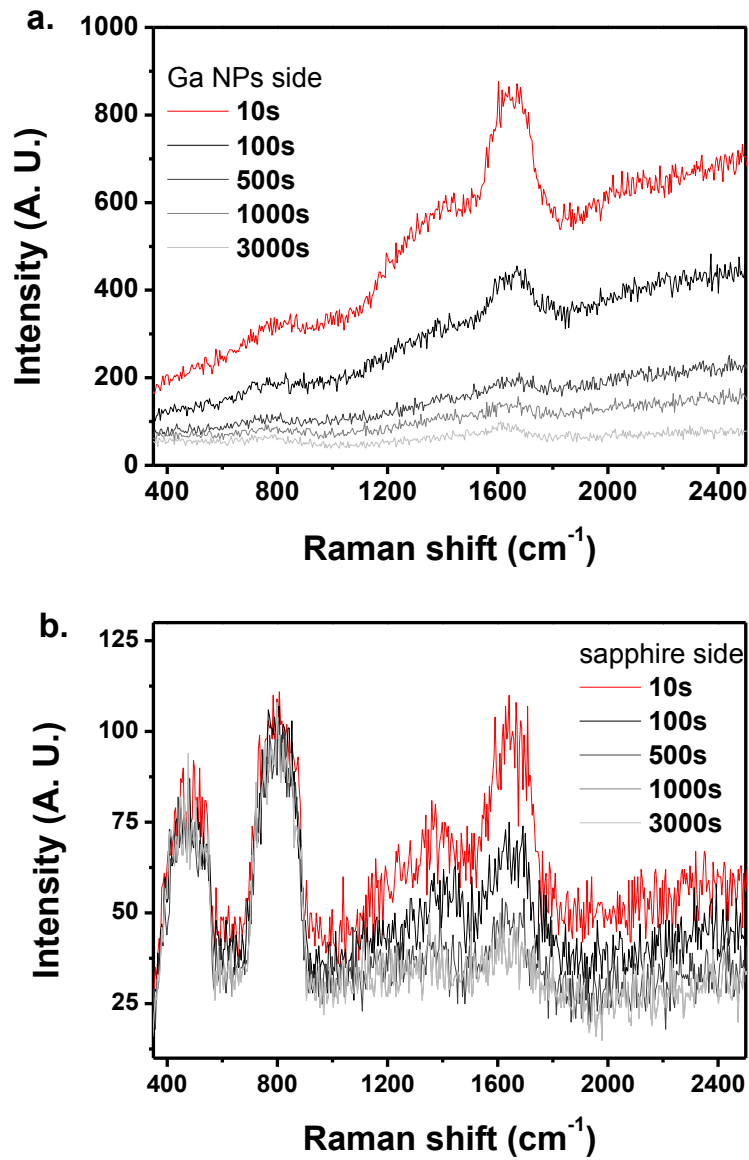


Figure 9.1: Temporal evolution of Raman spectra from CV on (a) Ga NP side in sample Y6 and (b) bare sapphire.

As time involves, peak intensity keeps decreasing. On Ga NP side, peak signal drops to half from 800 to 400 for the first 100 s, and gradually decreases to about 100 (1/10 of the initial intensity) at 3000 s. On sapphire side, decrease of signal almost saturates after 500 s where the end intensity is about half of the initial one. Notice that intensity here includes both Raman signal and fluorescence signal. Similar analysis as used in Section 8.2.4 is applied to separate the two signals which will be presented as follow.

First, Figure 9.2 shows the contour plot of Raman spectra of CV on Ga NP side in Y6 for the first 200 s, where characteristic Raman modes for CV are weakened over time. Different colors represent different Raman signal intensities. It suggests that photodegradation occurs during the Raman measurement. Strong local EM field induced by laser may damage CV and leave less analytes on sample surface. Therefore, fewer signals were captured when CV was exposed to laser illumination over time. The end products of the degradation are very complex including demethylated compounds, diarylmethane derivatives, and oxygenated compounds [216]. When chemical bonds are broken during degradation, corresponding Raman mode will disappear in Raman spectra. The overall Raman signal becomes weaker.

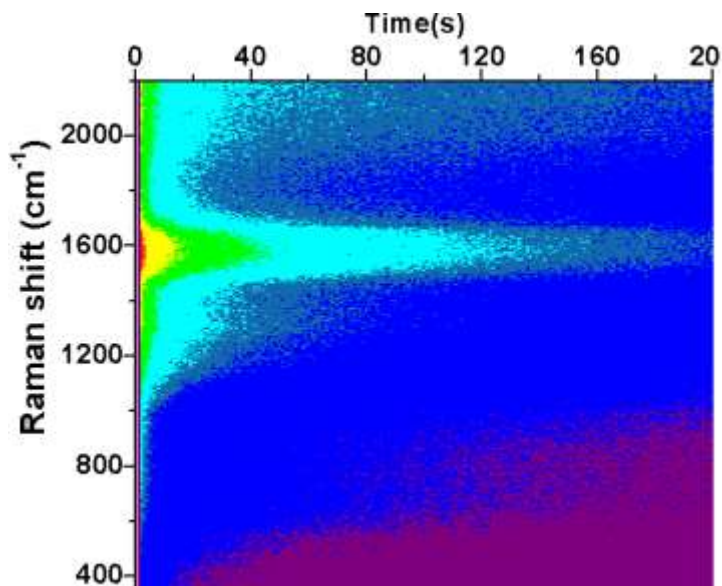


Figure 9.2: Temporal contour plot of Raman spectra from CV on Ga NP side in sample Y6 for the first 200 s.

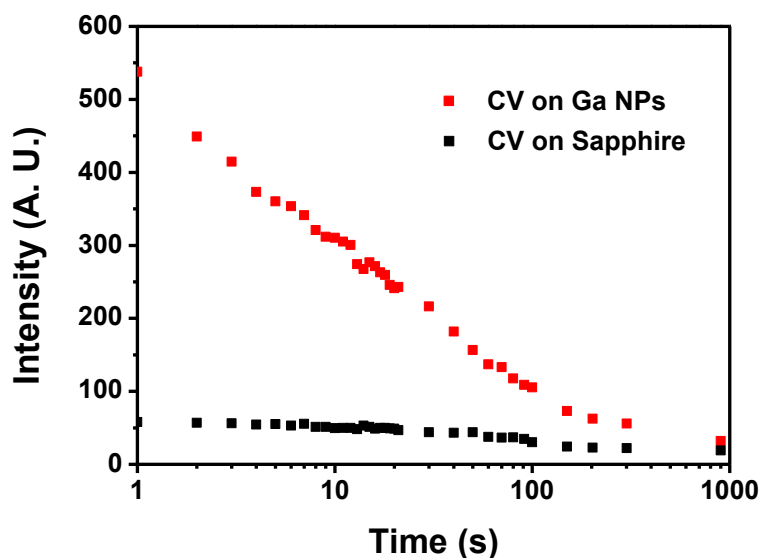


Figure 9.3: Raman intensities at 1617 cm^{-1} from CV on Ga NP and bare sapphire sides in sample Y6 for the first 1000 s.

Second, Figure 9.3 compares intensities for Raman mode at 1617 cm^{-1} of CV on Ga NP and sapphire for the first 1000 s in log scale. The absolute value of the slope indicates the signal decay speed. Raman signal from Ga NP side decays

much faster than that from sapphire side. Different degradation processes implies the enhanced photodegradation of CV on Ga. Similar to SERS and SEF principles, Ga NPs can enhance surrounding EM field to exceed damage threshold of analytes and therefore induce enhanced photodegradation [217].

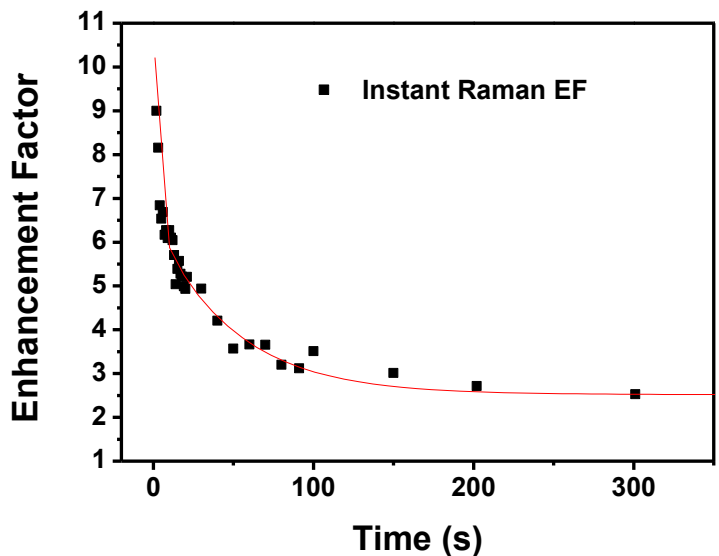


Figure 9.4: Direct Raman signal enhancement factor of sample Y6 for the first 1000 s.

Figure 9.4 shows the instantaneous direct enhancement factor for Raman signals for the first 1000 s. EF also decays exponentially over time and saturates at approximate 2. In the last chapter, Raman spectra were integrated for 180 s which is an averaged EF of instantaneous values and therefore is underestimated. It is one of the reasons that overall EF is modest comparing to theoretical EF estimated in Section 2.2.

As discussed in Chapter 1, photodegradation itself is very important in environmental and chemical applications. The observation of enhanced photodegradation on Ga NPs provides new possibilities for its UV plasmonic applications.

9.2 Spatial analysis

Another contribution to the modest overall EF is the variance of local EF on sample surface. As discussed in the last chapter, strongest enhancement may be originated from interparticle gap between a pair of small and large NPs, known as hotspot. Because of the statistical distributions of particle size and spacing, the varied contributions of localized enhancement factors responsible for both strengthening the spectra and damaging the CV cannot be estimated *ab initio*. However, it may be estimated experimentally following the work of Fang et al. in which the intensity of the spectra is monitored as a function of pump intensity [218-219]. This approach utilizes the fact that analyte is damaged during SERS measurement. For a very weak excitation, well below the damage threshold of the analyte, the spectra should not deteriorate. As the pump intensity is increased, the local EM field intensity in hotspots with the largest enhancement factors will rise above the damage threshold, decreasing the Raman signal in proportion to the hotspot's contribution. Further increases in laser intensity will

allow hotspots with weaker enhancement factors to reach the damage threshold, so a histogram of hotspot areal coverage and enhancement factor contribution may be ascertained through this method.

Therefore, Raman spectra were measured under a series of excitation laser powers on Ga NPs side of sample Y6 using the same setup shown in Chapter 8. Following the principle of this method, laser beams with four pump intensities 498, 836, 1890, and 2780 W/cm² were firstly used to examine the time and pump intensity dependence.

Figure 9.5a, b shows normalized fluorescence and Raman intensities from CV for the first 400 s on sample Y6 Ga NPs side. Signal intensities are normalized to fluorescence and Raman intensities at the first second respectively. Note that both signals rapidly decay, and a biexponential fit of the fluorescence and Raman decays reveals weakly pump intensity-dependent characteristic time scales on the order of $\tau_{\text{fast}} = 4, 2$ and $\tau_{\text{slow}} = 60$ and 50 s, respectively. The actual values and uncertainties of the decay constants are given in Table 9.1. Clearly the UV laser is damaging the CV, particularly in the regions where the field concentration is highest, and the majority of the enhancement and damage occurs in the first few seconds [220]. In Figure 9.5b, normal Raman intensity under highest power illumination (black curve) ends at lowest leftover signal

level, which indicates that more CV was damaged as the pump intensity increases, local EM field strength will exceed the damage threshold in more areas. Therefore, we may apply this method on our samples to investigate the distribution of local enhancement factor.

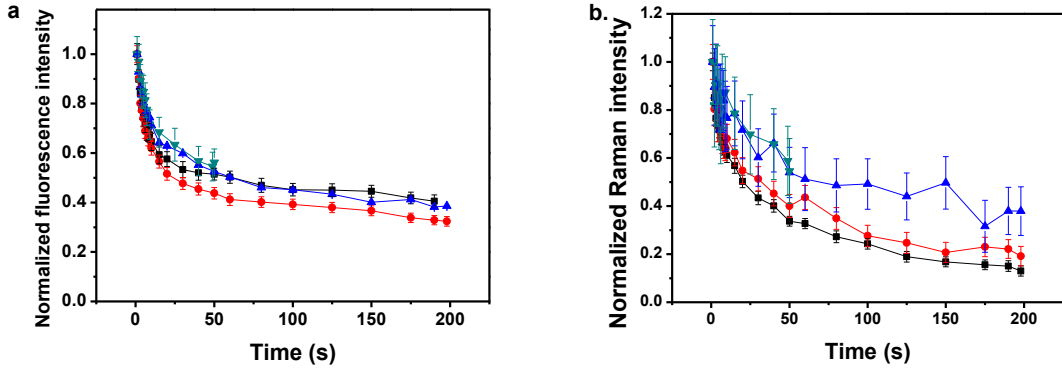


Figure 9.5: Time-dependent normalized (a) fluorescence and (b) Raman signals at 1617 cm^{-1} from CV on Ga NP side in sample Y6 excited by four different laser pump intensities.

Table 9.1: Time constants for the fast and slow decays of the fluorescence and Raman signals under four different laser pump intensities. (Numbers in the parentheses represent the least significant figures)

Pump Intensity (10^2W/cm^2)	Fluorescence		Raman	
	τ_{fast} (s)	τ_{slow} (s)	τ_{fast} (s)	τ_{slow} (s)
27.85	3.94(38)	62.5(128)	2.15(33)	50.9(39)
18.91	4.53(63)	53.6(122)	1.38(43)	55.8(73)
8.356	4.22(59)	56.7(72)	1.39(101)	48.5(73)
4.974	4.86(233)	068(233)	–	54(78)

Following the work by Fang et al. [218-219], a series of Raman spectra were measured under different laser pump intensities. In order to obtain local enhancement distribution on Ga NPs surface, let's first examine how local EF distribution impacts Raman spectra under different laser powers mathematically. Since the local EF is not uniform on the surface, let's assume the probability density function of enhancement factor η on the sample surface is $p(\eta)$. Therefore, the overall enhancement G shall be,

$$G = \int_{\eta_{\min}}^{\eta_{\max}} p(\eta)\eta d\eta \quad (9.1)$$

For Raman measurement without damage, the final Raman signal intensity I shall be proportional to G given that analytes are uniformly coated. When damage occurs, analytes at the site with the highest enhancement factor are damaged first. Therefore, a cutoff η_{cr} is defined as the critical enhancement factor with which the enhanced field intensity at this site is equal to the damage field intensity threshold. Therefore, the leftover active enhancement will be,

$$G' = \int_{\eta_{\min}}^{\eta_{\text{cr}}} p(\eta)\eta d\eta \quad (9.2)$$

In the experiments, it is easier to measure local EM field intensity. Rewrite Equation 9.1 and 9.2 with the distribution of local EM field enhancement g , $p(g)$:

$$G = \int_{g_{\min}}^{g_{\max}} p(g)g^4 dg \quad (9.3a)$$

$$G' = \int_{g_{\min}}^{g_{\text{cr}}} p(g)g^4 dg \quad (9.3b)$$

This conversion assumes $\eta = g^4$ which is an approximation discussed in Section 8.2. It requires that the laser and Stokes Raman fields are simultaneously and equally enhanced. UV Raman signals are closer in wavelength to the Rayleigh-scattered laser light than in the visible or near-IR, and the Ga NP LSPR is broader than the comparable LSPR from Ag or Au NPs. Consequently, this critical assumption upon which this analysis depends, is more applicable in the UV than at lower energies.

In Equation 9.3b, g_{cr} is named the critical local field enhancement,

$$g_{cr} = \frac{E_{th}}{E_{in}} \quad (9.4)$$

which is the minimum local field enhancement required to raise incident local EM field E_{in} to exceed analyte damage threshold E_{th} . For all the sites with $g > g_{cr}$, $gE_{in} > E_{th}$. Therefore, analytes will be damaged at those sites and leftover signals will come from those sites with $g < g_{cr}$. Given that Raman signal intensity is proportional to the overall enhancement factor, the leftover relative intensity is,

$$\frac{I}{I_0} = \frac{G'}{G} \propto \int_{g_{min}}^{g_{cr}} p(g)g^4 dg \quad (9.5)$$

Recall that g_{cr} is a function of E_{in} in Equation 9.4. Therefore, leftover relative signal is also a function of E_{in} . Figure 9.6 plots the relative strength of Raman signals on sample Y6 after 500 s when signal saturates (normalized to the signal at the first second) as a function of inverse incident field strength. The top axis

labels the critical local field enhancement as defined in Equation 9.4 where $E_{th} = 1.5 \pm 0.3$ MV/m is the measured photochemical damage threshold for CV. It was measured as the incident field strength at which the intensity of the Raman signal stopped varying linearly with pump intensity and is consistent with the 1.5 MV/m damage threshold of acrylic polymers measured using nanosecond pulsewidth UV laser pulses at 355 nm [208][221].

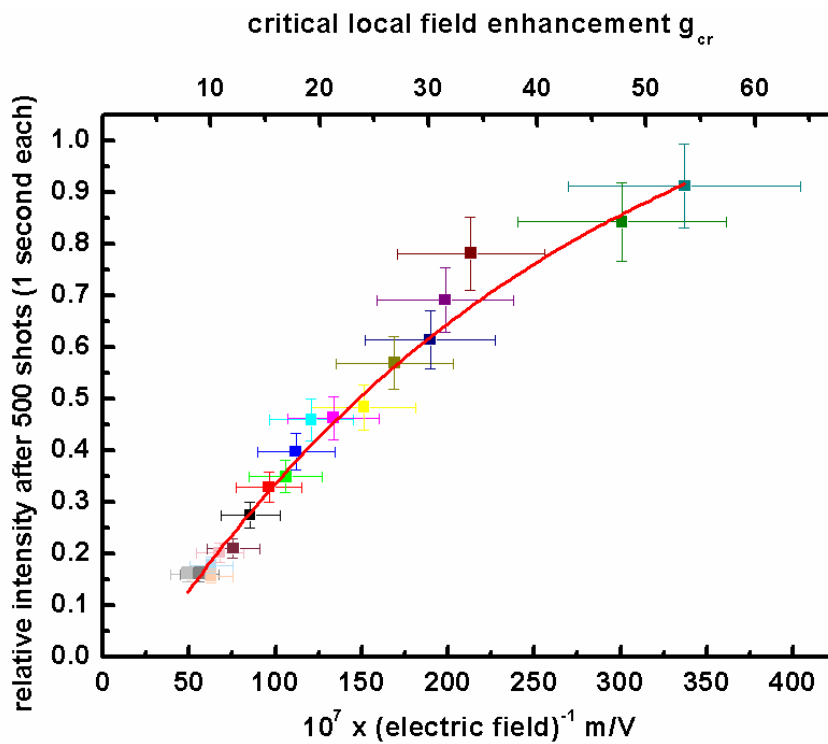


Figure 9.6: Dependence of relative Raman intensity at 1617 cm^{-1} from CV on Ga NP side in sample Y6 after 500 s on laser pump intensity normalized to the damage threshold of CV.

In Figure 9.6, the functional dependence of $\frac{I}{I_0}$ on g_{cr} is approximately,

$$\frac{I}{I_0} = A - Be^{-g_{cr}/\tau} \quad (9.6)$$

The three parameters can be obtained by fitting the curve in Figure 9.6 with the above equation. $A = 0.96 \pm 0.04$, $B = 1.29 \pm 0.02$, and $\tau = 19.6 \pm 2.1$. A represents the relative leftover signal when $g_{cr} \rightarrow \infty$. It should approach 1 as $g_{cr} \rightarrow \infty$ meaning no site has enhancement and therefore no damage occurs. The leftover signal intensity shall be the same as the initial signal intensity. The fitted value A is close to 1 within the experimental error. A, B, and τ determine the zero point of g_{cr} , which is 5 ± 2 . Theoretically, the zero point of g_{cr} shall be close to 1 as $g_{cr} = 1$ meaning the EM field intensities at all the sites exceed the damage threshold and therefore no Raman signal shall be left. The calculated zero point of g_{cr} from fitted parameters is a bit deviated from 1 as the measurement preciseness drops when the leftover Raman signals become very weak.

Compare Equation 9.6 with Equation 9.5. $p(g)$ shall have the form,

$$p(g) = C_1 e^{-g/\tau} g^{-4} \quad (9.7)$$

Given that $p(g)dg = p(\eta)d\eta$, and $\eta = g^4$, the probability density function $p(\eta)$ is,

$$p(\eta) = C_2 e^{-\eta^{0.25}/\tau} \eta^{-1.75} \quad (9.8)$$

where C_1 and C_2 are both normalization parameters. In order to normalize $p(\eta)$, η_{min} and η_{max} are needed. Here, $\eta_{min} = 2$ from Figure 9.4 as that's the saturated

overall EF over time. η_{\max} can be calculated from the weakest laser pump intensity that can damage CV. Due to the restriction in our experiments, the weakest signal we can measure is the data point on the most right in Figure 9.6 which is obviously not saturated. Therefore, we estimated that $\eta_{\max} = 60^4$ corresponding to g_{cr} where the end relative Raman intensity is 95% of saturated relative Raman signal value. Indeed, the choice of η_{\max} and η_{\min} will not affect resulted distribution significantly. By normalizing $p(\eta)$ with η_{\min} and η_{\max} , the probability density function of enhancement factor is

$$p(\eta) = 1.38e^{-\eta^{0.25}/19.6}\eta^{-1.75} \quad (9.9)$$

Two integrals of $p(\eta)$ are of great interests:

- i. Integral $\int_{\eta_1}^{\eta_2} p(\eta)d\eta$ represents the probability of sites with enhancement factor between η_1 and η_2 , which is actually the spatial distribution of enhancement factor on the surface. The integral calculates the surface area percentage where enhancement factor is between η_1 and η_2 .
- ii. Integral $\int_{\eta_1}^{\eta_2} p(\eta)\eta d\eta$ represents the overall enhancement for EF between η_1 and η_2 , which actually describes the signal contribution from the sites, hotspots, with EF between η_1 and η_2 .

Table 9.2 listed the hotspot spatial distribution (percentage of surface area calculated using $\int_{\eta_1}^{\eta_2} p(\eta)d\eta$) and corresponding Raman contribution distribution (percentage of total Raman signal calculated using $\int_{\eta_1}^{\eta_2} p(\eta)\eta d\eta$). Note that 86% of the spectral strength comes from less than 3% of the surface area, and enhancement factors as large as 10^7 are observed in really tiny portion of the surface locations. Consider the inter-particle gap in sample Y6, the average gap distance is around 10 nm, assume a 1 nm slice and half of the slice is the hotspot which has area 5 nm². That's about 1/ 10^7 of a beam spot area 50 μm^2 . 0.000088% of the surface area thus accounts for approximately 8 hotspots. It demonstrates again that only portion of the sample surface provides strong enhancement.

Table 9.2:

Contribution of the various site enhancements to the overall SERS signal.

Raman Enhancement Factor η_R	Percentage of Surface Area	Percentage Contribution to SERS Signal
$>10^7$	0.000088%	2.24%
$10^6 - 10^7$	0.0044%	24.2%
$10^5 - 10^6$	0.043%	25.3%
$10^4 - 10^5$	0.334%	20.3%
$10^3 - 10^4$	2.25%	14.0%
$10^2 - 10^3$	14.0%	8.78%
$<10^2$	83.4%	5.26%

$\int_{\eta_{\min}}^{\eta_{\max}} p(\eta)\eta d\eta \sim 90$ which is the expected overall enhancement from this sample Y6. It is larger than the direct EF $\eta_R = 22$ reported in the last chapter. Recall that the Raman spectra were integrated for 180 s during the measurement. The resulted enhancement factor is actually averaged over the first 180 s during which analyte damage occurs. Overall enhancement factor is therefore smaller than the calculation value assuming no damage. Also, the spectra plotted in Figure 8.4, Figures 9.1 ~ 9.4, and Figure 9.6 are three different data sets measured at different time. The direct comparisons among them are more qualitatively.

In conclusion, both temporal and spatial variances deteriorate overall signal enhancement. Temporal analysis of Raman signals on sample Y6 reveals surface-enhanced photodegradation (SEPD) process of CV on Ga NPs. Further experiments on sample Y6 excited by laser with a series of pump intensities reveals enhancement factor and signal contribution distributions over surface area. Only small portion (3%) of the surface area contributes to the majority of overall enhancement (86%). Local enhancement factor as large as 10^7 was obtained experimentally, which leaves great potential for future optimization of Ga nanostructures for UV plasmonics.

10. Conclusions and Perspectives

10.1 Conclusions

We have demonstrated that Gallium is a compelling UV plasmonic material through estimation and modeling, controlled synthesis, spatial and optical characterization, and UV SERS, UV SEF, and UV SEPD demonstration.

Plasmonic features of Ga and Ga NPs were estimated by Rayleigh scattering, Mie scattering, and numerical DDA methods. Rayleigh scattering results showed that the LSPR energies of nano-scale Ga NPs are within the UV range unlike the vis-NIR resonant Ag and Au NPs. Mie scattering results confirmed the UV resonances and revealed the size-dependent LSPR. Ga NPs with radii smaller than 60 nm possess LSPR energies within the UV range. The local field enhancement was also comparable to the performance of Au in the visible range while Ga NPs had a 3 ~ 4 times larger bandwidth than that of Au. DDA calculations on truncated NPs displayed a split in the lower energy “in-plane” and high energy “out-of-plane” modes. The presence of sapphire substrate redshifted the LSPR of Ga NP ensemble.

Ga NPs were grown in UHV MBE chamber. 99.99999% pure Ga flux impinged onto solid supports and formed self-assembled randomly distributed array of

hemispherical truncated NPs confirmed by SEM and AFM. Dosage and temperature controlled the NP formation. NP deposition can be halted when its LSPR reaches the desired value which is monitored by in situ SE. For a short deposition time, NP ensembles possess unimodal size distribution compared to the bimodal size distribution for longer deposition times, which is driven by surface diffusion. SE data measured at 70° confirmed the UV resonance of Ga NPs. NPs with a radius ranging from approximate 20 nm to 70 nm showed the LSPR from approximately 4.5 eV to 1.9 eV which demonstrated again its wide resonance tunability.

With Lorentz model fitting, Ga NP ensembles on solid supports behave like a single NP. Both the resonant energy and the damping constant of the lower energy in-plane mode decreased as $1/d$ with respect to the average NP diameter. However, variable-angle reflectance, VASE, and VAMM measurements reveal an unpredicted size-dependent dispersion and depolarization feature at near normal incidence which originates from the multiparticle effects and needs further exploration.

Three samples with Ga NP ensembles on sapphire deposited at 300K were used for UV plasmonic applications. Their mean radii are 23 nm, 26 nm, and 70 nm with a LSPR energy at 4.5 eV, 3.8 eV and 1.95 eV. A 5 nm film of crystal violet

was spin-coated upon these nanoparticles following excitation by a HeCd laser operating at 325 nm. A direct Raman enhancement factor of 5, 6 and 22 were reported for the three samples by comparing the Raman signal intensities at the 1617 cm^{-1} Raman mode. And the direct fluorescence enhancement factor of 2, 3, and 9 were obtained accordingly. Raman spectra were then measured over time and under the excitation of different laser powers. Photodegradation occurred at the beginning of laser excitation and saturated over time, which implied the existence of a strong local enhancement at the hotspots. Measured local Raman enhancement factors exceeding 10^7 demonstrated the potential of Ga NP arrays for plasmonically enhanced ultraviolet detection and remediation.

We demonstrated, for the first time, UV SERS, UV SEF, and UV SEPD on Ga NP arrays in experiments. The difference between a high local Raman enhancement factor exceeding 10^7 at hotspots and a modest overall signal enhancement suggests potential improvement of modeling and synthesis of Ga nanostructures are necessary.

10.2 Perspectives

10.2.1 Improved structures and extended applications

In our experiment, NPs are randomly distributed on solid supports with a bell-shape size distribution. Only a portion of the NPs are in a resonant state. Also, hotspots occur mainly between large and small NPs. As discussed in Chapter 9, these areas account for less than 3% of the sample surface. The overall averaged enhancement is far below the highest possible enhancement. Ideally, an array of monodispersed NP pairs, consisting of small and large NPs with a gap in the optimized dimension, will form an array of equally enhanced hotspots and thus strongly increase the overall enhancement. An attempt has been made to control size dispersion and interparticle distance as discussed in Chapter 5 by controlling the deposition temperature. Other approaches like lithography may be applied to this problem but will raise the difficulty and the cost [222].

The analyte used in the demonstration was crystal violet. As the enhancement majorly comes from the EM origin, the type of analyte should have minimal effect on the performance. Biomolecules, like nucleic acid or DNA, are of great interest in UV plasmonics. One of the advantages of UV SERS is its great potential in detecting biomolecules with their UV absorption resonance as discussed in Chapter 1. In addition to UV SERS, SEF, and SEPD, Ga

nanostructures may also be applied to other applications, like biosensing, bioimaging, and high efficiency solar cell, in the scope of LSP UV resonance.

10.2.2 Corrected modeling and spatially resolved characterization

In order to guide the synthesis of Ga NP pairs, where hotspot exists, models shall be developed to calculate light scattering or local EM field distribution from at least two NPs. Modeling in Chapter 2 was majorly considering single NP. This ignored the significant contribution from interparticle coupling. As mentioned at the end of Chapter 2, DDA, FDTD and the T-matrix method can be used to calculate light scattering from an array of nonspherical objects numerically. For the T-matrix, the object shall be axiosymmetric [223]. Calculation using these methods can confirm the presence of hotspots and also obtain an optimized value of radii and interparticle distance for NP pairs to guide synthesis.

Another correction on the model is the composition of Ga NPs. Previous research showed coexistence of liquid and solid phases of Ga in Ga NPs [83]. At room temperature, single Ga NP consists of a liquid phase shell and a solid phase core. Calculation suggests that liquid phase Ga reveals a larger enhancement and a bluer resonance energy than the solid phase Ga under same conditions [224]. Models discussed in Chapter 2 were for homogenous materials. Co-existence of different Ga phases requires nanoshell models for plasmon resonance

calculations [225]. This increases the difficulty of modeling but also provides another degree of freedom to tune the LSPR energy.

In addition to modeling, direct measurement of hotspots is also highly desirable. Modern techniques have been developed for spatially resolved optical measurements including spatially resolved SERS (SR SERS) [222], dark field optical microscopy [226], and near-field scanning optical microscopy (NSOM) [227]. Due to the optical diffraction limit discussed in Chapter 1, the spatial resolution of these measurements cannot reach below several hundred nanometers. The interparticle distance in our Ga NP ensembles is approximately 10 ~ 20 nm as shown in Chapter 5 which is far smaller than the resolution limit. Therefore, it is not applicable to use the above techniques to directly probe hotspots in our samples. Instead of photons, electron beams may be used to increase the resolution due to their much higher energy and thus smaller equivalent wavelength. Electron energy loss spectroscopy (EELS) [228] and cathodoluminescence (CL) [229] are recently adopted by plasmonics researchers for plasmon resonance characterization. Similar to SEM, the resolution of EELS and CL are usually around 1 ~ 2 nm given that the condition of the electron beam is fairly below the particle and interparticle dimensions of our Ga NP ensembles. Electron beams are used to excite plasmon modes and induce photon emissions.

Photon intensities are measured at each position over the sample and therefore can be used to infer local excitability.

10.2.3 UV plasmonic materials

While the ultimate goal of this research is to search for an ideal UV plasmonic materials and structures, this search may not be limited to Ga. Theoretical estimations have been reported to compare varieties of metals for their plasmonic properties in UV [64][230], including Ga, Mg, Al, Tl, In, and Pb. In addition to their plasmonic features, their material properties for handling and applications are also essential. Here, we generalize the criteria for UV plasmonics materials:

- i. Plasmon resonance in UV
- ii. Large local field enhancement
- iii. Wide tunability
- iv. Easy and cost effective synthesis
- v. Non-selective (on analyte)
- vi. Reproducibility and Stability (under temperature fluctuation and air exposure)
- vii. Environmental and human friendly (nontoxic)

As discussed in previous chapters, Ga is still an ideal material given these criteria although its local field enhancement in UV is not the highest comparing to Al and Mg. In order to benefit from both plasmonic and material features, multi-species structures may be developed to include two or more materials in alloy or nanoshell forms [81][82].

With matured modeling and improved synthesis, our vision is to unfold the full potential of gallium in nanoplasmonics, to continue searching for novel materials and structures, and to expand their applications in ultraviolet plasmonics.

References

- [1] I. Newton, "A letter of Mr. Isaac Newton, professor of the mathematicks in the University of Cambridge; containing his new theory about light and colors: Sent by the author to the publisher from Cambridge, Febr. 6. 1671/72; in order to be communicated to the R. Society", *Philosophical Transactions of the Royal Society of London* **6**, 3075 (1671).
- [2] J. Maxwell, "A treatise on electricity and magnetism", Clarendon Press, Oxford, 1873.
- [3] D. D. Ebbing, and R. Wentworth, "Introductory chemistry" 2nd Ed., Houghton Mifflin, US, 1998.
- [4] H. Hertz, "Electric waves ", Dover Publications, New York, 1893.
- [5] P. Villard, "Sur la réflexion et la réfraction des rayons cathodiques et des rayons déviés du radium", *Comptes rendus* **130**, 1010 (1900).
- [6] D. Burne, "Light", Dorling Kindersley, London 1992.
- [7] P. E. Hockberger, "A history of ultraviolet photobiology for humans, animals and microorganisms", *Photochemistry and Photobiology* **76**, 561 (2002).
- [8] J. E. Pickett, "Review and kinetic analysis of the photodegradation of UV absorbers", *Macromolecular Symposia* **115**, 127 (1997)
- [9] B. Singh and N. Sharma, "Mechanistic implications of plastic degradation", *Polymer Degradation and Stability* **93**, 561 (2008).
- [10] Z. Nie and E. Kumacheva, "Patterning surfaces with functional polymers", *Nature Materials* **7**, 277 (2008).
- [11] S. Pimputkar, J. S. Speck, S. P. DenBaars and S. Nakamura, "Prospects for LED Lighting", *Nature Photonics* **3**, 180 (2009).

- [12] K. Kneipp, H. Kneipp, I. Itzkan, R. R. Dasari, and M. S. Feld, "Ultrasensitive chemical analysis by Raman spectroscopy", *Chemical Reviews* **99**, 2957 (1999).
- [13] J. G. Grasselli, and B. J. Bulkin, "Analytical Raman spectroscopy", John Wiley & Sons, Chichester, 1991.
- [14] J. J. Laserna, "Modern techniques in Raman spectroscopy", John Wiley & Sons, Chichester, 1996.
- [15] I. R. Lewis, and H. Edwards, "Handbook of Raman spectroscopy", Marcel Dekker, New York, 2001.
- [16] S. Nie, and S. R. Emory, "Probing Single Molecules and Single Nanoparticles by Surface-Enhanced Raman Scattering", *Science* **21**, 1102 (1997)
- [17] S. A. Asher, *Ultraviolet Raman spectrometry*, John Wiley & Sons, Chichester 2002.
- [18] D. P. Strommen, and K. Nakamoto, "Resonance Raman spectroscopy", *Journal of Chemical Education* **54**, 474 (1977).
- [19] A. M. Zaitsev, "Optical properties of diamond", Springer, New York, 2001.
- [20] C. F. Klingshirm, "Semiconductor optics" 3rd Ed, Springer, New York, 2007.
- [21] S. A. Asher, "UV resonance Raman spectroscopy for analytical, physical, and biophysical chemsity. Part 1", *Analytical Chemistry* **65**, 59A (1993).
- [22] S. A. Asher, "UV resonance Raman spectroscopy for analytical, physical, and biophysical chemsity. Part 2", *Analytical Chemistry* **65**, 201A (1993).
- [23] S. A. Asher, M. Ludwig, and C. R. Johnson, "UV resonance Raman excitation profiles of the aromatic amino acids", *Journal of the American Chemical Society* **108**, 3186 (1986).

- [24] W. H. Nelson, R. Manoharan, and J. F. Sperry, "UV resonance Raman spectroscopy", *Applied Spectroscopy Reviews* **27**, 67 (1992).
- [25] S. A. Asher, "UV resonance raman studies of molecular structure and dynamics", *Annual Review of Physical Chemistry* **39**, 537 (1988).
- [26] A. Taguchi, N. Hayazawa, K. Furusawa, H. Ishitobi, and S. Kawata, "Deep-UV tip-enhanced Raman scattering," *Journal of Raman Spectroscopy* **40**, 1324 (2009).
- [27] N. Mattiucci, G. D'auganno, H. O. Everitt, J. V. Foreman, J. M. Callahan, M. C. Buncick, and M. J. Bloemer, "Ultraviolet surface-enhanced Raman scattering at the plasmonic band edge of a metallic grating", *Optics Express* **20**, 1868 (2012).
- [28] R. Z. Lei, W. Tsai, I. Aberg, T. B. O'Reilly, J. L. Hoyt, D. A. Antoniadis, H. I. Smith, A. J. Paul, M. L. Green, J. Li, and R. Hull, "Strain relaxation in patterned strained silicon directly on insulator structures", *Applied Physics Letters* **85**, 251926 (2005).
- [29] D. A. Tenne, P. Turner, J. D. Schmitz, M. Biegalski, Y. L. Li, L. Q. Chen, A. Soukiassian, S. Trolier-McKinstry, D. G. Schlom, X. X. Xi, D. D. Fong, P. H. Fuoss, J. A. Eastman, G. B. Stephenson, C. Thompson, and S. K. Streiffer, "Ferroelectricity in ultrathin BaTiO₃ films: Probing the size effect by ultraviolet Raman spectroscopy", *Physical Review Letters* **103**, 177601 (2009).
- [30] E. Abbe. "A contribution to the theory of the microscope and the nature of microscopic vision". *Proceedings of the Bristol Naturalists' Society* **1**, 20 (1874).
- [31] "Strain measurements of a Si cap layer deposited on a SiGe substrate determination of Ge content", HORIBA Jobin Yvon Raman Application Note.
- [32] V. Pajcini, C. H. Munro, R. W. Bormett, R. E. Witkowaski, and S. A. Asher, "UV Raman microspectroscopy: Spectral and spatial selectivity with sensitivity and simplicity", *Applied Spectroscopy* **51**, 81 (1997).

- [33] M. Fleischmann, P. J. Hendra, and A. J. McQuillan, "Raman spectra of pyridine adsorbed at a silver electrode", *Chemical Physics Letters* **26**, 163 (1974).
- [34] D. L. Jeanmaire, R. P. Van Duyne, "Surface Raman spectroelectrochemistry: Part I. Heterocyclic, aromatic, and aliphatic amines adsorbed on the anodized silver electrode", *Journal of Electroanalytical Chemistry and Interfacial Electrochemistry* **84**, 1 (1977).
- [35] W. Kim, V. P. Safonov, V. M. Shalaev, and R. L. Armstrong, "Fractals in microcavities: Giant coupled, multiplicative enhancement of optical responses", *Physical Review Letters* **82**, 4811 (1999).
- [36] T. Vo-Dinh, "Surface-enhanced Raman spectroscopy using metallic nanostructures", *Trends in Analytical Chemistry* **17**, 557 (1998).
- [37] S. Schlucker, "SERS microscopy: Nanoparticle probes and biomedical applications", *ChemPhysChem* **10**, 1344 (2009).
- [38] R. Bogue, "Nanosensors: A review of recent progress", *Sensor Review* **28**, 12 (2008).
- [39] J. N. Anker, W. P. Hall, O. Lyandres, N. C. Shah, J. Zhao, and R. P. Van Duyn, "Biosensing with plasmonic nanosensors", *Nature Materials* **7**, 442 (2008).
- [40] K. Kneipp, Y. Wang, H. Kneipp, L. T. Perelman, I. Itzkan, R. R. Dasari, and M. S. Feld, "Single molecule detection using surface-enhanced Raman scattering (SERS)", *Physical Review Letters* **78**, 1667 (1997)
- [41] K. Kneipp, H. Kneipp, G. Deinum, I. Itzkan, R. R. Dasari, and M. S. Feld, "Single-molecule detection of a cyanine dye in silver colloidal solution using near-infrared surface-enhanced Raman scattering", *Applied Spectroscopy* **52**, 175 (1998).
- [42] X.-M. Qian, and S. M. Nie, "Single-molecule and single-nanoparticle SERS : from fundamental mechanisms to biomedical applications", *Chemical Society Reviews* **37**, 912 (2008).

- [43] K. Kneipp, A. S. Abigail, H. Kneipp, K. Badizadegan, N. Yoshizawa, C. Boone, K. E. Shafer-Peltier, J. T. Motz, R. R. Dasari, and M. S. Feld, "Surface-enhanced Raman spectroscopy in single living cells using gold nanoparticles", *Applied Spectroscopy* **56**, 150 (2002).
- [44] M. Moskovits, "Surface-enhanced spectroscopy", *Reviews of Modern Physics* **57**, 783 (1985).
- [45] G. McNay, D. Eustace, W. E. Smith, K. Faulds, and D. Graham, "Surface-enhanced Raman scattering (SERS) and Surface-enhanced resonance Raman scattering (SERRS): A review of applications", *Applied Spectroscopy* **65**, 825 (2011).
- [46] G. C. Schatz, M. A. Young, and R. P. Van Duyne, "Electromagnetic mechanism of SERS", *Surface-Enhanced Raman Scattering: Topics in Applied Physics* **103**, 19 (2006).
- [47] B. Sharma, R. R. Frontiera, A.-I. Henry, E. Ringe, and R. P. Van Duyne, "SERS: Materials, applications, and the future", *Materials Today* **15**, 16 (2012).
- [48] Z. Q. Tian, "Surface-enhanced Raman spectroscopy: Advancements and applications", *Journal of Raman Spectroscopy* **36**, 466 (2005).
- [49] K. Kneipp, Y. Wang, H. Kneipp, I. Itzkan, R. R. Dasari, and M. S. Feld, "Population Pumping of Excited Vibrational States by Spontaneous Surface-Enhanced Raman Scattering", *Physical Review Letters* **76**, 2444 (1996).
- [50] A. Campion, and P. Kambhampati, "Surface-enhanced Raman scattering", *Chemical Society Reviews* **27**, 241 (1998).
- [51] I. Chou, M. Benford, H. Beier, M. Wang, N. Jing, T. A. Good, J. Kameoka, and G. L. Coté, "Nanofluidic Biosensing for β -amyloid Detection Using Surface Enhanced Raman Spectroscopy (SERS)", *Nano Letters* **8**, 1729 (2008).
- [52] R. M. Christie, "Fluorescent dyes", *Review of Progress in Coloration and Related Topics* **23**, 1 (1993).

- [53] S. Weiss, "Fluorescence spectroscopy of single biomolecules", *Science* **12**, 1675 (1999).
- [54] J. R. Lakowicz, "Principles of fluorescence spectroscopy" 3rd Ed, Springer, New York, 2006.
- [55] M.-A. Mycek, B. W. Pogue, "Handbook of biomedical fluorescence", Marcel Dekker, New York, 2003.
- [56] D. L. Taylor, A. S. Waggoner, F. Lanni, R. F. Murphy, and R. R. Birge, "Applications of fluorescence in the biomedical sciences", Alan R Liss, New York, 1986.
- [57] J. R. Lakowicz, C. D. Geddes, I. Gryczynski, J. Malicka, Z. Gryczynski, K. Aslan, J. Lukomska, E. Matveeva, J. Zhang, R. Badugu, and J. Huang, "Advances in surface-enhanced fluorescence", *Journal of Fluorescence* **14**, 425 (2004).
- [58] P. Hildebrandt, and M. Stockburger, "Surface-enhanced resonance Raman spectroscopy of Rhodamine 6G adsorbed on colloidal silver", *Journal of Physical Chemistry* **88**, 5935 (1984).
- [59] A. R. Guerrero, Y. Zhang, and R. F. Aroca, "Experimental confirmation of local field enhancement determining far-field measurements with shell-isolated silver nanoparticles", *Small* **8**, 2964 (2012).
- [60] A. M. Gabudean, M. Focsan, and S. Astilean, "Gold nanorods performing as dual-modal nanoprobe via metal-enhanced fluorescence (MEF) and surface-enhanced Raman scattering (SERS)", *Journal of Physical Chemistry C* **116**, 12240 (2012).
- [61] C. F. Bohren, and D.R. Huffman, "Absorption and scattering of light by small particles" Vol. 1, John Wiley & Sons, New York, 1998.
- [62] E. Hutter, and J. H. Fendler, "Exploitation of localized surface plasmon resonance", *Advanced Materials* **16**, 1685 (2004).
- [63] K. Kneipp, H. Kneipp, and J. Kneipp, "Surface-enhanced Raman scattering in local optical fields of silver and gold nanoaggregates - from single-molecule Raman spectroscopy to ultrasensitive probing in live cells", *Accounts of Chemical Research* **39**, 443 (2006).

- [64] E. J. Zeman, and G. C. Schatz, "An accurate electromagnetic theory study of surface enhancement factors for silver, gold, copper, lithium, sodium, aluminum, gallium, indium, zinc, and cadmium", *Journal of Physical Chemistry* **91**, 634 (1987).
- [65] B. Ren, X.-F. Lin, Z.-L. Yang, G.-K. Liu, R. F. Aroca, B.-W. Mao, and Z.-Q. Tian, "Surface-enhanced Raman scattering in the ultraviolet spectral region: UV-SERS on rhodium and ruthenium electrodes", *Journal of the American Chemical Society* **125**, 9598 (2003).
- [66] L. Cui, S. Mahajan, R. M. Cole, B. Soares, P. N. Bartlett, J. J. Baumberg, I. P. Hayward, B. Ben, A. E. Russell, and Z. Q. Tian, "UV SERS at well ordered Pd sphere segment void (SSV) nanostructures", *Physical Chemistry Chemical Physics* **11**, 1023 (2009)
- [67] X.-F. Lin, B. Ren, Z.-L. Yang, G.-K. Liu, and Z.-Q. Tian, "Surface-enhanced Raman spectroscopy with ultraviolet excitation", *Journal of Raman Spectroscopy* **36**, 606 (2005).
- [68] P. Wang, and G. Wu, "Ultraviolet laser excited surface enhanced Raman scattering of thiocyanate ion on the Au electrode", *Chemical Physics Letters* **385**, 96 (2004).
- [69] J. W. Wang, W. N. Wang, and Y. Fan, "Surface-enhanced Raman scattering studies on the adsorption of p-nitrobenzoic acid at Au electrode under different potential with ultraviolet excitation", *Vibrational Spectroscopy* **40**, 197 (2006).
- [70] L Cui, A. Wang, D.-Y. Wu, B. Ren, and Z.-Q. Tian, "Shaping and shelling Pt and Pd nanoparticles for ultraviolet laser excited surface-enhanced Raman scattering", *Journal of Physical Chemistry C* **112**, 17618 (2008).
- [71] L. Cui, D.-Y. Wu, A. Wang, B. Ren, and Z.-Q. Tian, "Charge-transfer enhancement involved in the SERS of adenine on Rh and Pd demonstrated by ultraviolet to visible laser excitation", *Journal of Physical Chemistry C* **114**, 16588 (2010).
- [72] T. Dorfer, M. Schmitt, and J. Popp, "Deep-UV surface-enhanced Raman scattering", *Journal of Raman Spectroscopy* **38**, 1379 (2007).

- [73] S. K. Jha, Z. Ahmed, M. Agio, Y. Ekinici, and J. F. Loffler, "Deep-UV surface-enhanced resonance Raman scattering of adenine on aluminum nanoparticle arrays", *Journal of the American Chemical Society* **134**, 1966 (2012).
- [74] P. Wu, M. Losurdo, T. H. Kim, G. Bruno, H. O. Everitt, and A. S. Brown, "Real-time plasmon resonance tuning of liquid Ga nanoparticles by in situ spectroscopic ellipsometry", *Applied Physics Letters* **90**, 103119 (2007).
- [75] P. Wu, M. Losurdo, T. H. Kim, G. Bruno, and A. S. Brown, "In situ spectroscopic ellipsometry to monitor surface plasmon resonant group-III metals deposited by molecular beam epitaxy", *Journal of Vacuum Science & Technology B* **25**, 1019 (2007).
- [76] P. Wu, M. Losurdo, T. H. Kim, G. Bruno, and A. S. Brown, "Plasmonic gallium nanoparticles on polar semiconductors: Interplay between nanoparticle wetting, localized surface plasmon dynamics, and interface charge", *Langmuir* **25**, 924 (2009).
- [77] Y. Gogotsi, "Nanomaterials Handbook", CRC Press, Boca Raton, 2006.
- [78] T. Braun, A. Schubert, and S. Zsindely, "Nanoscience and nanotechnology on the balance", *Scientometrics* **38**, 321 (1997).
- [79] M. Faraday, "Experimental relations of gold (and other metals) to light", *Philosophical Transactions of the Royal Society of London* **147**, 145 (1857).
- [80] H. S. Zhou, I. Honma, H. Komiyama, and J. W. Haus, "Controlled synthesis and quantum-size effect in gold-coated nanoparticles", *Physical Review B* **50**, 12052 (1994).
- [81] P. C. Wu, M. Losurdo, T.-H. Kim, B. Garcia-Cueto, F. Moreno, G. Bruno, and A. S. Brown, "Ga-Mg core-shell nanosystem for a novel full color plasmonics", *Journal of Physical Chemistry C* **115**, 13571 (2011).
- [82] P. C. Wu, T.-H. Kim, A. Suvorova, M. Giangregorio, M. Saunders, G. Bruno, A. S. Brown, and M. Losurdo, "GaMg alloy nanoparticles for broadly tunable plasmonics", *Small* **7**, 751 (2011).

- [83] S. Pochon, K. F. MacDonald, R. J. Knize, and N. I. Zheludev, "Phase coexistence in gallium nanoparticles controlled by electron excitation", *Physical Review Letters* **92**, 145702 (2004).
- [84] B. O'Regan, and M. Gratzel, "A low-cost, high-efficiency solar cell based on dye-sensitized colloidal TiO₂ films", *Nature* **353**, 737 (1991).
- [85] V. L. Colvin, M. C. Schlamp, and A. P. Alivisatos, "Light-emitting diodes made from cadmium selenide nanocrystals and a semiconducting polymer", *Nature* **370**, 354 (1994).
- [86] P. X. Gao, Y. Ding, W. Mai, W. L. Hughes, C. Lao, and Z. L. Wang, "Conversion of Zinc Oxide nanobelts into superlattice-structured nanohelices", *Science* **309**, 1700 (2005).
- [87] M. C. Daniel, and D. Astruc, "Gold nanoparticles: Assembly, supramolecular chemistry, quantum-size-related properties, and applications toward biology, catalysis, and nanotechnology", *Chemical Reviews* **104**, 293 (2004).
- [88] A. M. Gobin, M. H. Lee, N. J. Halas, W. D. James, R. A. Drezek, and J. L. West, "Near-infrared resonant nanoshells for combined optical imaging and photothermal cancer therapy", *Nano Letters* **7**, 1929 (2007)
- [89] P. Drude, "Zur Elektronentheorie der metalle", *Annalen der Physik* **306**, 566 (1900); P. Drude, "Zur Elektronentheorie der metalle; II. teil. galvanomagnetische und thermomagnetische effecte". *Annalen der Physik* **308**, 369 (1900)
- [90] U. Kreibig, and M. Vollmer, "Optical properties of metal clusters", Springer, Berlin, 1995.
- [91] A. V. Sokolov, "Optical properties of metals", Elsevier, New York, 1967.
- [92] R. B. M. Schasfoort, and A. J. Tudos, "Handbook of surface plasmon resonance", Royal Society of Chemistry, Cambridge, 2008.
- [93] K. A. Willets, and R. P. Van Duyne, "Localized surface plasmon resonance spectroscopy and sensing", *Annual Reviews of Physical Chemistry* **58**, 267 (2007).

- [94] M. A. Ordal, L. L. Long, R. J. Bell, S. E. Bell, R. R. Bell, R. W. Alexander Jr, and C. A. Ward, "Optical properties of the metals Al, Co, Cu, Au, Fe, Pb, Ni, Pd, Pt, Ag, Ti, and W in the infrared and far infrared", *Applied Optics* **22**, 1099 (1983).
- [95] G. Mie, "Beiträge zur optik trüber medien, speziell kolloidaler metallösungen", *Annalen der Physik* **330**, 377 (1908).
- [96] K. L. Kelly, E. Coronado, L. L. Zhao, and G. C. Schatz, "The optical properties of metal nanoparticles: The influence of size, shape, and dielectric environment", *Journal of Physical Chemistry B* **107**, 668 (2003).
- [97] K.-H. Su, Q.-H. Wei, X. Zhang, J. J. Mock, D. R. Smith, and S. Schultz, "Interparticle coupling effects on plasmon resonances of nanogold particles", *Nano Letters* **3**, 1087 (2003)
- [98] M. Shopa, K. Kolwas, A. Derkachova, and G. Derkachov, "Dipole and quadrupole surface plasmon resonances contributions in formation of near-field images of a gold nanosphere", *Opto-Electronics Review* **18**, 421 (2010).
- [99] A. D. McFarland, and R. P. Van Duyne, "Single silver nanoparticles as real-time optical sensors with zeptomole sensitivity", *Nano Letters* **3**, 1057 (2003).
- [100] J. J. Mock, R. T. Hill, A. Degiron, S. Zauscher, A. Chilkoti, and D. R. Smith, "Distance-dependent plasmon resonant coupling between a gold nanoparticle and gold film", *Nano Letters* **8**, 2245 (2008).
- [101] G. Sun, and J. B. Khurgin, "Optimization of the nanolens consisting of coupled metal nanoparticles: An analytical approach", *Applied Physics Letters* **98**, 153115 (2011).
- [102] A. O. Pinchuk, and G. C. Schatz, "Nanoparticle optical properties: Far- and near-field electrodynamic coupling in a chain of silver spherical nanoparticles", *Material Science and Engineering: B* **149**, 251 (2008).

- [103] S. Eustis, and M. A. El-Sayes, "Why gold nanoparticles are more precious than pretty gold: Noble metal surface plasmon resonance and its enhancement of the radiative and nonradiative properties of nanocrystals of different shapes", *Chemical Society Reviews* **35**, 209 (2006).
- [104] J. Parsons, C. P. Burrows, J. R. Sambles, and W. L. Barnes, "A comparison of techniques used to simulate the scattering of electromagnetic radiation by metallic nanostructures", *Journal of Modern Optics* **57**, 356 (2010).
- [105] J. Strutt, "On the scattering of light by small particles", *Philosophical Magazine* **41**, 447 (1871).
- [106] S. Franzen, "Intrinsic Limitations on the $|E|^4$ Dependence of the Enhancement Factor for Surface-Enhanced Raman Scattering", *Journal of Physical Chemistry C* **113**, 5912 (2009)
- [107] M. Born, and E. Wolf, "Principles of optics" 7th Ed, Cambridge University Press, Cambridge, 1999.
- [108] J. B. Jackson, S. L. Westcott, L. R. Hirsch, J. L. West, and N. J. Halas, "Controlling the surface enhanced Raman effect via the nanoshell geometry", *Applied Physics Letters* **82**, 257 (2003).
- [109] M. Quinten, "Optical properties of nanoparticl system", Wiley-VCH Verlag & Co, Weinheim, 2011.
- [110] W. J. Wiscombe, "Improved Mie scattering algorithms", *Applied Optics* **19**, 1505 (1980).
- [111] S. Lal, S. Link, and N. J. Halas, "Nano-optics from sensing to waveguiding", *Nature Photonics* **1**, 641 (2007).
- [112] T. Klar, M. Perner, S. Grosse, G. von Plessen, W. Spirkel, and J. Feldmann, "Surface-plasmon resonances in single metallic nanoparticles", *Physical Review Letters* **80**, 4249 (1998).
- [113] P. Laven, MiePlot v4.3, Geneva, Switzerland.

- [114] H. DeVoe, "Optical properties of molecular aggregates. I. classical model of electronic absorption and refraction", *Journal of Chemical Physics* **41**, 393 (1964).
- [115] E. M. Purcell, and C. R. Pennypacker, "Scattering and absorption of light by nonspherical dielectric grains", *Astrophysical Journal* **186**, 705 (1973).
- [116] A. Brioude, and M. P. Pileni, "Silver nanodisks: Optical properties study using the discrete dipole approximation method", *Journal of Physical Chemistry B* **109**, 23371 (2005).
- [117] A. Brioude, X. C. Jiang, and M. P. Pileni, "Optical properties of gold nanorods: DDA simulations supported by experiments", *Journal of Physical Chemistry B* **109**, 13138 (2005).
- [118] B. T. Draine, and P. J. Flatau, "Discrete-dipole approximation for scattering calculations", *Journal of the Optical Society of America A* **11**, 1491 (1994).
- [119] M. A. Yurkin, and A. G. Hoekstra, "The discrete dipole approximation: An overview and recent developments", *Journal of Quantitative Spectroscopy and Radiative Transfer* **106**, 558 (2007).
- [120] M. A. Yurkin¹, A. G. Hoekstra, R. S. Brock, and J. Q. Lu, "Systematic comparison of the discrete dipole approximation and the finite difference time domain method for large dielectric scatterers", *Optics Express* **15**, 17902 (2007).
- [121] T. Wriedt, and U. Comber, "Comparison of computational scattering methods", *Journal of Quantitative Spectroscopy and Radiative Transfer* **60**, 411 (1998).
- [122] P. Albella, B. Garcia-Cueto, F. Gonzalez, F. Moreno, P. C. Wu, T.-H. Kim, A. S. Brown, Y. Yang, H. O. Everitt, and G. Videen, "Shape matters: Plasmonic nanoparticle shape enhances interaction with dielectric substrate", *Nano Letters* **11**, 3531 (2011).
- [123] E. Bartholinus, "Experiments with the double refracting Iceland crystal which led to the discovery of a marvelous and strange refraction", *cph*, 1669.

- [124] C. Brosseau, "Chapter 3 - Polarization and coherence optics: Historical perspective, status, and future directions", *Progress in Optics* **54**, 149 (2010).
- [125] N. Kaiser, "Review of the fundamentals of thin-film growth", *Applied Optics* **41**, 3053 (2002).
- [126] D. E. Aspnes, "Studies of surface, thin film and interface properties by automatic spectroscopic ellipsometry", *Journal of Vacuum Science and Technology* **18**, 289 (1981).
- [127] M. Losurdo, G. Bruno, T. H. Kim, S. Choi, A. Brown, and A. Moto, "Nucleation and growth mode of the molecular beam epitaxy of GaN on 4-SiC exploiting real time spectroscopic ellipsometry", *Journal of Crystal Growth* **284**, 156 (2005).
- [128] D. Bi, J. Zhang, B. Chakraborty, and R. P. Behringer, "Jamming by Shear", *Nature* **480**, 355 (2011)
- [129] J. Lindqvist, and U. Akesson, "Image analysis applied to engineering geology, a literature review", *Bulletin of Engineering Geology and the Environment* **60**, 117 (2001).
- [130] B. Drvillion, "Spectroscopic ellipsometry in the infrared range", *Thin Solid Films* **313**, 625 (1998).
- [131] T. W. Cronin, N. Shashar, R. L. Caldwell, J. Marshall, A. G. Cheroske, and T.-H. Chiou, "Polarization vision and its role in biological signaling" *integrative and comparative biology* **43**, 549 (2003).
- [132] R. C. Jones, "A new calculus for the treatment of optical systems", *Journal of the Optical Society of America* **31**, 488 (1941).
- [133] S.-Y. Lu, R. A. Chipman, "Mueller matrices and the degree of polarization", *Optics Communications* **146**, 146 (1998).
- [134] D. H. Goldstein, "Polarized light" 3rd Ed, CRC Press, Boca Raton, 2011.

- [135] J. J. Stamnes, and G. S. Sithambaranathan, "Reflection and refraction of an arbitrary electromagnetic wave at a plane interface separating an isotropic and a biaxial medium", *Journal of the Optical Society of America A* **18**, 3119 (2001).
- [136] D. E. Aspnes, "Expanding horizons: New developments in ellipsometry and polarimetry", *Thin Solid Films* **455**, 3 (2004).
- [137] J. Orear, "Fundamental Physics" 2th Ed, John Wiley and Sons, 1967.
- [138] K. Vedam, "Spectroscopic ellipsometry: A historical overview", *Thin Solid Films* **313**, 1 (1998).
- [139] Maria Losurdo, M. Bergmair, G. Bruno, *et al.*, "Spectroscopic ellipsometry and polarimetry for materials and systems analysis at the nanometer scale: State-of-the-art, potential, and perspectives", *Journal of Nanoparticle Research* **11**, 1521 (2009).
- [140] M. T. Swihart, "Vapor-phase synthesis of nanoparticles", *Current Opinion in Colloid & Interface Science* **8**, 127 (2003).
- [141] D. L. Feldheim, and C. A. Foss, "Metal nanoparticles: Synthesis, characterization, and applications", Marcel Dekker, Inc., New York, 2002.
- [142] A. Y. Cho, and J. R. Arthur, "Molecular beam epitaxy", *Progress in Solid State Chemistry* **10**, 157 (1975).
- [143] F. Rinaldi, "Basics of molecular beam epitaxy (MBE)", Annual Report, Optoelectronics Department, University of Ulm, 2002.
- [144] J. R. Arthur, "Molecular beam epitaxy", *Surface Science* **500**, 189 (2002).
- [145] K. A. Bertness, A. Roshko, L. M. Mansfield, T. E. Harvey, and N. A. Sanford, "Mechanism for spontaneous growth of GaN nanowires with molecular beam epitaxy", *Journal of Crystal Growth* **310**, 3154 (2008).
- [146] A. P. Alivisatos, "Semiconductor clusters, nanocrystals, and quantum dots", *Science* **271**, 933 (1996).

- [147] T. Maho, T. Kuroda, S. Sanguinetti, T. Ochiai, T. Tateno, J. Kim, T. Noda, M. Kawabe, K. Sakoda, G. Kido, and N. Koguchi, "Self-assembly of concentric quantum double rings", *Nano Letters* **5**, 425 (2005).
- [148] C.-Z. Chang, J. Zhang, and X. Feng *et al.*, "Experimental observation of the quantum anomalous hall effect in a magnetic topological insulator", *Science* **340**, 167 (2013)
- [149] K. Prabhakaran, K. V. P. Muhammed Shafi, A. Ulman, and T. Ogino, "Nanoparticle-induced light emission from multi-functionalized silicon", *Advanced Materials* **13**, 1859 (2001)
- [150] J. Blackman, "Handbook of metal physics: Metallic nanoparticles", Elsevier, Amsterdam, 2009.
- [151] H. Brune, "Microscopic view of epitaxial metal growth: Nucleation and aggregation", *Surface Science Reports* **31**, 125 (1998).
- [152] J. W. Evans, P. A. Thiel, and M. C. Bartelt, "Morphological evolution during epitaxial thin film growth: Formation of 2D islands and 3D mounds", *Surface Science Reports* **61**, 1 (2006).
- [153] T. K. Sau, and A. L. Rogach, "Complex-shaped metal nanoparticles: Bottom-up syntheses and applications", Wiley-VCH, Weinheim, 2012.
- [154] S. A. Chamber, "Epitaxial growth and properties of thin film oxides", *Surface Science Reports* **39**, 105 (2000).
- [155] M. Hida, A. Sakakibara, and H. Kamiyabu, "Surface-tension and supercooling phenomenon of liquid Ga", *Journal of the Japan Institute of Metals* **53**, 1263 (1989).
- [156] E. Sondergard, R. Kofman, P. Cheyssac, and A. Stella, "Production of nanostructures by self-organization of liquid Volumer-Weber films", *Surface Science* **364**, 467 (1996).
- [157] M. Zinke-Allmang, L. C. Feldman, and M. H. Grabow, "Clustering on surfaces", *Surface Science Report* **16**, 377 (1992).
- [158] J. A. Venables, "Atomic process in crystal growth", *Surface Science* **299**, 798 (1994).

- [159] Z. Zhang, and M. G. Lagally, "Atomistic progresses in the early stages of thin-film growth", *Science* **276**, 377 (1997).
- [160] S. Choi, T.-H. Kim, A. Brown, H. O. Everitt, M. Losurdo, G. Bruno, and A. Moto, "Kinetics of gallium adsorption and desorption on (0001) gallium nitride surfaces", *Applied Physics Letter* **89**, 181915 (2006).
- [161] K. Ploog, "Molecular beam epitaxy of III-V compounds", *III-V Semiconductors: Crystals* **3**, 73 (1980).
- [162] K. W. Kolasinski, "Surface science: Foundations of catalysis and nanoscience", John Wiley & Sons, Chichester, 2008.
- [163] C. S. Barrett, and F. J. Spooner, "Lattice constant of gallium at 297K", *Nature* **207**, 1382 (1965).
- [164] E. Meyer, "Atomic force microscopy", *Progress in Surface Science* **41**, 3 (1992).
- [165] K. Kalantar-zadeh, and B. Fry, "Nanotechnology-enabled sensor", Springer, New York, 2008.
- [166] A. Mechler, J. Kopniczky, J. Kokavecz, A. Hoel, C.-G. Granqvist, and P. Heszler, "Anomalies in nanostructure size measurements by AFM", *Physical Review B* **72**, 125407 (2005).
- [167] C. Ratsch, A. Zangwill, P. Smilauer, and D. D. Vvedensky, "Saturation and scaling of epitaxial island densities", *Physical Review Letters* **72**, 3194 (1994).
- [168] G. C. Schartz, "Electrodynamics of nonspherical noble metal nanoparticles and nanoparticle aggregates", *Journal of Molecular Structure: THEOCHEM* **573**, 73 (2001).
- [169] D. E. Aspnes, "Optical properties of thin films", *Thin Solid Films* **89**, 249 (1982).
- [170] E. G. Bortchagovsky, V. Z. Lozovski, and T. O. Mishakova, "Model for the effective medium approximation of nanostructured layers with the account of interparticle interactions", *SPIE Proceedings* **8070**, 807018 (2011).

- [171] T. W. H. Oates, H. Sugime, and S. Noda, "Combinatorial surface-enhanced Raman spectroscopy and spectroscopic ellipsometry of silver island films", *Journal of Physical Chemistry C* **113**, 4820 (2009).
- [172] T. W. H. Oates, H. Womeester, and H. Arwin, "Characterization of plasmonic effects in thin films and metamaterials using spectroscopic ellipsometry", *Progress in Surface Science* **86**, 328 (2011).
- [173] H. Fujiwara, "Spectroscopic Ellipsometry: Principles and Applications", John Wiley & Sons, Chichester, 2007.
- [174] G. E. Jellison, Jr, "Spectroscopic ellipsometry data analysis: measured versus calculated quantities", *Thin Solid Films* **313**, 33 (1998).
- [175] S. Berciaud, L. Cognet, P. Tamarat, and B. Lounis, "Observation of intrinsic size effects in the optical response of individual gold nanoparticles", *Nano Letters* **5**, 515 (2005).
- [176] D. Tonova, M. Patrini, P. Tognini, A. Stella, P. Cheyssac, and R. Kofman, "Ellipsometric study of optical properties of liquid Ga nanoparticles", *Journal of Physics: Condensed Matter* **11**, 2211 (1999).
- [177] D. Bedeaux, J. Vlieger, "Optical properties of surfaces" 2nd Ed, Imperial College Press, London, 2004.
- [178] T. Smith, "Effect of surface roughness on ellipsometry of aluminum", *Surface Science* **56**, 252 (1976).
- [179] J. A. Woollam, B. D. Johs, C. M. Herzinger, J. N. Hilfiker, R. A. Synowicki, and C. L. Bungay, "Overview of variable-angle spectroscopic ellipsometry (VASE): I. Basic theory and typical applications", *SPIE Proceedings* **CR72**, 3 (1999).
- [180] B. D. Johs, J. A. Woollam, C. M. Herzinger, J. N. Hilfiker, R. A. Synowicki, and C. L. Bungay, "Overview of variable-angle spectroscopic ellipsometry (VASE): II. Advanced applications", *SPIE proceedings* **CR72**, 29 (1999).

- [181] J. A. Woollam, P. G. Snyder, and M. C. Rost, "Variable angle spectroscopic ellipsometry: A non-destructive characterization technique for ultrathin and multilayer materials", *Thin Solid Films* **166**, 317 (1988).
- [182] H.-L. Zhang, S. D. Evans, J. R. Henderson, "Spectroscopic ellipsometric evaluation of gold nanoparticle thin films fabricated using layer-by-layer self-assembly", *Advanced Materials* **15**, 531 (2003) .
- [183] T. W. H. Oates, M. Ranjan, S. Facsko, and H. Arwin, "Highly anisotropic effective dielectric functions of silver nanoparticle arrays", *Optics Express* **19**, 2014 (2011).
- [184] S.-Y. Lu, R. A. Chipman, "Mueller matrices and the degree of polarization", *Optics Communications* **146**, 141 (1998).
- [185] M. Francoeur, P. G. Venkata, and M. P. Menguc, "Sensitivity analysis for characterization of gold nanoparticles and agglomerates via surface plasmon scattering patterns", *Journal of Quantitative Spectroscopy and Radiative Transfer* **106**, 44 (2007).
- [186] M. M. Asian, M. P. Menguc, and G. Videen, "Characterization of metallic nano-particles via surface wave scattering: B. Physical concept and numerical experiments", *Journal of Quantitative Spectroscopy and Radiative Transfer* **93**, 207 (2005).
- [187] D. M. Anderson, and R. Barakat, "Necessary and sufficient conditions for a Mueller matrix to be derivable from a Jones matrix", *Journal of the Optical Society of America A* **11**, 2305 (1994).
- [188] P. D. Rogers, T. D. Kang, T. Zhou, M. Kotelyanskii, and A. A. Sirenko, "Mueller matrices for anisotropic metamaterials generated using 4×4 matrix formalism", *Thin Solid Films* **519**, 2668 (2011).
- [189] A. Laskarakis, S. Logothetidis, E. Pavlopoulou, and M. Gioti, "Mueller matrix spectroscopic ellipsometry: Formulation and application", *Thin Solid Films* **455**, 43 (2004).
- [190] N. Ghosh, P. K. Gupta, A. Pradhan, S. K. Majumder, "Anomalous behavior of depolarization of light in a turbid medium", *Physics Letters A* **354**, 236 (2006).

- [191] M. Xu, R. R. Alfano, "Random walk of polarized light in turbid media", *Physical Review Letters* **95**, 213901 (2005).
- [192] J. R. Ferraro and K. Nakamoto, "Introductory Raman spectroscopy" 2nd Ed, Academic Press, London, 2003.
- [193] E. Smith and G. Dent, "Modern Raman spectroscopy: A practical approach", Wiley, Chichester, 2005.
- [194] D. A. Long, "The Raman effect: A unified Treatment of the theory of Raman scattering by molecules", Wiley, Chichester, 2002.
- [195] G. W. King, "Spectroscopy and molecular structure", Holt, Rinehart and Winston, 1964.
- [196] M. Kerker, D.-S. Wang, and H. Chew, "Surface enhanced Raman scattering (SERS) by molecules adsorbed at spherical particles: errata". *Applied Optics* **19**, 4159 (1980).
- [197] D.-S. Wang and M. Kerker, "Enhanced Raman scattering by molecules adsorbed at the surface of colloidal spheroids", *Physical Review B* **24**, 1777 (1981).
- [198] P. L. Stiles, J. A. Dieringer, N. C. Shah, and R. P. Van Duyne, "Surface-enhanced Raman spectroscopy", *Annual Reviews of Analytical Chemistry* **1**, 601 (2008).
- [199] S. L. McCall, P. M. Platzman, and P. A. Wolff, "Surface enhanced Raman scattering", *Physics Letters A* **77**, 381 (1980).
- [200] T. M. Cotton, R. A. Uphaus, D. Mobius, "Distance dependence of surface-enhanced resonance Raman enhancement in Langmuir-Blodgett dye multilayers", *Journal of Physical Chemistry* **90**, 6071 (1986).
- [201] C. S. S. R. Kumar, "Raman spectroscopy for nanomaterials characterization", Springer, Verlag, 2012.
- [202] M. Moskovits and D. P. Dilella, "Intense quadrupole transitions in the spectra of molecules near metal surfaces", *Journal of Chemical Physics* **77**, 1655 (1982).

- [203] X.-M. Lin, Y. Cui, Y.-H. Xu, B. Ren, And Z.-Q. Tian, "Surface-enhanced Raman spectroscopy: Substrate-related issues", *Analytical and Bioanalytical Chemistry* **394**, 1729 (2009).
- [204] M. J. Natan, "Surface enhanced Raman scattering", *Faraday Discussions* **132**, 321 (2006).
- [205] M. Kadleikova, J. Breza, and M. Vesely, "Raman spectra of synthetic sapphire", *Microelectronics Journal* **32**, 955 (2001).
- [206] R. D. Lillie, "H. J. Conn's biological stains: A handbook on the nature and uses of the dyes employed in the biological laboratory", Williams & Wilkins, Baltimore, 1977.
- [207] E. J. Liang, X. L. Ye, and W. Kiefer, "Surface-enhanced Raman spectroscopy of crystal violet in the presence of halide and halate ions with near-infrared wavelength excitation", *Journal of Physical Chemistry A* **101**, 7330 (1997).
- [208] M. V. Canameres, C. Chenal, R. L. Birke, and J. R. Lombardi, "DFT, SERS, and single-molecule SERS of crystal violet", *Journal of Physical Chemistry C* **112**, 20295 (2008).
- [209] K. R. Lantz, "Organic/Inorganic hybrid nanocomposite infrared photodetection by intraband absorption", (Doctoral dissertation), Duke University, Durham, 2011.
- [210] I. Gontijo, M. Boroditsky, E. Yablonovitch, S. Keller, U. K. Mishra, and S. P. DenBaars, "Coupling of InGaN quantum-well photoluminescence to silver surface plasmons", *Physical Review B* **60**, 11564 (1999).
- [211] A. Neogi, C.-W. Lee, H. O. Everitt, T. Kuroda, A. Tackeuchi, and E. Yablonovitch, "Enhancement of spontaneous recombination rate in a quantum well by resonant surface plasmon coupling", *Physical Review B* **66**, 153305 (2002).
- [212] S. Kuhn, U. Hakanson, L. Rogobete, and V. Sandoghdar, "Enhancement of single-molecule fluorescence using a gold nanoparticle as an optical nanoantenna", *Physical Review Letters* **97**, 017402 (2006).

- [213] G. Sun, J. B. Khurgin, and D. P. Tsai, "Comparative analysis of photoluminescence and Raman enhancement by metal nanoparticles", *Optical Letters* **37**, 1583 (2013).
- [214] P. C. Wu, C. G. Khoury, T.-H. Kim, Yang Yang, M. Losurdo, G. V. Bianco, T. Vo-Dinh, A. S. Brown, and H. O. Everitt, "Demonstration of surface-enhanced Raman scattering by tunable, plasmonic gallium nanoparticles", *Journal of American Chemical Society* **131**, 12032 (2009).
- [215] G. Sun and J. B. Khurgin, "Comparative study of field enhancement between isolated and coupled metal nanoparticles: An analytical approach", *Applied Physics Letters* **97**, 263110 (2010).
- [216] G. Favaro, D. Confortin, P. Pastore, and M. Brustolon, "Application of LC-MS and LC-MS-MS to the analysis of photo-decomposed crystal violet in the investigation of cultural heritage materials aging", *Journal of Mass Spectrometry* **47**, 1660 (2012).
- [217] N. P. W. Pieczonka, and R. F. Aroca, "Inherent complexities of trace detection by surface-enhanced Raman scattering", *ChemPhysChem* **6**, 2473 (2005)
- [218] Y. Fang, N.-H. Seong, and D. D. Dlott, "Measurement of the distribution of site enhancements in surface-enhanced Raman scattering", *Science* **321**, 388 (2008).
- [219] Y. Fang, H. Yang, P. Jiang, and D. D. Dlott, "The distributions of enhancement factors in close-packed and nonclose-packed surface-enhanced Raman substrates", *Journal of Raman Spectroscopy* **43**, 389 (2012).
- [220] E. J. Bjerneld, F. Svedberg, P. Johansson, and M. Kall, "Direct observation of heterogeneous photochemistry on aggregated Ag nanocrystals using Raman spectroscopy: The case of photoinduced degradation of aromatic amino acids", *Journal of Physical Chemistry A* **108**, 4187 (2004).
- [221] Y. Maezono, I. Yousuke, K. Kurosawa, M. Katto, and A. Yokotani, "Damage threshold of acrylic polymer jackets surrounded with optical fiber by UV laser", *SPIE Proceedings* **6346**, 63462O (2007).

- [222] J. C. Hulteen, and R. P. Van Duyne, "Nanosphere lithography: A materials general fabrication process for periodic particle array surfaces", *Journal of Vacuum Science and Technology* **13**, 1553 (1995).
- [223] M. I. Mishchenko, G. Videen, V. A. Babenko, N. G. Khlebtsov, and T. Wriedt, "T-matrix theory of electromagnetic scattering by particles and its applications: a comprehensive reference database", *Journal of Quantitative Spectroscopy and Radiative Transfer* **88**, 357 (2004).
- [224] M. G. Blaber, M. D. Arnold, and M. J. Ford, "A review of the optical properties of alloys and intermetallics for plasmonics", *Journal of Physics: Condensed Matter* **22**, 143201 (2010).
- [225] V. A. Fedotov, V. I. Emel'yanov, K. F. MacDonald, and N. I. Zheludev, "Optical properties of closely packed nanoparticle films: spheroids and nanoshells", *Journal of Optics A: Pure and Applied Optics* **6**, 155 (2004).
- [226] A. Moreau, C. Ciraci, J. J. Mock, R. T. Hill, Q. Wang, B. J. Wiley, A. Chilkoti, and D. R. Smith, "Controlled-reflectance surfaces with film-coupled colloidal nanoantennas", *Nature* **492**, 86 (2012)
- [227] M. Pelton, J. Aizpurua, and G. Bryant, "Metal-nanoparticle plasmonics", *Laser and Photonics Reviews* **2**, 136 (2008).
- [228] J. Nelayah, M. Kociak, O. Stephan, F. J. Garcia de Abajo, M. Tence, L. Henrard, D. Taverna, I. Pastoriza-Santos, L. M. Liz-Marzan, and C. Colliex, "Mapping surface plasmons on a single metallic nanoparticle", *Nature Physics* **3**, 348 (2007).
- [229] N. Yamamoto, K. Araya, and F. J. Garcia de Abajo, "Photon emission from silver particles induced by a high-energy electron beam", *Physical Review B* **64**, 205419 (2001).
- [230] J. M. McMahon, G. C. Schatz, and S. K. Gray, "Plasmonics in the ultraviolet with the poor metals Al, Ga, In, Sn, Ti, and Bi", *Physical Chemistry Chemical Physics* **13**, 5415 (2013).

Biography

Name: Yang Yang
Place of Birth: Nanjing, China
Education: B.Sc. in Physics, Nanjing University, 2007
Ph.D. in Physics, Duke University, 2013

Fellowships:

Summer Research Fellowship, Duke University, 2013
Walter Gordy Fellowship, Duke University, 2012
Katherine Goodman Stern Fellowship, Duke University, 2012
Graduate Teaching Fellow, Duke University, 2010
Graduate Student Conference Travel Fellowships, Duke University, 2011, 2012, 2013
Chen-Ning Yang Fellowship, Nanjing University, 2006
First Class Fellowship for Students with Specialties, Nanjing University, 2006
Samsung Fellowship, Nanjing University, 2005
Fellowship of National Science Fund for Fostering Talents in Basic Research, Nanjing University, 2005
First Class Renmin Fellowship, Nanjing University, 2004

Publications:

Yang Yang, N. Akozbek, M. J. Bloemer, T.-H. Kim, M. Losurdo, A. S. Brown, and H. O. Everitt, "An investigation of the ultraviolet plasmonic properties of gallium nanoparticles by spectroscopic ellipsometry" (manuscript in process).

Yang Yang, M. Knight, N. Halas, J. S. Casado, F. Moreno, T.-H. Kim, A. S. Brown, and H. O. Everitt, "Cathodoluminescence characterization and T-matrix modeling of the interparticle coupling effect in the ultraviolet-active plasmonic gallium nanoparticles" (manuscript in process).

Yang Yang, J. M. Callahan, T.-H. Kim, A. S. Brown and H. O. Everitt, "Ultraviolet nanoplasmonics: a demonstration of surface-enhanced Raman spectroscopy, fluorescence, and photodegradation using gallium nanoparticles", *Nano Letters* **13**, 2837 (2013).

C. Yi, T.-H. Kim, W. Jiao, **Yang Yang**, A. Lazarides, K. Hingerl, G. Bruno, A. S. Brown, and M. Losurdo, "Evidence of plasmonic coupling in gallium nanoparticles/graphene/SiC", *Small* **8**, 2721 (2012).

P. Albella, B. Garcia-Cueto, F. Gonzalez, F. Moreno, P. C. Wu, T.-H. Kim, A. S. Brown, **Yang Yang**, H. O. Everitt, and G. Videen, "Shape matters: plasmonic nanoparticle shape enhances interaction with dielectric substrate", *Nano Letters* **11**, 3531 (2011).

P. C. Wu, C. G. Khoury, T.-H. Kim, **Yang Yang**, M. Losurdo, G. V. Bianco, T. Vo-Dinh, A. S. Brown, and H. O. Everitt, "Demonstration of surface-enhanced Raman scattering by tunable, plasmonic gallium nanoparticles", *Journal of American Chemical Society* **131**, 12032 (2009).

Yang Yang, Y. Pan, J. Zhou and S. Wang, "Demonstration of polarization using double color laser", *Physics Experimentation* **27**, 46 (2007).

Presentations:

Yang Yang, T.-H. Kim, N. Akozbek, A.S. Brown and H. O. Everitt, "Spectroscopic ellipsometric studies of randomly distributed plasmonic gallium nanoparticles", American Physical Society (APS) March Meeting 2013 G20.10, Baltimore MD, March 2013.

C. E. Yi, T.-H. Kim, **Yang Yang**, M. Losurdo, and A. S. Brown, "Ga nanoparticle/graphene platforms: plasmonic and charge transfer interactions", American Physical Society (APS) March Meeting 2013 R5.6, Baltimore MD, March 2013.

Yang Yang, J. Callahan, T.-H. King, M. Losurdo, G. Bruno, A. S. Brown and H. O. Everitt, "An effective medium formulation to estimate the plasmonic dispersion of a randomly distributed gallium nanoparticle ensemble", American Physical Society (APS) March Meeting 2012 Z18.8, Boston MA, March 2012.

M. Edirisooriya, T.-H. Kim, A. R. Dedigama, **Yang Yang** and A. S. Brown, "The electrical nature of structural defects in InSb synthesized by molecular beam epitaxy on Si (100) and GaAs (100)", Electronic Materials Conference (EMC) 2011 JJ5, Santa Barbara CA, June 2011.

C. E. Yi, T.-H. Kim, **Yang Yang**, and A.S. Brown, "Gallium nanoparticles decorating graphene: size selective growth and properties", Material Research Society (MRS) Spring Meeting 2011 M9.12, San Francisco CA, April 2011.

Yang Yang, J. Callahan, K. Lantz, J. Foreman, P. C. Wu, T.-H. King, A. S. Brown and H. O. Everitt, "Observation of UV surface-enhanced Raman spectra using Ga nanoparticles", American Physical Society (APS) March Meeting 2011 Q32.3, Dallas TX, March 2011.

Yang Yang, P.C. Wu, T-H. Kim, H.O. Everitt and A.S. Brown, 2010 Material Research Society Spring Meeting D8.6, San Francisco CA, April 2010.

Yang Yang, P. C. Wu, T.-H. Kim, A. S. Brown and H. O. Everitt, "Gallium nanoparticle plasmonics", American Physical Society (APS) March Meeting 2010 Y14.5, Portland OR, March 2010.

Yang Yang, "Students: made in China, contribute to the world", American Physical Society (APS) March Meeting 2010 T8.4 (invited), Portland OR, March 2010.